EAST EUROPEAN JOURNAL OF PHYSICS. 3. 608-616 (2026)
DOI:10.26565/2312-4334-2026-3-56 ISSN 2312-4334

LATERAL PHOTOEFFECT IN METAL–OXIDE–SEMICONDUCTOR STRUCTURES BASED ON MONOCRYSTALLINE SILICON

E.U. Arzikulov[1,2]*, R.M. Usanov[1], Sh.J. Quvondiqov[1], Teng Lui[1,2], D.T. Bobonov[3], S.A. Sattarov[1,3]

[1]*Samarkand State University named after Sharof Rashidov, 140001, University blv. 15, Samarkand, Uzbekistan*
[2]*School of Material Science and Engineering, Shenyang Aerospace University, 37 Daoyi South Avenue, Shenyang, China*
[3]*Jizzakh Polytechnic Institute, Jizzakh, Uzbekistan*
**Corresponding author email: eshkuvata@gmail.com*
Received June 10, 2026; revised August 10, 2026; accepted August 26, 2026

This paper presents the fabrication technology and experimental results of the lateral photoeffect (LPE) study in Co/SiO₂/n-Si⟨P, Zn⟩ metal-oxide-semiconductor (MOS) structures. The structures were prepared based on initial n-type silicon samples (ρ=1.05 Ω×cm), thermally annealed samples (ρ=1.07 Ω×cm), and highly Zn-compensated n-type silicon samples with specific resistivities of 5.04 Ω×cm, 156.86 Ω×cm, and 1800 Ω×cm, respectively. According to the experimental results, the dependence of the lateral photovoltage (LPV) magnitude on the distance between the contacts in the fabricated MOS structures exhibits a linear character. It was found that the maximum value of the lateral photovoltage increases significantly with increasing specific electrical resistivity in highly Zn-compensated n-type silicon samples. In particular, for the sample with ρ = 1800 Ω×cm, the maximum LPV reached ±16.83 mV at a distance of ±2.3 mm. This result demonstrates the high sensitivity of the LPE in structures based on highly compensated silicon. The obtained results are in good agreement with the energy band diagrams that consider the influence of deep energy levels associated with zinc atoms at the SiO₂/Si interface and the charge carrier concentration.
Keywords: *Lateral photoeffect; Highly compensated silicon; Metal-oxide-semiconductor structure; Lateral photovoltage; Interface states; Diffusion; Electron-beam evaporation; Thin film*

INTRODUCTION

The rapid development of science and technology in the modern era has significantly increased the demand for advanced materials with improved properties compared to existing ones. This trend has intensified the interest in the synthesis of new materials and the in-depth investigation of their physical characteristics. In particular, MOS structures play a crucial role in the development of modern nanoelectronics, high-sensitivity sensors, and position-sensitive detectors (PSDs) [1–3]. The LPE observed in MOS structures can be effectively utilized in the fabrication of PSDs [1–5]. The LPE is a phenomenon in which a photovoltage arises between the contacts when a focused light spot is incident on the semiconductor surface. The magnitude of this effect and its linear dependence on the distance between the contacts determine the accuracy and sensitivity of the detector.

In recent years, although the dependence of the LPE in MOS structures on the type and thickness of the metal and oxide layers has been relatively well investigated [2, 3, 5], its dependence on key semiconductor substrate parameters – such as the conductivity type, specific electrical resistivity, charge carrier concentration, and carrier mobility – remains insufficiently studied. In particular, the investigation of the LPE in MOS structures based on highly compensated silicon containing deep-level impurities is considered a highly relevant and topical issue.

Zinc (Zn) atoms, when diffused into silicon, create a series of deep acceptor and donor levels, significantly altering the electrophysical, recombination, and photoelectric properties of silicon [6, 7, 18]. As a result, highly compensated n-Si⟨P,Zn⟩ samples exhibit high specific resistivity (10^2–10^4 Ω×cm). Consequently, MOS structures fabricated on the basis of such samples can possess new functional properties.

The objective of this study is to develop the fabrication technology for Co/SiO₂/n-Si⟨P, Zn⟩ MOS structures and to experimentally determine how the resistivity of the semiconductor substrate affects the magnitude and sensitivity of the lateral photovoltage (LPV). Based on the above, the development of the fabrication technology for Co/SiO₂/n-Si⟨P, Zn⟩ MOS structures and the experimental study of the LPE in these structures, particularly the determination of the effect of specific resistivity on the magnitude and sensitivity of the LPV, are of significant scientific and practical importance. In this work, Co/SiO₂/n-Si⟨P⟩ and Co/SiO₂/n-Si⟨P, Zn⟩ MOS structures were synthesized on the basis of initial Silicone Electronic doped with Phosphorous (SEP-1).

Co/SiO₂/n-Si⟨P⟩ and Co/SiO₂/n-Si⟨P, Zn⟩ MOS Structure Fabrication Technology

To fabricate the Co/SiO₂/n-Si⟨P⟩ and Co/SiO₂/n-Si⟨P, Zn⟩ MOS structures, monocrystalline silicon (n-Si⟨P⟩) wafers doped with phosphorus atoms during crystal growth were initially used as substrates. The samples had dimensions of 8×4×1 mm³, a room-temperature resistivity of approximately 1 Ω×cm, and a crystallographic orientation of [111] along

Cite as: E.U. Arzikulov, R.M. Usanov, Sh.J. Quvondiqov, Teng Lui, D.T. Bobonov, S.A. Sattarov, East Eur. J. Phys. 3, 608 (2026), https://doi.org/10.26565/2312-4334-2026-3-56

the longitudinal direction. Subsequently, highly compensated n-Si⟨P, Zn⟩ samples exhibiting different conductivity types and a wide range of room-temperature electrical resistivities were synthesized. For the preparation of these samples, the high-temperature diffusion method was employed [19].

As is well known, the introduction of zinc atoms into silicon by the high-temperature diffusion method leads to the formation of acceptor levels with ionization energies of $E_v + 0.31$ eV and $E_v + 0.55$ eV. In addition, shallow acceptor levels with ionization energies of $E_v + 0.08$ eV, $E_i + 0.09$ eV, and $E_v + 0.13$ eV are formed, which are generally attributed to complexes of zinc atoms with Group III elements of the periodic table. In brief, the incorporation of zinc into silicon substantially alters its electrophysical, recombination, and photoelectric properties. As a result, highly compensated p(n)-Si<P, Zn> samples can be considered proMOSing novel materials for applications in modern micro- and nanoelectronics.

These same initial n-Si⟨P⟩ substrates (described above) were used for the diffusion process. Zinc with a purity of 99,96% was used as the diffusion source for introducing Zn atoms into the selected n-Si<P> samples. Using the temperature-dependent expressions for the diffusion coefficient and solubility of zinc in silicon, the diffusion temperature and duration required to obtain samples with different resistivities were determined in accordance with the procedure described in Ref. [19].

Highly compensated n-Si<P, Zn> samples were synthesized by the high-temperature diffusion method using a technique that takes into account the partial pressure of the diffusant vapor [20]. To remove the zinc-enriched surface layers formed during the high-temperature diffusion process, both mechanical and chemical treatment procedures were applied, and an average layer thickness of approximately 50 μm was removed from each side of the samples. As a result, relatively homogeneously doped, n-type, highly compensated n-Si<P, Zn> samples with room-temperature resistivities in the range of $10^2 \div 10^4$ Ω×cm were obtained. MOS structures were fabricated using the initial n-Si<P> samples, the n-Si<P> samples thermally annealed at the zinc diffusion temperature, and the synthesized highly compensated n-Si<P, Zn> samples. The primary objective of fabricating these structures was to distinguish and clarify the effects of thermal annealing and zinc incorporation on the measured characteristics.

The main parameters of the investigated samples before and after the diffusion process (electrical resistivity, mobility, and charge carrier concentration) were determined by Hall effect measurements. In this procedure, the native oxide layer on the initial samples and the zinc-enriched surface layers of the diffused samples were first removed. Subsequently, ohmic contacts were formed on the lateral sides of the samples using silver-based conductive adhesive. The corresponding measurements were then carried out as described in Ref. [9].

The parameters of the silicon samples before and after the diffusion process are presented in Table 1.

Table 1. Electrophysical parameters of the initial and Zn-diffused n-Si⟨P⟩ and n-Si⟨P, Zn⟩ samples before and after the diffusion process

Sample	ρ, Ω×cm	μ, $cm^2/(V \cdot s)$	n, cm^{-3}	Fermi level, eV
n–Si<P>, initial sample	1.05	1188.43	$5.01 \cdot 10^{15}$	0.254541
n–Si<P> (thermally annealed initial sample)	1.07	1167.32	$4.99 \cdot 10^{15}$	0.254659
n–Si<P, Zn>	5.04	650.8	$1.9 \cdot 10^{15}$	0.283144
n–Si<P, Zn>	156.86	690.26	$5.77 \cdot 10^{13}$	0.318301
n–Si<P, Zn>	1800	808	$4.28 \cdot 10^{12}$	0.39504

In the next stage, all samples whose parameters are presented in Table 2 were prepared for use as semiconductor substrates for the fabrication of MOS structures. The formation of the required oxide layer on the surface of these substrates was carried out in two steps. In the first step, the naturally formed oxide (SiO_2) layer resulting from various ambient processes was removed by immersing the samples in hydrofluoric acid (HF) for 15 s. The second step involved the growth of a silicon dioxide layer with a thickness of 2÷4 nm. This process was performed by immersing the samples (after the first step) in nitric acid (HNO_3) at a temperature of 121°C for 15 min [10]. It should be noted that oxidation in nitric acid is known to produce a relatively high density of oxide traps and interface states at the Si–SiO_2 interface [22].

After the formation of the SiO_2 oxide layer with the required thickness, a thin layer of metallic cobalt was deposited on top of it using electron-beam or thermal evaporation in vacuum, as well as magnetron sputtering techniques. The thickness of the metal layer was experimentally verified by spectroscopic ellipsometry. In this case, the oxide layer thickness was 3 nm, while the cobalt layer thickness was 10 nm.

For the investigation of the LFE in the synthesized Co/SiO_2/n-Si⟨P⟩ and Co/SiO_2/n-Si<P, Zn> MOS structures, the measurement setup described in Ref. [5] was used. The schematic diagram of the device is shown in Figure 1.

Since the magnitude of the LPV depends on parameters such as the charge carrier concentration and mobility in the semiconductor substrate, it was studied at optimal values of the metal and oxide layer thicknesses ($d_{ox} \approx 3$ nm, $d_m \approx 10$ nm). To measure the LPV, two point-like ohmic contacts were formed on the surface of the metal layer of all fabricated MOS structures using a conductive silver adhesive, as shown in Figure 1. A copper wire with a thickness of 50 μm was then placed onto this contact area, after which an additional layer of silver paste was applied and the structure was dried for 6 hours. After the silver paste had solidified, it was thermally treated using a Micro SET M RA laser welding system to ensure mechanical stability, resulting in a mechanically robust and reliable ohmic contact. The ohmicity of the

contacts was verified by measuring the current–voltage (I–V) characteristics between the contacts formed on the metal surface of the fabricated structures. Figure 1b presents the I–V characteristics of the thin Co layer in Co/SiO_2/n-Si<P, Zn> MOS structure based on an n-Si<P, Zn> substrate with a resistivity of 1800 Ω×cm. As can be seen, the dependence of the current flowing through the Co metal layer on the applied voltage between the surface contacts is linear.

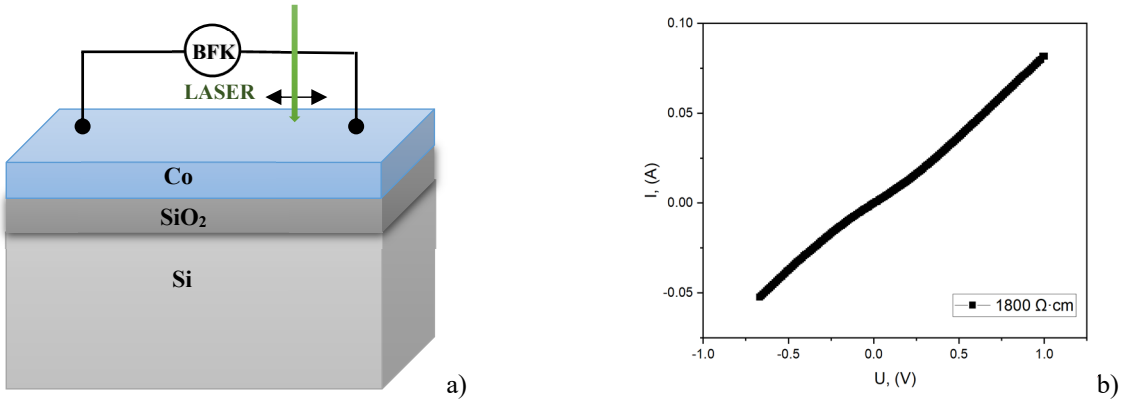

Figure 1. (a) Schematic view of the Co/SiO_2/n-Si hybrid structure and the measurement setup for lateral photovoltage, and (b) I–V characteristics of the metal layer of the Co/SiO_2/n-Si hybrid structure.

Experimental Results and Their Analysis

The I–V characteristics of the synthesized Co/SiO_2/n-Si<P> and Co/SiO_2/p(n)-Si<P, Zn> MOS structures were measured in the vertical direction with respect to the structure. In this configuration, one terminal of the external bias voltage source was connected to the ohmic contact formed on the thin metal film, while the other terminal was connected to the contact formed on the rear side of the semiconductor substrate. Subsequently, the polarity of the applied voltage source was reversed, and the I–V characteristics were measured again. The obtained results are presented in Figure 2.

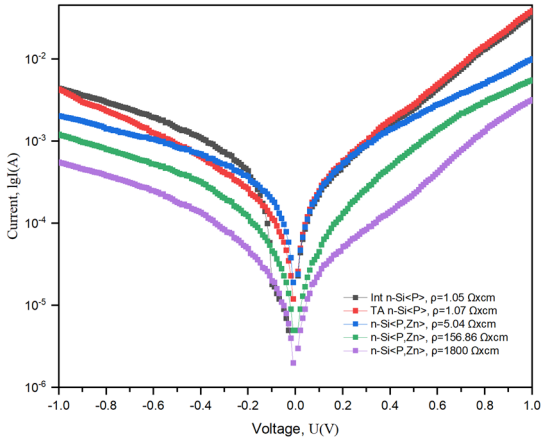

Figure 2. I–V characteristics of Co/SiO_2/n-Si<P> and Co/SiO_2/n-Si<P, Zn> MOS structures.

As can be seen from Figure 2, the I–V characteristics of the MOS structures fabricated on the initial samples, the samples annealed at the zinc diffusion temperature, and the samples with incorporated zinc atoms exhibit a typical behavior characteristic of such structures. Using the experimentally measured I–V characteristics of all synthesized Co/SiO_2/n-Si<P> and Co/SiO_2/n-Si<P, Zn> structures, the barrier height was calculated based on Refs. [11] and [12]. The calculated results are presented in Table 2.

Table 2. Schottky barrier heights of the Co/SiO_2/n–Si⟨P⟩ and Co/SiO_2/n–Si⟨P, Zn⟩ MOS structures, calculated from the I–V characteristics.

Q.s.	Structure	Resistivity of the Si substrate, Ω×cm	Potential barrier height, ϕ_B, eV
1	Co/SiO_2/n–Si<P> structure based on the initial sample	1.05	0.4734
2	Co/SiO_2/n–Si<P> structure based on the initial sample thermally annealed at 1150°C	1.07	0.4722
3	Co/SiO_2/n–Si<P, Zn> structure	5.04	0.4378
4	Co/SiO_2/n–Si<P, Zn> structure	156.86	0.5463
5	Co/ SiO_2/n–Si<P, Zn> structure	1800	0.4798

As can be seen from Table 2, a well-defined potential barrier is formed in the investigated samples. The differences in the barrier height values observed in the Co/SiO_2/n-Si<P, Zn> structures may be associated with the modification of impurity-induced surface states formed by zinc atoms, as well as changes in the charge states at the SiO_2/n-Si<P, Zn> interface.

Surface condition has a significant impact on the electrical parameters of MOS structures. Therefore, we studied the surface condition of a pure semiconductor substrate, a substrate with a tunnel-thin oxide layer, and a substrate with a thin metallic cobalt layer at room temperature using an FusionScope Scanning Electron Microscope (SEM). This modern SEM microscope allows for surface examination of substrates in both SEM and Atomic Force Microscopy (AFM) modes. The results are shown in Figure 3.

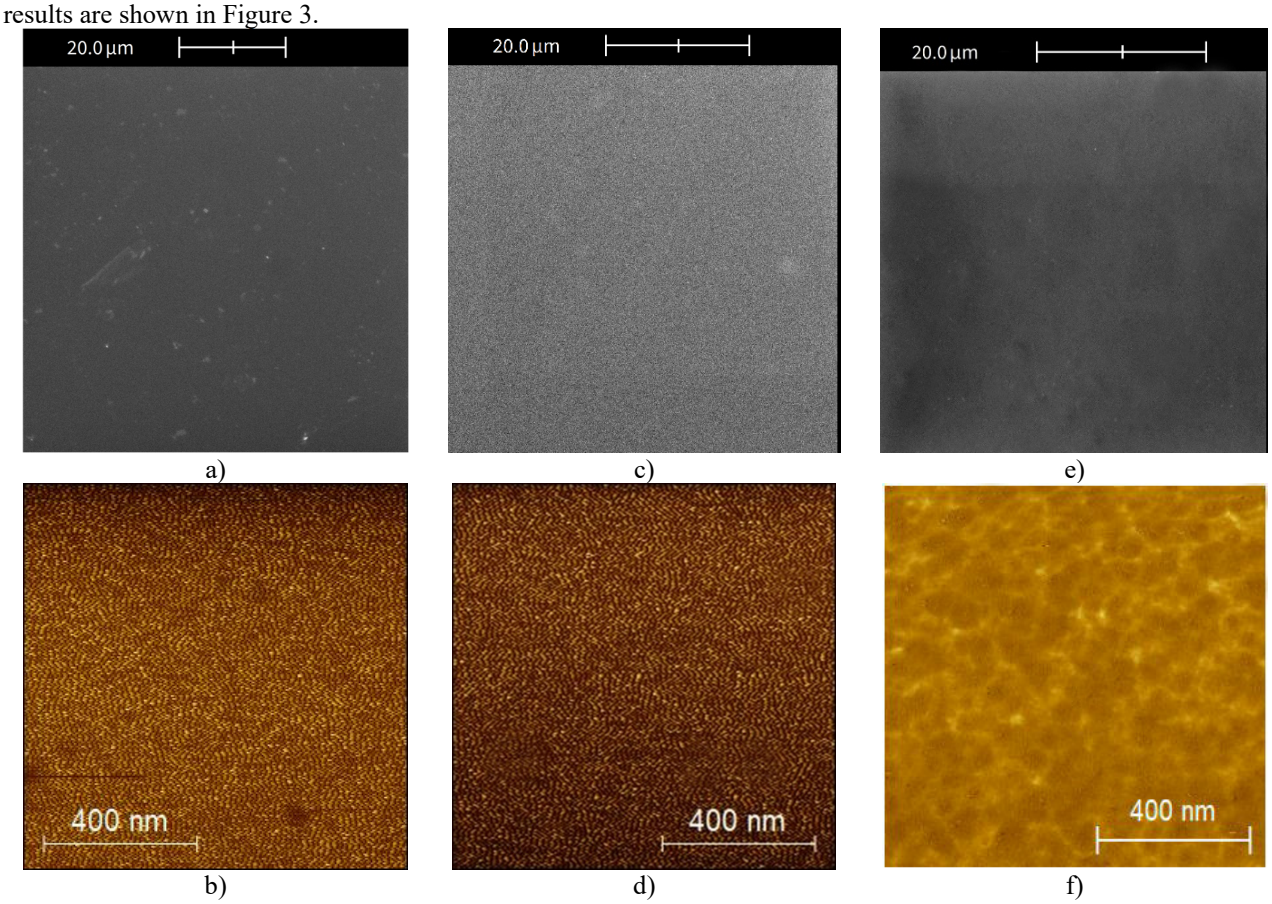

Figure 3. SEM and AFM images of the Co/SiO_2/n-Si hybrid structures: (a, b) initial silicon surface; (c, d) silicon surface after chemical cleaning; (e, f) SEM and AFM images of the cobalt thin films.

Figure 3 presents the surface morphology of the Co/SiO_2/n-Si hybrid structures at three critical stages: the initial state, post-chemical cleaning, and following the deposition of the Co thin film, as characterised by Scanning Electron Microscopy (SEM) and Atomic Force Microscopy (AFM). Figures 3(a) and 3(b) display the surface of the initial silicon substrate. The SEM micrograph (Figure 3a) reveals the presence of residual macroscopic particulate contaminants on the uncleaned surface. Corroborating this observation, the AFM topographical analysis (Figure 3b) demonstrates an initial root-mean-square (RMS) surface roughness (R_q) of 59.19 nm. Following the chemical cleaning procedure, a drastic morphological improvement is observed. The SEM image in Figure 3(c) shows the successful elimination of the surface impurities, yielding a highly pristine and uniform silicon surface. The corresponding AFM image (Figure 3d) confirms this planarization, exhibiting a substantial decrease in the surface roughness to 2,42 nm, thereby validating the efficacy of the chemical treatment. Figures 3(e) and 3(f) illustrate the surface characteristics after the Co thin film deposition. While the macroscopic SEM image (Figure 3e) suggests the formation of a highly smooth and uniform Co layer with an apparent roughness of 2.69 nm, the high-resolution AFM topography (Figure 3f) provides a deeper insight into the nanoscale growth dynamics. The AFM image reveals that the Co layer forms via the Volmer-Weber (island) [21] growth mechanism, characterised by discrete nanostructured formations. In the regime of ultra-thin metallic films, this island-like morphology plays a pivotal role in determining the electrical transport properties of the structure. The discrete granular nature of the film significantly enhances conduction electron scattering at the boundaries of these islands, which leads to a pronounced increase in the sheet resistance (R_s) of the metal layer.

The dependence of the measured LPV on the distance between the contacts in Co/SiO_2/n-Si<P> and Co/SiO_2/p-Si<P, Zn> MOS structures is shown in Figure 4.

As can be seen from the figure, in all investigated structures the dependence of the LPV on the distance between the contacts exhibits an approximately quasi-linear behavior.

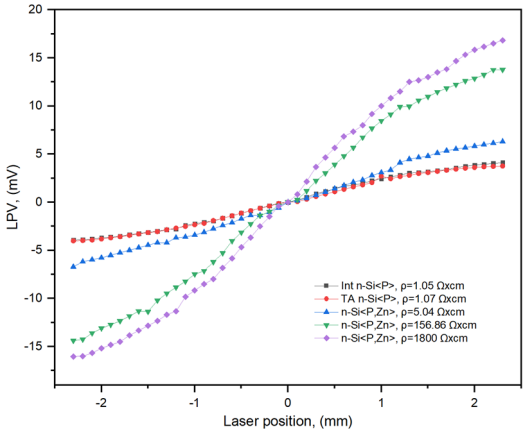

Figure 4. Dependence of the LPV magnitude on the laser beam position

To evaluate the linearity of such dependences, the nonlinearity coefficient δ and the correlation coefficient r, defined by the following expressions, are used [3].

$$Nonlinearity = \delta = \frac{2\times RMS}{maximum\ value\ of\ LPV}, \tag{1}$$

here, RMS denotes the standard deviation (root mean square deviation), and r is the correlation coefficient

$$y - \bar{y} = r\frac{\sigma_y}{\sigma_x}(x - \bar{x}), \tag{2}$$

where $\sigma_x, \sigma_y -$ are the standard (root mean square) deviations.

In addition, the sensitivity coefficient k, which determines the practical applicability of the investigated structures and is defined by the following expression, is calculated using Eq. (3):

$$k = \frac{d(LPV)}{dx}. \tag{3}$$

Under the given experimental conditions, it was found that the maximum LPV value in Co/SiO₂/n-Si<P>-based MOS structures strongly depends on the resistivity of the semiconductor substrate. In particular, in the initial and thermally treated Co/SiO₂/n-Si<P> samples with relatively low resistivity, the maximum LPV values were comparatively small, amounting to ±4.11 mV and ±3.76 mV, respectively. At the same time, in Co/SiO₂/n-Si<P, Zn> samples, the maximum LPV value increased significantly with increasing resistivity. For samples with resistivities of 5.04 Ω×cm, 156.86 Ω×cm, and 1800 Ω×cm, the corresponding LPV maxima reached ±6.31 mV, ±13.77 mV, and ±16.83 mV, respectively.

The values of the parameters related to nonlinearity for the dependence of the LPV on the distance between contacts in the synthesized Co/SiO₂/n-Si<P> and Co/SiO₂/p-Si<P, Zn> MOS structures, i.e., the quantities defined by Eqs. (1)-(3), were calculated based on the experimental results. The obtained calculation results are presented in Table 3.

Table 3. Position sensitivity (k), Correlation coefficient (r), and nonlinearity (δ) coefficients of the LPV response for the investigated Co/SiO₂/n–Si⟨P⟩ and Co/SiO₂/n–Si⟨P, Zn⟩ MOS structures

Sample	ρ, Ω×cm	k, mV/mm	r	δ, %
Co/SiO₂/n–Si<P>	1.05	1.9966	0.9944	7.18
Co/SiO₂/n–Si<P>	1.07	1.9504	0.9950	7.34
Co/SiO₂/p–Si<P,Zn>	5.04	2.9929	0.9976	4.43
Co/SiO₂/p–Si<P,Zn>	156.86	6.8451	0.9961	5.84
Co/SiO₂/p–Si<P,Zn>	1800	8.1887	0.9943	7.25

Within the scope of this study, the effect of the semiconductor substrate resistivity on the position sensitivity characteristics of Co/SiO₂/n-Si<P> and Co/SiO₂/p-Si<P, Zn> MOS structures was investigated. The obtained experimental results demonstrate that with an increase in resistivity, the position sensitivity coefficient k of the device increases from 1.9966 mV/mm to 8.1887 mV/mm. This behavior can be explained by the redistribution of charge carriers in high-resistivity samples.

The fact that the correlation coefficient r for all samples lies in the range 0,9943÷0,9976 confirms a sufficiently high degree of linearity between the LPV values and the coordinate. This represents an important advantage for the potential application of MOS structures as position-sensing devices.

The nonlinearity degree δ was found to vary in the range of 4.43% to 7.34%, remaining within the accepted technological criterion (δ < 15%) [13] in all cases. At the same time, the minimum nonlinearity value (4.43%) was observed for the sample with a resistivity of 5.04 Ω×cm, indicating an optimal operating regime of the device in this range. Although high-resistivity samples provide higher sensitivity, they are also characterized by a slight increase in nonlinearity, which indicates a trade-off between sensitivity and accuracy.

DISCUSSION OF EXPERIMENTAL RESULTS

To explain the obtained results from a physical point of view, the energy band diagrams of the investigated Co/SiO_2/n-Si<P> and Co/SiO_2/n-Si<P, Zn> structures were constructed theoretically in analogy with Ref. [4].

In a Me/SiO_2/Si structure, when the metal film is non-uniformly illuminated, the transmitted light generates electron–hole pairs in the illuminated region of silicon. These carriers then diffuse toward the existing space-charge region in silicon and are separated by the internal electric field of the structure. The magnitude and direction of this field depend on the value and sign of the built-in potential barrier $q\varphi_i$. This potential is determined by the difference between the work functions of the metal and silicon. It should be noted that the electron work function of silicon depends on the type and concentration of the doping impurity.

In this study, we used semiconductor substrates fabricated from industrial SEP-1 silicon, doped with phosphorus during crystal growth, as well as highly compensated n-Si<P, Zn> samples obtained by high-temperature diffusion. The electron work function of silicon can be estimated by the following equation:

$$q\varphi_s = q\chi_{Si} + (E_F - E_C), \tag{4}$$

here $q\chi_{Si} = 4.05\ eV$ −is the electron affinity of silicon, and $E_F - E_C$ − is the energy distance between the Fermi level and the conduction band edge. For the n-Si<P> case, $E_F - E_C$ − is determined by the expression: $E_F - E_C = kTln(N_C/N_D)$ where N_C is the effective density of states at the conduction band edge, which at 300 K is $N_C = 2.8 \cdot 10^{19}\ cm^{-3}$ [8], and N_D is the electron concentration in the sample at room temperature. For the n-Si<P> (111) sample with resistivity ρ = 1.05 Ω×cm, the donor concentration is $N_D = 5.01 \cdot 10^{15} cm^{-3}$ and $E_F - E_C = 0.22\ eV$. Accordingly, the electron work function is found to be 4.27 eV.

Similarly to the n-Si<P> sample, for n-Si<P, Zn> (111) samples with resistivities of ρ = 5.04, 156.86, and 1800 Ω×cm, the donor (electron) concentrations are $N_D = 1.9 \cdot 10^{15};\ 5.77 \cdot 10^{13};\ 4.28 \cdot 10^{12} cm^{-3}$, respectively. The corresponding values of $(E_F - E_C)$ are found to be 0.28 eV, 0.39 eV, and 0.46 eV.

For the energy band diagram of the Co/SiO_2/n-Si<P, Zn> structure, the following values can be obtained. For example, for an n-Si<P, Zn> sample with a room-temperature resistivity of ρ = 1800 Ω×cm, the donor concentration is $N_D = 4.28 \cdot 10^{12} cm^{-3}$ and $E_F - E_C = 0.46$. Consequently, the electron work function for this sample is 4.51 eV. Using the same approach, the electron work functions for the remaining n-Si<P, Zn> samples are found to be 4.33 eV and 4.44 eV, respectively.

Taking into account that the electron work function of cobalt is 4,40 eV, the resulting potential values in n-Si<P> and n-Si<P, Zn> samples are found to be 0.13 eV, 0.07 eV, −0.04 eV, and −0.06 eV, respectively. In the initial samples and in the n-Si<P, Zn> structure with a resistivity of 5.05 Ω·cm, the energy bands at the SiO_2/Si interface are bent upward, and the resulting internal electric field is directed from silicon toward the cobalt film.

Based on these data, the equilibrium band diagrams of the Co/SiO_2/n-Si<P> and Co/SiO_2/n-Si<P, Zn> structures were constructed, as shown in Figure 6. The analysis of the band diagrams indicates that in the Co/SiO_2/n-Si<P> structure, and in the Co/SiO_2/n-Si<P, Zn> structure with a resistivity of 5.05 Ω×cm, the upward band bending is more pronounced compared to the Co/SiO_2/n-Si<P, Zn> structures. In this case, $\varphi_S = E_i(0) - E_i = 0.13\ eV$ and $\varphi_F = E_F - E_i = 0.22\ eV$, and since $\varphi_S < \varphi_F$, an accumulation layer is formed at the SiO_2/Si interface instead of an inversion layer. In contrast, in Co/SiO_2/n-Si<P, Zn> structures with resistivities of 156.86 and 1800 Ω×cm, the bands are bent downward, leading to the formation of a depletion layer at the SiO_2/Si interface (Figure 6b). In this case, the internal electric field is directed from the thin cobalt film toward the silicon substrate. This, in turn, results in the drift of photogenerated holes toward the SiO_2/Si interface in the initial Co/SiO_2/n-Si<P> structure and in the Co/SiO_2/n-Si<P, Zn> structure with 5.05 Ω×cm resistivity, whereas in the Co/SiO_2/n-Si<P, Zn> structures with resistivities of 156,86 and 1800 Ω×cm, electrons are attracted toward this interface.

Figures 6(a) and 6(b) show the energy band diagrams of the Co/SiO_2/n-Si<P> and Co/SiO_2/n-Si<P, Zn> structures, respectively, taking into account interface states.

These figures clearly show that, for Co/SiO_2/n-Si<P, Zn> structures with resistivities of 156.86 and 1800 Ω×cm, taking into account interface states leads to negative potential values ($q\varphi_i = -0.04\ eV\ and\ -0.06\ eV$, respectively) and a reversal of the band bending direction. As a result, a depletion n-type layer is formed at the SiO_2/Si interface. The direction of the electric field is also reversed, so that, unlike the ideal case, photogenerated holes rather than electrons are attracted toward the SiO_2/Si interface. For the Co/SiO_2/n-Si<P> structure, the band bending is reduced to about 0.03 eV, and, as in the ideal case, no inversion layer is formed at the SiO_2/Si interface (as shown in Figure 6a), where $\varphi_S = 0.13\ eV$, $\varphi_F = 0.22\ eV$ and $\varphi_S < \varphi_F$. Thus, considering only interface states at the SiO_2/Si boundary leads to different directions

of the internal electric field in Co/SiO₂/n-Si<P> and Co/SiO₂/n-Si<P, Zn> structures, which in turn results in corresponding changes in the current transport mechanisms in the investigated structures.

As can be seen from Figure 4, under the given conditions, the observed maximum value of the LPV in the Co/SiO₂/p-Si<P, Zn> structure is approximately four times higher than that in the Co/SiO₂/n-Si<P> structure.

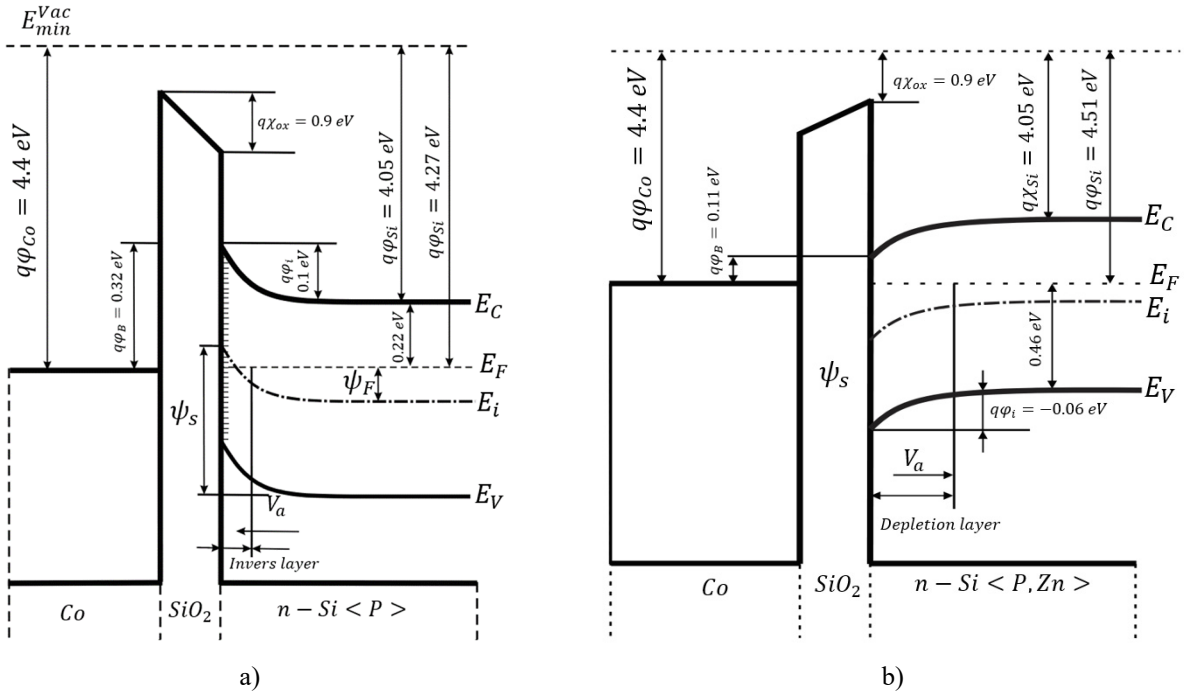

Figure 6. Energy band diagrams of Co/SiO₂/n-Si<P> (a) and Co/SiO₂/n-Si<P, Zn> (b) structures at the SiO₂/Si interface, taking into account interface states

These values correspond to the ohmic contact region and show a significant deviation from the results reported for similar structures investigated in other studies [2]. Such a pronounced difference in the results may be attributed to several factors. The first possible reason is the difference in the laser beam power used in our study and in other works [2,3] on LPV investigation. The LPV value strongly and nonlinearly depends on the incident laser power; in particular, an increase in laser power leads to an increase in LPV, which can cause significant discrepancies between the measured values in different studies. The second reason may be the differences in the thicknesses of the oxide and metal layers in the investigated structures. These layer thicknesses have a strong influence on the LPV magnitude [2]. The third reason may be the differences in the semiconductor substrate parameters used in the fabrication of the structures, such as charge carrier concentration and mobility, as well as the differences in interface states at the SiO₂/Si boundary compared to those reported in other studies [4]. All the factors mentioned above may lead to significant differences in the obtained experimental results.

When the structure is illuminated, the reduction of the potential barrier is determined by the following expression [4]:

$$qV_a = kT\ln\left[1 + \frac{F_0}{sn_0}\left(1 - \frac{\exp(-\alpha d)}{1+\alpha L_{eff}}\right)\right], \tag{5}$$

here k is the Boltzmann constant, T is the temperature, q is the electron charge, F_0 is the photon flux density incident on the silicon surface, $s = \vartheta_T/4$ (where $\vartheta_T -$ is the average thermal velocity of charge carriers), $n_0 -$ is the concentration of majority carriers at the SiO₂/n-Si interface under dark conditions, $\alpha -$is the optical absorption coefficient, $d -$is the space-charge region width, and $L_{eff} -$ is the effective diffusion length of minority carriers. By substituting the values of the majority carrier concentration at the SiO₂/Si interface for the Co/SiO₂/n-Si<P> and Co/SiO₂/n-Si<P, Zn> structures into Eq. (1), the following approximately values of qV_a are obtained: ~$1.34\cdot10^{-9}$ eV and ~$2.21\cdot10^{-9}$ eV, respectively.

As noted above, in Co/SiO₂/n-Si<P> and Co/SiO₂/n-Si<P, Zn> structures, a linear relationship between the laser spot position and the lateral photovoltage is observed in some cases, while in other structures an exponential decay behavior is also present. Such dependences can be explained by the fact that the metal film on the structure surface serves only to induce band bending in the silicon near the SiO₂/Si interface, whereas the LPV generation process takes place in the near-surface region of silicon. Depending on the degree of band bending, accumulation, depletion, or inversion layers are formed in the subsurface region of silicon, leading to the formation of p–n, p^-–n–, (n^-–n) or p^+–n, (n^+–n), etc. junctions, to which the theory of the LPV effect can be applied. For example, in the Co/SiO₂/n-Si<P> structure, an inversion layer and a p–n junction formed by the silicon bulk are created at the SiO₂/Si interface. In this case, excess photogenerated

carriers act as majority carriers in both p- and n-type regions. For this structure, the diffusion theory of the LPV effect, based on the continuity equation of the total current of majority carriers and the linear dependence of LPV on the light spot position, can be derived and is given in the following form [4]:

$$LPV = K_1\left[e^{\beta|\varphi_i|}\right](|x_1| - |x_2|), \quad (6)$$

Here K_1 – is the proportionality coefficient, β=q/(kT), φ_i – is the built-in potential, and x_1, x_2 – are the distances from the illumination point to the contacts. From Eq. (6), it can be seen that the magnitude of the LPV increases exponentially with an increase in the generated potential and becomes zero at the midpoint between the contacts (i.e., when $x_1 = x_2$), exhibiting a linear variation across the contact spacing. This behavior is experimentally observed in Co/SiO_2/n-Si<P> and Co/SiO_2/n-Si<P, Zn> structures, as shown in Figure 4.

CONCLUSIONS

In this study, Zn atoms were introduced into initial KEF-1 n-Si⟨P⟩ samples (ρ ≈ 1.05 Ω×cm) using a high-temperature diffusion method, resulting in the synthesis of strongly compensated n-Si⟨P, Zn⟩ samples with various resistivity levels (ρ = 5.04, 156.86, and 1800 Ω×cm). Based on these substrates, Co/SiO_2/n-Si⟨P, Zn⟩ MOS structures were fabricated, and a reproducible technology for their preparation was developed.

Based on the obtained results, it can be concluded that by optimizing the resistivity of the semiconductor substrate in Co/SiO_2/n-Si<P, Zn> MOS structures, it is possible to develop position-sensitive devices with high sensitivity. These findings broaden the prospects for the application of MOS-based PSD devices in optoelectronic and sensor systems requiring high precision.

In Co/SiO_2/n-Si⟨P, Zn⟩ MOS structures, an increase in the resistivity of the n-Si⟨P, Zn⟩ substrate has a significant influence on the fundamental physical mechanisms of the LPV effect. The experimental results showed that the dependence of LPV on the distance between contacts exhibits a highly accurate linear behavior in the fabricated structures. With increasing resistivity, a substantial increase in the maximum LPV value was observed. In particular, the maximum LPV value of ±4.11 mV in the initial n-Si⟨P⟩ samples increased to ±16.83 mV in the highly compensated sample with ρ = 1800 Ω×cm, corresponding to an approximately fourfold enhancement. At the same time, the position sensitivity coefficient increased from k = 1.9966 V/mm to 8.1887 V/mm. The correlation coefficient ranged within r = 0.9943–0.9976, confirming a high degree of linearity, while the nonlinearity remained within δ = 4.43–7.34%, fully satisfying the accepted technological criterion (δ < 15%).

The obtained results are in good agreement with the energy band diagrams constructed by taking into account the interface states at the SiO_2/Si boundary and the redistribution of charge carrier concentration. In MOS structures fabricated on strongly compensated (high-resistivity) silicon substrates obtained via Zn diffusion, an efficient formation of the internal electric field and redistribution of charge carriers occur, which leads to a significant enhancement of LPV sensitivity.

The results of this study demonstrate the potential application of MOS structures based on Zn-high compensated n-Si⟨P, Zn⟩ as proMOSing materials for the development of position-sensitive detectors (PSDs), high-precision optoelectronic sensors, and nanoelectronic devices. Furthermore, these findings establish a scientific basis for designing high-sensitivity, high-linearity, and high-accuracy devices by further tailoring the semiconductor substrate resistivity and interface states in MOS structures.

It is worth noting that some commercially available position-sensitive detectors, as well as certain devices reported in the literature, reportedly employ silicon substrates with considerably higher resistivity than the maximum investigated in the present work. It should be emphasized, however, that the present study already covers a broad resistivity range — from ~1 Ω×cm in the initial n-Si ⟨P⟩ samples to 1800 Ω×cm in the highly Zn-compensated samples; extending this range toward even higher resistivities represents a promising direction for future research. It is also worth noting that, based on the physical mechanism underlying the LPE, deep-level-compensated silicon substrates such as those used in this study are expected to provide considerably higher LPV sensitivity than nominally pure (uncompensated) high-resistivity silicon of comparable resistivity, owing to the more efficient formation of the internal electric field associated with deep-level compensation; a direct experimental comparison between the two substrate types remains an interesting subject for future work. In addition, since the SiO_2 layer in this work was formed by oxidation in nitric acid, exploring alternative oxidation methods to further reduce interface-state density and improve device performance represents another promising direction for our future research.

ORCID

E.U. Arzikulov, https://orcid.org/0000-0001-9179-3402; **R.M. Usanov,** https://orcid.org/0000-0003-2738-7535

REFERENCES

[1] Wallmark, J. "A New Semiconductor Photocell Using Lateral Photoeffect," Proc. IRE, **45**, 474–483 (1957). https://doi.org/10.1109/JRPROC.1957.278435

[2] Xiao, S.Q., Wang, H., Zhao, Z.C., Gu, Y.Z., Xia, Y.X., and Wang, Z.H. "The Co-Film-Thickness Dependent Lateral Photoeffect in Co-SiO_2-Si Metal-Oxide-Semiconductor Structures," Opt. Express, **16**, 3798 (2008). https://doi.org/10.1364/OE.16.003798

[3] Xiao, S.Q., Wang, H., Yu, C.Q., Xia, Y.X., Lu, J.J., Jin, Q.Y., and Wang, Z.H. "A Novel Position-Sensitive Detector Based on Metal–Oxide–Semiconductor Structures of Co–SiO_2 –Si," New J. Phys. **10**, 033018 (2008). https://doi.org/10.1088/1367-2630/10/3/033018
[4] T.A. Pisarenko, V.V. Balashev, V.A. Vikulov, A.A. Dimitriev, and V.V. Korobtsov, "Comparative Study of the Lateral Photovoltaic Effect in Fe_3O_4/SiO_2/n-Si and Fe_3O_4/SiO_2/p-Si Structures," Phys. Solid State, **60**, 1316–1322 (2018). https://doi.org/10.1134/S1063783418070223
[5] Arzikulov, E.U., Nurimov, A.D., Salakhitdinov, F.A., Ashirov, U.A., Sharafova, T.S., Khujanov, A.Sh., Usanov, R.M., "Lateral Photoelectric Effect In Iron-Silicon Dioxide-Compensated Silicon Hybrid Structures," East Eur. J. Phys. (4), 159–166 (2023). https://doi.org/10.26565/2312-4334-2023-4-17
[6] Fuller, C.S., and Morin, F.J., "Diffusion and Electrical Behavior of Zinc in Silicon," Phys. Rev. **105**, 379–384 (1957). https://doi.org/10.1103/PhysRev.105.379
[7] R.O. Carlson, "Double-Acceptor Behavior of Zinc in Silicon," Phys. Rev. **108**, 1390–1393 (1957). https://doi.org/10.1103/PhysRev.108.1390
[8] S.M. Sze, and K.K. Ng, *Physics of Semiconductor Devices*, 3rd ed. (Wiley-Interscience, Hoboken, N.J, 2007).
[9] E.V. Kuchis, *Galvanomagnetic Effects and Methods of Their Investigation*, (Radio i Svyaz Publishers, Moscow, 1990).
[10] H. Angermann, "Conditioning of Si-Interfaces by Wet-Chemical Oxidation: Electronic Interface Properties Study by Surface Photovoltage Measurements," Appl. Surf. Sci. **312**, 3–16 (2014). https://doi.org/10.1016/j.apsusc.2014.05.087
[11] A.R. Deniz, Z. Çaldıran, Ö. Metin, K. Meral, and Ş. Aydoğan, "The Investigation of the Electrical Properties of Fe_3O_4/n-Si Heterojunctions in a Wide Temperature Range," J. Colloid Interface Sci. **473**, 172–181 (2016). https://doi.org/10.1016/j.jcis.2016.04.006
[12] S.K. Cheung, and N.W. Cheung, "Extraction of Schottky Diode Parameters from Forward Current-Voltage Characteristics," Appl. Phys. Lett. **49**, 85–87 (1986). https://doi.org/10.1063/1.97359
[13] E. Fortunato, G. Lavareda, R. Martins, F. Soares, and L. Fernandes, "Large-Area 1D Thin-Film Position-Sensitive Detector with High Detection Resolution," Sens. Actuators Phys. **51**, 135–142 (1995). https://doi.org/10.1016/0924-4247(95)01214-1
[14] R. Cong, S. Qiao, J. Liu, J. Mi, W. Yu, B. Liang, G. Fu, *et al*., "Ultrafast, and Self-Powered Visible-Near-Infrared Optical Position-Sensitive Detector Based on a CVD-Prepared Vertically Standing Few-Layer MoS_2 /Si Heterojunction," Adv. Sci. **5**, 1700502 (2018). https://doi.org/10.1002/advs.201700502
[15] X. Dong, D. Zheng, J. Lu, Y. Niu, and H. Wang, "Selectively Enhanced Violet and Infrared Position Sensitive Photodetectors Based on RTA Treated ZnO/Si," Appl. Surf. Sci. **566**, 150687 (2021). https://doi.org/10.1016/j.apsusc.2021.150687
[16] X. Wang, B. Song, M. Huo, Y. Song, Z. Lv, Y. Zhang, Y. Wang, *et al*., "Fast and Sensitive Lateral Photovoltaic Effects in Fe_3O_4/Si Schottky Junction," RSC Adv. **5**, 65048–65051 (2015). https://doi.org/10.1039/C5RA11872G
[17] J.R. Sun, C.M. Xiong, B.G. Shen, P.Y. Wang, and Y.X. Weng, "Manganite-Based Heterojunction and Its Photovoltaic Effects," Appl. Phys. Lett. **84**, 2611–2613 (2004). https://doi.org/10.1063/1.1702128
[18] M.K. Bakhadyrkhanov, N.F. Zikrillaev, and E.U. Arzikulov, "Influence of diffusant vapor pressure on the concentration of electroactive atoms and the degree of compensation in Si⟨Zn⟩ samples," Pis'ma v ZhTF, **17**(12). 1–4 (1991). (in Russian)
[19] M.K. Baxadirxanov, N.F. Zikrillayev, and E.U. Arzikulov, "Vliyaniye uprugosti parov diffuzanta na konsentrasiyu elektroaktivnыx atomov i stepen kompensasii obrazsov Si⟨Zn⟩," Pisma v JTF, **17**(12), 1–4 (1991). (in Russian)
[20] Q.S. Ayupov, M.K. Baxadirxanov, N.F. Zikrillaev, and X.M. Iliev, *Physical phenomena in silicon in an extremely non-equilibrium state*, (Lambert Academic Publishing, 2019).
[21] Y. Shiratsuchi, T. Murakami, Y. Endo, and M. Yamamoto, "Evolution of Magnetic State of Ultrathin Co Films with Volmer–Weber Growth," Jpn. J. Appl. Phys. **44**(12R), 8456 (2005). https://doi.org/10.1143/JJAP.44.8456
[22] H.K. Asuha, O. Maida, M. Takahashi, and H. Iwasa, "Nitric acid oxidation of Si to form ultrathin silicon dioxide layers with a low leakage current density," J. Appl. Phys. **94**(11), 7328–7335 (2003). https://doi.org/10.1063/1.1621720

ЛАТЕРАЛЬНИЙ ФОТОЕФЕКТ У СТРУКТУРАХ МЕТАЛ–ОКСИД–НАПІВПРОВІДНИК НА ОСНОВІ МОНОКРИСТАЛІЧНОГО КРЕМНІЮ

Е.У. Арзікулов[1,2], Р.М. Усанов[1], Ш.Дж. Кувондіков[1], Тенг Луй[1,2], Д.Т. Бобонов[3], С.А. Саттаров[1,3]
[1]Самаркандський державний університет імені Шарофа Рашидова,
140001, Університетський бульвар, 15, Самарканд, Узбекистан
[2]Школа матеріалознавства та інженерії, Шеньянський аерокосмічний університет,
проспект Даої Саут, 37, Шеньян, Китай
[3]Джизакський політехнічний інститут, Джизак, Узбекистан

У цій статті представлено технологію виготовлення та експериментальні результати дослідження латерального фотоефекту (ЛФЕ) в метал-оксид-напівпровідникових (МОП) структурах Co/SiO_2/n-Si⟨P, Zn⟩. Структури були виготовлені на основі вихідних зразків кремнію n-типу (ρ=1,05 Ом×см), термічно відпалених зразків (ρ=1,07 Ом×см) та висококомпенсованих Zn зразків кремнію n-типу з питомим опором 5,04 Ом×см, 156,86 Ом×см та 1800 Ом×см відповідно. Згідно з експериментальними результатами, залежність величини латеральної фото-ерс (ЛФЕ) від відстані між контактами у виготовлених МОН-структурах має лінійний характер. Було виявлено, що максимальне значення латеральної фото-ерс значно зростає зі збільшенням питомого електричного опору у висококомпенсованих Zn зразках кремнію n-типу. Зокрема, для зразка з ρ = 1800 Ом×см максимальне ЛФЕ досягло ±16,83 мВ на відстані ±2,3 мм. Цей результат демонструє високу чутливість ЛФЕ в структурах на основі висококомпенсованого кремнію. Отримані результати добре узгоджуються з діаграмами енергетичних зон, які враховують вплив глибоких енергетичних рівнів, пов'язаних з атомами цинку на межі розділу SiO_2/Si, та концентрацію носіїв заряду.

Ключові слова: *латеральний фотоефект; висококомпенсований кремній; структура метал-оксид-напівпровідник; латеральна фотоенергія; стани на межі розділу; дифузія; електронно-променеве випаровування; тонка плівка*

East European Journal of Physics. 3. 617-628 (2026)
DOI:10.26565/2312-4334-2026-3-57 ISSN 2312-4334

ELECTRICAL, MECHANICAL AND OPTICAL PROPERTIES OF POLYAMIDE-6 COMPOSITES WITH CARBON NANOTUBES UNDER IRRADIATION

T.M. Pinchuk-Rugal[1], O.P. Dmytrenko[1], M.P. Kulish[1], A.I. Misiura[1,2]*, A.I. Momot[1], M.A. Alieksandrov[3], I. M. Danylenko[3], Yu.A. Onanko[4], O.M. Melnychenko[5]

[1]*Taras Shevchenko National University of Kyiv, 64, Volodymyrska St., 01033 Kyiv, Ukraine*
[2]*E.O. Paton Electric Welding Institute of NAS of Ukraine, 11 Kazymyra Malevycha St., 03680 Kyiv, Ukraine*
[3]*V.E. Lashkaryov Institute of Semiconductor Physics of NAS of Ukraine, 41, Nauky ave., Kyiv, 03028, Ukraine*
[4]*Department of Drainage, Institute of Water Problems and Land Reclamation of the National Academy of Agrarian Sciences of Ukraine, 37 Vasylkivska Str., Kyiv, 03022, Ukraine*
[5]*SE "RADMA", L.V. Pisarzhevsky Institute of Physical Chemistry of NAS of Ukraine, 31, pr. Nauky Ave., 03680 Kyiv, Ukraine*
**Corresponding Author e-mail: andrii_misiura@ukr.net*
Received March 26, 2026; revised August 15, 2026; accepted August 28, 2026

The dependence of the degree of crystallinity, the dynamic mechanical modulus, and the shear at frequency of ~1 MHz on the content of nanotubes was investigated for unirradiated PA-6/MWCNT nanocomposites. An increase in the degree of crystallinity and a decrease in these moduli with increasing CNT content were found, which is explained by the fact that CNTs in the polymer matrix act as nucleation centers of the crystalline *α*-phase, as well as nanoparticles disrupting interatomic bonds in chains and between macromolecules. These nanocomposites were irradiated with electrons $E_e \approx 1.8$ MeV and an absorption dose of 10 MRad (100 kGy), 20 MRad (200 kGy). The dependence of electrical conductivity, dynamic mechanical moduli, Raman scattering, and fast photoluminescence emission on the CNT content was measured. Irradiation has been shown to have complex effects on the properties mentioned above. Electrons can contribute to both the destruction of chains and the establishment of the crystalline phase, as well as the healing of damage caused by nanotubes through the recombination of electrons with free radicals. Radiation functionalization often leads to changes in the Raman spectra and the energy structure of electrons within the band gap. These changes are associated with the presence of local states related to the amorphous phase and structural defects. The restructuring of the FL spectra can also be affected, potentially impacting the formation of the conducting cluster.
Keywords: *Polyamide-6; Nanocomposites; Electrical conductivity; Degree of crystallinity; Dynamic moduli; Raman spectra; Fluorescence; Electron irradiation*

1. INTRODUCTION

Polyamides belong to a widespread class of acyclic and alicyclic polymers that include alkanes and amide groups –*NH–C–O*. These polymers have a simpler molecular structure with single numbering [1] and a more complex structure defined by double numbering [2]. The presence of polypeptide bonds in polyamides resembles the structure of proteins, and therefore, such polymers can serve as a model for studying the structural features of these biosystems. Among polyamides, polyamide-6 (PA-6, nylon-6) is the most affordable and widely used in various industries, especially in textiles and medicine. Polyamide-6 is characterized by a wide range of important physical and mechanical properties and high thermal and chemical resistance.

PA-6 is susceptible to the formation and rearrangement of crystalline phases with temperature changes. Thus, upon rapid cooling from the melt to low temperatures, crystallization occurs, forming a metastable γ phase. Its peculiarity is the close values of the lattice basis parameters ($\overrightarrow{|a|} \approx \overrightarrow{|b|}$), due to the twisting of the macromolecular chains. When the temperature is increased to 130 °C, a transition to a more stable *α*-phase with a triclinic structure is observed. This phase is characterized by a significant difference in the lattice parameters $\overrightarrow{|a|} \neq \overrightarrow{|b|}$. At a Brill temperature of $T_{Brill} \approx 160$ °C, a Brill transition is observed in the α-phase, where $\overrightarrow{|a|} \approx \overrightarrow{|b|}$. In addition, a transition from the crystalline *α*-phase to the *α*-phase with a pseudohexagonal structure is possible with increasing temperature [3, 4]. In contrast to the *γ*-phase, for which X-ray diffraction shows the presence of only one peak at $2\theta = 21.5°$ for λ_{Cu}, a similar pattern indicates the appearance of two peaks 200 ($2\theta = 20.13°$) and 002/202 ($2\theta = 23.85°$) [5].

For PA-6 fibers, the crystallization temperature $T_c = 189$°C and the melting point corresponding to reheating $T_m = 222$°C, respectively, the melting enthalpy $\Delta H_{M2} = 52$ J/g [6]. The sintering temperature for the amorphous component is $T_g = 54$°C. The tensile modulus is 2590 MPa at an elongation of about 100%.

Physical properties of PA-6, whose molecular structure is given by:

$$[–NH–C–O–(CH_2)_5]_n$$

depend significantly on the presence of a polar group capable of forming an interchain hydrogen bond (N-H...O=C), which largely determines the crystal polymorphism. The presence of such bonds in the *α*-phase is accompanied by features of the sheet structure.

Cite as: T.M. Pinchuk-Rugal, O.P. Dmytrenko, M.P. Kulish, A.I. Misiura, A.I. Momot, M.A. Alieksandrov, I.M. Danylenko, Yu.A. Onanko, O.M. Melnychenko, East Eur. J. Phys. 3, 617 (2026), https://doi.org/10.26565/2312-4334-2026-3-57

The appearance of such sheets leads to the indicated asymmetry of the lattice base plane in comparison with its higher energy for the γ-phase. The presence of different phases of amide polar groups in the chains of hydrogen bonds between macromolecules indicates the possibility of a wide modification of PA-6 properties due to the structural and radiation functionalization of this polymer, which is accompanied by changes in the important properties of these materials. Numerous studies have shown that one of the potentially most important materials for structural functionalization of polyomides is multi-walled carbon nanotubes (MWCNTs), which are characterized by high strength, thermal and electrical conductivity, and are affordable nanostructures [7, 8]. A significant effect on the modification of polyamide properties also occurs when irradiated with γ-photons [9]. At the same time, most studies on the structural and radiative functionalization of polyamides are aimed at studying mechanical and calorimetric properties and, to some extent, various photophysical changes, such as fluorescence, which is of considerable interest.

The aim of this work is to study the electrical conductivity and optical properties of polyamide-6 and its composites with MWCNTs under radiation functionalization via high-energy electron irradiation, to establish the mechanisms underlying the modification of these properties with increasing dose rate.

2. MATERIALS AND METHODS

The composites investigated were based on polyamide 6 (PA-6) filled with multi-walled nanotubes (MWNTs). The composite samples were obtained by hot pressing; for this purpose, a mechanical mixture of polymer powder and nanotubes was placed in a closed metal mold at T = 230°C and an external pressure of 30 MPa. The samples were obtained as discs with a diameter of 30 mm and a thickness of approximately 2 mm. The concentrations were 0-0.015 vol. pt. of MWCNTs.

The crystal structure of PA-6/MWCNT nanocomposites was determined using an X-ray diffractometer (DRON-3 M) with monochromatic CuKα (λ = 0.154178 nm) radiation.

To investigate the mechanical properties of PA-MWCNT nanocomposites, a computerized ultrasonic velocity meter KERN-4 was used. The dynamic Young's modulus was determined by the formula $E = \rho V^2_l$, where ρ is the density of the sample, V_l is the velocity of quasi-longitudinal elastic ultrasonic waves. The dynamic shear modulus was obtained by the equation: $G = \rho V^2_{tr}$, where V_{tr} is the velocity of quasi-transverse ultrasonic elastic waves.

The Raman and FL spectra were recorded using a Horiba Jobin Yvon T64000 triple spectrometer (Japan) with Ar-Kr ion (λ_L=488 nm) and He-Cd (λ_L=325 nm) lasers, respectively. The measurements were performed at room temperature.

The electron irradiation was carried out with the linear accelerator ILU-6 with energy E_e=1.8 MeV, absorption doses of 10 MRad (100 kGy) and 20 MRad (200 kGy) at the temperature T = 333 K.

3. RESULTS AND DISCUSSION

3.1. Quantum chemical calculations

Quantum chemical studies were performed on polyamide dimer and trimer molecules. Calculations were carried out using the Gaussian 09 software package and the density functional theory (DFT) method, with the B3LYP hybrid functional and 6-31G(d) basis set. Fig. 1-2 show the optimised geometry of the polyamide dimer and trimer molecules (one of the conformers).

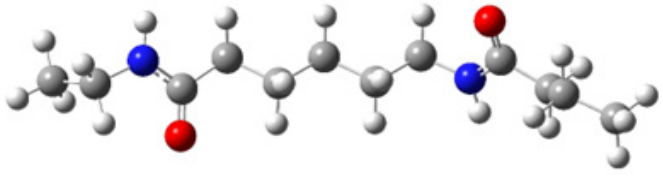

Figure 1. Optimized geometry of the polyamide dimer

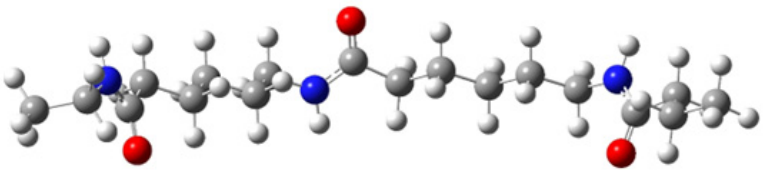

Figure 2. Optimized geometry of the polyamide trimmer

The natural vibrations of polyamide molecules were calculated. A scale factor of 0.9614 was applied to the frequencies [10]. As can be seen in Fig. 3, the Raman scattering spectra of the monomer, dimer, and trimer are almost identical. The valence vibrations of C=O and N–H are not sensitive to the length of the polymer chain and are found at frequencies of 1709 cm^{-1} and 3483±1 cm^{-1}. The broad band near 3000 cm^{-1} corresponds to the valence vibrations of C-H.

Figure 4 shows the calculated Raman scattering spectra resulting from the combination of polyamide molecules within the frequency range of 800–1,600 cm^{-1}.

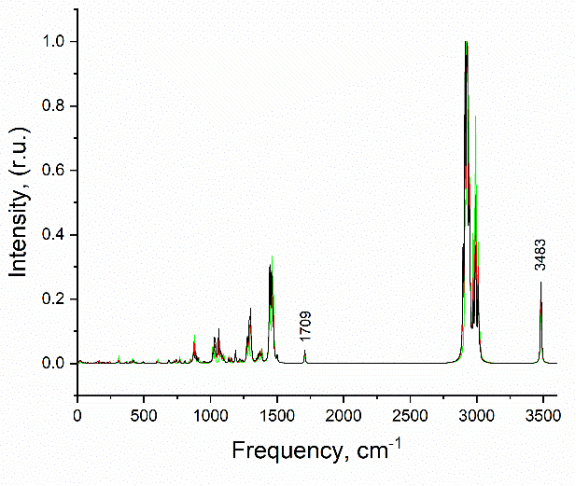

Figure 3. Raman scattering spectra for the monomer (green line), dimer (red line) and trimer (black line) of the polyamide

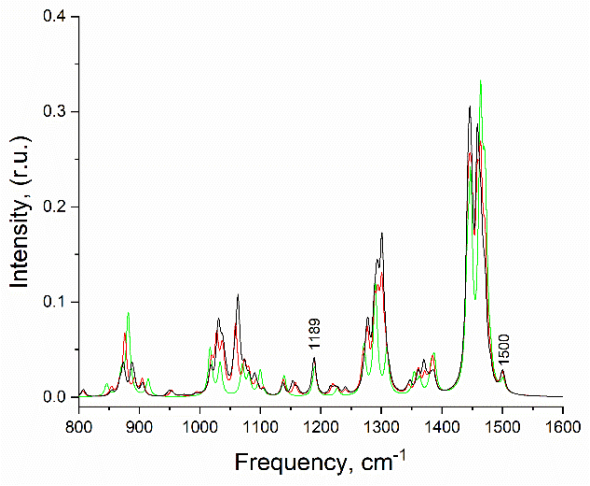

Figure 4. Raman scattering spectra of the monomer (green line), dimer (red line) and trimer (black line) of the polyamide, within the 800–1600 cm^{-1} range

Table 1 presents the calculated frequencies of the main fundamental oscillations of polyamide chains.

Table 1. Frequencies of the main fundamental oscillations of polyamide chains.

	monomer	dimer	trimer
	Frequency, cm^{-1}		
Valence vibrations N–H	3483	3482	3484
Valence vibrations C=O	1709	1709	1709
Deformation vibrations N–H	-	-	1500

3.2. Electrical conductivity and mechanical properties of PA-6-MWCNT nanocomposites

Filling PA-6 with nanotubes and increasing the concentration of nanotubes leads to a significant decrease in resistivity. While the resistivity of pure PA-6 is $\rho \approx 10^{13}$ Ω·cm, it drops to $1.4 \cdot 10^{7}$ Ω-cm at 6 wt.% CNT content and to $2.8 \cdot 10^{1}$ Ω·cm at 12 wt. % CNT content. A similar decrease in resistivity is also observed for other fillers, such as carbon black, but at higher concentrations [11].

The electrical conductivity at AC current (σ_{AC}) in the frequency range of 10^{-3}-10^{7} for pure PA-6 increases linearly, and with the addition of MWCNTs, regions of constant conductivity appear for $\sigma_{DC} = \sigma_{AC}$ at a nanotube concentration of 4 wt.%, the electrical conductivity is constant over the entire frequency range and is equal to $\sigma_{DC} = \sigma_{AC} = 10^{-3}$ S/cm. At the same time, the ratio of the intensities of the D- and G-bands inherent in MWCNTs changes. The behavior of σ_{AC} changes when not only MWCNTs but also N_a–A+A are added to PA-6. The latter compound improves the dispersion of the MWCNTs in the PA-6 matrix, as shown by TEM images. The improvement in dispersion is accompanied by an increase in σ_{DC} by several orders of magnitude [12]. The electrical resistivity of PA-6 and other polyamides depends not only on the CNT content, but also on the mixing temperature of the components and the rotational speed during the mixing of the CNTs in the polymer matrix, which affects the filler dispersion index and, in turn, leads to changes in calorimetric parameters such as melting point, crystallization temperature and their enthalpies [13]. The electrical conductivity of filler networks is affected not only by the melt state but also by the crystallization of the polymer matrix [14].

Since the dispersion of the nanotubes plays a significant role in the electrical conductivity behavior, there are a large number of nanotube modifications for their grafting to macrochains of polymers, including PA-6. One of these methods involves the application of a thin layer of polyethylene to the surface of the CNTs. Such catalyzed polymerization of nanotubes allows not only to take advantage of the significant aspect ratio inherent in CNTs, but also to significantly improve their dispersion due to reduced aggregation while maintaining a low percolation threshold in nanocomposites. At the same time, the properties of PA-6/MWCNT nanocomposites are enhanced, allowing for their wide use in antistatic devices, in the production of sensors for absorbing electromagnetic radiation in radar applications, and in the production of conductive rubber. Thus, the percolation threshold for uncoated PA-6/ MWCNT nanocomposites is 0.4 wt. %, and for PA-6/ MWCNT nanocomposites (with polyethylene coating of the CNT surface) it decreases to 0.1 wt.%. The value of $\sigma_0 = 6.0 \cdot 10^{-5}$ S/cm for PA-6/MWCNT was significantly lower than $\sigma_0 = 3.0 \cdot 10^{-3}$ S/cm for PA-6/ MWCNT (coated with PE). These differences are explained by the morphology of the composites, depending on the modification of the polymer matrix and fillers, in which the matrix area separating the conductive nanotubes changes. As a consequence, the conductivity of the nanotubes in the matrix is attenuated by electron transfer through potential barriers present in the region of the conductive cluster. In addition to reducing the percolation threshold in PA-6/MWCNT nanocomposites (with a PE layer on the surface), the electrical conductivity at 1 wt.% MWCNT increases by eight orders of magnitude, and for the PA-6/MWCNT nanocomposite by only five orders of magnitude compared to pure PA-6.

The properties of PA-6/MWCNT nanocomposites are influenced not only by the modification of nanotubes aimed at improving their dispersion but also by the method of nanocomposite production, which involves the creation of a segregated heterophase structure of nanocomposites. This structure involves the formation of nanotube layers on the surface of polymer matrix blocks. For PE and PVC nanocomposites, a significant decrease in the percolation threshold is observed when these segregated structures are formed [15-19]. For other systems, such as PEG, and PPG, similar low values of φ_c have not been observed [20]. For PA-6/ MWCNT nanocomposites it is interesting to use the method of creating segregated structures. If the percolation thresholds for PE/MWCNT and PVC/MWCNT are $\varphi_{cPE} = 0.00099$ vol.pt. and $\varphi_{cPVC} = 0.0001$ vol.pt., respectively, then $\varphi_{cPA\text{-}6} = 0.041$ vol.pt. ($t=1.65$, $\sigma_0 = 2.24$ S/cm.) The electrical conductivity of pure PA-6 exceeds its known value of ~10^{-13} S/cm and is ~10^{-10} S/cm. In the region below the percolation interval, a slow increase in electrical conductivity is observed due to the jump charge transfer mechanism. In the percolation region, the increase in electrical conductivity is about six orders of magnitude, which is typical for systems with percolation behavior of conductivity. At the same time, the observed differences indicate the importance of the thermal history during the preparation of the nanocomposites and the absence of the expected segregated structure.

It can be assumed that the result obtained is a consequence of the peculiarities of the morphology of PA-6 and PA-6/MWCNT, which is different from other polymers in the formation of nanocomposites with CNTs.

Figure 5 shows the behavior of Young's modulus and dynamic mechanical properties obtained for the elastic state at a frequency of 1 MHz.

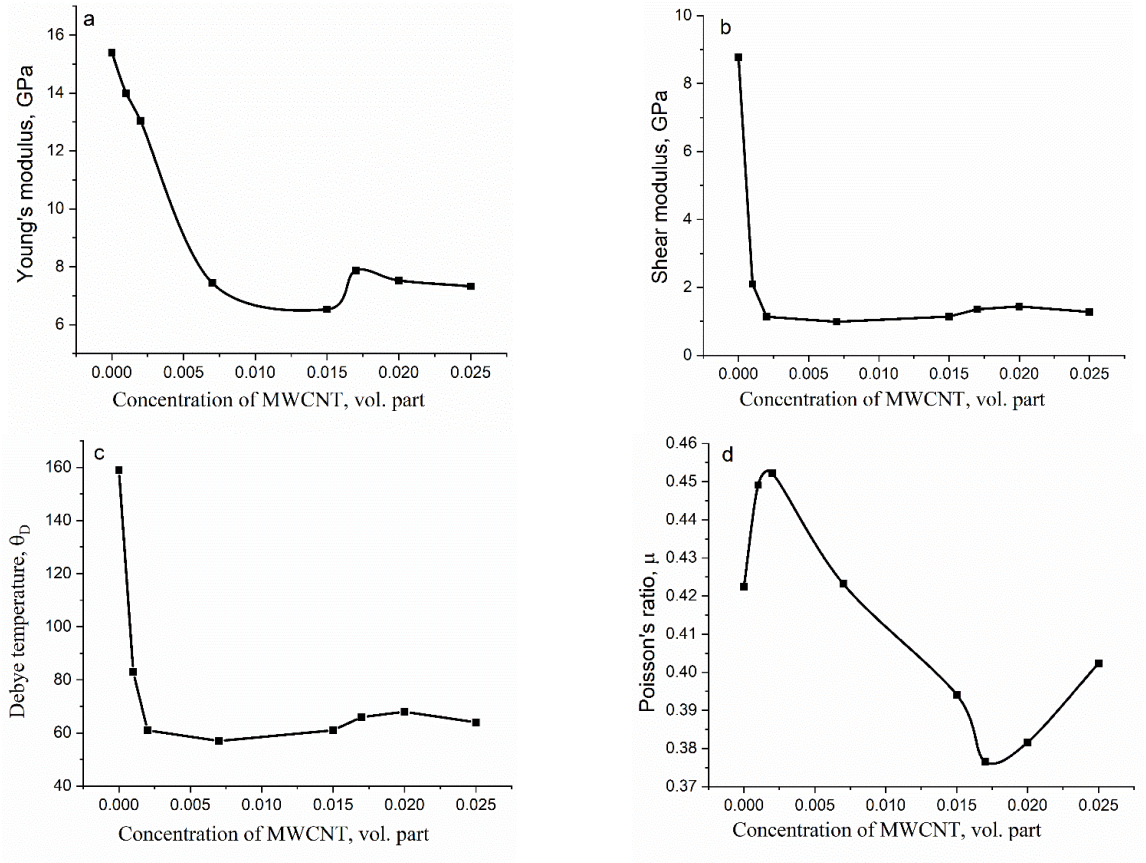

Figure 5. Dynamic moduli of Young's modulus (a) and shear (b), Poisson's ratio (c), Debye temperature (d) for PA-6/MWCNT composites at different filler locations in the elastic region at a sound frequency of 1 MHz

These dependencies differ from the behavior of the statistical modulus, which takes into account not only the elastic but also the relaxation properties of the deformation [11]. It can be seen that the highest values of the moduli occur for pure PA-6. With the addition of nanotubes, the elastic properties of polyamide deteriorate. A slight increase in the modulus occurs in the interval of conductive network formation. The presence of nanotubes may lead to the destruction of the structure of the previously established α-phase, which is also formed by hydrogen bonds. Another reason may be the interaction of nanotubes with amide groups of macrochains, which affects their elastic properties. On the other hand, the above-mentioned interaction with macromolecules and the crystalline phase can counteract the formation of agglomerates with nanotubes. This in turn helps the nanotubes to act as active centers of crystallite nucleation. As can be seen from Figure 6, the degree of crystallinity increases as the nanotube content increases.

If the degree of crystallinity increases slowly from 55 to 60 % at a low MWCNT content, then as the concentration of MWCNTs is further increased, the degree of crystallinity increases rapidly from 60 to 75 %. In the case of nanotube agglomeration, the opposite effect is expected. The significant values of the degree of crystallinity are noteworthy. The

presence of a large number of crystallites prevents the formation of a conductive cluster, which affects the increased values of the percolation threshold and a decrease in the increase of electrical conductivity in the percolation region. The absence of a segregated distribution of MWCNTs is also evidenced by the value of t = 1.65, which is close to the theoretical value of t = 2 in the random distribution of nanotubes. On the other hand, the unusual nature of electrical conductivity and mechanical properties is confirmed by the value of σ_0= 2.24 S/cm, although this value is significantly lower for most nanocomposites [21].

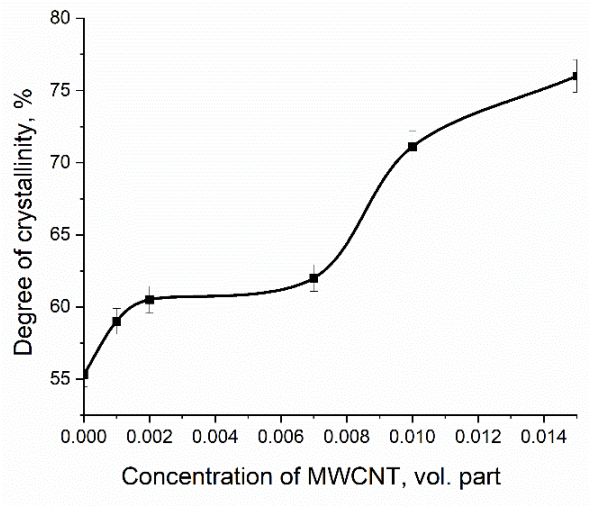

Figure 6. Dependence of the degree of crystallinity on the content of nanotubes in PA-6/ MWCNT composites

3.3. Radiation modification of the properties of PA-6 polyamide and PA-6/MWCNT nanocomposites

The peculiarities of the structure of polyamides, including PA-6, and the possibility of their modification within a wide range will allow them to be used to solve various problems. For example, by annealing at different temperatures, which allows to obtain different initial crystalline phases, it is possible to significantly influence the absorption in the THz range caused by vibrations parallel and perpendicular to the molecular chain [22]. The addition of certain additives can significantly increase the fire resistance [8]. Of interest is not only the filling of polyamides with CNTs, but also their deposition on the surface of polymers, since this makes it possible to create surfaces that do not trap proteins from the bloodstream, thus expanding the possibilities of using polyamides as implants in medicine [23]. A special place in modifying the properties of polyamides is occupied by radiation functionalization. Such functionalization is mainly performed using γ-irradiation or high-energy electron bombardment with different absorption doses.

Upon γ-irradiation of polyamide with 6,12 γ-photons with a dose increase from 0 to 300 kGy, an increase in the degree of crystallinity in the range of ~15 to ~19% is observed.

The melting point T_m undergoes a more complex restructuring at similar doses. At lower doses (up to ~50 kGy), T_m increases and after passing the maximum, it decreases. The study of the IR absorption spectra of samples irradiated with doses of 100 and 200 kGy, compared to the unirradiated ones, shows a significant restructuring of the spectra in the whole range, but mainly in the region of *N–H* valence vibrations in interchain hydrogen bonds and amide bands caused by vibrations in *–NH–C–O–* groups. These results indicate that an increase in the dose of γ-irradiation with an increase in the degree of crystallinity leads mainly to the destruction of crystallites [22]. In addition, γ-irradiation induces morphological changes in polyamides [23].

Comparison of Raman spectra for polyamide 6,12 irradiated with γ-photons at doses of 15, 50, 100, 200, and 300 kGy with unirradiated samples confirms the destruction of crystallites due to the destruction of molecular chains, which leads to an increase in the molar content of oligomers with increasing dose.

This chain degradation is mainly realized as a consequence of radiation damage to amide groups [2, 9]. Raman scattering for γ-irradiated crystalline samples in the form of PA 6,12 fibers depends on their orientation and temperature (dose of 50 kGy). At T ≈ 110°C, sharp changes in the intensities of the bands associated with the valence vibrations of the CH_2 and *C–C* groups are observed. Similar changes in intensity are observed for a temperature of 80 °C at different doses. The obtained results indicate that γ-irradiation affects not only the formation or degradation of crystallites but also changes the Brill transition point with the appearance of a stable modified γ-phase in the dose range from 50 to 100 kGy [24]. In the case of electron irradiation of PA-6 with an energy of 1.3 MeV and doses of 100, 200, 300, and 400 kGy at room temperature, there are noticeable changes in the intensity of many IR absorption bands.

The most significant changes are in the spectral regions caused by the vibrational modes of the amide, metal groups, *C–C* bonds, and *N–H* groups responsible for hydrogen bonding between the chains. It is important to note that the nature of these changes is not linearly related to the increase in dose. Exposure to different doses of PA-6 affects sample morphology, melting point T_m, melting enthalpy, and X-ray diffraction. If for an unirradiated sample T_m = 220 °C and melting enthalpy ΔH_M = 57.33 J/g, then these values decrease with increasing dose during irradiation, and at 400 kGy

they are equal to 215 °C and 27.52 J/g, respectively. The surface of spherulites is destroyed with increasing dose for irradiated samples. In addition, the diffraction peaks corresponding to the α-phase lose their intensity with increasing dose. These results indicate that electron irradiation reduces crystal properties [25].

3.3.1. Electrical conductivity and mechanical properties of radiation functionalized PA-6/MWCNT nanocomposites

Irradiation with electrons of energy E_e1.8 MeV leads to the formation of the simplest class of radiation defects, namely Frenkel pairs, and is accompanied by the appearance of free radicals due to the absence of dominant spontaneous recombination. It is shown that the appearance of radiation-stimulated radicals can lead to the rupture of bonds in the amide group of PA-6 chains, interchain hydrogen bonds, and cross-links in the region of methylene groups of CH_2. It is difficult to predict the mechanisms of radiation damage, but it is obvious that their priority depends on the dose level. At high doses, radiation degradation of materials can also be expected. In nanocomposites with MWCNTs, the situation is even more complicated due to the influence of incorporated nanotubes. At the same time, changes in the effect of nanotubes on the polymer matrix due to radiation defect formation in CNTs cannot be included [26, 27].

To interpret the results of radiation functionalization of PA-6/MWCNT nanocomposites in a wide dose interval of electron irradiation, it is advisable to extend the effect of low doses, e.g. 10-20 MRad (100-200 kGy).

Figure 7 shows the dependence of the electrical conductivity of the PA-6/MWCNT nanocomposite on the nanotube content after electron irradiation with a dose of 10 MRad and 20 MRad(100-200 kGy).

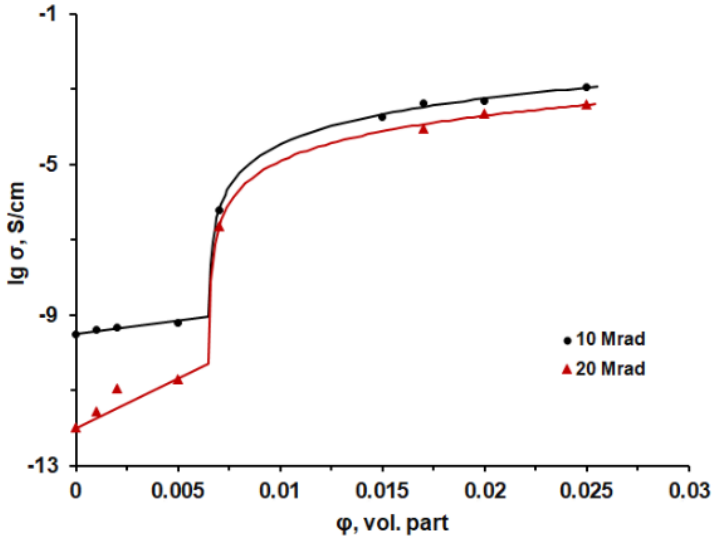

Figure 7. Dependence of the electrical conductivity at DC for PA-6/MWCNT nanocomposites on the content of nanotubes after electron irradiation (E=1.8 MeV) with an absorption dose of 10 MRad (100 kGy) and 20 MRad (200 kGy)

The use of the scaling dependence to describe the behavior of the electrical conductivity at constant current, σdc, yields result that differ from those obtained for PA-6/MWCNT nanocomposites without irradiation [28]. Thus, the following values were obtained for the composite irradiated with 10 MRad $\varphi_c = 0.0065$ vol. pt., $t = 2.08$, $\sigma_0 = 4.46$ S/cm. When this composite was irradiated with a dose of 20 MRad, the values obtained for the fitting parameters of the percolation equation were very close $\varphi_c = 0.0065$ vol. pt., $t = 2.06$, $\sigma_0 = 1.42$ S/cm.

The electrical conductivity in the percolation region increases by a jump of about four orders of magnitude. We observe a decrease in the percolation threshold and a slight decrease in electrical conductivity within the percolation region. Additionally, there is a more homogeneous filler distribution and a slight increase in σ_0. These changes result from structural transformations in the PA-6 polymer matrix under irradiation, which affect the formation of the conductive cluster. A decrease in the electrical conductivity of the composite after irradiation with a dose of 20 MRad in the pre-percolation region may indicate radiation-induced damage to polymer chains and the formation of defects that impair charge transfer.

Figure 8 shows the dynamic mechanical characteristics describing the elastic properties of PA-6/MWCNT nanocomposites irradiated with a dose of 10 MRad (100 kGy) and 20 MRad (200 kGy).

Although a slight decrease in the studied values is observed, the dependencies of mechanical characteristics on the absorbed dose of 20 Mrad remain similar. A radiation dose of 20 MRad is insufficient to cause significant changes to the mechanical properties of composites.

Compared with the results presented in Fig. 5, the changes in dynamic and shear moduli with increasing nanotube concentration are largely preserved relative to unirradiated composites and tend to decrease with increasing filler content. At the same time, the values of shear moduli for irradiated composites exceed those of unirradiated samples at higher nanotube contents.

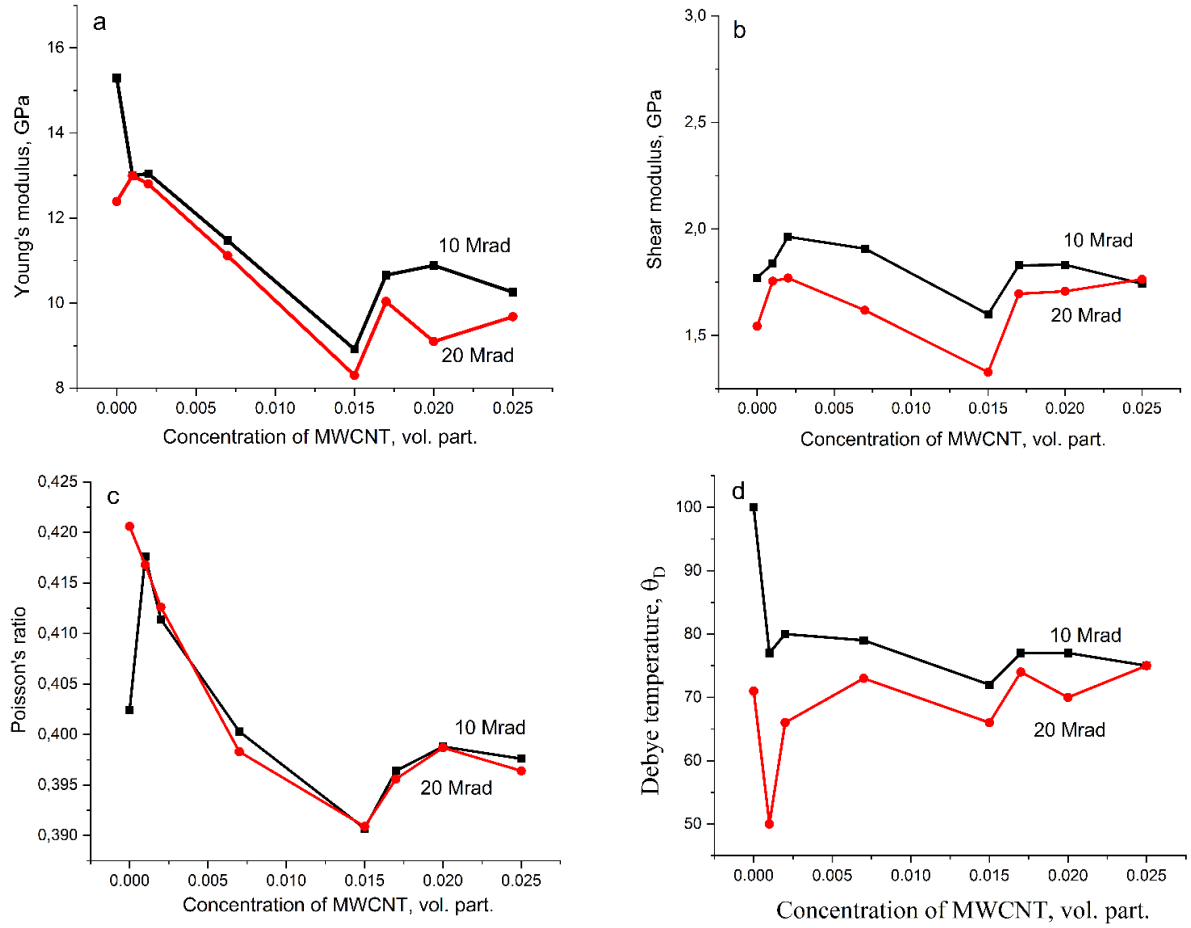

Figure 8. Dynamic Young's and shear moduli, Poisson's ratio, Debye temperature for PA-6/MWCNT composites at different filler locations after electron irradiation (E_e = 1.8 MeV) with an absorption dose of 10 MRad (100 kGy) and 20 MRad (200 kGy) in the elastic region at a sound frequency of 1 MHz

3.3.2. Raman scattering and fluorescence of radiation functionalized PA-6/MWCNT nanocomposites

For unirradiated PA-6/MWCNT nanocomposites, a significant Raman spectrum restructuring was observed with increasing nanotube content. Such changes occur for many bands of vibrational modes, especially those associated with valence vibrations of asymmetric and symmetric vibrations of CH_2 (2931, 2901, 2,871 cm^{-1}), amide-I ($C=O$), 1631 cm^{-1}), CH_2 (bending 1446 cm^{-1}), amide III (1276 cm^{-1}), valence stretching of $C–C$ (1121 cm^{-1}, etc.) [22].

Damage to the bonds within the chains by nanotubes contributes to a decrease in the elastic properties of the polymer matrix.

Irradiation of nanocomposites leads to an additional restructuring of the Raman spectra, which can be seen in Figure 9.

Compared to the unirradiated nanocomposite with 0.001 vol. pt. CNTs, irradiation resulted in slight changes in the scattering spectrum. At the same time, while maintaining the general picture of the bands, a slight shift of them is observed, for example, the amide I band from 1631 cm^{-1} to 1636 cm^{-1} and a redistribution of intensities, mainly for the valence vibrations of CH_2 groups. When a nanocomposite with 0.005 vol. pt. CNTs is irradiated, the spectrum returns to the appearance characteristic of nanocomposites with lower CNT content compared to the unirradiated one. While for the unirradiated sample, the most intense band is at 1306 cm^{-1} (CH_2 torsion), the less intense bands are at 1129 cm^{-1} ($C–C$ valence), 1443 cm^{-1} (CH_2 bending), 1639 cm^{-1} (amide I), for the irradiated nanocomposite the bands at 1125 cm^{-1}, 1445 cm^{-1}, 1636 cm^{-1} are more intense. Similar deviations in the shifts and relative intensities of the bands also occur for higher concentrations of MWCNTs.

Thus, the Raman spectra of each of the irradiated composites undergo changes indicating intramolecular vibrations of both nanotubes and radiation damage. At the same time, despite the general deterioration of the elastic properties induced by CNTs, a slight improvement is observed as a result of electron bombardment. The radiation damage may be insignificant at the chosen dose (100 kGy), and due to the recombination of electrons with free radicals formed as a result of the interaction of CNTs with the polymer matrix, the circuit damage is healed, leading to an improvement in the elastic properties of the matrix. Other mechanisms of influence of mechanical and radiation damage to the chains and their manifestations on the elastic properties of nanocomposites and the formation of conductive clusters in them are also possible. It is known that PA-6 polymers are characterized by fast fluorescence, i.e. delayed fluorescence (FL) with

backlighting. The fast fluorescence spectra for the α and γ crystalline phases are different and their appearance depends on the excitation wavelength. For example, when excited at λ_{ex} = 267 nm, the α phase band appears with emission maxima at 340 and 390 nm, and the maximum of the γ phase emission band is at 500 nm. Excitation at λ_{ex} = 400 nm gives the same spectra for both phases with a maximum of 480 nm. Changing λ_{ex} from 300 to 312 nm for the α-phase results in a switch in intensity from a band with a maximum of 340 nm to a band with a maximum of 390 nm. This behavior of fast FL is explained as a consequence of the recombination of photoinduced charges with an almost continuous energy distribution [24, 25].

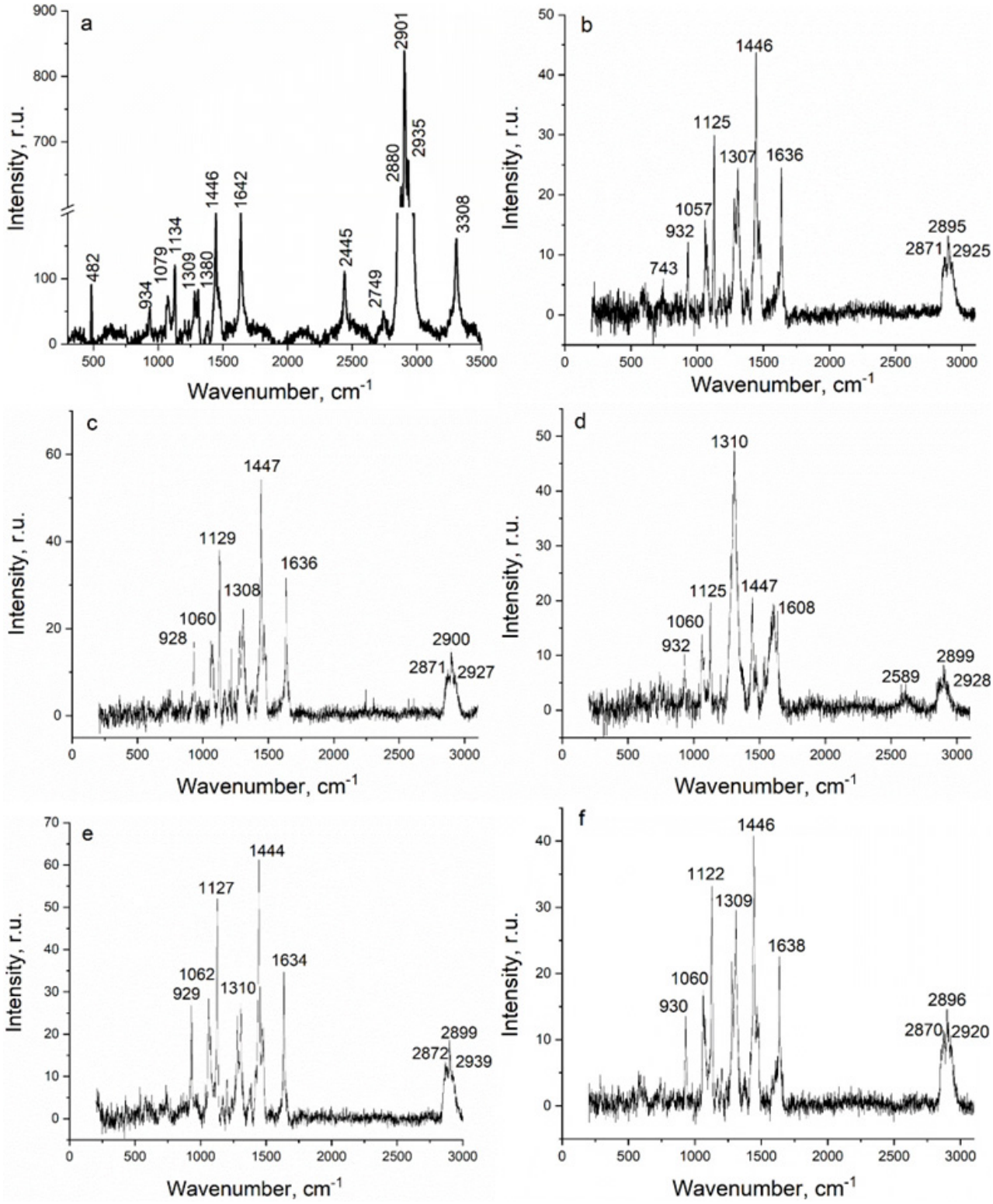

Figure 9. Raman spectra of PA-6/MWCNT nanocomposites with a nanotube content of 0 (a), 0.001 (b), 0.002 (c), 0.005 (d), 0.007 (e), 0.015 vol. pt. (f) after electron irradiation (E_e = 1.8 MeV) with an absorption dose of 10 MRad (100 kGy).

Fig. 10 shows the fast FL spectra for pure PA-6 and PA-6/MWCNT composites after radiation functionalization.

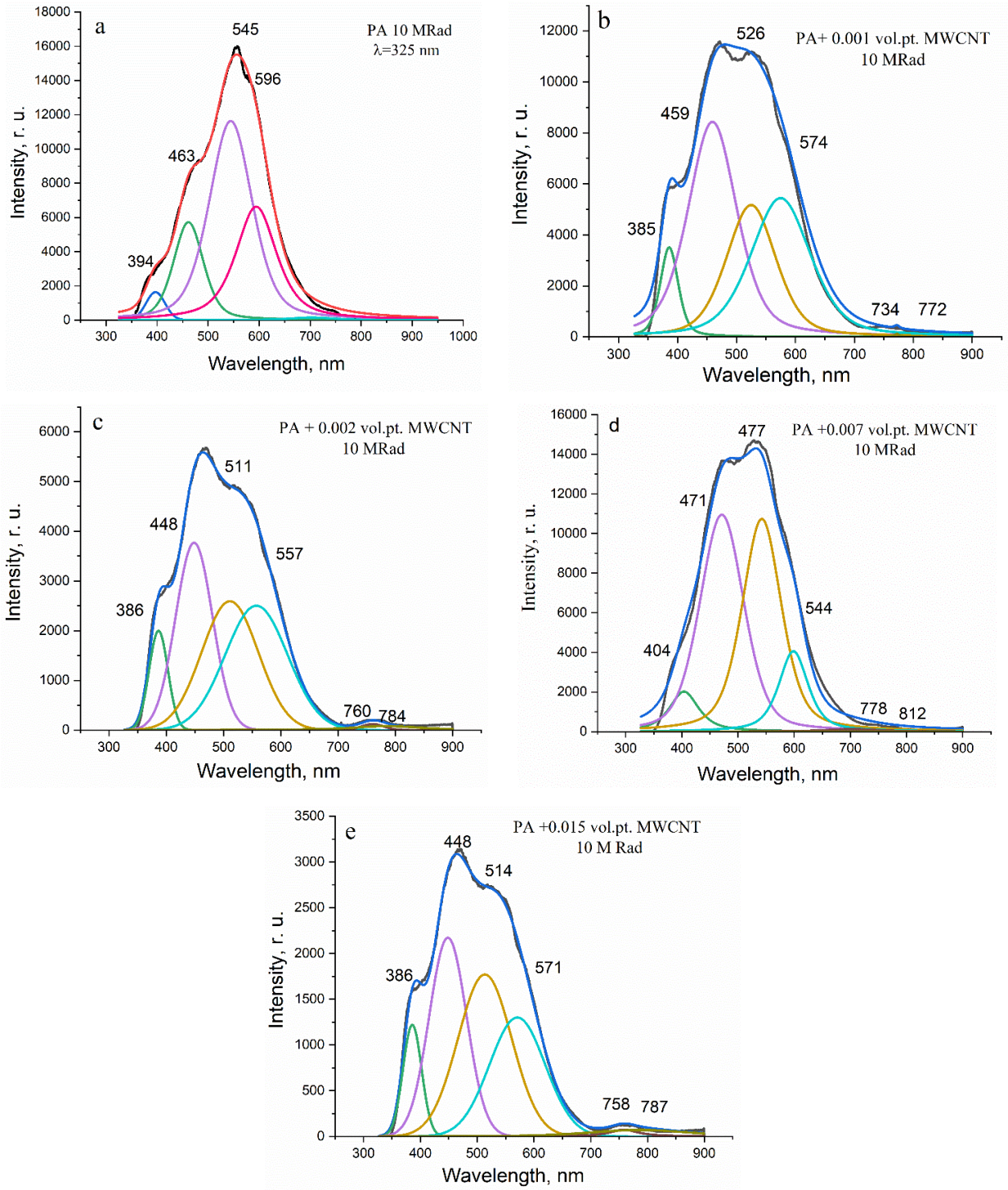

Figure 10. Fast FL spectra of PA-6/MWCNT nanocomposites with a nanotube content of 0 (a), 0.001 (b), 0.002 (c), 0.007 (d), 0.015 vol. pt. (e) after electron irradiation (E_e = 1.8 MeV) with an absorption dose of 10 MRad (100 kGy), individual bands correspond to the fitting components

In the case of pure PA-6, irradiation leads to a restructuring of the FL spectrum, which is manifested in an increase in the intensity of the spectrum. More significant band changes in the FL emission band are observed for the nanocomposite with 0.001 vol. pt. MWCNTs. Thus, for the non-irradiated composite, the main component of the FL band is located at 545 nm (λ_{ex} = 325 nm), and there are also kinks at 391, 467, 606, 742, and 782 nm. Irradiation leads to two main emission components at 459 and 526 nm. The intensity of the components at 385 and 574 nm varies. The introduction of 0.002 vol. pt. MWCNT for the unirradiated polymer composite does not change the shape of the band much. At the same time, irradiation results in the appearance of two components at 448 and 511 nm and kinks at 386 and 557 nm.

For an unirradiated nanocomposite with 0.007 vol. pt. MWCNTs, two main peaks appear at 464 and 540 nm, and two peaks appear at 399 and 598 nm. In the irradiated nanocomposite, two main peaks appear at 471 and 477 nm and two peaks at 404 and 544 nm. Similarly, in the case of the non-irradiated nanocomposite with 0.015 vol. pt. MWCNTs, there are two peaks at 460 and 543 nm and two peaks at 391 and 600 nm. Irradiation at a dose of 10 MRad (100 kGy) is accompanied by a significant band restructuring with the appearance of three components at 386, 448, and 514 nm and a bend at 571 nm.

Thus, the introduction of fillers (MWCNTs) affects the nature of electronic transitions due to the presence of a quasi-continuous spectrum of electron energy, which are local charge states. These local states correspond to the presence of disorder due to the presence of an amorphous phase and defects in the crystal structure. The behavior of the FL spectra shows that in unirradiated composites, the nanotubes have little effect on the rearrangement of the energy levels of the local charge states. It can be assumed that this energy spectrum is primarily determined by the state of the polymer itself. On the other hand, a certain restructuring of the spectra considered with an increase in the CNT content indicates that the nanotubes have a greater effect not on the morphology of the composites, but on the structure of the chains. In this case, the destruction of the chains is possible, accompanied by a decrease in the elastic properties of the Raman scattering spectra. The peculiarity of functionalization of nanocomposites is associated with the effects of electron irradiation with the energy of bombarding charges E_e=1.8 MeV and a dose of 10 MRad (100 kGy). The mechanisms of irradiation have proved to be quite complex and are associated not only with the possible degradation of intramolecular and intermolecular bonds, which in turn determines the energy spectrum of electrons in the interstitial space, as well as the degree of crystallinity of the α-phase.

In addition, electrons can recombine with free radicals formed due to the presence of nanotubes. These mechanisms can also affect the formation of conductive networks and thus lead to a decrease in the percolation threshold.

4. CONCLUSIONS

The preparation of PA-6/MWCNT nanocomposites leads to an increase in the degree of crystallinity with an increase in the content of CNTs, which for this polymer matrix act as nucleation centers of crystallites of a more stable α-phase. With an increase in the concentration of nanotubes in non-irradiated nanocomposites, the effect of electrical conductivity percolation with a percolation threshold of 0.0141 vol. pt. is observed.

Simultaneously, the values of dynamic Young's modulus and shear measured at an ultrasonic frequency of 1 MHz decrease, indicating mechanical damage of polymer macrochains by nanotubes. At the same time, the Raman light scattering spectra are restructured with a shift of most bands and changes in their relative intensity. The fast phase spectra at different MWCNT contents change little, indicating that the nanotubes have little effect on the morphology of the nanocomposites.

As a result, irradiation with electrons of E_e=1.8 MeV with a dose of 10 MRad (100 kGy) and 20 MRad (200 KGy) affects the electrical conductivity (the percolation threshold decreases to 0.0065 vol. pt.), changes the nature of the drop in the dynamic Young's moduli and shear, which is explained by the healing of defects caused by the breakdown of bonds in the circuits by nanotubes.

The destruction of bonds is also indicated by a significant restructuring of the spectra of Raman scattering. For different irradiated PA-6/MWCNT nanocomposites, both the shift of vibrational modes and the restructuring of the relative intensity are observed.

The appearance of intramolecular and intermolecular defects and changes in the amorphous phase occurring during irradiation leads to changes in the energy spectra of local charge states, which in turn affects the behavior of recombination transitions involving local states. As a result of such rearrangement, the fast fluorescence emission spectra for each of the irradiated PA-6/MWCNT nanocomposites change. This, in turn, indicates that these nanocomposites have complex mechanisms of degradation of the intramolecular structure of the presence of fillers, which, on the one hand, form the energy structure within the gap, and, on the other hand, affect changes in the conducting cluster, which leads to a decrease in the percolation threshold in the electrical conductivity of irradiated nanocomposites.

ORCID

Tatiana Pinchuk-Rugal, https://orcid.org/0000-0003-2417-9220; **Oksana Dmytrenko**, https://orcid.org/0000-0002-4271-4234;
Mykola Kulish, https://orcid.org/0000-0002-7409-8560; **Andrii Misiura**, https://orcid.org/0000-0001-9918-1670;
Andriy Momot, https://orcid.org/0000-0001-8162-0161; **Maksim Alieksandrov**, https://orcid.org/0000-0002-9691-5170;
Ihor Danylenko, https://orcid.org/0000-0002-8740-204X; **Yurii Onanko**, https://orcid.org/0000-0002-7231-1188;
Oleksii Melnychenko, https://orcid.org/0000-0002-7787-7674

REFERENCES

[1] T. Arnal, P. Eisenberg, M.J. Abad, A. Ares-Pernas, and C.R. Bernal, "Multifunctional nanocomposites based on a polyamide 6/polyamide 12 blend and multi-walled carbon nanotubes," Polymer Engineering and Science **64**(3), 1246–1257 (2024). https://doi.org/10.1002/pen.26611

[2] J. Arquinto, J. Harada, D.P. De Castro, and L.G. De Andrade E Silva, "Effects of E-Beam irradiation on the chemical, thermal, and mechanical properties of polyamide-6, polyamide-6.6, and polypropylene used in conveyor belt rollers," Materials Research **28**(suppl 1), (2025). https://doi.org/10.1590/1980-5373-MR-2025-0068

[3] P.V. Kodgire, A.R. Bhattacharyya, S. Bose, N. Gupta, A.R. Kulkarni, and A. Misra, "Control of multiwall carbon nanotubes dispersion in polyamide6 matrix: An assessment through electrical conductivity," Chemical Physics Letters **432**(4–6), 480–485 (2006). https://doi.org/10.1016/j.cplett.2006.10.088

[4] B. Krause, P. Pötschke, and L. Häußler, "Influence of small scale melt mixing conditions on electrical resistivity of carbon nanotube-polyamide composites," Composites Science and Technology **69**(10), 1505–1515 (2008). https://doi.org/10.1016/j.compscitech.2008.07.007

[5] H. Li, X. Tuo, B.-H. Guo, J. Yu, and Z.-X. Guo, "Comparison of three interfacial conductive networks formed in carbon Black-Filled PA6/PBT blends," Polymers **13**(17), 2926 (2021). https://doi.org/10.3390/polym13172926

[6] P. Liu, "Modifications of carbon nanotubes with polymers," European Polymer Journal **41**(11), 2693–2703 (2005). https://doi.org/10.1016/j.eurpolymj.2005.05.017

[7] A. Šehić, J. Vasiljević, A. Demšar, M. Leskovšek, V. Bukošek, J. Medved, M. Čolović, I. Jerman, and B. Simončič, "Polyamide 6 composite fibers with incorporated mixtures of melamine cyanurate, carbon nanotubes, and carbon black," Journal of Applied Polymer Science **136**(5), (2018). https://doi.org/10.1002/app.47007

[8] V. Arumugam, A. Góra, and V. Lipik, "Influence of Graphene, Carbon Nanotubes, and Carbon Black Incorporated into Polyamide Yarn on Fabric Properties," Textiles **4**(4), 442–458 (2024). https://doi.org/10.3390/textiles4040026

[9] M. Kaplan, B. Krause, N. Smolka, and I. Kuehnert, "Systematic optimization of conductive PA6/Carbon black nanocomposites through integrated Rheological–Electrical characterization and melt spinning analysis," Fibers and Polymers, (2026). https://doi.org/10.1007/s12221-026-01372-1

[10] A.P. Scott, and L. Radom, "Harmonic Vibrational Frequencies: an evaluation of Hartree−Fock, Møller−Plesset, quadratic configuration interaction, density functional theory, and semiempirical scale factors," The Journal of Physical Chemistry **100**(41), 16502–16513 (1996). https://doi.org/10.1021/jp960976r

[11] S. Huang, T. Liu, W. Zhang, W.C. Tjiu, C. He, and X. Lu, "Grafting polyamide 6 onto multi-walled carbon nanotubes using microwave irradiation," Polymer International **59**(10), 1346–1349 (2010). https://doi.org/10.1002/pi.2873

[12] C. Menchaca, B. Manoun, G. Martínez-Barrera, V.M. Castaño, and H. López-Valdivia, "In situ high-temperature Raman study of crystalline nylon 6,12 fibers gamma-irradiated in argon atmosphere," Journal of Physics and Chemistry of Solids **67**(9–10), 2111–2118 (2006). https://doi.org/10.1016/j.jpcs.2006.05.017

[13] M. Ovsik, M. Stanek, and M. Bednarik, "Evaluation of Cross-Linked Polyamide 6 Micro-Indentation properties: TAIC concentration and electron radiation intensity," Materials **16**(6), 2391 (2023). https://doi.org/10.3390/ma16062391

[14] C. Menchaca, A. Alvarez-Castillo, G. Martinez-Barrera, H. Lopez-Valdivia, H. Carrasco, and V.M. Castano, "Mechanisms for the modification of nylon 6,12 by gamma irradiation," International Journal of Materials and Product Technology **19**(6), 521 (2003). https://doi.org/10.1504/ijmpt.2003.003468

[15] H. Suzuki, S. Ishii, C. Otani, and H. Hoshina, "Low-frequency vibrations of polyamide-6 as a function of temperature and thermal history investigated by terahertz absorption spectroscopy," European Polymer Journal **67**, 284–291 (2015). https://doi.org/10.1016/j.eurpolymj.2015.04.009

[16] M.O. Lisunova, Ye.P. Mamunya, N.I. Lebovka, and A.V. Melezhyk, "Percolation behaviour of ultrahigh molecular weight polyethylene/multi-walled carbon nanotubes composites," European Polymer Journal **43**(3), 949–958 (2006). https://doi.org/10.1016/j.eurpolymj.2006.12.015

[17] Ye.P. Mamunya, V.V. Davydenko, P. Pissis, and E.V. Lebedev, "Electrical and thermal conductivity of polymers filled with metal powders," European Polymer Journal **38**(9), 1887–1897 (2002). https://doi.org/10.1016/s0014-3057(02)00064-2

[18] E. Auyang, M. Ouyang, A. Laycock, H. Blake, T.D. Tetley, T.W. Gant, A.E. Willis, and S. Wright, "Fabrication of microplastic and nanoplastic particles and fibres for use in pulmonary toxicity studies," Particle and Fibre Toxicology **22**(1), 30 (2025). https://doi.org/10.1186/s12989-025-00641-w

[19] M.A. Alieksandrov, T.M. Pinchuk-Rugal, O.P. Dmytrenko, M.P. Kulish, V.V. Shlapatska, and V.M. Tkach, "Radiation-Stimulated Formation of Polyene Structures in Polyethylene Nanocomposites with Multi-walled Carbon Nanotubes," in *Springer Proceedings in Physics*, (2019), pp. 323–332. https://doi.org/10.1007/978-3-030-17759-1_22

[20] T.M. Pinchuk-Rugal, M.P. Kulish, O.P. Dmytrenko, A.I. Momot, A.I. Misiura, M.A. Alieksandrov, V.M. Popruzhko, O.F. Kolomys, and V.V. Shlapatska, "Mechanisms of formation of polyene structures in radiation-functionalized PVC-MWCNT polymer nanocomposites," Vibrational Spectroscopy **125**, 103495 (2023). https://doi.org/10.1016/j.vibspec.2023.103495

[21] M.A. Alieksandrov, A.M. Gaponov, T.M. Pinchuk-Rugal, O.P. Dmytrenko, A. Naumenko, V.M. Popruzhko, and M.P. Kulish, "Conjugate Formation in Films of Polyethylene Glycol and Polypropylene Glycol Nanocomposites with MultiWall Carbon Nanotubes," in *Springer Proceedings in Physics*, (2021), pp. 143–152. https://doi.org/10.1007/978-3-030-74800-5_9

[22] V.M. Popruzhko, O.P. Dmytrenko, M.P. Kulish, T.M. Pinchuk-Rugal, A.I. Misiura, O.L. Pavlenko, A.I. Momot, T.O. Busko, A.P. Onanko, M.A. Alieksandrov, and V.V. Strelchuk, "Electrical and optical properties of polyamide 6 nanocomposites with multi-walled carbon nanotubes," Journal of Molecular Liquids **390**, 123152 (2023). https://doi.org/10.1016/j.molliq.2023.123152

[23] M. Avbar, G.H.M. De Oliveira, and S. De Traglia Amancio-Filho, "Enhancing Mechanical Properties of Polyamide 66 with Carbon-Based Nano-Fillers: A Review," Journal of Composites Science **9**(1), 48 (2025). https://doi.org/10.3390/jcs9010048

[24] M.V. Vasnetsov, "Observation of room-temperature afterglow in Polyamide-6 under UV excitation," Semiconductor Physics Quantum Electronics & Optoelectronics **22**(3), 333–337 (2019). https://doi.org/10.15407/spqeo22.03.333

[25] M.V. Vasnetsov, V.V. Ponevchinsky, D.O. Plutenko, G.V. Klishevich, A.A. Mitryaev, O.I. Gudymenko, and V.P. Kladko, "Luminescence peculiarities of polyamide-6 α and γ forms," Applied Physics B **127**(4), (2021). https://doi.org/10.1007/s00340-021-07601-0

[26] M.D. Murad, B.A. Al-Mayyahi, and A.F.Abbas, "Synthesis and characterization of new fluorescence polyamides," New Materials Compounds and Applications **9**(2), 309-325 (2025). https://doi.org/10.62476/nmca.92309

ЕЛЕКТРИЧНІ, МЕХАНІЧНІ ТА ОПТИЧНІ ВЛАСТИВОСТІ КОМПОЗИТІВ ПОЛІАМІДУ-6 З ВУГЛЕЦЕВИМИ НАНОТРУБКАМИ ПІД ВПЛИВОМ ОПРОМІНЕННЯ

Т.М. Пінчук-Ругаль[1], О.П. Дмитренко[1], М.П. Куліш[1], А.І. Місюра[1,2], А.І. Момот[1], М.А. Алєксандров[3], І.М. Даниленко[3], Ю.А. Онанко[4], О.М. Мельниченко[5]

[1]Київський національний університет імені Тараса Шевченка, вул. Володимирська, 64/13, 01033, Київ, Україна
[2]Інститут електрозварювання ім. Є.О. Патона НАН України, вул. Казимира Малевича, 11, 03150, Київ, Україна
[3]Інститут фізики напівпровідників імені В.Є. Лашкарьова НАН України, проспект Науки, 45, 02000, Київ, Україна
[4]Інститут водних проблем і меліорації НААН, вул. Васильківська, 37, 03022, Київ, Україна
[5]«Радма» Інститут фізичної хімії імені Л. В. Писаржевського НАН України, проспект Науки, 31, 03028, Київ, Україна

Досліджено залежність ступеня кристалічності, динамічного механічного модуля та зсуву на частоті ~1 МГц від вмісту нанотрубок для неопромінених нанокомпозитів ПА-6/БВНТ. Встановлено збільшення ступеня кристалічності та зменшення вказаних модулів зі зростанням вмісту вуглецевих нанотрубок, що пояснюється тим, що вуглецеві нанотрубки в полімерній матриці виступають як центри зарадкоутворення кристалічної α-фази, а також як наночастинки, що руйнують міжатомні зв'язки в ланцюгах та між макромолекулами. Проведено опромінення вказаних нанокомпозитів електронами $E_e \approx 1{,}8$ МеВ з поглинутою дозою 10 МРад (100 кГр) та 20 МРад (200 кГр). Виміряно залежність електропровідності, динамічних механічних модулів, комбінаційного розсіювання та швидкої фотолюмінісценції від вмісту вуглецевих нанотрубок. Показано, що опромінення має складний вплив на вищезазначені властивості. Електрони можуть сприяти як руйнуванню ланцюгів, так і встановленню кристалічної фази, а також загоєнню пошкоджень, спричинених нанотрубками, шляхом рекомбінації електронів з вільними радикалами. Радіаційна функціоналізація широко проявляється в змінах спектрів КРС та енергетичній структурі електронів у забороненій зоні. Ці зміни пов'язані з наявністю локальних станів, зв’язаних з аморфною фазою та структурними дефектами. Це, в свою чергу, проявляється на перебудові спектрів ФЛ і може впливати на формування провідного кластера

Ключові слова: *поліамід-6; нанокомпозити; електропровідність; ступінь кристалічності; динамічні модулі; КРС; флуоресценція; електронне опромінення*

EAST EUROPEAN JOURNAL OF PHYSICS. 3. 629-636 (2026)
DOI:10.26565/2312-4334-2026-3-58 ISSN 2312-4334

NANOPARTICLES AS PROBES OF THE ELECTRON ENERGY RELAXATION LENGTH IN A DC GLOW DISCHARGE

V. Lisovskiy*, S. Dudin, A. Shakhnazarian, S. Rezunenko
V.N. Karazin Kharkiv National University, 4 Svobody Sq., Kharkiv, 61022, Ukraine
**Corresponding Author email: lisovskiy@karazin.ua*
Received June 1, 2026; revised August 8, 2026; accepted August 23, 2026

A new method is proposed for determining the electron energy relaxation length in a DC glow discharge using nanoparticles as diagnostic probes. The method is based on nanoparticle confinement near the first field reversal point in the negative glow. At this position, a local maximum of the plasma potential forms a shallow potential pit for negatively charged nanoparticles. The position of the field reversal point can therefore be determined from the location of a nanoparticle cloud visualized by laser light scattering. Together with the measured cathode-layer thickness and the known interelectrode distance, this allows the electron energy relaxation length to be estimated using an analytical relation between these quantities. The method was demonstrated experimentally in an acetylene discharge, where nanoparticles are naturally formed by plasma polymerization. The electron energy relaxation length was found to increase, on average, with increasing discharge voltage. The experimentally estimated values were approximately 1.5 times larger than those calculated using an analytical model based on the first Townsend ionization coefficient. The discrepancy may partly result from the assumption of a constant electric field in the cathode layer adopted in the analytical model. The proposed method can also be extended to gases that do not form nanoparticles naturally by introducing preformed nanoparticles or by producing them initially in a suitable gas mixture.
Keywords: *Electron energy relaxation length; Nanoparticles; DC glow discharge; Potential pit; Ambipolar diffusion*

I. INTRODUCTION

In gas-discharge plasmas and plasma technologies, nonlocal heating of charged particles is often encountered, in which the regions where the particles gain high energy and where they dissipate this energy are spatially separated. For example, in negative ion sources [1–6], positive or negative ions extracted from the plasma are accelerated by an extractor and directed into a low-pressure gas volume (transport region) with no electric field, where they lose their energy through collisions with gas molecules.

In a DC discharge, electrons released from the cathode surface due to ion-induced electron emission gain considerable energy in the strong electric field of the cathode layer [7–15]. These electrons then leave the cathode layer and enter the negative glow, where the electric field is weak and may even reverse its direction. Since the electrons cannot gain energy in this region, they undergo elastic and inelastic collisions with gas molecules, lose the energy acquired in the cathode layer, and, in a sufficiently long discharge gap, eventually thermalize [16–20]. The distance over which this energy-loss process occurs is referred to as the electron energy relaxation length [7, 20]. Using known cross sections for electron collisions with gas molecules, the electron energy relaxation length can be calculated. However, even for an inert gas such as argon, the dependences of the energy relaxation length on electron energy calculated by different authors differ considerably, not only quantitatively but also qualitatively [18,19]. Therefore, it is useful to obtain at least an estimate of the electron energy relaxation length in various gases used in plasma technologies.

To our knowledge, micrometer-sized particles were first employed to estimate internal parameters of a gas-discharge plasma by the authors of Ref. [21], who used them to determine the electron temperature. Subsequently, charged micro- and nanoparticles have frequently been used to investigate electric fields in DC discharges and radio-frequency capacitively coupled discharges (see, for example, Ref. [22] and references therein).

Four different methods are commonly used to introduce nanoparticles into a gas discharge. Nanoparticles can be produced in advance, size-selected, and placed on an additional surface other than an electrode; a voltage pulse can then be applied in the plasma to lift the particles from the surface and form a nanoparticle cloud [23,24]. Alternatively, the cathode can be sputtered by ion bombardment in a DC discharge [25–29] or an arc discharge [30], with the sputtered atoms subsequently forming nano- and microparticles in the plasma. Preformed nanoparticles can also be introduced directly into the plasma volume using a dispenser [31–35]. Finally, a discharge can be generated in a gas whose molecules undergo dissociation to form monomers capable of producing nanoparticles through volume plasma polymerization [36–43].

DC glow discharges in acetylene are of interest for plasma processing because plasma polymerization leads to the deposition of carbon-containing films on electrode surfaces and discharge-tube walls [44–48]. By varying the discharge conditions, coatings ranging from polymer-like films to graphite [47] and even graphene [48] can be obtained. Of particular importance for the present work, however, is that under certain discharge conditions plasma polymerization also occurs in the plasma volume, resulting in the formation of nanoparticles [40].

Cite as: V. Lisovskiy, S. Dudin, A. Shakhnazarian, S. Rezunenko, East Eur. J. Phys. 3, 629 (2026), https://doi.org/10.26565/2312-4334-2026-3-58

These nanoparticles are formed predominantly in the negative glow and, after acquiring a negative charge, can be confined near the first field reversal point [7,40]. At this position, the local maximum of the plasma potential forms a shallow potential pit for negatively charged nanoparticles. The position of the first field reversal point is related to the energy relaxation of high-energy electrons emerging from the cathode layer into the negative glow. Therefore, the experimentally measurable position of the nanoparticle cloud can potentially be used as a diagnostic of the electron energy relaxation length.

In this work, we develop the physical basis of this diagnostic method and demonstrate it experimentally in a DC glow discharge in acetylene. The position of the nanoparticle cloud and the cathode-layer thickness are determined from discharge images and used to estimate the electron energy relaxation length. The obtained values are compared with those calculated using an analytical model based on the first Townsend ionization coefficient.

II. EXPERIMENTAL SETUP

The experimental setup used in this study is shown in Fig. 1. A cylindrical quartz discharge tube was positioned horizontally. Its inner diameter was 80 mm. Both electrodes were planar and made of stainless steel. The stationary cathode also served as a flange of the discharge tube and was supplied with a voltage of 0–1500 V from a power supply. The movable inner electrode served as a grounded anode. In the experiments reported in this work, the distance between the electrodes was fixed at 76.2 mm.

The experiments were performed in acetylene, which was introduced into the discharge chamber at a flow rate of up to 5 sccm (standard cubic centimeters per minute). Most experiments were carried out at a gas pressure of 0.2 Torr. The pressure was measured using a capacitance manometer (Baratron, MKS Instruments, USA) with an operating range from 1 mTorr to 1 Torr. A backing pump and a turbomolecular pump were used to evacuate the discharge chamber.

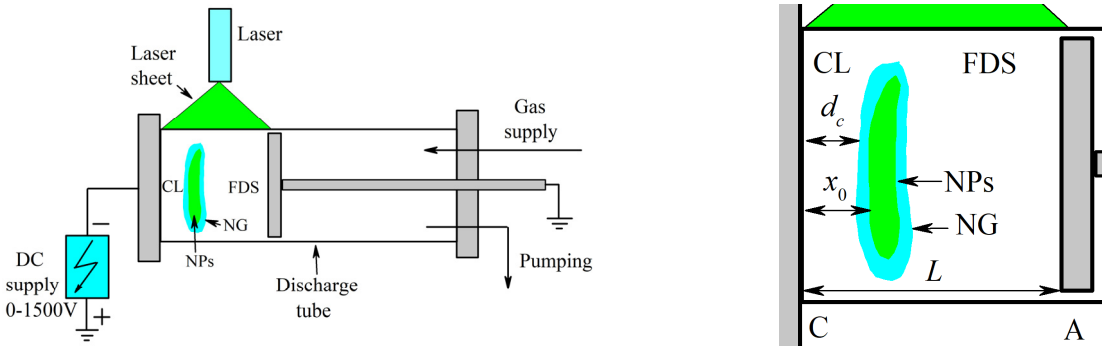

Figure 1. Schematic of the discharge chamber with a DC glow discharge

The nanoparticles are too small to be observed with the naked eye. Therefore, a green laser with a wavelength of 532 nm was used for their *in-situ* visualization. A cylindrical lens was used to split the laser beam into a light sheet, making it possible to observe a two-dimensional cross section of the nanoparticle cloud. This was sufficient for the purposes of the present study. If necessary, however, the three-dimensional shape of the cloud could also be determined by scanning it with the light sheet. Naturally, efficient light scattering by the nanoparticles requires sufficiently large particle sizes (several tens of nanometers or larger) as well as a sufficiently high nanoparticle concentration. These requirements determine the range of acetylene pressures investigated in this study (0.05–0.2 Torr). Under these conditions, nanoparticle formation and the increase in their size and number are sufficiently intense, while the DC discharge remains “short,” i.e., no positive column is formed. This issue is discussed in more detail below.

III. DC DISCHARGE STRUCTURE AND NANOPARTICLE FORMATION AND CONFINEMENT

In general, the DC discharge is one of the most extensively studied types of gas discharges. It is commonly generated in a cylindrical tube with planar electrodes located at its ends. After gas breakdown, a discharge with the following sequence of regions is formed. Adjacent to the cathode is the so-called cathode layer, across which a high voltage drop (several hundred volts or more) occurs. In Figs. 1 and 2, the cathode is denoted by C and the cathode layer by CL. The next region is the negative glow (NG), which gradually transits into the Faraday dark space (FDS). If the anode (A) is located within the Faraday dark space, such a discharge is conventionally referred to as a short discharge. In contrast, in a sufficiently long tube and/or at high gas pressure, a positive column and an anode layer with an anode glow may additionally appear. As mentioned above, all experiments were performed with a short discharge. Since the voltage drops across the negative glow and the Faraday dark space are small (several volts or less) [7,10,15,49], the voltage drop across the cathode layer can be considered approximately equal to the potential difference between the electrodes.

Figure 2 shows two photographs of the discharge. First, immediately after ignition, the discharge was photographed with the laser switched off [Fig. 2(a)]. The discharge structure described above, consisting of the cathode layer, negative glow, and Faraday dark space, can be clearly seen. When the light sheet is subsequently switched on, a

thin nanoparticle cloud appears in the negative glow after several seconds (or tens of seconds, depending on the gas pressure and the voltage between the electrodes), as indicated by NPs in Fig. 2(b). With time, the cloud may expand and become deformed [40], but in the present work we are specifically interested in the case of a thin nanoparticle cloud.

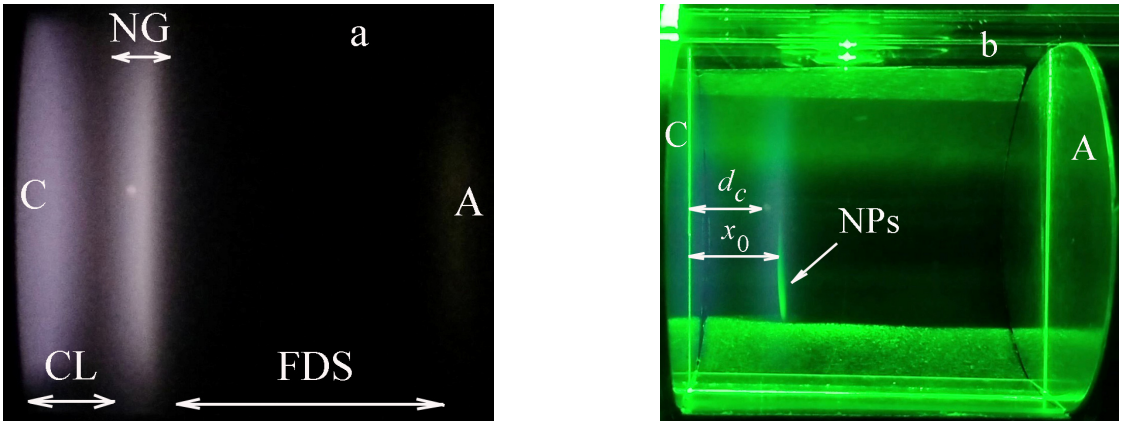

Figure 2. Photographs of the acetylene discharge at a pressure of 0.2 Torr with the light sheet (a) switched off and (b) switched on, at an interelectrode voltage of 440 V

To clarify why the nanoparticle cloud forms specifically in the negative glow, we consider the processes occurring in this region as well as in the cathode layer. Qualitative axial distributions of the electric field E, potential φ, positive ion density n_i, and electron density n_e in a short discharge are shown in Fig. 3.

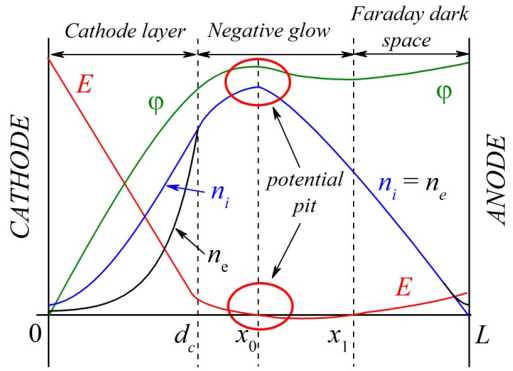

Figure 3. Axial distributions of the electric field E, potential φ, electron density n_e, and positive ion density n_i in a short discharge gap without a positive column

The cathode surface is bombarded by positive ions produced by ionization of acetylene molecules by high-energy electrons in the cathode layer and in the adjacent part of the negative glow. A strong electric field exists in the cathode layer. It reaches its maximum near the cathode surface and decreases almost linearly with increasing distance from the cathode. At the cathode-layer boundary ($x = d_c$), the electric field is small, but it reaches zero only within the negative glow, where the axial distributions of the electron and positive ion densities exhibit maxima, at a distance $x = x_0$ from the cathode. This position is referred to as the first field reversal point. The zero electric field means that the electrostatic potential reaches an extremum at this point, a maximum in the present case. For negatively charged particles, this local maximum of the electrostatic potential corresponds to a minimum of their potential energy and therefore forms a shallow potential pit in the vicinity of x_0. Its depth is usually small, less than 1 V [40]. A second field reversal point, at $x = x_1$, occurs near the boundary between the negative glow and the Faraday dark space.

Cold electrons and negatively charged nanoparticles can be confined in the shallow potential pit near the first field reversal point x_0. They cannot move toward the cathode because the strong electric field drives them back into the negative glow. Nor can they move toward the anode, because the electric field on the other side of x_0 drives them back. Therefore, the nanoparticle cloud initially formed in the negative glow is narrow and located near x_0. Naturally, when the nanoparticle concentration and particle size become sufficiently large, the cloud may broaden due to deformation of the potential pit by the charged nanoparticles [40]. In the present work, however, we consider specifically the case of a thin nanoparticle cloud.

Electrons are emitted from the cathode surface due to ion-induced electron emission and enter the strong electric field of the cathode layer. As they travel through the layer, they acquire considerable energy and ionize gas molecules. Some electrons emitted from the cathode or produced by ionization near its surface can traverse almost the entire cathode layer with little energy loss, undergoing only one or a few inelastic collisions with gas molecules, and

consequently acquire high energies approaching $e \cdot U_c$, where e is the elementary charge and U_c is the voltage drop across the cathode layer. A flux of such high-energy electrons therefore emerges from the cathode layer into the negative glow. There, these electrons begin to lose energy intensively through collisions with gas molecules, exciting their electronic states and ionizing them. As a result, a bright negative glow is observed; its intensity maximum coincides with the maximum plasma density, where the electric field reaches zero and reverses its direction.

High-energy electrons not only ionize and excite gas molecules. Collisions of these electrons with acetylene molecules may lead to dissociation with the formation of C_2H radicals, as well as to dissociative electron attachment resulting in the formation of C_2H^- negative ions. These C_2H and C_2H^- species can combine with C_2H_2 molecules to form more complex molecules; thus, they effectively act as monomers capable of forming long polymer chains. A list of the corresponding reactions is given, for example, in Ref. [40]. As these reactions continue, nanoparticles are eventually formed.

In general, the negative glow is an optimal region of a DC discharge for nanoparticle formation and confinement. It contains fluxes of high-energy electrons capable of producing C_2H and C_2H^-. At the same time, it contains a potential pit for negatively charged nanoparticles and negative ions, provided that negative ions can be formed in the gas under investigation.

An additional requirement of our method is the horizontal orientation of the discharge tube containing vertically oriented planar electrodes. If the electrodes are horizontal and the cathode is located at the bottom, sufficiently large nanoparticles are not confined at the first field reversal point x_0; instead, gravity causes them to settle toward the cathode-layer boundary or even penetrate slightly into the cathode layer. If the anode is located at the bottom, the nanoparticles formed in the plasma cannot be confined by the shallow potential pit [40] and fall onto the anode surface [50]. With horizontal electrodes, the nanoparticles are confined in the plasma by the axial electric field responsible for carrying the discharge current.

In our discharge chamber with vertically oriented electrodes, however, the situation is different. The axial electric field is now directed horizontally, whereas gravity acts vertically. The nanoparticles are confined in the plasma volume by the radial ambipolar electric field that arises because a fraction of the high-energy electrons escapes to the tube wall. The wall becomes negatively charged and repels cold electrons back into the plasma. At the same time, a small flux of positive ions reaches the wall from the plasma, accompanied by an equally small flux of high-energy electrons. Therefore, unlike the axial electric field, the ambipolar electric field does not carry the discharge current [49].

The accumulation of negative ions and negatively charged nanoparticles in the plasma leads to a substantial reduction in the ambipolar electric field [51-55]. At sufficiently high concentrations, the field may decrease to zero and even reverse its direction [56]. More generally, the presence of negative ions, in addition to electrons and positive ions, can substantially affect the structure and properties of discharge plasmas [57-68]. Negative ions are produced by electron attachment to gas molecules [49]; this process therefore results in the loss of free electrons that would otherwise ionize gas molecules and carry the discharge current.

IV. METHOD FOR DETERMINING THE ELECTRON ENERGY RELAXATION LENGTH USING NANOPARTICLES

We now consider how nanoparticles synthesized in a DC discharge can be used as a diagnostic tool for estimating the energy relaxation length of electrons that travel from the cathode surface to the cathode-layer boundary with almost no collisions with gas molecules and, consequently, lose little energy. Such electrons have high energies, which can reach $e \cdot U_c$, where U_c is the voltage drop across the cathode layer. These electrons are responsible for the ionization of gas molecules and for sustaining the discharge, and they also carry a substantial fraction of the discharge current through the negative glow [16,17].

As shown experimentally above, the nanoparticle cloud forms and is confined in the negative glow near the so-called first field reversal point, located at a distance x_0 from the cathode. We now consider the location of the first field reversal point shown in Fig. 3. J. P. Boeuf and L. C. Pitchford [7] proposed an analytical model of a DC glow discharge and obtained the following expression for the position of the field reversal:

$$\frac{x_0 - d_c}{L - d_c} = -\Lambda \cdot ln\left[\Lambda \cdot \left(1 - \mathrm{e}^{-1/\Lambda}\right)\right], \tag{1}$$

where L is the distance between the electrodes, $\Lambda = \lambda/(L - d_c)$, and λ is the distance over which the energy relaxation of electrons accelerated in the cathode layer and entering the negative glow occurs.

Equation (1) can readily be rewritten as

$$x_0 = d_c - \lambda \cdot ln\left[\frac{\lambda}{L - d_c} \cdot \left(1 - exp\left(-\frac{L - d_c}{\lambda}\right)\right)\right]. \tag{2}$$

Subsequently, in analytical models of a DC glow discharge, the authors of Ref. [20] obtained the same expression, Eq. (2), but for the position of the maximum plasma density in the negative glow. We therefore conclude that the field reversal occurs at the position where the plasma density reaches its maximum.

Since the interelectrode distance L is known, while the cathode-layer thickness d_c and the coordinate of the first field reversal point x_0 can be determined from photographs of the discharge, Eq. (2) can be used to estimate the electron energy relaxation length λ. The corresponding results for an acetylene pressure of 0.2 Torr are shown in Fig. 4. Both the cathode-layer thickness d_c and the coordinate of the first field reversal point x_0 decrease monotonically with increasing voltage between the electrodes. The electron energy relaxation lengths λ obtained in the present work are shown by solid blue squares. On average, λ increases monotonically with the voltage U.

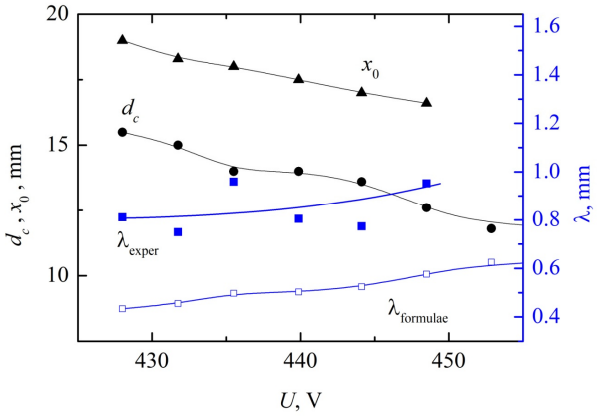

Figure 4. Cathode-layer thickness d_c, coordinate of the first field reversal point x_0, and electron energy relaxation length λ as functions of the interelectrode voltage U at an acetylene pressure of 0.2 Torr. Solid blue squares show the values obtained in the present work; open blue squares show the values calculated using Eq. (3) [20]

The authors of Ref. [20] obtained the following expression for λ:

$$\lambda = \frac{U_c - Bpd_c}{\alpha_{CF} Bpd_c}, \tag{3}$$

where α_{CF} is the first Townsend ionization coefficient, for which Ref. [20] proposed the following expression:

$$\alpha_{CF} = Ap \cdot exp\left(-\frac{Bpd_c}{U_c}\right). \tag{4}$$

Thus, the authors of Ref. [20] assumed that, in the strong electric field of the cathode layer, the ionization rate is determined by the potential difference traversed by the electrons rather than by the local electric field. Therefore, Eqs. (3) and (4) use the average electric field in the cathode layer, U_c/d_c.

We recall that all experiments were performed under conditions where no positive column was present in the DC glow discharge. Since the voltage drops across the negative glow and the Faraday dark space are very small compared with the voltage drop U_c across the cathode layer, for the purposes of our estimates we can assume that U_c is equal to the voltage U between the electrodes, which can be readily measured.

It remains to determine the constants A and B to be used in Eq. (4) for acetylene. For this purpose, we used the BOLSIG+ code [69] with electron–acetylene collision cross sections from Refs. [70,71]. The resulting values of the first Townsend ionization coefficient are shown in Fig. 5 by solid circles and are well approximated by the following expression:

$$\alpha = 33 \cdot p \cdot exp\left(-\frac{450}{E/p}\right). \tag{5}$$

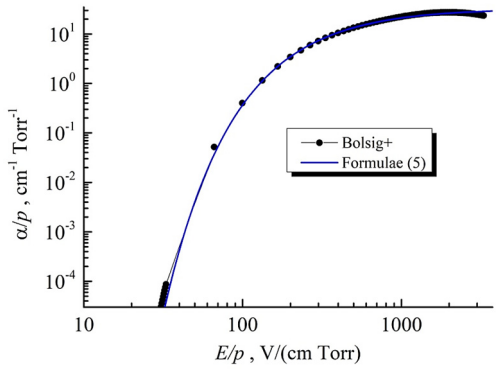

Figure 5. Ratio of the first Townsend ionization coefficient α to the gas pressure p, as a function of the reduced electric field E/p for acetylene. Solid circles show the results calculated using the BOLSIG+ code; the blue line represents the approximation given by Eq. (5)

Thus, the constants $A = 33$ cm^{-1} Torr^{-1} and $B = 450$ V/(cm Torr) should be used in Eq. (4). These constants were then substituted into Eqs. (3) and (4), and the calculated results were added to Fig. 4 as open blue squares. As can be seen from the figure, the experimentally estimated electron energy relaxation lengths λ are approximately 1.5 times larger than the values calculated using Eq. (3). However, that equation was derived assuming a constant electric field in the cathode layer, i.e., a linear potential profile across the layer, which is a rather crude approximation.

V. CONCLUSIONS

In this work, we developed the physical basis of a new method for determining the electron energy relaxation length in a DC glow discharge using nanoparticles as diagnostic probes. In a horizontal discharge tube with vertically oriented electrodes, nanoparticles can be confined in the negative glow near the first field reversal point. The local maximum of the plasma potential at this position forms a shallow potential pit for negatively charged nanoparticles. Since the coordinate of the nanoparticle cloud can be determined experimentally using laser light scattering, it provides a direct measure of the position of the first field reversal point. Combined with the measured cathode-layer thickness and the known interelectrode distance, this coordinate makes it possible to estimate the electron energy relaxation length using an analytical relation between these quantities.

The method was demonstrated experimentally for a DC glow discharge in acetylene, where nanoparticles are formed naturally as a result of plasma polymerization. The cathode-layer thickness and the position of the nanoparticle cloud were determined from discharge images over a range of discharge voltages, and the corresponding electron energy relaxation lengths were obtained. The estimated relaxation length increased with increasing discharge voltage. For comparison, the electron energy relaxation length was also calculated using an analytical model based on the first Townsend ionization coefficient. The required Townsend coefficients for acetylene were obtained using BOLSIG+ and approximated by the conventional exponential dependence on the reduced electric field. The experimentally estimated electron energy relaxation lengths were approximately 1.5 times larger than those predicted by the analytical model. This difference may be attributed, at least in part, to the assumption of a constant electric field in the cathode layer used in the analytical model, whereas the actual electric field varies substantially across the layer.

The proposed method is not restricted to gases in which nanoparticles are formed naturally. Nanoparticles can first be produced in a suitable gas mixture and subsequently retained in the discharge after the nanoparticle-forming component is removed. Alternatively, preformed nanoparticles can be introduced into the plasma from an external source. Once negatively charged and confined near the first field reversal point, the nanoparticles can serve as probes of its position. Thus, the proposed approach can potentially be used to estimate the electron energy relaxation length in a wide range of gases employed in low-pressure plasma applications.

ORCID

V. Lisovskiy, https://orcid.org/0000-0002-6339-4516; **S. Dudin,** https://orcid.org/0000-0001-9161-4654;
A. Shakhnazarian, https://orcid.org/0009-0000-2951-0969; **S. Rezunenko,** https://orcid.org/0009-0001-5871-495X

REFERENCES

[1] I. Sereda, Y. Hrechko, I. Babenko, and M. Azarenkov, Vacuum, **200**, 111006 (2022). https://doi.org/10.1016/j.vacuum.2022.111006
[2] M. Bacal, editor, *Physics and Applications of Hydrogen Negative Ion Sources* (Springer, Cham, Switzerland, 2023). https://doi.org/10.1007/978-3-031-21476-9
[3] I. Sereda, Y. Hrechko, and M. Azarenkov, Phys. Plasmas **31**, 053516 (2024). https://doi.org/10.1063/5.0202579
[4] L. Yang, Y. Xie, X. Peng, D. S. Stepanov, J. Pan, and Ch. Hu, Phys. Plasmas **32**, 033510 (2025). https://doi.org/10.1063/5.0249289
[5] I. Sereda, Y. Hrechko, M. Azarenkov, and K. Sereda, Intern. J. Hydrogen Energy, **109**, 1321 (2025). https://doi.org/10.1016/j.ijhydene.2025.02.222
[6] I. Sereda, Y. Hrechko, K. Sereda, and O. Vorobiov, East European Journal of Physics **2**, 470 (2026). https://doi.org/10.26565/2312-4334-2026-2-52
[7] J. P. Boeuf, and L. C. Pitchford, J. Phys. D: Appl. Phys. **28**, 2083 (1995). https://doi.org/10.1088/0022-3727/28/10/013
[8] K. Rózsa, A. Gallagher, and Z. Donkó, Physical Review E **52**, 913 (1995). https://doi.org/10.1103/PhysRevE.52.913
[9] C.V. Budtz-Jørgensen, J. Bøttiger, and P. Kringhøj, Vacuum **56**, 9 (2000). https://doi.org/10.1016/S0042-207X(99)00160-8
[10] V.A. Lisovskiy, and S.D. Yakovin, Technical Physics Letters 26, 891 (2000). https://doi.org/10.1134/1.1321230
[11] Z. Donkó, J. Appl. Phys. **88**, 2226 (2000). https://doi.org/10.1063/1.1288008
[12] V.A. Lisovskiy, V.A. Derevianko, and V.D. Yegorenkov, Vacuum **103**, 49 (2014). https://doi.org/10.1016/j.vacuum.2013.12.008
[13] A. Michau, G. Lombardi, L. Colina Delacqua, M. Redolfi, C. Arnas, P. Jestin, X. Bonnin, and K. Hassouni, Plasma Chem. Plasma Process 32,451 (2012). https://doi.org/10.1007/s11090-012-9357-0
[14] Y. Y. Lau, D. Li, and D. P. Chernin, Phys. Plasmas **30**, 093104 (2023). https://doi.org/10.1063/5.0169276
[15] V. Lisovskiy, S. Dudin, A. Shakhnazarian, S. Rezunenko, V. Yegorenkov, Phys. Plasmas **32**, 083501 (2025). https://doi.org/10.1063/5.0275627
[16] L. D. Tsendin, Physics-Uspekhi **53**, 133 (2010). https://doi.org/10.3367/UFNe.0180.201002b.0139
[17] V. A. Lisovskiy, K. P. Artushenko, and V. D. Yegorenkov, Phys. Plasmas, **24,** 053501 (2017). https://doi.org/10.1063/1.4982211

[18] S. Siepa, S. Danko, T.V. Tsankov, Th. Mussenbrock, and U. Czarnetzki, J. Phys. D: Appl. Phys. **47**, 445201 (2014). https://doi.org/10.1088/0022-3727/47/44/445201
[19] C. Yuan, J. Yao, E.A. Bogdanov, A.A. Kudryavtsev, K.M. Rabadanov, and Z. Zhou, Phys. Plasmas **26**, 023509 (2019). https://doi.org/10.1063/1.5082698
[20] A. A. Kudryavtsev, A. V. Morin, and L. D. Tsendin, Tech. Phys. **53**, 1029 (2008). https://doi.org/10.1134/S1063784208080100
[21] T. C. Anestos, and C. D. Hendricks, J. Appl. Phys. **45**, 1176 (1974). https://doi.org/10.1063/1.1663385
[22] J. C. A. van Huijstee, L. S. Matthews, and T. W. Hyde, Phys. Plasmas **32**, 113703 (2025). https://doi.org/10.1063/5.0287405
[23] E. Thomas, IEEE Trans. Plasma Sci. **30**, 88 (2002). https://doi.org/10.1109/TPS.2002.1003937
[24] E. Thomas, Phys. Scripta **2001**, 20 (2006). https://doi.org/10.1238/Physica.Topical.089a00020
[25] G. M. Jellum, and D. B. Graves, J. Appl. Phys. **67**, 6490 (1990). https://doi.org/10.1063/1.346081
[26] C. Dominique, and C. Arnas, J. Appl. Phys. **101**, 123304 (2007). https://doi.org/10.1063/1.2748365
[27] C. Arnas, A. Michau, G. Lombardi, L. Couëdel, and K. Kishor Kumar, Phys. Plasmas **20**, 013705 (2013). https://doi.org/10.1063/1.4776681
[28] K. Kishor Kumar, L. Couëdel, and C. Arnas, Phys. Plasmas **20**, 043707 (2013). https://doi.org/10.1063/1.4802809
[29] S. Barbosa, F. R. A. Onofri, L. Couëdel, M. Wozniak, C. Montet, C. Pelcé, C. Arnas, L. Boufendi, E. Kovacevic, J. Berndt, and C. Grisolia, J. Plasma Phys. **82**, 615820403 (2016). https://doi.org/10.1017/S0022377816000714
[30] I. Langmuir, C. G. Found, and A. F. Dittmer, Science **60**, 392 (1924). https://doi.org/10.1126/science.60.1557.392
[31] J. Niemann, V. Schneider, and H. Kersten, Phys. Plasmas **32**, 013510 (2025). https://doi.org/10.1063/5.0243765
[32] P. Gogoi, B. Chutia, P. Sut, Y. Bailung, N. C. Adhikary, and H. Bailung, Phys. Plasmas **31**, 023706 (2024). https://doi.org/10.1063/5.0177617
[33] L. Wimmer, A.S. Schmitz, M. Kretschmer, and M.H. Thoma, Phys. Plasmas **31**, 043702 (2024). https://doi.org/10.1063/5.0190499
[34] J. Goswami, N. Das, D. Goswami, S.S. Kausik, and B.K. Saikia, Phys. Plasmas **33**, 013701 (2026). https://doi.org/10.1063/5.0306369
[35] J. C. A. van Huijstee, L. S. Matthews, and T. W. Hyde. Phys. Plasmas **32**, 113703 (2025). https://doi.org/10.1063/5.0287405
[36] A. R. Westwood, European Polymer Journal **7**, 377 (1971). https://doi.org/10.1016/0014-3057(71)90008-5
[37] R. Liepins, and K. Sakaoku, J. Appl. Polym. Sci. **16**, 2633 (1972). https://doi.org/10.1002/app.1972.070161016
[38] V. Lisovskiy, A. Minenkov, S. Dudin, S. Bogatyrenko, P. Platonov, and V. Yegorenkov, ACS Omega 7, 47941 (2022). https://doi.org/10.1021/acsomega.2c05846
[39] L. Worner, E. Kovacevic, J. Berndt, H. M. Thomas, M. H. Thoma, L. Boufendi, and G. E. Morfill, New Journal of Physics **14**, 023024 (2012). https://doi.org/10.1088/1367-2630/14/2/023024
[40] V. Lisovskiy, S. Dudin, S. Bogatyrenko, A. Shakhnazarian, and S. Rezunenko, Phys. Plasmas **33**, 083704 (2026); https://doi.org/10.1063/5.0326778
[41] J. Winter, J. Berndt, S.-H. Hong, E. Kovacevic, I. Stefanovic, and O. Stepanovic, Plasma Sources Sci. Technol. **18**, 034010 (2009). https://doi.org/10.1088/0963-0252/18/3/034010
[42] E. Kovacevic, J. Berndt, Th. Strunskus, and L. Boufendi, J. Appl. Phys. **112**, 013303 (2012). https://doi.org/10.1063/1.4731751
[43] E. Kovačević, J. Berndt, I. Stefanović, H.-W. Becker, C. Godde, Th. Strunskus, J. Winter, and L. Boufendi, J. Appl. Phys. **105**, 104910 (2009). http://dx.doi.org/10.1063/1.3129318
[44] S.M. Miladinović, V. Vriendt, S. A. Robotham, F. Maseri, S. Lucas, and C.L. Wilkins, J. Am. Soc. Mass Spectrometry **21**, 411 (2010). https://doi.org/10.1016/j.jasms.2009.11.005
[45] A. Moshonov, and Y. Avny, J. Appl. Polymer Sci. **25**, 771 (1980). https://doi.org/10.1002/app.1980.070250506
[46] B. Alvarez, A. Sarmiento-Santos, and E. Vera-López, J. Phys.: Conf. Series **1386**, 012044 (2019). https://doi.org/10.1088/1742-6596/1386/1/012044
[47] B. Alvarez, A. Sarmiento-Santos, and Y. Hernandez, J. Phys.: Conf. Series **1386**, 012042 (2019). https://doi.org/10.1088/1742-6596/1386/1/012042
[48] B. Alvarez, A. Sarmiento-Santos, and Y. Hernandez, J. Phys.: Conf. Series **1386**, 012014 (2019). https://doi.org/10.1088/1742-6596/1386/1/012014
[49] Yu. P. Raizer, *Gas discharge physics*, (Springer, Berlin, 1991).
[50] L. Couëdel, K. Kishor Kumar, and C. Arnas, Phys. Plasmas **21**, 123703 (2014). https://doi.org/10.1063/1.4903465
[51] J. B. Thompson, Proc. Phys. Soc. **73**, 818 (1959). https://doi.org/10.1088/0370-1328/73/5/416
[52] A. J. Lichtenberg, V. Vahedi, M. A. Lieberman, and T. Rognlien, J. Appl. Phys. **75**, 2339 (1994). https://doi.org/10.1063/1.356252
[53] E. Stoffels, W. W. Stoffels, D. Vender, M. Haverlag, G. M. W. Kroesen, and F. J. de Hoog, Contrib. Plasma Phys. **35**, 331 (1995). https://doi.org/10.1002/ctpp.2150350404
[54] Y. T. Lee, M. A. Lieberman, A. J. Lichtenberg, F. Bose, H. Baltes, and R. Patrick, J. Vac. Sci. Technol. A **15**, 113 (1997). https://doi.org/10.1116/1.580452
[55] V. Lisovskiy, and V. Yegorenkov, Europhysics Letters **99**, 35002 (2012). https://doi.org/10.1209/0295-5075/99/35002
[56] V. Lisovskiy, S. Dudin, S. Bogatyrenko, S. Rezunenko, and V. Yegorenkov, East European Journal of Physics **2**, 445 (2026). https://doi.org/10.26565/2312-4334-2026-2-50
[57] M. Mao, J. Benedikt, A. Consoli, and A. Bogaerts, J. Phys. D: Appl. Phys. **41**, 225201 (2008). https://doi.org/10.1088/0022-3727/41/22/225201
[58] S. V. Dudin, S. D. Yakovin, and A. V. Zykov, East European Journal of Physics **3**, 606 (2023). https://doi.org/10.26565/2312-4334-2023-3-72
[59] V. O. Litvinov, I. I. Okseniuk, D. I. Shevchenko, and V. V. Bobkov, East European Journal of Physics **3**, 10 (2023). https://doi.org/10.26565/2312-4334-2023-3-01
[60] V. Lisovskiy, S. Dudin, A. Shakhnazarian, P. Platonov, and V. Yegorenkov, East European Journal of Physics **3**, 172 (2024). https://doi.org/10.26565/2312-4334-2024-3-17

[61] T. Wang, Sh. Rauf, N. Friedrichs, I. Korolov, J. Kenney, and J. Schulze, Phys. Plasmas 33, 023501 (2026) https://doi.org/10.1063/5.0300388
[62] X. K. Wang, R. Masheyeva, Y. X. Liu, Y. H. Song, P. Hartmann, Z. Donko, and J. Schulze, Plasma Sources Sci. Technol. **33**, 085006 (2024). https://doi.org/10.1088/1361-6595/ad69c0
[63] R. Masheyeva, M. Vass, M. Myrzaly, C.-B. Tian, K. Dzhumagulova, J. Schulze, Z. Donko, and P. Hartmann, Plasma Sources Sci. Technol. **34**, 045017 (2025). https://doi.org/10.1088/1361-6595/adcb6b
[64] H. Luo, J. Kenney, S. Rauf, I. Korolov, and J. Schulze, Plasma Sources Sci. Technol. **32**, 115018 (2023). https://doi.org/10.1088/1361-6595/ad0d06
[65] A. Derzsi, M. Vass, R. Masheyeva, B. Horvath, Z. Donko, and P. Hartmann, Plasma Sources Sci. Technol. **33**, 025005 (2024). https://doi.org/10.1088/1361-6595/ad1fd5
[66] J. Sangma, N. Sharma, M. Chakraborty, and M. Bandyopadhyay, Phys. Plasmas **29**, 033501 (2022). https://doi.org/10.1063/5.0078194
[67] G.-H. Huang, S.-Y. Xing, F. Gao, and Y.-N. Wang, Phys. Plasmas **32**, 123507 (2025). https://doi.org/10.1063/5.0300603
[68] I. Tanarro, R. J. Peláez, and V. J Herrero, Plasma Phys. Control. Fusion **67**, 035014 (2025). https://doi.org/10.1088/1361-6587/adb17b
[69] G.J.M. Hagelaar, and L.C. Pitchford, Plasma Sources Sci. Technol. **14**, 722 (2005). https://doi.org/10.1088/0963-0252/14/4/011
[70] L.C. Pitchford, L.L. Alves, K. Bartschat, S.F. Biagi, M.C. Bordage *et al*, Plasma Process. Polym. 14, 1600098 (2017). https://doi.org/10.1002/ppap.201600098
[71] M. Hayashi, *Electron collision cross sections determined from beam and swarm data by Boltzmann analysis*, in *Nonequilibrium Processes in Partially Ionized Gases*, edited by M. Capitelli, and J.N. Bardsley, (Plenum Press, New York, 1990). https://doi.org/10.1007/978-1-4615-3780-9

НАНОЧАСТИНКИ ЯК ЗОНДИ ДЛЯ ВИЗНАЧЕННЯ ДОВЖИНИ РЕЛАКСАЦІЇ ЕНЕРГІЇ ЕЛЕКТРОНІВ У ТЛІЮЧОМУ РОЗРЯДІ ПОСТІЙНОГО СТРУМУ

В. Лісовський, С. Дудін, А. Шахназарян, С. Резуненко
Харківський національний університет імені В.Н. Каразіна, майдан Свободи 4, Харків, 61022, Україна

Запропоновано нову методику визначення довжини релаксації енергії електронів у тліючому розряді постійного струму з використанням наночастинок як діагностичних зондів. Методика ґрунтується на утриманні наночастинок поблизу першої точки зворотності електричного поля в негативному світінні. У цій області локальний максимум потенціалу плазми утворює потенціальну яму для негативно заряджених наночастинок. Таким чином, положення точки зворотності електричного поля можна визначити за розташуванням хмари наночастинок, яку було візуалізовано за допомогою розсіювання лазерного випромінювання. Разом із виміряною товщиною катодного шару та відомою відстанню між електродами це дозволяє оцінити довжину релаксації енергії електронів за допомогою аналітичного співвідношення між цими величинами. Методику експериментально продемонстровано в розряді в ацетилені, де наночастинки природним чином утворюються внаслідок плазмової полімеризації. Встановлено, що в середньому довжина релаксації енергії електронів збільшується зі зростанням напруги розряду. Експериментально оцінені значення виявилися приблизно в 1,5 раза більшими за значення, розраховані за допомогою аналітичної моделі, що ґрунтується на першому коефіцієнті іонізації Таунсенда. Ця розбіжність може бути частково зумовлена припущенням про постійну напруженість електричного поля в катодному шарі, прийнятим в аналітичній моделі. Запропоновану методику також можна поширити на гази, в яких наночастинки природним чином не утворюються, шляхом введення попередньо сформованих наночастинок або їх початкового формування у відповідній газовій суміші.

Ключові слова: *довжина релаксації енергії електронів; наночастинки; розряд постійного струму; потенціальна яма; амбіполярна дифузія*

EAST EUROPEAN JOURNAL OF PHYSICS. 3. 637-642 (2026)
DOI:10.26565/2312-4334-2026-3-59 ISSN 2312-4334

PRODUCING HIGH-PURITY LEAD BY A COMPREHENSIVE REFINING METHOD

Olexii P. Shcherban, Olexandr I. Kondrik, Dmytro O. Solopikhin
National Science Center "Kharkiv Institute of Physics and Technology" N.A.S. of Ukraine,
1 Akademicheskaya St., 61108 Kharkiv, Ukraine
Corresponding Author email: shcherban@kipt.kharkov.ua
Received May 14, 2026; revised July 30, 2025; accepted August 12, 2026

The thermodynamics of redox reactions of the formation of lead oxide and impurity oxides during filtration in an argon atmosphere and Pb distillation under vacuum (~0.5 Pa) was studied. The strength of impurity oxides relative to lead oxide during oxidizing refining and distillation of lead was estimated by the absolute value of the change in Gibbs free energy. A comprehensive distillation refining process of lead was investigated, which includes the stages, such as filtration (oxidizing refining) in an argon atmosphere and lead purification from non-volatile and volatile impurities by evaporation of the metal in a vacuum with condensation of the vapor into a hot liquid phase ($T_{cond} \approx 0.85\ T_{evap}$). Experimental results of the application of a comprehensive process for obtaining high-purity lead of the C000 grade with a total content of majority impurities (in the amount) of 99.9996 mass % are presented.
Keywords: *Lead; Impurity oxides; Lead oxide; Oxygen potential; Gibbs free energy; Lead purification; Oxidizing refining; Filtrtion, Vacuum distillation*

1. INTRODUCTION

High-purity lead is characterized by the three grades: C0000 (99.9999 %, here and below the concentration of elements is given in mass percent), C000 (99.9996 %), C00 (99.9985 %). The majority of impurities are Ag, Cu, Zn, Bi, Sb, Fe, Tl, Hg, Cd, and Ni, with contents of 10-4–10^{-7} %. The above grades of high-purity lead are the product of after purification of lead of lower grades: C0 (99.992 %), C1 (99.985 %), C2 (99.95 %), C3 (99.9 %), which are obtained by processing crude lead, which has the following composition: 96-99 % Pb, 0.05-2.4 % Cu, up to 0.45 % As, 0.6-0.9 % Sb, up to 0.2 % Sn, 0.005-0.07 % Bi, up to 0.6 % Ag [1]. Recently, archaeological lead has attracted particular interest, as it is valued for its low content of the radioactive isotope ^{210}Pb.

High-purity lead (with a basic substance content of 99.99 % and above) is critical in industries where even trace impurities of other metals can affect device accuracy or the stability of chemical reactions, particularly in nuclear physics, semiconductor technology, the production of chemically pure reagents, and scientific applications. High-purity lead serves as a standard reference for complex chemical analyses and spectroscopy. It is widely used as a reliable X-ray and gamma radiation shield, for the manufacture of containers for transporting and storing radioactive substances (isotopes) in medicine and industry, and in batteries for backup power systems where minimal self-discharge and a long service life are required (for example, in space technology or submarine cables). High-purity lead is the basis for precision instrument-making, where it is used to create special alloys and solders, and contact degradation because of impurities that can cause corrosion or resistance changes is unacceptable. Lead is added to special types of glass (e.g., dense flint glass) to increase the refractive index and dispersion of light [2]. High-purity raw material ensures the absence of extraneous color shades and bubbles in telescope and objective lenses. In scientific research (for example, in low-background measurements), special purified archaeological lead with minimal natural radioactive isotopes is used to avoid interfering with highly sensitive sensors. Scintillation crystals of $^{arch}PbWO_4$ and $^{arch}PbMoO_4$ were grown of such lead [3, 4]. Examples of promising applications of low-background experiments using scintillation crystals made of purified archaeological lead can be found in [5-9].

The task of refining the crude alloy is to remove impurities and increase the lead content to standard norms. During refining, noble metals, copper, bismuth, arsenic, antimony, and tin are extracted from lead. At present, most plants use the pyrometallurgical method of lead refining. The fire (pyrometallurgical) method of crude metal refining uses differences in the physical and chemical properties of lead and impurity elements: solubility, melting or boiling point, oxidizing ability or affinity for sulfur, and the ability to form compounds that do not dissolve in the lead melt. During pyrometallurgical refining, impurities are sequentially removed from crude lead in various ways: copper - by liquation and by treating the melt with elemental sulfur; tellurium - by treating the melt with metallic sodium in the presence of caustic soda; arsenic, antimony and tin - by their oxidation; silver and gold - by using metallic zinc; zinc - by oxidation in a lead bath or in an alkaline melt, by vacuuming, and other methods; bismuth is removed with calcium, magnesium, and antimony (in this case, lead is contaminated with these elements); calcium, magnesium, and antimony - by high-quality refining [1].

One method of deep metal refining is vacuum distillation [10, 11]. Distillation is attractive because it can achieve high metal purity with high yield and is environmentally clean. However, simple distillation does not provide the

Cite as: O.P. Shcherban, O.I. Kondrik, D.O. Solopikhin, East Eur. J. Phys. 3, 637 (2026), https://doi.org/10.26565/2312-4334-2026-3-59

required degree of strong removal of separate impurities from lead. A more effective approach to purifying the metal is a comprehensive one.

A feature of lead is that it belongs to fusible metals (T_{melt} = 600.5 K) and is characterized by low vapor pressure at the melting point ($4.3 \cdot 10^{-7}$ Pa) [12]. Analysis of the vapor-pressure dependence on temperature shows that an acceptable rate of lead evaporation in vacuum distillation corresponds to a melt temperature of 1200 ÷ 1250 K. These physical features of lead require new approaches to distillation purification and the development of special devices for their implementation.

In the ISSPMT NSC KIPT, a comprehensive process for lead purification was proposed and a special device for distilling Pb in vacuum was patented. The proposed developments were implemented for the deep purification of archaeological lead [13].

The comprehensive process includes filtration of the initial metal (oxidizing refining) to remove surface contaminants, impurity oxides and lead, various inclusions, followed by vacuum distillation to remove volatile and non-volatile impurities with condensation of metal vapor into the liquid phase at high temperature. This approach has proven effective, but the influence of redox reactions between impurity oxides and lead oxide on impurity behavior during lead filtration and distillation has not been investigated.

The purpose of this work is to study and analyze the thermodynamics of redox reactions of impurity oxides and lead oxide during melting of the initial lead in an inert gas atmosphere and vacuum and its distillation in vacuum, as well as experimental studies of the comprehensive process of the distillation method for obtaining high-purity lead (> 99.9995 %).

2. THERMODYNAMIC ANALYSIS OF REDOX REACTIONS OF IMPURITIES DURING LEAD MELTING AND DISTILLATION

In this work, we carried out a thermodynamic analysis of the oxidation reactions of Pb and the impurities contained in it. We analyzed the content of the following oxygen-active impurities in lead: calcium, sodium, magnesium, arsenic, zinc, silver, iron, copper, tin, antimony, and bismuth. They can be removed from Pb in the form of their stable oxides CaO, Na_2O, MgO, As_2O_3, ZnO, Ag_2O, FeO, CuO, Cu_2O, SnO_2, Sb_2O_3, Bi_2O_3. This removal of impurities can be accomplished by the oxidizing refining of lead which in turn forms with oxygen the stable oxide PbO. The removal of metal impurities from lead in the form of oxides occurs under the condition of greater strength of these oxides compared to the strength of PbO in certain ranges of temperature and pressure changes in the surrounding gas environment. The main characteristic of the strength (stability) of metal impurities oxides MeO is their oxygen potential $\pi_{(MeO)}$, or the decrease in Gibbs free energy ΔG_{MeO} during the formation of oxide compounds. To estimate the strength of metal-impurity oxides in molten lead under atmospheric pressure, the change in standard Gibbs energy, ΔG^0_{MeO}, can be used. The main reaction of oxidizing refining is:

$$\frac{2n}{m}\mathrm{Me} + 2\mathrm{PbO} = \frac{2}{m}\mathrm{Me_nO_m} + \mathrm{Pb}. \quad (1)$$

Here, m and n are indices reflecting the valence ratios of the atoms in the compounds. That is, impurities (Me) replace lead in lead oxide, releasing pure lead, i.e., purifying it.

To compare the oxygen potentials of the formed impurity oxides with each other, the changes in ΔG^0_{MeO} were determined per mole of oxygen, i.e. for reactions that in the general case proceed according to the equation:

$$\frac{2n}{m}\mathrm{Me} + \mathrm{O_2} = \frac{2}{m}\mathrm{Me_nO_m}. \quad (2)$$

In this case, the equilibrium constant of reaction (2) for partial pressures is of the form: $K_p = \frac{a^{2/m}_{Me_nO_m}}{a^{2n/m}_{Me} \cdot (P_{O_2})}$, where a_{Me} and $a_{Me_nO_m}$ – the activity of metal impurities and their oxides, accordingly; P_{O_2} – equilibrium oxygen pressure, which the standard energy change ΔG^o is associated by the relation:

$$\Delta G^o = -RT \cdot \ln K_p = -RT \cdot \ln \frac{1}{(P_{O_2})_{Me_nO_m}} = RT \cdot \ln (P_{O_2})_{Me_nO_m}. \quad (3)$$

At a constant activity of Me_nO_m, which can be taken as unity, the partial pressure of oxygen in the system, which serves as a measure of the strength of the oxide, will be determined by the vapor pressure of the metal being refined in the gas phase. With a decrease in the metal vapor pressure at a constant temperature in the system, the value of $(P_{O_2})_{Me_nO_m}$ increases. That is, a decrease in the metal vapor pressure reduces the strength of the oxide. The vapor pressure of a metal in the gas phase can be reduced using a vacuum. We change the strength of the oxide by reducing the overall pressure in the system. For practical calculations of the effect of vacuum on the strength of oxides, it is convenient to use the change in the standard Gibbs energy corrected for the decrease in pressure from 1 atm., or P = 10^5 Pa. The value of the correction for the transition from the condensed state to the gaseous that with pressure P is determined by the expression (3).

The cases of formation of divalent metal oxide MeO, provided that the boiling point of the metal $T_{boil}(Me)$ is less than the boiling point of the oxide $T_{boil}(MeO)$, and also when $T_{boil}(Me) > T_{boil}(MeO)$ were considered in [14]. With taking into account corresponded stoichiometric coefficients and generalizing the consideration to the case of the formation of an oxide of the M_nO_m type, for the first condition ($T_{boil}(Me_nO_m) > T_{boil}(Me)$, the oxygen potential of the formed oxides Me_nO_m is equal to:

$$\pi^0_{Me_nO_n} = \Delta G^0_{Me_nO_m} - \frac{2n}{m}RT\cdot\ln P \quad (4)$$

In a similar manner and in the case when the boiling point (sublimation) of the oxide $T_{boil}(Me_nO_m)$ is lower than the boiling point of the metal $T_{boil}(Me)$, the correction for reduced pressure is introduced with the opposite sign:

$$\pi^0_{Me_nO_n} = \Delta G^0_{Me_nO_m} + \frac{2}{m}RT\cdot\ln P \quad (5)$$

The detailed description of the model used to calculate the dependences of the change in Gibbs free energy ΔG on temperature and pressure during the formation of impurity oxides in the liquid and vapor phases is also given in [15] with using the example of oxidizing refining in the process of obtaining high-purity tellurium by a comprehensive method.

When transforming to the base 10 logarithm $\ln(x) \approx 2.3026\cdot\lg(x)$ and using the expression for the universal gas constant in joules (R = 8.31 J/mol·K), we have:

$$\pi^0_{Me_nO_n} = \Delta G^0_1 - \frac{2n}{m}19.145T\cdot\lg\left(\frac{P}{1.013\cdot10^5}\right) (T_{boil}(Me_nO_m) > T_{boil}(Me)) \quad (6)$$

$$\pi^0_{Me_nO_n} = \Delta G^0_1 + \frac{2}{m}19.145T\cdot\lg\left(\frac{P}{1.013\cdot10^5}\right) (T_{boil}(Me_nO_m) < T_{boil}(Me)) \quad (7)$$

It was necessary to investigate the influence of atmospheric pressure of the gas medium and vacuum on the strength of oxides in the low-temperature range T = 600 ÷ 1120 K. Calculations of changes in the standard Gibbs energy $\Delta G^0(T)$ and $\Delta G(P, T)$ during the formation of base metal oxide (PbO) and impurity oxides in the liquid and gaseous phases were performed using formulas (6) and (7). The graphs of the obtained dependences are shown in Fig. 1 and Fig. 2. The Ag_2O compound decomposes already at the temperature of ~ 500 K [16], therefore it was not considered.

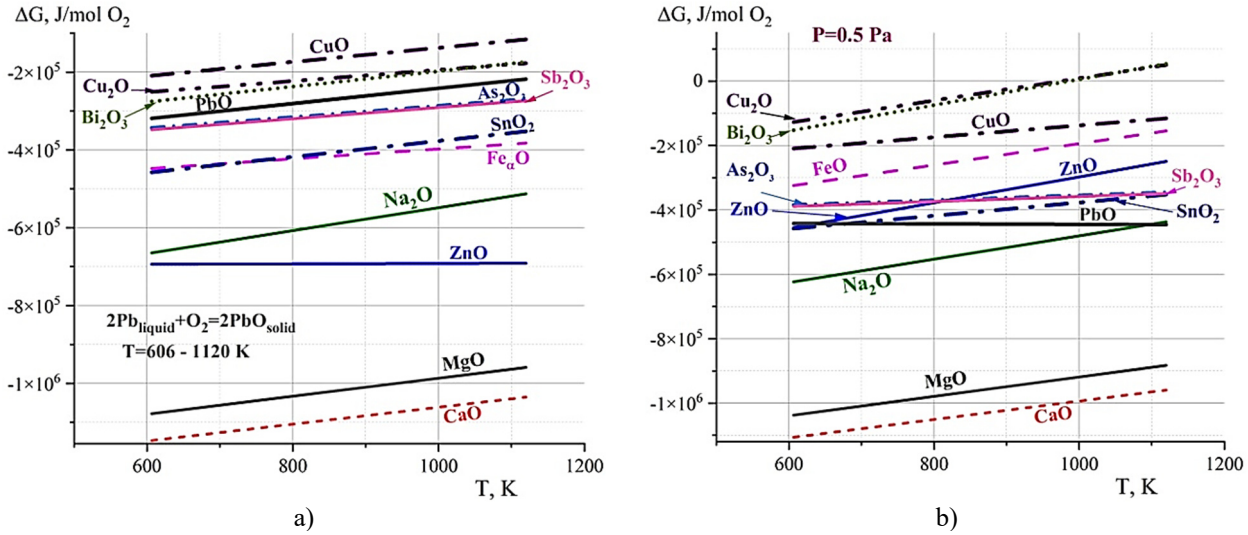

Figure 1. Change in Gibbs potential during the formation of PbO and oxides of impurities Ca, Na, Mg, As, Zn, Fe, Cu, Sn, Sb, Bi in the lead liquid phase during melting in an argon atmosphere, (a) and in a vacuum of 0.5 Pa, (b) in the temperature range of 600 ÷ 1100 K

Analysis of the obtained calculations shows that when melting lead in an argon atmosphere, there are more stable oxides (CaO, MgO, ZnO, Na_2O, $Fe_\alpha O$, SnO_2) in it relative to PbO than when melting in a vacuum (CaO, MgO, Na_2O). The stable oxides concentrate in the lead oxide and are removed from the melt by filtration. As shown in the graphs, as temperature increases, the change in Gibbs potential during oxide formation decreases slightly in absolute value, indicating decreased stability.

Thus, calculations show that a more effective removal of impurities in the form of their oxides by oxidizing refining of molten lead will be carrying out its filtration process in an argon atmosphere and at low temperatures (near the melting temperature of lead in the range of ~ 600 ÷ 650 K).

Fig. 2 shows calculated dependences of the change in the Gibbs potential during the formation of PbO and oxides of impurities in the lead liquid phase in temperature region which includes the temperatures (1200 ÷ 1250) K of the distillation purification process of lead in the vacuum of 0.5 Pa.

It can be seen that at high temperatures, the oxides that are stable relative to PbO and the oxides of the remaining impurities are CaO and MgO, which during the distillation process will collect on the surface of the melt and remain as a residue in the crucible. The formation of metal impurity oxides located above PbO will be difficult, since they have a low absolute change in Gibbs energy and therefore are not stable.

The thermodynamic calculations performed, along with their analysis, were taken into account when planning and carrying out the lead purification process using a comprehensive refining method (oxidizing refining and vacuum distillation).

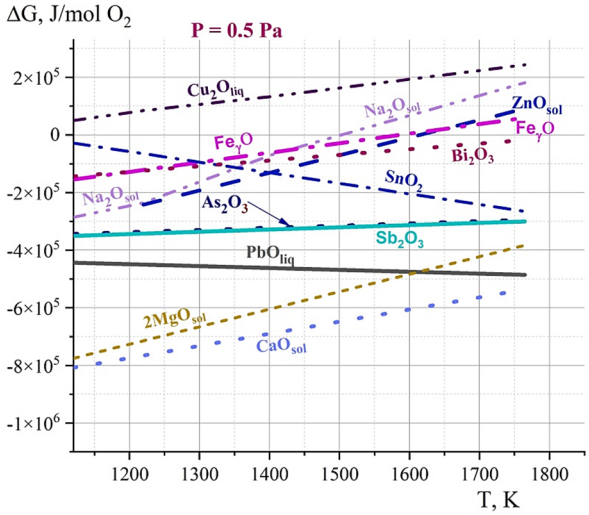

Figure 2. Change in the Gibbs potential during a formation of PbO and oxides of Ca, Na, Mg, As, Zn, Fe, Cu, Sn, Sb, Bi impurities in the lead liquid phase in the vacuum of 0.5 Pa in the high-temperature region of 1120 ÷ 1765 K

3. EXPERIMENTAL STUDIES OF THE COMPREHENSIVE PROCESS OF PRODUCING HIGH-PURITY LEAD BY DISTILLATION METHOD

The distillation method of refining is based on the difference in the composition of the liquid mixture being separated and the vapor formed of it. This difference is estimated by the value of the separation coefficient α. The theoretical foundations of the distillation method of metal purification are presented in [17-19].

The ideal separation coefficient α_i during molecular evaporation is defined as

$$\alpha_i = \frac{p_A^0\sqrt{M_B}}{p_B^0\sqrt{M_A}} \tag{8}$$

where p_A^0, p_{AB}^0 - are the vapor pressures of the pure base and impurity components A and B; M_A and M_B are the molecular weights of components A and B, respectively.

Using expression (8), the ideal impurity separation coefficients α_i were calculated at different temperatures, including the lead distillation temperature. By the value of α_i, the impurities in lead can be divided into volatile (Zn, Te, Mg, Sr, Tl, Bi, Ca, Li etc.) with $\alpha_i \sim 10^{-2}$–10^{-5} and non-volatile (Mn, Ag, Al, Ni, Co, Cu, Sn, Si, Cr, Fe, U etc.) with $\alpha_i \sim 10^{2}$–10^{9}. For most impurity elements, α_i differs significantly from 1, suggesting effective purification of lead by vacuum distillation. The values of α_i allow us to estimate the lead refining efficiency of volatile and non-volatile impurities, accounting for the yield of usable lead (losses) [13].

The basic stages of the integrated lead refining process were as follows. The first stage is filtration of liquid lead to remove surface contaminants, oxides of impurities and base metal, various inclusions and partially low-melting metals. The second stage is the distillation of the metal with condensation into a superheated liquid phase to remove volatile and non-volatile impurities.

To implement the integrated method of deep refining, we used a previously developed special device for filtering metals in an argon atmosphere [20] and a special distillation device for distilling Pb in a vacuum [13], the schemes are given in the indicated references, where the processes of filtration and distillation of lead are also described in detail. The filtration and distillation devices were made of high-purity dense graphite (MPG-7 grade) with minimal impurities, characterized by chemical inertness towards lead. Filtration was carried out in a device that combines this process with pouring the metal into measuring ingots. Fig. 3 shows the photos of ingots of filtered lead (a) and distillate (b) of refined lead weighing ~ 1 kg each. If necessary, the lead distillate was also poured into measuring ingots through the filter.

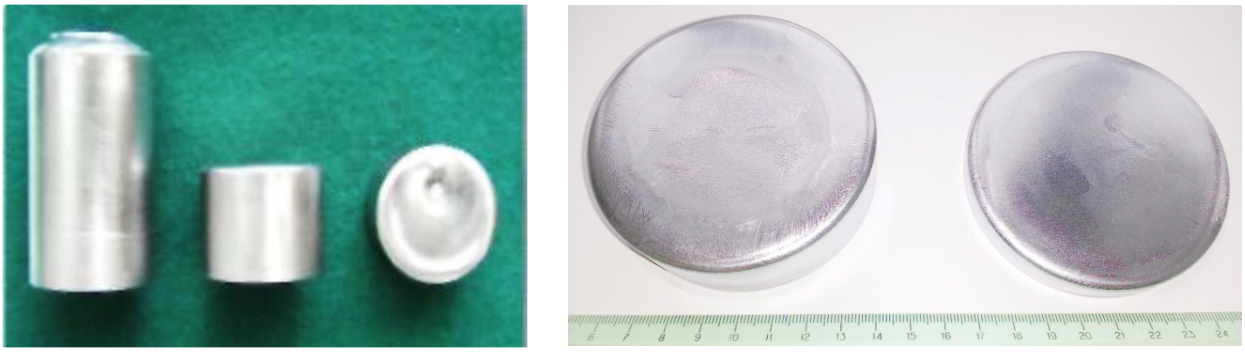

a) b)

Figure 3. Ingots of filtered initial lead (a) and distillation-refined lead (b)

4. RESULTS AND DISCUSSIONS

The initial material for experimental studies of the efficiency of lead purification by the comprehensive method was C0-grade technical lead. The concentration of impurities in it, as well as in that after filtration and distillation, is given in Table 1.

The impurity content in the lead samples was determined by high-resolution laser mass spectrometry. The random error of the analysis results is characterized by the relative standard deviation of 0.15-0.30.

Table 1 lists only the impurity elements regulated by standard norms for impurity content in lead. The purity of the initial lead in terms of the sum of impurities is ~ 99.992 %, which corresponds to the standard C0 grade. Analysis of the results obtained shows that the efficiency of oxidizing refining for individual impurities is 2 - 4 times. The efficiency of the oxidizing refining process can be increased by improving the device for intensifying the redox reactions of impurities in the lead melt, more complete collection of oxides from the surface of the melt, and removal of oxides by filtration.

Table 1. The content of majority impurities in the initial lead, after filtration and distillation in vacuum (distillate)

Impurity	Mass fraction of impurities, no more		
	Initial (C0)	after filtration	distillate (C000)
	$n \cdot 10^{-4}$ %		
Ca	3	1	0.2
Na	5	3	0.1
Mg	2	1	0.3
As	3	2	0.1
Zn	7	5	0.2
Ag	2	1	0.1
Fe	8	2	1
Cu	5	2	0.2
Sn	4	2	1
Sb	6	3	0.3
Bi	35	10	0.4
Pb, %	99.992	99.997	99.9996

If we evaluate the efficiency of distillation purification relative to filtered lead, it ranges from 2 times (Fe, Sn) to 10-30 times (Sb, Na). The low lead purification of Fe and Sn is probably due to the deviation from the ideal behavior of these impurities in lead (non-compliance with ideal separation coefficients). In general, an experimental study on the use of a comprehensive distillation method for lead purification showed that it allows the production of lead C000 grade (99.9996 %) from lead of technical C0 grade (99.992 %), an improvement of almost two orders of magnitude.

The comprehensive process described in this work for obtaining high-purity metals using oxidizing refining was applied to metals such as cadmium and zinc [21].

5. CONCLUSIONS

A thermodynamic analysis of the oxidation reactions of Pb and the impurities Ca, Na, Mg, As, Zn, Fe, Cu, Sn, Sb, Bi present in it during the melting of lead in an argon atmosphere and distillation in a vacuum was carried out. Stable and unstable impurity oxides in relation to the main lead oxide were determined by calculating the change (decrease) in the Gibbs free energy ΔG_{MeO}. These calculations make it possible to determine impurity behavior and plan the choice of technological conditions for the complex lead refining process.

The efficiency of oxidizing refining of lead by filtration of liquid metal according to the scheme of a comprehensive process of distillation purification of lead was investigated. This method reduces the content of major

impurities in the initial lead by 2-4 times. Improving the filtration device can increase the efficiency of the oxidizing refining process.

This paper presents results from experimental investigations of the comprehensive process of distillation refining of lead. Investigations show that the efficiency of this process increases by almost two orders of magnitude (from 99.992 % in the initial material to 99.9996 % in the purified product). The purity of such lead meets the standard norms for high-purity lead of the C000 grade.

ORCID

Olexii P. Shcherban, https://orcid.org/0000-0002-6004-0579; **Olexandr I. Kondrik,** https://orcid.org/0000-0001-9428-4830; **Dmytro O. Solopikhin,** https://orcid.org/0000-0003-1426-8713

REFERENCES

[1] A.M. Verkhovlyuk, A.V. Narivsky, and V.G. Mohylatenko, *Technologies for obtaining metals and alloys for foundry production*, (Vinichenko Publishing House, Kyiv, 2016). (in Ukrainian).
[2] B.C. Jamalaiah, L.R. Moorthy, and H.J. Seo, Journal of Non-Crystalline Solids, **358**(2), 204 (2012). https://doi.org/10.1016/j.jnoncrysol.2011.09.007
[3] S. Nagorny, L. Pattavina, M.B. Kosmyna, B.P. Nazarenko, S. Nisi, L. Pagnanini, S. Pirro, *et al*., Journal of Physics: Conf. Series. **841,** 012025 (2017). https://doi.org/10.1088/1742-6596/841/1/012025
[4] A.G. Yakubovskaya, I.A. Tupitsyna, and A.M. Dubovik, Problems of Atomic Science and Technology. **1**(137), 204, (2022). https://doi.org/10.46813/2022-137-204
[5] L. Pattavina, N. Ferreiro Iachellini, and I. Tamborra, Phys. Rev. D, **102**(6), 063001 (2020). https://doi.org/10.1103/PhysRevD.102.063001
[6] L. Pattavina, N. Iachellini, L. Pagnanini, L. Canonica, E. Celi, M. Clemenza, F. Ferroni, *et al*., J. Cosmol. Astropart. Phys. **10**, 064 (2021). http://dx.doi.org/10.1088/1475-7516/2021/10/064
[7] N.F. Iachellini, L. Pattavina, A.H. Abdelhameed, A. Bento, L. Canonica, F. Danevich, O.M. Dubovik, *et al*., J. Low Temp. Phys. **209**(5–6), 872 (2022). https://doi.org/10.1007/s10909-022-02823-8
[8] J.W. Beeman, G. Benato, C. Bucci, L. Canonica, P. Carniti, E. Celi, M. Clemenza, *et al*., Applied Radiation and Isotopes. **194**, 110704 (2023). https://doi.org/10.1016/j.apradiso.2023.110704
[9] D. Alloni, G. Benato, P. Carniti, M. Cataldo, L. Chen, M. Clemenza, M. Consonni, *et al*., Physical review D**, 111**, 103050 (2025). https://doi.org/10.1103/wcvd-rk1f
[10] V.E. Ivanov, I.I. Papirov, G.F. Tikhinsky, and V.M. Amonenko, *Pure and ultrapure metals*, (Metallurgia, Mscow1965). (in Russian)
[11] V.A. Pazukhin, and A.Ya. Fisher, *Separation and refining of metals in vacuum*, (Moscow: Metallurgy, 1969). (in Russian)
[12] A.N. Nesmeyanov, *Vapor Pressure of Chemical Elements,* (Moscow: Publishing House of the USSR Academy of Sciences, 1961). (in Russian)
[13] R.S. Boiko, V.D. Virich, F.A. Danevich, T. I. Dovbush, G. P. Kovtun, S. S. Nagornyi, S. Nisi, *et al*., Inorganic Materials, **47**(6), 645 (2011). https://doi.org/10.1134/S0020168511060069
[14] E. A. Kazachkov, *Calculations on the theory of metallurgical processes*, (Metallurgy, Moscow, 1988). (in Russian)
[15] O.P. Shcherban, D.O. Solopikhin, and O.I. Kondrik, Polish journal of science, **80**, 39 (2024). https://doi.org/10.5281/zenodo.14176578
[16] I.S. Kulikov, *Thermodynamics of oxides,* Reference, (Metallurgy, Moscow, 1986). (in Russian)
[17] G.G. Devyatyh, and Yu.E. Elliev, *Introduction to the theory of deep cleaning substances*, (Metallurgiya, 1973). (in Russian)
[18] A.I. Belyaev, *Fiziko-himicheskie osnovy ochistki metallov i poluprovodnikovyh materialov*, (Metallurgiya, Moscow, 1973). (in Russian)
[19] G.G. Devyatyh, and Yu.E. Elliev, *Glubokaya ochistka veshchestv*, (Vysshaya shkola, Moscow, 1974). (in Russian)
[20] G.P. Kovtun, and O.P. Shcherban, Patent Ukraine No. 1246, 2002. (in Ukrainian)
[21] O.P. Shcherban, D.O. Solopikhin, O.I. Kondrik, and V.D. Virich, Problems of Atomic Science and Technology **1**(161), 15 (2026). https://doi.org/10.46813/2026-161-015

ОТРИМАННЯ СВИНЦЮ ВИСОКОЇ ЧИСТОТИ КОМПЛЕКСНИМ МЕТОДОМ РАФІНУВАННЯ

Олексій П. Щербань, Олександр І. Кондрик, Дмитро О. Солопіхін

Національний науковий центр «Харківський фізико-технічний інститут» НАН України, вул. Академічна, 1, 61108, Харків, Україна

Досліджено термодинаміку окисно-відновлювальних реакцій утворення оксиду свинцю і оксидів домішок при фільтрації у атмосфері аргону і дистиляції Pb у вакуумі ~ 0,5 Па. По абсолютній величині зміни вільної енергії Гіббса оцінено міцності оксидів домішок по відношенню до оксиду свинцю при окисному рафінуванні і дистиляції свинцю. Досліджено комплексний процес дистиляційного рафінування свинцю, який включає такі етапи як фільтрацію (окисне рафінування) в атмосфері аргону і очистку свинцю від важколетких і легколетких домішок шляхом випаровування металу у вакуумі з конденсацією пару у гарячу рідку фазу ($T_{конд.} \approx 0{,}85\ T_{вип.}$). Наведено експериментальні результати застосування комплексного процесу для отримання свинцю високої чистоти марки С000 з сумарним вмістом основних домішок на рівні 99,9996 мас. %.

Ключові слова: *свинець; оксиди домішок; оксид свинцю; кисневий потенціал; вільна енергія Гіббса; очистка свинцю; окисне рафінування; фільтрація; дистиляція у вакуумі*

East European Journal of Physics. 3. 643-653 (2026)
DOI: 10.26565/2312-4334-2026-3-60 ISSN 2312-4334

ELECTRONIC STRUCTURE AND INTERMOLECULAR INTERACTIONS OF THE BENZOIC ACID–ETHANOL COMPLEX: RAMAN SPECTROSCOPY, DFT, AND MOLECULAR DOCKING ANALYSIS

Abduvakhid Jumabaev[1], Hakim Hushvaktov[1], Ahmad Absanov[1], Asliddin Norkulov[1], Zokhid Ernazarov[1], Leonid Bulavin[2]
[1]Samarkand State University named after Sharof Rashidov, 15 University Blvd, 140104, Samarkand, Uzbekistan
[2]Taras Shevchenko National University of Kyiv (64/13, Volodymyrska Str., Kyiv 01601, Ukraine
Corresponding Author e-mail: erudni67@gmail.com
Received June 1, 2026; revised August 13, 2026; accepted August 27, 2026

In this work, we investigated intermolecular interactions in benzoic acid and its ethanol solutions using Raman spectroscopy and quantum-chemical approaches. Analysis of the Raman spectra revealed that adding ethanol induces significant changes in benzoic acid's vibrational spectrum. These changes are primarily due to solvent effects and hydrogen-bond formation and are most pronounced in the vibrational modes corresponding to the carboxyl group. The near-invariance of the aromatic ring confirms the preservation of the structural integrity of the molecule. Theoretical calculations were performed at the DFT level, providing a thorough analysis of the system's electronic structure and energetic characteristics. The molecular electrostatic potential (MEP) surface was used to identify reactive sites within the molecule; the oxygen atoms of the carboxyl group emerged as the principal electron-rich nucleophilic centers, while the –OH group of ethanol played a significant role in hydrogen bond formation. HOMO–LUMO orbital analysis demonstrated a redistribution of electron density during complex formation and an increase in the reactivity of the system. Molecular docking results also confirmed benzoic acid's ability to interact with a biologically active binding site. During the calculations, the molecule adopted a stable conformation within the protein's active site, forming a complex through hydrogen bonds and other weak intermolecular interactions. These findings align with the MEP and electronic structure analyses, showing a close link between the molecule's quantum-chemical properties and its potential biological activity. The investigations reveal the mechanism of intermolecular interactions in the benzoic acid–ethanol system and provide a comprehensive explanation of how these interactions influence the molecule's vibrational properties, electronic structure, and behavior in a biological environment.
Key words: *Raman spectroscopy; Ab initio calculations; Hydrogen bonding; Benzoic acid; Ethanol; Molecular electrostatic potential (MEP) surface; AIM; FMO; Molecular docking*

1. INTRODUCTION

One of the main directions of current scientific research is the in-depth study of biologically active compounds and the elucidation of their mechanisms of action on living organisms. From this perspective, aromatic carboxylic acids—and benzoic acid in particular—are among the compounds of significant importance in pharmaceuticals, the food industry, and biological systems. Widely used as an antiseptic and preservative, this substance also attracts interest because it can interact with biologically active molecules [1–5]. Modern computational methods, including molecular docking, are among the most important tools for determining molecular behavior in biological systems [6]. This method allows the determination of binding energy, stability, and optimal configuration between a ligand and a biological target (e.g., a protein) [7]. As a result, it provides essential information about the compound's potential biological activity [8]. In addition, HOMO–LUMO theory plays a central role in studying the electronic structure of a molecule [9]. The energy levels of the HOMO (Highest Occupied Molecular Orbital) and LUMO (Lowest Unoccupied Molecular Orbital) enable assessment of the molecule's chemical reactivity and stability [10]. Furthermore, Molecular Electrostatic Potential (MEP) analysis reveals the electrostatic charge distribution within the molecule, allowing the identification of reactive centers (electrophilic and nucleophilic attack sites) [11]. Atoms in Molecules (AIM) theory is widely used to deepen understanding of intermolecular interactions [12]. This approach enables determination of bond nature and molecular stability through topological analysis of electron-density distribution [13]. Experimentally, vibrational spectroscopy—particularly Raman spectroscopy—is important for determining the structural and dynamic properties of molecules [14]. Raman spectra provide precise information about the bonds, functional groups, and intermolecular interactions within a molecule [15].

In this work, we comprehensively study the molecular properties of benzoic acid and analyze its interaction with biologically active systems using molecular docking [16]. In addition, the electronic structure and reactivity of the molecule are evaluated using MEP, HOMO–LUMO, and AIM methods, and its vibrational properties are determined based on Raman spectroscopy [17]. Together, these approaches deepen understanding of the compound's physicochemical and biological properties [18].

Cite as: A. Jumabaev, H. Hushvaktov, A. Absanov, A. Norkulov, Z. Ernazarov, L. Bulavin, East Eur. J. Phys. 3, 643 (2026), https://doi.org/10.26565/2312-4334-2026-3-60

2. EXPERIMENTAL AND THEORETICAL METHODS

2.1 Experimental method

We used chemically pure benzoic acid and ethanol mixtures in the liquid state at concentrations of 0.9, 0.7, 0.5, 0.3, and 0.1 mol/L. The samples were further purified according to the procedures described in [19].

All experiments were conducted at room temperature and ambient atmospheric pressure. We recorded benzoic acid and its ethanol solutions at various concentrations on an InVia Raman spectrometer equipped with a diffraction grating of 1200 lines/mm. The acquisition time was 10 s and the spectral resolution was 0.01 cm^{-1}. A Spectrum Stabilized Laser Module (532 nm, 50 mW) was used as the excitation light source. The scattered radiation was recorded using a Renishaw CCD Camera detector.

2.2 Computational method

Quantum-chemical calculations were performed using the Gaussian 09W program [20] at the density functional theory (DFT) level, employing the 6-311++G(d,p) basis set and the B3LYP (Becke–3–Lee–Yang–Parr) hybrid functional [21–22]. Spectral analyses were performed using Origin 8.5 [23], and molecular geometry was optimized using GaussView 6 [24]. Molecular docking calculations were performed using the PyRx platform, employing the AutoDock Vina algorithm.

2.3 Molecular Docking Method

In this study, molecular docking calculations were performed to determine the probable interactions of the benzoic acid molecule with the 5IKR enzyme. The three-dimensional crystal structure of the protein was downloaded from the RCSB Protein Data Bank (PDB ID: 5IKR) and prepared for subsequent calculations. During preparation, crystallographic water molecules were removed, polar hydrogen atoms were added to the protein structure, and appropriate charges were assigned. Benzoic acid was selected as the ligand, and its geometry was optimized by quantum-chemical methods. For docking calculations, the neutral form of benzoic acid was employed. The optimized structure was then converted to the PDBQT format required for docking calculations. Molecular docking calculations were performed using the PyRx platform with the AutoDock Vina algorithm [25]. Grid parameters were set to fully encompass the active site of the enzyme, enabling the identification of probable binding conformations of the ligand. The active site was defined using a grid box centered at X = 23.5 Å, Y = 28.7 Å, and Z = 19.4 Å, with dimensions of 25 × 25 × 25 Å. These parameters ensured complete coverage of the binding pocket and enabled the identification of probable binding conformations of the ligand. The obtained results, including binding energies and ligand–protein interaction types, were visualized and analyzed in detail using the Discovery Studio software [26].

3. RESULTS AND DISCUSSION

3.1. Vibrational Frequency Analysis

In this study, the Raman spectra of benzoic acid (BeAc) and its mixtures with ethanol (EtOH) were investigated over a broad spectral range (500–2000 cm^{-1}). The primary focus of the work was on identifying intermolecular interactions—particularly the formation of hydrogen bonds and their effects on vibrational properties. Raman spectroscopy enables the identification of the internal vibrational modes of molecules, thereby providing insight into their structures and interaction mechanisms [27–28]. The spectrum of pure benzoic acid exhibited a series of well-defined and intense peaks. In particular, the signal at 615 cm^{-1} corresponds to the out-of-plane C–H deformation vibration of the aromatic ring. The peak located near 790 cm^{-1} represents C–H bending vibrations within the ring and is characteristic of aromatic systems [29]. The strong peak observed at 1009 cm^{-1} is associated with the symmetric "breathing" vibration of the ring and serves as an important indicator for identifying the aromatic nucleus [30]. In the mid-frequency region, C–H in-plane vibrations are observed at 1132 cm^{-1}, while C–O bond stretching vibrations of the carboxyl group appear at 1288 cm^{-1}. C–H deformation at 1442 cm^{-1} and C=C vibrations of the aromatic ring at 1608 cm^{-1} are also recorded. These results confirm that the aromatic structure and functional groups of the molecule are preserved in their original state [31]. Upon addition of ethanol, significant changes were observed in the spectrum. In the low-frequency region (618–628 cm^{-1} and 792–799 cm^{-1}), the peaks remain essentially unchanged, indicating that the aromatic ring is stable with respect to external perturbations. However, a downshift of the main peak at 1009 cm^{-1} to the 990–1003 cm^{-1} range was observed. This red shift indicates an intensification of intermolecular interactions, specifically the formation of hydrogen bonds [32]. A similar phenomenon is observed in the 1080–1092 cm^{-1} region, where the positions of the C–C and C–O bond vibrations undergo slight changes—evidence for the redistribution of electron density within the system. The C–O stretching vibrations in the 1270–1280 cm^{-1} range show the most pronounced changes: the shift and increase in intensity of these peaks indicate the formation of hydrogen bonds between benzoic acid and ethanol molecules [33]. In the high-frequency region, particularly in the 1448–1457 cm^{-1} range, peak intensities increase, confirming the participation of ethanol molecules in the mixture. At the same time, the aromatic C=C vibrations in the 1600–1608 cm^{-1} range remain virtually unchanged. This result indicates that the interaction occurs predominantly around the carboxyl group, while the aromatic ring remains structurally nearly unaffected [34].

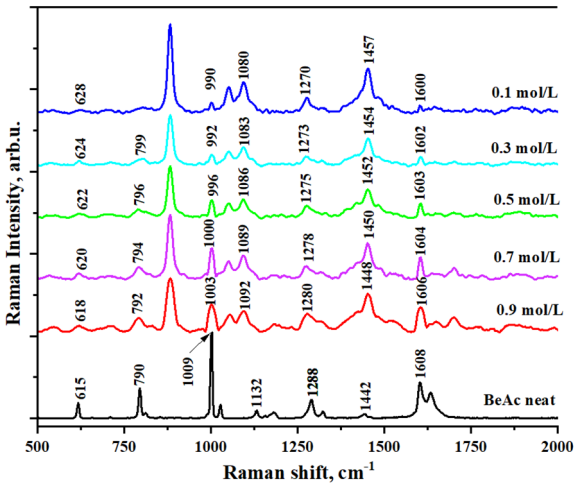

Figure 1. Raman scattering spectra of benzoic acid (BeAc) and its ethanol solutions in the 500–2000 cm^{-1} range

Within the scope of this study, the intermolecular interactions and solvation processes occurring in the binary benzoic acid–ethanol system were thoroughly investigated by Raman spectroscopy (2800–3200 cm^{-1} region), and it was scientifically demonstrated that the observed changes in this system are not merely the result of physical mixing, but rather a consequence of complex thermodynamic and structural reorganization, as evidenced by the following primary mechanisms: (1) Observation of polarization and red-shift in aromatic C–H bonds. In the spectrum of the pure aromatic compound, the peak at 3074 cm^{-1}—characteristic of the stretching vibrations of the =C–H bonds of the benzene ring and observed with high intensity—was found to gradually shift toward lower wavenumbers, reaching 3066 cm^{-1}, as ethanol was added to the system and as the concentration of the solution was progressively diluted (from 0.9 mol/L to 0.1 mol/L). This spectral shift is directly attributed to the disruption of the stable dimer structures formed by benzoic acid molecules and the subsequent formation of a completely new solvation shell involving ethanol molecules, because when the hydroxyl groups of ethanol actively interact with the π-electron cloud of the aromatic ring and with the carboxyl group, the electron density of the =C–H bond is redistributed, and the vibrational energy of this bond decreases appreciably. (2) Dynamics of aliphatic chains and reorganization of solvent microstructure. The 2920–2980 cm^{-1} region of the obtained spectra directly reflects the symmetric and asymmetric stretching vibrations of the $–CH_3$ and $–CH_2$ groups of the ethanol molecule. A change in acid concentration strongly affects the regional distribution of these aliphatic vibrations: in particular, the strong peaks observed at 2930 cm^{-1} and 2975 cm^{-1} at a concentration of 0.9 mol/L were found to shift to 2922 cm^{-1} and 2964 cm^{-1}, respectively, as the system was diluted to 0.1 mol/L. This microdynamics demonstrates that the characteristic macrostructural hydrogen bond network of ethanol is disrupted under the influence of the solute and transitions to a new energetic environment; that is, as the acid content increases, ethanol molecules tend to cluster around acid molecules rather than forming mutual associates, which in turn leads to an increase in steric hindrance and a redistribution of vibrational frequencies in the microenvironment.

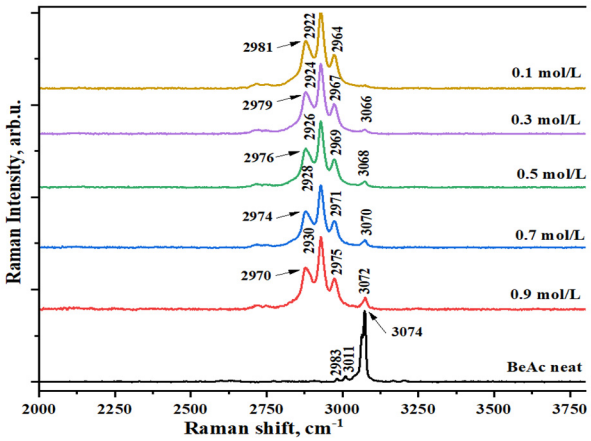

Figure 2. Raman scattering spectra of benzoic acid (BeAc) and its ethanol solutions in the 2000–3800 cm^{-1} range

3.2 Molecular Electrostatic Potential (MEP)

The molecular electrostatic potential (MEP), also known as the molecular potential surface map, is useful for visualizing the charge distribution in benzoic acid and its ethanol complexes, as well as for studying charge-dependent

parameters such as electrophilic–nucleophilic processes and bonding interactions. Determining the MEP helps identify the reactive sites of the molecule [35–37]. Figure 3 presents the MEP visualized using a color-coded scheme. Regions are colored according to the level of electrostatic potential, increasing in the order: deep red < yellow < green < blue [38]. The molecular electrostatic potential (MEP) surface maps visually represent the charge distribution in the benzoic acid monomer, dimer, and benzoic acid + ethanol complexes. They play an important role in studying charge-dependent parameters such as electrophilic and nucleophilic reactions and bonding. An additional purpose of determining the electrostatic potential is to identify the reactive regions of the molecule. The MEP map in the range of -4.389×10^{-2} eV to $+4.389 \times 10^{-2}$ eV clearly shows the charge distribution in the benzoic acid monomer. The oxygen atoms of the carboxyl (C=O) group appear in the deepest red, indicating a higher concentration of electrons—this region is therefore nucleophilic. Yellow regions are moderately electron-rich, green regions are nearly neutral, and blue regions represent electron-deficient electrophilic sites. Regarding vibrations, stretching vibrations of the C=O and O–H bonds, as well as intra-ring C–C bond vibrations, are predominantly observed. The MEP map in the range of -3.127×10^{-2} eV to $+3.127 \times 10^{-2}$ eV shows the redistribution of charges in the benzoic acid dimer. The oxygen atoms of the carboxyl (C=O) group again appear in red, indicating an electron-rich (nucleophilic) region. The intensification of colors between the two molecules reflects their mutual attraction and the formation of hydrogen bonds. Blue regions are electron-deficient and possess electrophilic character. In this configuration, the vibrations also change: in particular, the O–H bond is elongated due to hydrogen bond formation, causing a downshift in its vibrational frequency, and the C=O vibration shifts slightly as well. The MEP map in the range of -3.841×10^{-2} eV to $+3.841 \times 10^{-2}$ eV shows the charge distribution in the benzoic acid + 1 ethanol complex. The oxygen atoms of the carboxyl (C=O) group appear in the deepest red, indicating an electron-rich nucleophilic region. The hydrogen of the –OH group of ethanol is relatively positive, and it is precisely between these two sites that a hydrogen bond forms. The color gradient (red–yellow–green–blue) represents a gradual decrease in charge density: yellow regions are intermediate, green regions are nearly neutral, and blue regions are electron-deficient electrophilic zones. As a result of this interaction, the vibrations of the O–H and C=O bonds shift slightly, confirming the formation of the complex. The MEP map in the range of -5.464×10^{-2} eV to $+5.464 \times 10^{-2}$ eV shows an even stronger redistribution of charges in the complex involving benzoic acid and 2 ethanol molecules. The oxygen atoms of the carboxyl (C=O) group appear in the deepest red, confirming that they constitute the primary nucleophilic center. The hydrogens of the –OH groups of the two ethanol molecules are more positive, and the formation of multiple hydrogen bonds through them is clearly visible. The color gradient (red–yellow–green–blue) illustrates a stepwise decrease in charge density: yellow regions are intermediate, green regions are nearly neutral, and blue regions are electron-deficient electrophilic zones. Consequently, the intermolecular interactions in this complex are stronger, and the vibrations of the O–H and C=O bonds shift considerably.

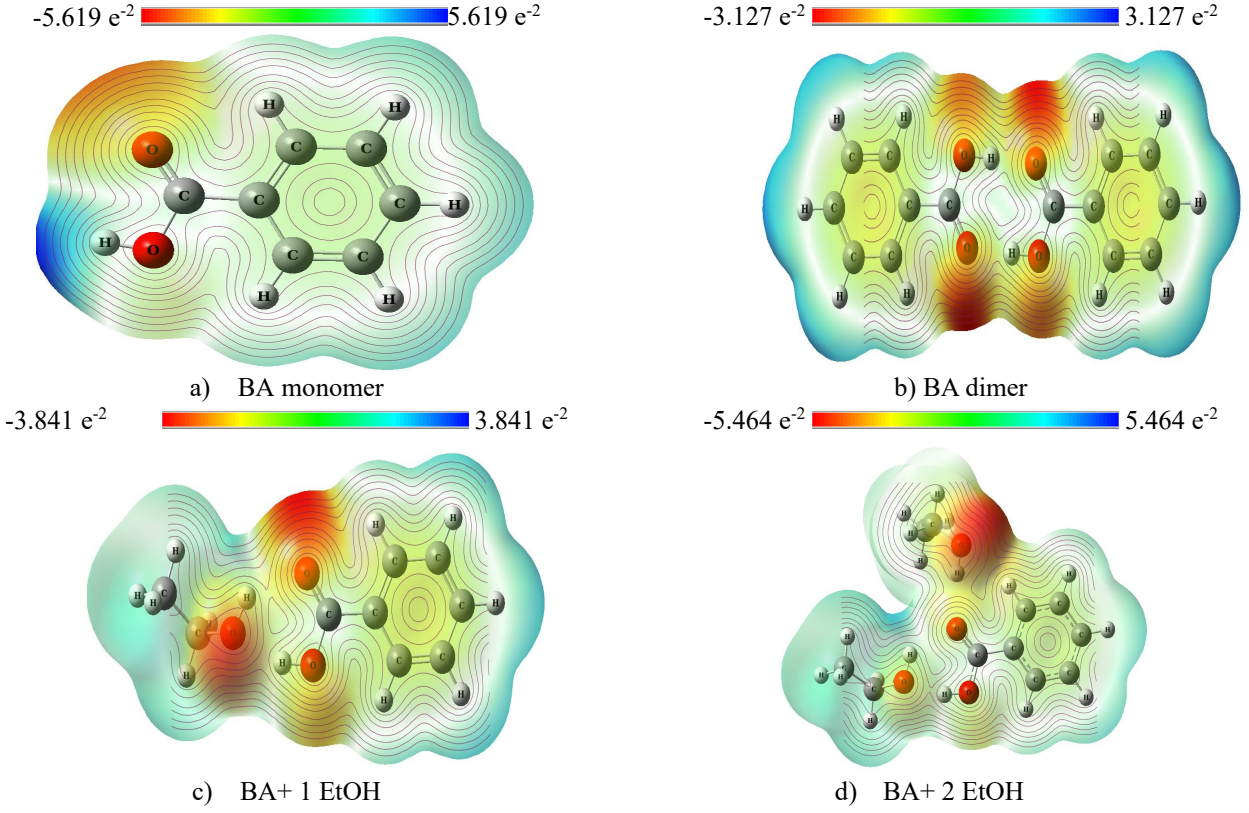

Figure 3. MEP diagram for Benzoic Acid (BA) + Ethanol complexes

3.3 Frontier Molecular Orbital (FMO) Analysis

Frontier molecular orbitals are regarded as important theoretical parameters for interpreting the electronic structure of molecules and their chemical reactivity. The Highest Occupied Molecular Orbital (HOMO) and the Lowest Unoccupied Molecular Orbital (LUMO) describe the outer electronic configuration of the molecule and are of fundamental significance in explaining the mechanisms of reactions involving electron transfer. The HOMO energy level reflects the electron-donating capability of the molecule. If the HOMO energy is relatively high, such molecules readily participate as electron donors and exhibit high activity in nucleophilic or oxidation processes. The LUMO, in contrast, is considered the orbital most susceptible to electron acceptance. If the energy level of this orbital is low, the molecule is well-positioned to accept external electrons and may effectively participate in electrophilic reactions [39–40]. Accordingly, the energy gap (ΔE) between the HOMO and LUMO orbitals is considered one of the primary indicators for assessing the reactivity and stability of a molecular system. A small energy gap indicates high sensitivity of the molecule to external perturbations—particularly electronic excitation—reflecting its greater participation in chemical processes. Conversely, a large ΔE value implies a lower probability of electron transfer, indicating that the molecular system is relatively stable and less reactive. Frontier molecular orbital theory is one of the most widely used quantum-chemical approaches for studying the electronic, optical, and chemical properties of molecules [41]. Based on HOMO and LUMO energy values, a number of global reactivity parameters can also be determined. For instance, chemical hardness (η) is expressed through the difference between HOMO and LUMO energies as:

$$\eta = \frac{E_{LUMO} - E_{HOMO}}{2} \tag{1}$$

This parameter characterizes the resistance of the molecular system to electronic perturbations. Chemical potential (μ) is determined from the following relation:

$$\mu = -\frac{E_{HOMO} + E_{LUMO}}{2} \tag{2}$$

This quantity reflects the tendency of the molecule to attract or donate electrons. Based on these parameters, the electrophilicity index (ω) is also calculated:

$$\omega = \frac{\mu^2}{2\eta} \tag{3}$$

The electrophilicity index is an important indicator for evaluating the electron-accepting capability of the molecule.

Figure 4 displays the spatial distribution of HOMO and LUMO orbitals and the energy gap (ΔE) between them for the benzoic acid molecule and its complexes with ethanol. Table 1 presents the quantum-chemical parameters determined on the basis of HOMO and LUMO energy values, including chemical hardness (η), softness (S), electrophilicity index (ω), and electronegativity (χ). Analysis of the obtained results shows that the benzoic acid + 2 ethanol complex possesses the largest dipole moment, indicating that the intermolecular interactions in this system are relatively strong. In contrast, the benzoic acid + 1 ethanol complex exhibits a lower dipole moment, reflecting a relatively weaker degree of polarization in the system.

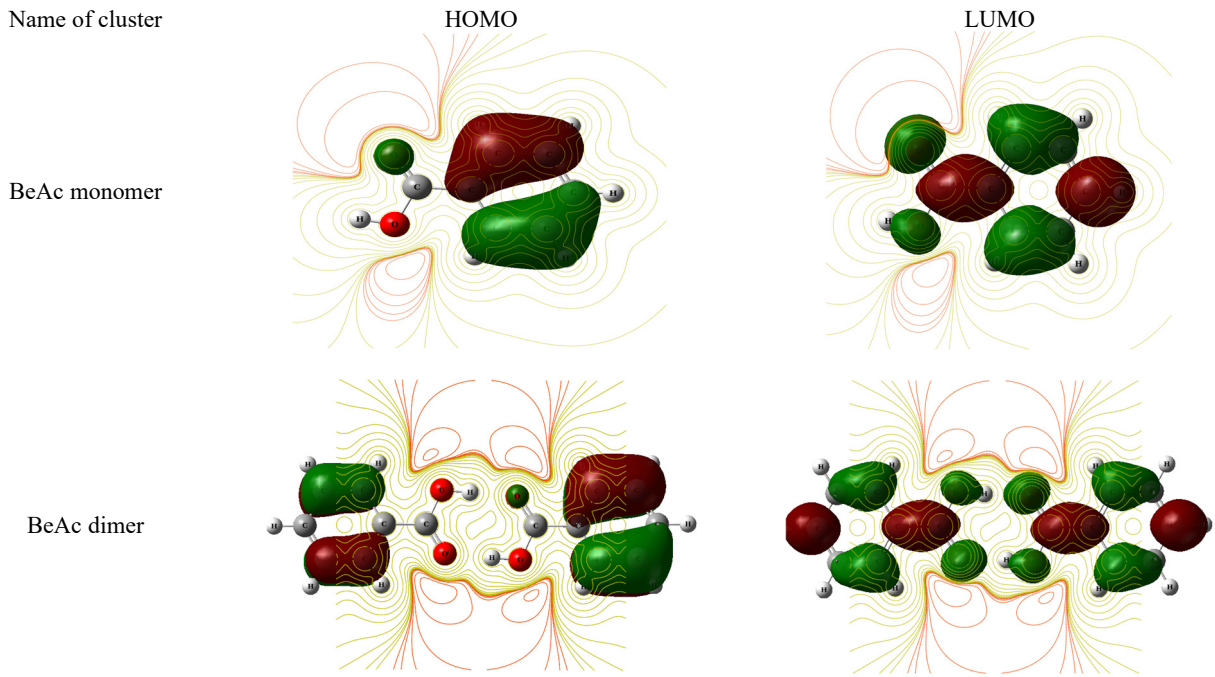

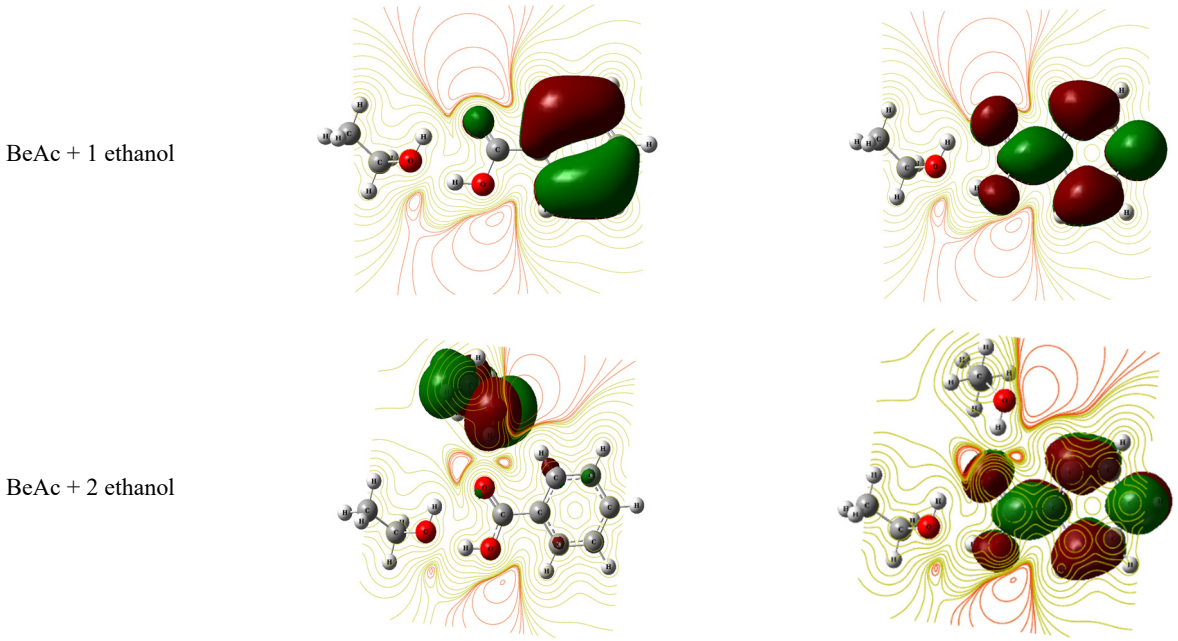

Figure 4. Frontier molecular orbital diagram of benzoic acid and its solutions

The HOMO–LUMO energy gap is one of the key indicators characterizing the electronic structure and chemical stability of a molecule. According to the calculation results, the HOMO–LUMO energy gap for the benzoic acid monomer is 130.32 kcal/mol, and in the dimer form this value is 129.45 kcal/mol. In the complexes formed with a solvent, this parameter was found to be 130.58 kcal/mol for benzoic acid + 1 ethanol, and 123.2 kcal/mol for the benzoic acid + 2 ethanol complex. The ionization potential was also analyzed, with values of 172.11 kcal/mol (benzoic acid monomer), 173.34 kcal/mol (benzoic acid dimer), 169.35 kcal/mol (benzoic acid + 1 ethanol), and 164.86 kcal/mol (benzoic acid + 2 ethanol), respectively. Furthermore, the largest value of the electrophilicity index was found to be 101.8367 kcal/mol, belonging to the benzoic acid monomer.

Table 1. Thermodynamic and chemical parameters of the title compounds

Parameters	BeAc monomer	BeAc dimer	BeAc + 1Ethanol	BeAc + 2Ethanol
Dipole moment (Debye) μ	2.126105	0.005329	1.190733	2.624885
Total energy (Thermal) (kcal/mol)	76.731	155.274	131.706	186.431
Zero-point vibrational energy (kcal/mol)	72.24695	145.47773	123.78239	174.65551
E_{HOMO}	-172.11	-173.34	-169.35	-164.86
E_{LUMO}	-41.79	-43.89	-38.77	-41.66
E_{LUMO} - E_{HOMO}	130.32	129.45	130.58	123.2
Global hardness (η) = ½(E_{LUMO}-E_{HOMO})	56.16	64.725	65.29	61.6
Chemical potential (μ) = ½(E_{LUMO}+E_{HOMO})	-106.95	-108.61	-104.06	-103.26
IP = -E_{HOMO}	172.11	173.34	169.35	164.86
EA = -E_{LUMO}	41.79	43.89	38.77	41.66
Electrophilicity index (ω) = $\mu^2/2\eta$	101.8367	91.1250	82.9260	86.5473

3.4 Atoms in Molecules (AIM) Analysis for Complexes of Benzoic Acid

Atoms in molecules (AIM) analysis is widely used to identify non-covalent interactions in molecular systems [42]. As a result of interactions between two atoms through electron density, a bond path emerges, giving rise to critical points (CPs) in the electron density. At such points, the gradient of the electron density vanishes [43]. The presence of hydrogen bonds or other interactions in molecular complexes is confirmed through the topological analysis of electron density. Figure 5 presents topological parameters for the BeAc dimer, BeAc + 1 ethanol, and BeAc + 2 ethanol complexes: the electron density ρ(r), the Laplacian of the electron density $\nabla^2\rho(r)$, the energy density H(r), the Lagrangian kinetic energy density G(r), and the potential energy density V(r) at the bond critical points (BCPs). These quantities provide extensive information about the nature of the interactions (Table 2).

According to the data presented in Table 2, the Laplacian of the electron density $\nabla^2\rho(r)$ varies in the following ranges: 0.1386–0.1388 a.u. for the BeAc dimer, 0.0681–0.1249 a.u. for BeAc + 1 ethanol, and 0.0328–0.1304 a.u. for BeAc + 2 ethanol. These positive values indicate a local depletion of electron density, confirming that the intermolecular interactions belong to the closed-shell type and are characterized by hydrogen bonds.

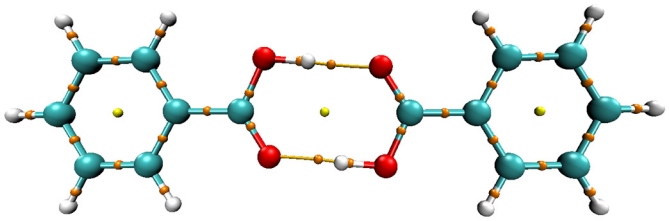

a) BeAc dimer

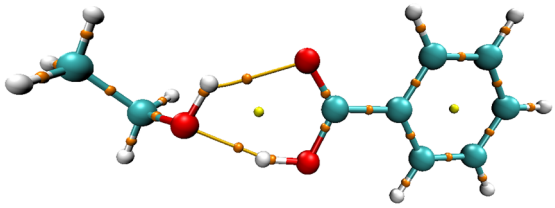

b) BeAc + 1 ethanol

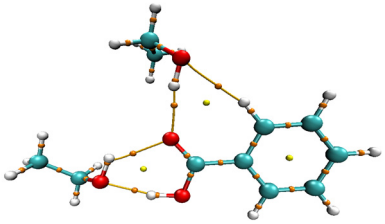

c) BeAc + 2 ethanol

Figure 5. Molecular diagrams of the title complexes. (a) BeAc dimer; (b) BeAc + 1 ethanol; (c) BeAc + 2 ethanol

Table 2. Topological parameters of the title complexes (BeAc, BeAc + ethanol)

Name of cluster	X(H)-bonds	Bond length *r, Å*	Density of all electrons $\rho(r)$	Lagrangian kinetic energy *G(r)*	Potential energy density *V(r)*	Energy density *H(r)*	Laplacian of electron density $\nabla^2\rho(r)$	Bond energy $E_{int} \approx -V(r)/2$, kcal/mol
BeAc dimer	2(O)…30(H)	1.66415	0.0478	0.0401	-0.0455	0.0054	0.1386	14.2758
	15(H)…23(O)	1.66337	0.0479	0.0402	-0.0456	0.0054	0.1388	14.2758
BeAc + 1 ethanol	2(O)…24(H)	2.01938	0.0232	0.0186	-0.0169	0.0016	0.0807	5.3023
	15(H)…16(O)	1.75013	0.0398	0.0334	-0.0356	0.0021	0.1249	11.1696
BeAc + 2 ethanol	2(O)…24(H)	2.10706	0.0196	0.0155	-0.0139	0.0015	0.0681	4.3612
	2(O)…33(H)	1.92863	0.0241	0.0209	-0.0183	0.0026	0.0940	5.7417
	10(H)…25(O)	2.42144	0.0091	0.0068	-0.0054	0.0013	0.0328	1.6942
	15(H)…16(O)	1.72156	0.0424	0.0357	-0.0389	0.0031	0.1304	12.2051

The energy density H(r) values for the BeAc dimer and its ethanol complexes are observed in different ranges: 0.0054 a.u. for the dimer, 0.0015–0.0021 a.u. for complexes with one ethanol molecule, and 0.0013–0.0031 a.u. for systems involving two ethanol molecules. The positive values of H(r) in all cases indicate that the interactions present in these systems are not covalent but rather predominantly electrostatic in nature. This further confirms that they are closed-shell type interactions mediated by hydrogen bonds. This substantiates the existence of weak hydrogen bonds between the presented complexes [44–45]. Such hydrogen bonds are analogous in nature to van der Waals interactions. The formula $E_{int} = V(r)/2$ was used to calculate the bond energy [46]. In this work, it was applied to determine hydrogen bond energies, where V(r) is the potential energy density at the bond critical points. If the energy density value at the critical points is negative ($H_{DCP_s} < 0$), the bond has covalent character; if positive ($H_{DCP_s} > 0$), it has electrostatic character.

3.5. Molecular Docking

Molecular docking is one of the modern computational approaches for modeling interactions between biomolecules. In this method, the protein is treated as a receptor and the small molecule as a ligand, and their binding characteristics and stability are evaluated. The degree of binding is typically expressed in terms of free energy values [47]. The Swiss Target Prediction method was used to identify the target protein for molecular docking studies [48]. In this work, the benzoic acid molecule was selected as the ligand, and molecular docking analysis was performed to evaluate its biological activity. Cyclooxygenase-2 (PDB ID: 5IKR) was used as the target protein for the study. This protein is associated with inflammatory processes and is one of the important biological targets extensively studied in pharmaceutical research. Docking results showed that the benzoic acid molecule is accommodated appropriately within the active site of the protein

and forms several significant interactions. The best binding pose exhibited a binding affinity of −5.8 kcal/mol, indicating favorable interaction between benzoic acid and the active site of the protein.

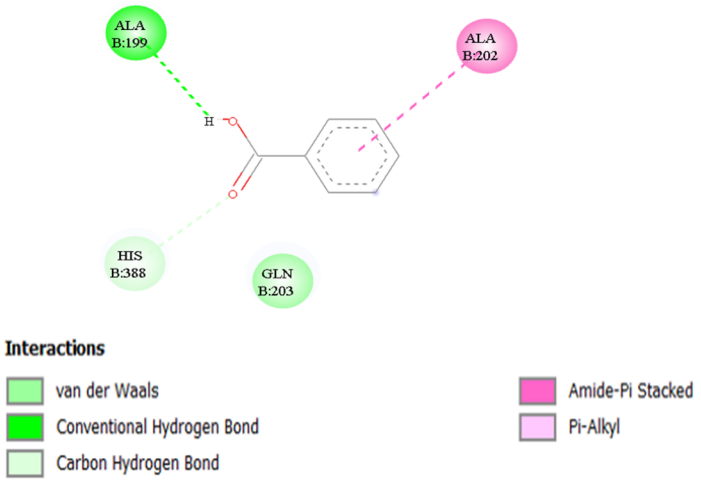

Figure 6. 2D interaction diagram of benzoic acid within the active site of the 5IKR protein

In particular, the hydrogen bond formed with the ALA (B:199) residue contributes significantly to the stability of the complex. The hydrogen-bond distance was estimated to be approximately 2.04 Å, indicating a relatively stable intermolecular interaction. Additionally, a hydrophobic π-alkyl interaction between the aromatic ring of the ligand and ALA (B:202) was observed. Furthermore, weak interactions—including van der Waals contacts and carbon–hydrogen bonds—were identified with the HIS (B:388) and GLN (B:203) amino acid residues. Such interactions contribute to the overall energetic stability of the complex. To provide a broader assessment of the docking results, the co-crystallized ligand mefenamic acid (ID8) was used as a reference molecule. Benzoic acid retained a favorable orientation within the binding cavity and formed intermolecular contacts that contributed to the stability of the resulting complex. The inclusion of the co-crystallized ligand as a reference molecule provided additional confidence in the reliability of the docking results and the predicted binding mode of benzoic acid. In general, the results demonstrate that the benzoic acid molecule possesses the capacity to bind to the 5IKR protein. This allows it to be considered as a potentially biologically active compound. However, additional experimental and theoretical investigations are required to reach more definitive conclusions.

a) ***b)***

Figure 7. (a) Overview of the 5IKR protein; (b) 3D interaction of benzoic acid with the 5IKR protein

This figure shows the three-dimensional binding pose of benzoic acid within the active site of Cyclooxygenase-2 (PDB ID: 5IKR). The interaction between the ligand and the protein is represented through hydrogen bond donor (pink) and acceptor (green) regions, illustrating how it accommodates within the active site. As seen from the figure, the functional groups of benzoic acid are positioned in close proximity to specific amino acid residues of the protein, forming weak yet relatively stable interactions with them. In particular, hydrogen bonds formed through the carboxyl group make a significant contribution to the spatial stability of the complex. Moreover, the donor and acceptor surfaces generated around the ligand are related to its electron density distribution, which enhances its compatibility with the active site and increases the probability of binding. These results confirm the existence of interactions between benzoic acid and the 5IKR protein and demonstrate its potential biological activity.

4. CONCLUSIONS

In this work, we investigated the intermolecular interactions in benzoic acid and ethanol mixtures in detail using Raman spectroscopy. Analysis of spectra from solutions prepared at various mole fractions showed significant shifts in

the principal vibrational bands due to changes in the solvent environment and, in particular, hydrogen-bond formation. Specifically, the shift of the vibrational mode of the aromatic ring of benzoic acid—characteristic at ~1009 cm^{-1}—toward lower frequencies (990–1003 cm^{-1}) unambiguously indicates the presence of intermolecular interactions. Additionally, shifts in the vibrations associated with C–O and O–H bonds, along with changes in their intensities, confirm complex formation. The analyses show that the aromatic ring structure remains virtually unchanged—that is, it is stable with respect to external perturbations. Conversely, the principal changes occur around the carboxyl functional group, identifying this region as the primary center of intermolecular interaction.

The quantum-chemical results fully corroborated the experimental observations. DFT calculations determined the electronic structure, charge distribution, and energetic parameters of the molecules, showing that electron density redistributes during complex formation. MEP maps identified the most reactive sites: the oxygen atoms of the carboxyl group participate as electron-rich (nucleophilic) centers, while the hydrogen of the –OH group of ethanol acts as a positive (electrophilic) center. HOMO–LUMO analysis revealed a decrease in the energy gap, indicating increased reactivity—an effect that intensifies as the number of ethanol molecules increases. AIM results provided an even more precise picture of the intermolecular interactions. The calculated parameters demonstrated that these bonds are non-covalent, being primarily electrostatic and characterized by weak hydrogen bonding. This indicates the predominance of closed-shell type interactions within the system. Molecular docking analysis allowed us to evaluate benzoic acid's ability to interact with biological systems. The results showed that it can form a stable complex with the Cyclooxygenase-2 (5IKR) protein, in which hydrogen bonds and hydrophobic interactions play a crucial role. This confirms the molecule's potential biological activity.

In conclusion, the investigations showed that intermolecular interactions in the benzoic acid–ethanol system are mediated primarily through hydrogen bonds, and that this process significantly influences the molecule's vibrational properties, electronic structure, and reactivity. The results are important not only for understanding the physicochemical properties of this system, but also for elucidating the molecule's behavior in a biological environment.

ORCID

Abduvakhid Jumabaev, https://orcid.org/0000-0002-4817-0290; **Hakim Hushvaktov,** https://orcid.org/0000-0001-9149-754X;
Asliddin Norkulov, https://orcid.org/0009-0008-2832-5962; **Leonid Bulavin,** https://orcid.org/0000-0002-8063-6441

REFERENCES

[1] Howard, D. L., Kjaergaard, H. G., Huang, J., & Meuwly, M. Infrared and near-infrared spectroscopy of acetylacetone and hexafluoroacetylacetone. The Journal of Physical Chemistry A, **119**(29), 7980–7990 (2015). https://doi.org/10.1021/acs.jpca.5b01863

[2] Trivella, A., Wassermann, T. N., Mestdagh, J. M., Tanner, C. M., Marinelli, F., Roubin, P., & Coussan, S. New insights into the photodynamics of acetylacetone: isomerization and fragmentation in low-temperature matrixes. Physical Chemistry Chemical Physics, **12**(29), 8300–8310 (2010). https://doi.org/10.1039/C003593A

[3] Jumabaev, A., Koyambo-Konzapa, S. J., Hushvaktov, H., Absanov, A., Khudaykulov, B., Holikulov, U., et al. Intermolecular interactions in water and ethanol solution of ethyl acetate: Raman, DFT, MEP, FMO, AIM, NCI-RDG, ELF, and LOL analyses. Journal of Molecular Modeling, **30**(10), 349 (2024). https://doi.org/10.1007/s00894-024-06147-0

[4] Jumabaev A., Absanov A., Ernazarov Z., Shodiyev A., Umarov S. Raman spectra and ab initio calculation analysis of intermolecular interactions in ethyl acetate, Journal of Samarkand State University, **139**(1), 5–12 (2023). https://doi.org/10.59251/2181-1296.2023.v4.139.1.2085

[5] Jumabaev A., Absanov A.A., Khudaykulov B.B., Ernazarov Z.I. Investigation of intermolecular interactions in butyl acetate using vibrational spectroscopy and nonempirical calculations, Uzbek Physical Journal. **25**(4), (2023). https://doi.org/10.52304/.v25i4.471

[6] Pinzi, L., & Rastelli, G. Molecular docking: shifting paradigms in drug discovery. International Journal of Molecular Sciences, **20**(18), 4331 (2019). https://doi.org/10.3390/ijms20184331

[7] Morris, G. M., Huey, R., Lindstrom, W., Sanner, M. F., Belew, R. K., Goodsell, D. S., & Olson, A. J. AutoDock4 and AutoDockTools4: Automated docking with selective receptor flexibility. Journal of Computational Chemistry, **30**(16), 2785–2791. https://doi.org/10.1002/jcc.21256

[8] Trott, O., & Olson, A. J. (2010). AutoDock Vina: improving the speed and accuracy of docking with a new scoring function, efficient optimization, and multithreading. Journal of Computational Chemistry, **31**(2), 455–461 (2009). https://doi.org/10.1002/jcc.21334

[9] Parr, R. G. *Density functional theory of atoms and molecules. In Horizons of Quantum Chemistry*, (Springer, Dordrecht, Netherlands, 1989), pp. 5–15. https://doi.org/10.1007/978-94-009-9027-2_2

[10] Koopmans, T. Ordering of wave functions and eigenenergies to the individual electrons of an atom, Physica, **1**, 104–113 (1933).

[11] Politzer, P., & Murray, J. S. The fundamental nature and role of the electrostatic potential in atoms and molecules. Theoretical Chemistry Accounts, **108**(3), 134–142 (2002). https://doi.org/10.1007/s00214-002-0363-9

[12] Bader, R. F. Everyman's derivation of the theory of atoms in molecules, The Journal of Physical Chemistry A, **111**(32), 7966-7972 (2007). https://doi.org/10.1021/jp073213k

[13] Koch, D., Pavanello, M., Shao, X., Ihara, M., Ayers, P. W., Matta, C. F., et al. The analysis of electron densities: From basics to emergent applications. Chemical Reviews, **124**(22), 12661–12737 (2024). https://doi.org/10.1021/acs.chemrev.4c00297

[14] John R. Ferraro, Kazuo Nakamoto and Chris W. Brown. *Introductory Raman Spectroscopy*, (Elsevier, 2003).

[15] Ferraro J.R., Nakamoto K., and Brown C.W. *Recent Developments in Atomic Force Microscopy and Raman Spectroscopy for Materials Characterization. Introductory Raman Spectroscopy*, (Academic Press, 2003). http://dx.doi.org/10.5772/intechopen.97257
[16] Daina, A., Michielin, O., & Zoete, V. Swiss Target Prediction: updated data and new features for efficient prediction of protein targets of small molecules. Nucleic Acids Research, **47**(W1), W357–W364 (2019). https://doi.org/10.1093/nar/gkz382
[17] Becke, A. D. Density-functional thermochemistry. III. The role of exact exchange. The Journal of Chemical Physics, **98**(7), 5648-5652 (1993). https://doi.org/10.1063/1.464913
[18] Burke, K. Perspective on density functional theory, The Journal of Chemical Physics, **136**(15), (2012). https://doi.org/10.1063/1.4704546
[19] Gordon, A. G., AND Ford, R. A. *The Chemist's Companion: A Handbook of Practical Data, Techniques, and References*, (Wiley, 1973).
[20] Frisch, M.J. et al. Gaussian 09, Revision D.01. Gaussian, Inc., Wallingford, (2009).
[21] Lee, C., Yang, W., & Parr, R. G. Development of the Colle-Salvetti correlation-energy formula into a functional of the electron density, Physical Review B, **37**(2), 785 (1988). https://doi.org/10.1103/PhysRevB.37.785
[22] Krishnan, R. B. J. S., Binkley, J. S., Seeger, R., & Pople, J. A. Self-consistent molecular orbital methods. XX. A basis set for correlated wave functions, The Journal of Chemical Physics, **72**(1), 650–654 (1980). https://doi.org/10.1063/1.438955
[23] Moberly, J. G., Bernards, M. T., Waynant, K. V. Key features and updates for Origin 2018, J. Cheminform., **10**(5), (2018). https://doi.org/10.1186/s13321-018-0259-x
[24] Dennington, R.; Keith, T. A.; and Millam, J. M. GaussView Version 6.0. Semichem Inc., Shawnee Mission, KS, (2016).
[25] Trott, O., & Olson, A. J. AutoDock Vina. Journal of Computational Chemistry, **31**(2), 455–461 (2010). https://doi.org/10.1002/jcc.21334
[26] Dallakyan, S., & Olson, A. J. Small-molecule library screening by docking with PyRx, in: *Chemical Biology: Methods and Protocols*, (Springer New York, 2014), pp. 243–250. https://doi.org/10.1007/978-1-4939-2269-7_19
[27] Smith, E., & Dent, G. *Modern Raman Spectroscopy: A Practical Approach*, (John Wiley & Sons, (2019).
[28] Kolesov, B. A. Hydrogen bonds: Raman spectroscopic study. International Journal of Molecular Sciences, **22**(10), 5380 (2021). https://doi.org/10.3390/ijms22105380
[29] Socrates, G. *Infrared and Raman Characteristic Group Frequencies: Tables and Charts*, (John Wiley & Sons, 2004).
[30] Ferraro, J. R., Nakamoto, K., Brown, C. W. *Introductory Raman Spectroscopy*, (Academic Press, 2003).
[31] Meenakshi, R. Experimental (FT-IR and FT-Raman) and spectroscopic investigations, electronic properties and conformational analysis. RSC Advances, **6**(26), 21822–21831 (2016). https://doi.org/10.1039/C6RA00092D
[32] Burikov, S., Dolenko, T., Patsaeva, S., Starokurov, Y., & Yuzhakov, V. Raman and IR spectroscopy research on hydrogen bonding in water–ethanol systems. Molecular Physics, **108**(18), 2427–2436 (2010). https://doi.org/10.1080/00268976.2010.516277
[33] Rozenberg, M., Loewenschuss, A., & Marcus, Y. An empirical correlation between stretching vibration redshift and hydrogen bond length. Physical Chemistry Chemical Physics, **2**(12), 2699–2702 (2000). https://doi.org/10.1039/B002216K
[34] Max, J. J., Chapados, C. Infrared spectroscopy of aqueous carboxylic acids. Journal of Chemical Physics, **116**, 4626–4642 (2002). https://doi.org/10.1021/jp036401t
[35] Suresh, C. H., Remya, G. S., & Anjalikrishna, P. K. Molecular electrostatic potential analysis: A powerful tool to interpret and predict chemical reactivity. Wiley Interdisciplinary Reviews: Computational Molecular Science, **12**(5), e1601 (2022). https://doi.org/10.1002/wcms.1601
[36] Koyambo-Konzapa S.-J., Oubella A., Issaoui N., et al., Molecular structure, spectroscopic (FT-IR, NMR and UV–Vis), electronic properties, molecular docking, and molecular dynamics studies on novel thiazolidinone derivative, J. Mol. Struct. **1318**, 139301 (2024). https://doi.org/10.1016/j.molstruc.2024.139301
[37] Jumabaev, A. et al. Insights into Amyl Acetate–Chloroform Interactions: Vibrational Spectroscopy and Quantum Topology Study. Ukrainian Journal of Physics, **71**(1), 28–38 (2026). https://doi.org/10.15407/ujpe71.1.28
[38] Jumabaev, A. et al. Vibrational spectra and computational study of amyl acetate: MEP, AIM, RDG, NCI, ELF, and LOL analysis. Ukr. J. Phys. **69**, 742 (2024). https://doi.org/10.15407/ujpe69.10.742
[39] Jalbout, A. F., Trzaskowski, B., & Hameed, A. J. Theoretical investigation of the electronic structure of 1-(3,4;3,5 and 3,6-bis-selenocyanato-phenyl)pyrrolidinofullerenes. Journal of Organometallic Chemistry, **691**(22), 4589–4594 (2006). https://doi.org/10.1016/j.jorganchem.2006.06.041
[40] Jalbout, A. F., Hameed, A. J., & Trzaskowski, B. Study of the structural and electronic properties of 1-(4,5 and 6-selenenyl derivatives-3-formyl-phenyl)pyrrolidinofullerenes. Journal of Organometallic Chemistry, **692**(5), 1039–1047 (2007). https://doi.org/10.1016/j.jorganchem.2006.10.068
[41] Khudaykulov, B., Norkulov, A., Holikulov, U., Absanov, A., Doroshenko, I., & Jumabaev, A. Raman and DFT study of non-covalent interactions in liquid benzophenone and its solutions. Low Temperature Physics, **51**(2), 220–230 (2025). https://doi.org/10.1063/10.0035406
[42] Akman, F., Issaoui, N., & Kazachenko, A. S. Intermolecular hydrogen bond interactions in the thiourea/water complexes: X-ray, DFT, NBO, AIM, and RDG analyses. Journal of Molecular Modeling, **26**(6), 161 (2020). https://doi.org/10.1007/s00894-020-04423-3
[43] Bader, R. F. Definition of molecular structure: by choice or by appeal to observation? The Journal of Physical Chemistry A, **114**(28), 7431–7444 (2010). https://doi.org/10.1021/jp102748b
[44] Rozas, I., Alkorta, I., & Elguero, J. Behavior of ylides containing N, O, and C atoms as hydrogen bond acceptors. Journal of the American Chemical Society, **122**(45), 11154–11161 (2000). https://doi.org/10.1021/ja0017864
[45] Tang, T. H., Deretey, E., Knak Jensen, S. J., & Csizmadia, I. G. Hydrogen bonds: Relation between lengths and electron densities at bond critical points. The European Physical Journal D, **37**(2), 217–222 (2006). https://doi.org/10.1140/epjd/e2005-00317-0
[46] Espinosa, E., Molins, E., & Lecomte, C. Hydrogen bond strengths revealed by topological analyses of experimentally observed electron densities. Chemical Physics Letters, **285**(3–4), 170–173 (1998). https://doi.org/10.1016/S0009-2614(98)00036-0

[47] Pinzi, L., & Rastelli, G. Molecular docking: shifting paradigms in drug discovery. International Journal of Molecular Sciences, **20**(18), 4331 (2019). https://doi.org/10.3390/ijms20184331
[48] Daina, A., Michielin, O., & Zoete, V. SwissTargetPrediction: updated data and new features for efficient prediction of protein targets of small molecules. Nucleic Acids Research, **47**(W1), W357–W364 (2019). https://doi.org/10.1093/nar/gkz382

ЕЛЕКТРОННА СТРУКТУРА ТА МІЖМОЛЕКУЛЯРНІ ВЗАЄМОДІЇ КОМПЛЕКСУ БЕНЗОЙНА КИСЛОТА–ЕТАНОЛ: СПЕКТРОСКОПІЯ КОРОБІНАЦІЙНОГО РАЗМІНУ, ДПФ ТА АНАЛІЗ МОЛЕКУЛЯРНОГО ДОКІНГУ

Абдувахід Джумабаєв[1], Хакім Хушвактов[1], Ахмад Абсанов[1], Асліддін Норкулов[1], Зохід Ерназаров[1], Леонід Булавін[2]
[1]Самаркандський державний університет імені Шарофа Рашидова,
140104, м. Самарканд, Узбекистан, Університетський бульвар, 15;
[2]Київський національний університет імені Тараса Шевченка (вул. Володимирська, 64/13, Київ 01601, Україна)

У цій роботі ми досліджували міжмолекулярні взаємодії в бензойній кислоті та її етанольних розчинах за допомогою раманівської спектроскопії та квантово-хімічних підходів. Аналіз спектрів комбінаційного розсіювання показав, що додавання етанолу викликає значні зміни в коливальному спектрі бензойної кислоти. Ці зміни в першу чергу зумовлені ефектами розчинника та утворенням водневих зв'язків і найбільш виражені в режимах коливань, що відповідають карбоксильній групі. Майже інваріантність ароматичного кільця підтверджує збереження структурної цілісності молекули. Теоретичні розрахунки були виконані на рівні DFT, що забезпечує ретельний аналіз електронної структури та енергетичних характеристик системи. Поверхню молекулярного електростатичного потенціалу (MEP) використовували для ідентифікації реакційноздатних центрів у молекулі; атоми кисню карбоксильної групи виникли як основні багаті електронами нуклеофільні центри, тоді як група –OH етанолу відіграла значну роль у формуванні водневих зв'язків. Орбітальний аналіз HOMO–LUMO продемонстрував перерозподіл електронної густини під час утворення комплексу та збільшення реакційної здатності системи. Результати молекулярного докінгу також підтвердили здатність бензойної кислоти взаємодіяти з біологічно активним сайтом зв'язування. Під час розрахунків молекула прийняла стабільну конформацію в межах активного центру білка, утворюючи комплекс через водневі зв'язки та інші слабкі міжмолекулярні взаємодії. Ці висновки узгоджуються з MEP та аналізом електронної структури, демонструючи тісний зв'язок між квантово-хімічними властивостями молекули та її потенційною біологічною активністю. Дослідження розкривають механізм міжмолекулярних взаємодій у системі бензойна кислота–етанол і дають вичерпне пояснення того, як ці взаємодії впливають на коливальні властивості молекули, електронну структуру та поведінку в біологічному середовищі.

Ключові слова: *раманівська спектроскопія; ab initio розрахунки; водневий зв'язок; бензойна кислота; етанол; поверхня молекулярного електростатичного потенціалу (МЕП); AIM; FMO; молекулярний докінг*

East European Journal of Physics. 3. 654-658 (2026)
DOI:10.26565/2312-4334-2026-3-61 ISSN 2312-4334

INTERACTIONS BETWEEN TECHNETIUM-99m RADIOPHARMACEUTICALS AND PLASMA PROTEINS: A MOLECULAR DOCKING STUDY

V. Trusova[1]*, P. Kuznietsov[2], I. Yakymenko[2], G. Gorbenko[1]
[1]*Department of Medical Physics and Biomedical Nanotechnologies, V.N. Karazin Kharkiv National University*
4 Svobody Sq., Kharkiv, 61022, Ukraine
[2]*O.I. Akhiezer Department for Nuclear Physics and High Energy Physics, V.N. Karazin Kharkiv National University*
4 Svobody Sq., Kharkiv, 61022, Ukraine
**Corresponding Author E-Mail: valerija.trusova@karazin.ua*
Received May 16, 2026, revised July 30, 2026; accepted August 5, 2026

Technetium-99m (^{99m}Tc) is the most widespread radionuclide with physicochemical characteristics highly suitable for diagnostic nuclear medicine. The radiopharmaceuticals obtained by complexation of ^{99m}Tc with ligating agents or targeting biomolecules are increasingly used for diagnostic purposes in oncology, cardiology, nephrology, neurology and other fields of medical practice. One factor that may influence clinical efficiency of ^{99m}Tc radiotracers involves their interactions with the proteins of human blood plasma. Most studies of such kind of interactions have been focused on albumin, while much less attention was given to other protein components of blood plasma. In the present work the molecular docking technique was employed to evaluate the possibility of association between a series of ^{99m}Tc radiopharmaceuticals and plasma proteins including transthyretin, fibrinogen, alpha1-acid glycoprotein, Fc and Fab fragments of immunoglobulin G. It was found that the investigated ^{99m}Tc compounds (except pertechnetate) form the strongest complexes with alpha1-acid glycoprotein and fibrinogen. The affinities of TcMED, TcDTPA, TcMAG, TcECD, TcDIS and TcMEB for alpha1-acid glycoprotein and fibrinogen appeared to be higher than those for albumin. The structural characteristics of both plasma proteins and ^{99m}Tc radiotracers were demonstrated to determine the amino acid composition of the binding sites. The presence of peptide fragments in the structure of ^{99m}Tc compounds was assumed to markedly increase their affinity for plasma proteins. The results obtained may be helpful for gaining deeper insights into biodistribution pattern of ^{99m}Tc radiopharmaceuticals.
Keywords: *Technetium-based radiotracers; Transthyretin; Fibrinogen; Alpha1-acid glycoprotein; Immunoglobulin G; Molecular docking*

Technetium 99m (^{99m}Tc) is known as a main radionuclide currently used for obtaining a variety of diagnostic radiopharmaceuticals for nuclear medicine [1-3]. Among the advantages of ^{99m}Tc-based radiotracers are their half-life (6 h) and gamma ray energy (140 keV) resulting in a minimum dose of patient irradiation, ability to accumulate in targeting tissues or organs, rapid blood clearance, availability from ^{99}Mo/^{99m}Tc generator, relatively low cost, etc. [4-6]. Due to its unique coordination chemistry with oxidation states ranging from -1 to +7, ^{99m}Tc can form complexes with diverse ligands containing O–, C–, N–, P–, S– donor centers [7-10]. The radiopharmaceuticals with N- and S-centers appeared to be most effective in assessment of renal function, the compounds with O-centers are highly suitable for myocardial imaging, while those with S- or P-centers can be used for heart imaging and bone scintigraphy [1]. Along with these characteristics, the efficiency of radiotracers is determined by their physicochemical parameters, including size and charge, partition coefficient, stability in vitro and in vivo, pharmacokinetic behavior and plasma protein binding [11, 12]. In our previous work we employed the molecular docking technique to perform a comparative analysis of the binding affinities of ^{99m}Tc radiopharmaceuticals for albumin, the most abundant plasma protein [13]. The aim of the present study was to analyze the binding of ^{99m}Tc-based radiotracers to other plasma proteins, such as transthyretin, fibrinogen, alpha1-acid glycoprotein, Fc and Fab fragments of immunoglobulin G. A set of twelve examined ^{99m}Tc-based radiotracers included Pertechnetate [^{99m}Tc]TcO_4–(TcPER), [^{99m}Tc]Tc-Sestamibi (TcSES), [^{99m}Tc]Tc-Tetrofosmin (TcTET), [^{99m}Tc]Tc-Medronate (TcMED), [^{99m}Tc]Tc-dimercaptosuccinic acid (TcDMSA), [^{99m}Tc]Tc-diethylenetriaminepentaacetate (TcDTPA), [^{99m}Tc]Tc-mercaptoacetyltriglycine (TcMAG), [^{99m}Tc]Tc-Exametazime (TcEXA), [^{99m}Tc]Tc-diisopropyl iminodiacetic acid (TcDIS), [^{99m}Tc]Tc-ethylene cysteine dimer (TcECD), [^{99m}Tc]Tc-Mebrofenin (TcMEB), and [^{99m}Tc]Tc-hydrazinonicotinic acid conjugate-H6F (TcHYN). The plasma proteins selected for this study play significant role in many biological processes. Transthyretin is responsible for transport of the thyroid hormone thyroxine and the retinol-binding protein. Mutations in this protein lead to its misfolding and aggregation into amyloid fibrils associated with cardiomyopathy or polyneuropathy on the development of inherited transthyretin amyloidosis [14]. Fibrinogen has multiple biological functions among which are promotion of platelet adhesion and aggregation, regulation of inflammatory response, triggering of hemostasis, leukocyte activation, wound healing, etc. [15]. Alpha1-acid glycoprotein has immunomodulatory properties and affects pharmacokinetics and pharmacodynamics of drugs and endogeneous ligands [16}. Immunoglobulin G is the major serum antibody capable of binding to and neutralizing various pathogens and toxins [17].

Cite as: V. Trusova, P. Kuznietsov, I. Yakymenko, G. Gorbenko, East Eur. J. Phys. 3, 654 (2026), https://doi.org/10.26565/2312-4334-2026-3-61

METHODS

The structures of the investigated ^{99m}Tc radiopharmaceuticals [18] were built in MarvinSketch (version 18.10.0) and the geometries were further optimized in Avogadro (version 1.1.0). Five human plasma proteins such as transthyretin (TTR, PDB ID 1BMZ), fibrinogen (FIB, PDB ID 3GHG), alpha1-acid glycoprotein (AGL, PDB ID 3KQ0), Fc fragment of immunoglobulin G (IFC, PDB ID 5JII) and Fab fragment of immunoglobulin G (IFA, PDB ID 7FAB) were selected as receptors for ^{99m}Tc radiotracers. Molecular docking was conducted using the HDOCK server (https://hdock.phys.hust.edu.cn/), a hybrid docking software which combines template-based modeling and free docking [19]. The most energetically favorable docking complexes were visualized with the VMD software (version 1.14).

RESULTS AND DISCUSSION

Presented in Table 1 are the best docking scores correlating with the binding affinities of the examined ^{99m}Tc radiopharmaceuticals for plasma proteins. The analysis of the docking results revealed that TcPER has the lowest binding affinities decreasing in the order TTR > FIB > IFC ≥ AGL > IFA. Notably, the complxes of TcPER with TTR, FIB, IFC and AGL appeared to be stronger than that with albumin (the best docking score -57.77 [20]). For the other compounds under study the binding affinities were found to decrease in the rows: ***TcSES***: FIB ≥ AGL > IFA > TTR > IFC; ***TcTET***: FIB > AGL > IFA >TTR ≥ IFC; ***TcMED***: FIB ≥ AGL >IFC> TTR > IFA; ***TcDMSA***: AGL > FIB > IFC> TTR > IFA; ***TcDTPA***: AGL > FIB > TTR > IFC > IFA; ***TcMAG***: AGL > FIB > TTR > IFA ≥ IFC; ***TcEXA***: AGL > FIB ≥ TTR > IFA > IFC; ***TcDIS***: AGL > FIB > IFA > IFC ≥ TTR; ***TcECD***: AGL > FIB > TTR > IFA > IFC; ***TcHYN***: AGL > IFA > FIB > IFC > TTR; ***TcMEB:*** AGL > FIB > TTR ≥ IFA > IFC.

Table 1. Best docking scores characterizing the binding affinities of technetium-99m radiopharmaceuticals for plasma proteins

^{99m}Tc radiotracer	Transthyretin	Fibrinogen	Alpha1 acid glycoprotein	Fc fragment of immunoglobulin G	Fab fragment of immunoglobulin G
TcPER	-72.28	-67.18	-62.15	-63.11	-57.68
TcSES	-130.04	-150.47	-147.49	-126.96	-133.99
TcTET	-128.87	-143.11S	-136.31	-128.64	-132.76
TcMED	-128.69	-144.68	-142.03	-129.35	-124.69
TcDMSA	-125.36	-150.29	-159.60	-128.40	-119.23
TcDTPA	-179.19	-188.16	-209.74	-153.90	-148.29
TcMAG	-139.62	-148.47	-154.83	-114.04	-116.00
TcEXA	-137.69	-139.34	-155.74	-110.53	-119.11
TcDIS	-146.40	-193.71	-229.05	-148.80	-167.56
TcECD	-126.08	-142.34	-154.67	-110.03	-113.64
TcHYN	-185.84	-233.39	-270.04	-213.38	-251.22
TcMEB	-159.73	-195.19	-223.21	-148.14	-156.76

It appeared that the investigated ^{99m}Tc radiotracers (except TcPER) display the highest affinity for AGL and FIB, while the lowest affinities in most cases are observed for IFC and IFA. The comparison of the best binding scores presented here with those obtained in our previous work for albumin [13] indicates that some ^{99m}Tc compounds are capable of associating with plasma proteins stronger than with albumin. These systems include: TcMED – FIB / AGL, TcDTPA – AGL, TcMAG – AGL / FIB, TcECD – AGL, TcDIS – AGL / FIB, TcMEB -– AGL / FIB.

Table 2. Interface residues in the complexes of technetium-99m radiopharmaceuticals with plasma proteins

^{99m}Tc radiotracer	Transthyretin	Fibrinogen	Alpha1 acid glycoprotein	Fc fragment of immunoglobulin G	Fab fragment of immunoglobulin G
TcPER	THR_{75B} LYS_{76B} TRP_{79B} PRO_{86B} PHE_{87B} HIS_{88B} HIS_{90B} ALA_{91B} LEU_{111B} SER_{112B} PRO_{113B} TYR_{114B} SER_{115B} TYR_{116B}	TRP_{293E} LEU_{294E} GLY_{295E} ASN_{296E} ASP_{297E} ILE_{299E} SER_{300E} PHE_{329E} VAL_{331E} GLN_{332E} TYR_{338E} PHE_{75E} TRP_{403E}	PHE_{32A} TYR_{37A} HIS_{97A} PHE_{98A} PHE_{114A} ASP_{115A} ASN_{117A} ASN_{121A} TRP_{122A} GLY_{123A}	ASP_{399A} SER_{400A} PHE_{405A} ASN_{390B} TYR_{391B} LYS_{392B} LYS_{409B} LEU_{410B} THR_{411B}	VAL_{3A} ARG_{91A} VAL_{92A} PHE_{93A} LEU_{45B} GLU_{46B} TRP_{47B} ILE_{48B} ASP_{60B}
TcSES	ILE_{84A} SER_{85A} PRO_{86A} PRO_{113A} PHE_{87A} TYR_{114A} THR_{96B} ALA_{97B} ASN_{98B} ASP_{99B} SER_{100B} ARG_{103B} TYR_{105B} VAL_{122B}	ARG_{149G} TYR_{422H} TRP_{424H} HIS_{429H} GLY_{430H} THR_{431H} ASP_{432H} SER_{443H} TRP_{444H} GLY_{1S} HIS_{2S} ARG_{3S} PRO_{4S}	TYR_{27A} ALA_{29A} SER_{30A} PHE_{32A} TYR_{37A} SER_{40A} VAL_{41A} GLU_{43A} ILE_{44A} THR_{47A} LEU_{62A} GLU_{64A} GLN_{66A} ARG_{68A} LEU_{79A} ILE_{88A} ARG_{90A} TYR_{91A} VAL_{92A} GLY_{93A}	LEU_{251B} MET_{252B} ILE_{253B} HIS_{433B} ASN_{434B} HIS_{435B} TYR_{436B} THR_{437B} GLN_{438B}	PRO_{8A} GLN_{40A} LEU_{41A} PRO_{42A} GLY_{43A} THR_{44A} GLU_{78A} ALA_{79A} ASP_{80A} TYR_{82A} GLY_{95A} GLY_{96A} THR_{97A} LYS_{98A} LEU_{99A} THR_{159A} PRO_{160A} SER_{161A} LYS_{162A} TYR_{168A}

^{99m}Tc radiotracer	Transthyretin	Fibrinogen	Alpha1 acid glycoprotein	Fc fragment of immunoglobulin G	Fab fragment of immunoglobulin G
			HIS_{97A} PHE_{98A} LEU_{112A} PHE_{114A} ASN_{117A} LEU_{124A} SER_{125A} TYR_{127A}		GLN_{39B} GLY_{42B} ARG_{43B} GLY_{44B}
TcMED	LYS_{76A} LYS_{80A} SER_{85A} PRO_{86A} PHE_{87A} HIS_{88A} GLU_{89A} TYR_{114A} PHE_{95B} THR_{96B} ALA_{97B} ASN_{98B} ASP_{99B} SER_{100B} GLY_{101B} ARG_{103B} TYR_{105B} VAL_{122B}	CYS_{45G} PRO_{46G} SER_{47G} GLY_{48G} CYS_{49G} CYS_{76H} PRO_{77H} THR_{78H} GLY_{79H} CYS_{80H} LEU_{82H} CYS_{19I} PRO_{20I} THR_{21I} THR_{22I} TYR_{43J} LYS_{44J} CYS_{45J} PRO_{46J} SER_{47J} GLY_{48J} THR_{78K} GLY_{79K} CYS_{80K} CYS_{19L} PRO_{20L} THR_{21L} THR_{22L}	PHE_{32A} TYR_{37A} VAL_{41A} VAL_{92A} GLU_{96A} HIS_{97A} PHE_{98A} ALA_{99A} PHE_{114A} ASP_{115A} VAL_{116A} ASN_{117A} ASN_{121A} TRP_{122A} GLY_{123A}	PRO_{244A} PRO_{245A} LYS_{246A} PRO_{247A} THR_{250A} LEU_{251A} HIS_{310A} TRP_{313A} LEU_{314A} SER_{337A} LYS_{338A} ALA_{339A} PRO_{374A} ASP_{376A} ILE_{377A} HIS_{429A} GLU_{430A}	SER_{110A} THR_{112A} SER_{133A} ASP_{134A} GLN_{163A} ASN_{165A} ALA_{169A} ALA_{141B} GLY_{166B} VAL_{167B} HIS_{168B} PHE_{170B} VAL_{185B} VAL_{186B} THR_{187B}
TcDMSA	LYS_{76A} PRO_{86A} PHE_{87A} HIS_{88A} TYR_{114A} PHE_{95B} THR_{96B} ASN_{98B} ASP_{99B} SER_{100B} GLY_{101B} ARG_{103B} TYR_{105B} VAL_{122B} THR_{123B}	LEU_{73J} TYR_{76J} GLN_{77J} ASN_{79J} ASN_{80J} SER_{83J} HIS_{84J} THR_{87J} SER_{108K} THR_{110K} SER_{111K} SER_{114K} PHE_{115K} LEU_{47L} VAL_{50L} GLU_{51L} THR_{54L} VAL_{57L}	TYR_{27A} SER_{30A} PHE_{32A} TYR_{37A} VAL_{41A} ILE_{44A} THR_{47A} PHE_{49A} LEU_{62A} GLU_{64A} GLN_{66A} ARG_{90A} VAL_{92A} HIS_{97A} LEU_{112A} PHE_{114A} SER_{125A} TYR_{127A}	PRO_{244A} PRO_{245A} LYS_{246A} PRO_{247A} LYS_{248A} THR_{250A} LEU_{251A} TRP_{313A} LEU_{314A} ILE_{336A} SER_{337A} LYS_{338A} ALA_{339A} PRO_{374A} ASP_{376A} ILE_{377A} MET_{428A} HIS_{429A} GLU_{430A}	GLN_{40A} LEU_{41A} PRO_{42A} GLY_{43A} THR_{44A} ALA_{79A} ASP_{80A} TYR_{82A} LYS_{98A} GLN_{39B} PRO_{40B} PRO_{41B} GLY_{42B} ARG_{43B} VAL_{92B} TYR_{94B}
TcDTPA	PHE_{95A} THR_{96A} ALA_{97A} ASN_{98A} ASP_{99A} SER_{100A} GLY_{101A} ARG_{103A} TYR_{105A} VAL_{122A} THR_{123A} LYS_{76B} SER_{85B} PRO_{86B} PHE_{87B} HIS_{88B} GLU_{89B} TYR_{114B}	PRO_{204K} VAL_{205K} VAL_{206K} GLY_{218K} GLY_{219K} GLU_{220K} THR_{221K} SER_{222K} GLU_{223K} TYR_{225K} ASN_{284K} TYR_{285K} SER_{201L} VAL_{202L} ASP_{203L} LYS_{206L} GLN_{210L} GLY_{214L} PHE_{215L} GLY_{216L} HIS_{217L}	TYR_{27A} VAL_{41A} ILE_{44A} THR_{47A} PHE_{49A} PHE_{51A} LEU_{62A} GLU_{64A} GLN_{66A} LEU_{79A} ILE_{88A} ARG_{90A} TYR_{110A} LEU_{112A} PHE_{114A} SER_{125A} TYR_{127A}	VAL_{273A} LYS_{274A} PHE_{275A} ASN_{276A} TRP_{277A} GLU_{283A} VAL_{284A} HIS_{285A} ASN_{286A} ALA_{287A} LYS_{288A} THR_{289A} SER_{304A} LEU_{306A}	SER_{110A} VAL_{111A} THR_{112A} LEU_{131A} ILE_{132A} SER_{133A} ASP_{134A} GLN_{163A} ASN_{165A} GLY_{166B} VAL_{167B} HIS_{168B} PHE_{170B} VAL_{185B} VAL_{186B} THR_{187B}
TcMAG	LYS_{76A} SER_{85A} PRO_{86A} PHE_{87A} HIS_{88A} GLU_{89A} TYR_{114A} PHE_{95B} THR_{96B} ALA_{97B} ASN_{98B} ASP_{99B} SER_{100B} GLY_{101B} ARG_{103B} TYR_{105B} VAL_{122B}	ASN_{79A} ASN_{80A} SER_{83A} HIS_{84A} THR_{87A} SER_{111B} SER_{112B} SER_{114B} PHE_{115B} GLN_{116B} TYR_{117B} MET_{118B} THR_{54C} SER_{55C} VAL_{57C} LYS_{58C} ILE_{61C}	TYR_{27A} SER_{30A} THR_{47A} PHE_{49A} PHE_{51A} LEU_{62A} GLU_{64A} LEU_{79A} ILE_{88A} ARG_{90A} TYR_{110A} LEU_{112A} PHE_{114A} SER_{125A} TYR_{127A}	VAL_{273B} LYS_{274B} PHE_{275B} ASN_{276B} TRP_{277B} GLU_{283B} VAL_{284B} HIS_{285B} ALA_{287B} THR_{289B} SER_{304B}	GLN_{40A} LEU_{41A} PRO_{42A} GLY_{43A} THR_{44A} ASP_{80A} TYR_{82A} GLN_{39B} PRO_{40B} PRO_{41B} GLY_{42B} ARG_{43B} GLY_{44B} VAL_{92B} TYR_{94B}
TcEXA	TRP_{41A} LYS_{70A} GLU_{72A} HIS_{90A} GLU_{92A} VAL_{94A} TRP_{41B} LYS_{70B} GLU_{2B} HIS_{90B} GLU_{92B}	TYR_{76A} ASN_{79A} ASN_{80A} SER_{83A} HIS_{84A} THR_{87A} THR_{110B} SER_{111B} SER_{114B} PHE_{115B} TYR_{117B} $ET_{118}B$ LYS_{53C} THR_{54C} VAL_{57C} LYS_{58C} ILE_{61C}	TYR_{27A} SER_{30A} PHE_{32A} VAL_{41A} ILE_{44A} THR_{47A} PHE_{49A} PHE_{51A} LEU_{62A} GLU_{64A} GLN_{66A} LEU_{79A} ARG_{90A} TYR_{110A} LEU_{112A} PHE_{114A} SER_{125A} TYR_{127A}	VAL_{273A} LYS_{274A} PHE_{275A} ASN_{276A} TRP_{277A} GLU_{283A} VAL_{284A} HIS_{285A} ASN_{286A} ALA_{287A} THR_{289A} SER_{304A} LEU_{306A}	GLY_{32A} HIS_{33A} ASN_{34A} LYS_{36A} TYR_{86A} ARG_{88A} SER_{89A} ARG_{91A} ILE_{100B} ALA_{101B} GLY_{102B} GLY_{103B}
TcECD	LYS_{76A} LYS_{80A} SER_{85A} PRO_{86A} PHE_{87A} HIS_{88A} GLU_{89A} TYR_{114A} PHE_{95B} THR_{96B} ALA_{97B} ASN_{98B}	TYR_{76J} ASN_{79J} ASN_{80J} SER_{83J} HIS_{84J} LEU_{86J} THR_{87J} SER_{111K} SER_{114K} PHE_{115K} TYR_{117K} LYS_{53L}	TYR_{27A} SER_{30A} PHE_{32A} VAL_{41A} ILE_{44A} THR_{47A} PHE_{49A} PHE_{51A} LEU_{62A} GLU_{64A} GLN_{66A} LEU_{79A}	PRO_{244A} PRO_{245A} LYS_{246A} PRO_{247A} THR_{250A} LEU_{251A} TRP_{313A} LEU_{314A} SER_{337A} LYS_{338A} ALA_{339A} PRO_{374A}	THR_{112A} LEU_{131A} SER_{133A} ASP_{134A} GLN_{163A} SER_{164A} ASN_{165A} HIS_{168B} THR_{169B} PHE_{170B} VAL_{185B} THR_{187B}

^{99m}Tc radiotracer	Transthyretin	Fibrinogen	Alpha1 acid glycoprotein	Fc fragment of immunoglobulin G	Fab fragment of immunoglobulin G
	ASP_{99B} ARG_{103B} TYR_{105B} VAL_{122B}	THR_{54L} SER_{55L} VAL_{57L} LYS_{58L} ILE_{61L}	ILE_{88A} ARG_{90A} TYR_{110A} LEU_{112A} PHE_{114A} SER_{125A} TYR_{127A}	ASP_{376A} ILE_{377A} HIS_{429A} GLU_{430A}	
TcMEB	THR_{96A} ALA_{97A} ASN_{98A} ASP_{99A} SER_{100A} GLY_{101A} ARG_{103A} TYR_{105A} VAL_{122A} LYS_{76B} LYS_{80B} PRO_{86B} PHE_{87B} TYR_{114B}	SER_{222K} TYR_{239K} ASP_{241K} ASN_{243K} THR_{244K} VAL_{251K} GLN_{253K} ASN_{254K} ARG_{255K} GLN_{256K} GLY_{287K} LEU_{288K} PRO_{289K} GLU_{313K} MET_{314K} GLU_{315K} LYS_{321K} LYS_{449K} MET_{450K} SER_{451K} MET_{452K} LYS_{453K}	TYR_{27A} SER_{30A} PHE_{32A} TYR_{37A} SER_{40A} VAL_{41A} ILE_{44A} THR_{47A} LEU_{62A} GLU_{64A} GLN_{66A} ARG_{68A} ARG_{90A} VAL_{92A} GLY_{93A} HIS_{97A} PHE_{114A} SER_{125A} TYR_{127A}	SER_{354A} ARG_{355A} ASP_{356A} TYR_{349B} THR_{350B} LEU_{351B} PRO_{352B} TRP_{417B} LYS_{439B} SER_{440B} LEU_{441B} SER_{442B} LEU_{443B} SER_{444B}	SER_{110A} VAL_{111A} THR_{112A} SER_{133A} ASP_{134A} GLN_{163A} THR_{139B} ALA_{141B} GLY_{166B} VAL_{167B} HIS_{168B} PHE_{170B} VAL_{185B} VAL_{186B} THR_{187B}

The analysis of interfacial amino acid residues showed that TcSES, TcMED, TcDMSA, TcDTPA, TcMAG, TcECD and TcMEB associate with essentially similar binding sites located at the interface between identical A and B chains of homotetrameric transthyretin molecule, while TcPER and TcEXA occupy distinct sites (Table 2). In contrast to transthyretin, for fibrinogen the similarity between the amino acids constituting the binding sites was observed only for TcMAG, TcEXA and TcECD, while the other compounds interacted with completely different sets of amino acid residues. In the case of AGL the binding motif common for TcSES, TcDMSA, TcDTPA, TcMAG, TcEXA, TcECD and TcMEB involves the residues TYR_{27A} VAL_{41A} ILE_{44A} THR_{47A} PHE_{49A} LEU_{62A} GLU_{64A} GLN_{66A} ARG_{90A} LEU_{112A} PHE_{114A} SER_{125A} TYR_{127A}, while the binding sites for TcPER and TcMED contain the only residue (PHE_{114A}) from the above binding motif. The Fc fragment of immunoglobulin G has essentially similar binding sites for TcMED, TcDMSA and TcECD, all containing the residues PRO_{244A} PRO_{245A} LYS_{246A} PRO_{247A} THR_{250A} LEU_{251A} TRP_{313A} LEU_{314A} SER_{337A} LYS_{338A} ALA_{339A} PRO_{374A} ASP_{376A} ILE_{377A} HIS_{429A} GLU_{430A}. Analogously, the sites for TcDTPA, TcMAG and TcEXA include similar residues such as VAL_{273B} LYS_{274B} PHE_{275B} ASN_{276B} TRP_{277B} GLU_{283B} VAL_{284B} HIS_{285B} ALA_{287B} THR_{289B} SER_{304B}. For the Fab fragment of immunoglobulin G similar binding modes were revealed for TcMED, TcDTPA and TcMEB, as well as for TcDMSA and TcMAG.

Overall, the above findings indicate that structural peculiarities of both ^{99m}Tc radiopharmaceutical and plasma protein determine the mode and strength of their complexation. For instance, the highest binding affinities observed for TcHYN for all examined proteins seem to arise from the presence of specific peptide (YLFFVFER) in its structure, in contrast to the other ^{99m}Tc compounds.

CONCLUSIONS

In summary, the molecular docking study of the interactions between twelve structurally different ^{99m}Tc radiopharmaceuticals and five functionally important proteins of human blood plasma revealed that: (i) the explored ^{99m}Tc compounds (except pertechnetate) showed the highest affinity for alpha1-acid glycoprotein and fibrinogen, while the lowest affinities were observed for Fc and Fab fragments of immunoglobulin G; (ii) the affinities of TcMED, TcDTPA, TcMAG, TcECD, TcDIS, TcMEB for alpha1-acid glycoprotein, and the affinities of TcMED, TcMAG, TcDIS, TcMEB for fibrinogen are higher than the corresponding parameters for albumin; (iii) among the ^{99m}Tc compounds under study TcHYN forms the strongest complexes with plasma proteins; iv) the amino acid composition of the binding sites shows both similarities and differences depending on the structural features of ^{99m}Tc radiotracers and plasma proteins. These findings suggest that pharmacokinetics and pharmacodynamics of ^{99m}Tc radiopharmaceuticals can be affected by their complexation with functional proteins of human blood plasma that have to be taken into account while using these compounds in clinical practice.

Acknowledgements

This work was supported by the Ministry of Education and Science of Ukraine (the project № Д3/174-2025).

ORCID IDs

Valeriya Trusova, https://orcid.org/0000-0002-7087-071X; **Galyna Gorbenko,** https://orcid.org/0000-0002-0954-5053
Pylyp Kuznietsov, https://orcid.org/0000-0001-8477-1395, **Ivan Yakymenko,** https://orcid.org/0000-0002-0194-8376

REFERENCES

[1] M.U. Akbar, M.R. Ahmad, A. Shaheen, and S. Mushtaq, J. Radioanal. Nucl. Chem. **310**, 477–493 (2016). https://doi.org/10.1007/s10967-016-5019-7
[2] T. J. Ruth, Annu. Rev. Nucl. Part. Sci. **70**, 77–94 (2020). https://doi.org/10.1146/annurev-nucl-032020-021829
[3] M. T. Ma, Front. Chem. Biol. **4**, 1729615 (2026). https://doi.org/10.3389/fchbi.2025.1729615
[4] G. M. Currie, and E. M. Rohren, Semin. Nucl. Med. **55**, 829-840 (2025). https://doi.org/10.1053/j.semnuclmed.2025.01.005

[5] E. Strub, D. Badea, J. Bruns, A. Frontera, N. Mayordomo, A. Sakhonenkova, M. R. Jungfer, M. Wickleder, C.Yong, and M. Zegke, Eur. J. Inorg. Chem. **28**, e202400780 (2025). https://doi.org/10.1002/ejic.202400780
[6] N. Ahmed, and M. Zia, J. Acad. Radiol. **6**, 143–159 (2023). https://doi.org/10.1007/s42058-023-00128-7
[7] A. Maruk, A. Bruskin, and G. Kodina, Radiochemistry **53**, 341–353 (2011). https://doi.org/10.1134/S1066362211040011
[8] I. Ibrahim, J. Radioanal. Nucl. Chem, **281**, 669–674 (2009). https://doi.org/10.1007/s10967-009-0040-8
[9] M. Sanad, Radiochemistry **55**, 539–544 (2013). https://doi.org/10.1134/S1066362213050159
[10] E. von Guggenberg, H. Dietrich, I. Skvortsova, M. Gabriel, I. Virgolini, and C. Decristoforo, Eur. J. Nucl. Med. Mol. Imaging **34**, 1209–1218 (2007). https://doi.org/10.1007/s00259-006-0348-3
[11] Y. Arano, Ann. Nucl. Med. **16**, 79–93 (2002). https://doi.org/10.1007/BF02993710
[12] A. S. Dzik-Jurasz, Br. J. Radiol. **76**, 98–109 (2003). https://doi.org/10.1259/bjr/25833499
[13] V. Trusova, U. Malovytsia, P. Kuznietsov, I. Yakymenko, and G. Gorbenko, East Eur. J. Phys. **2**, 405-411 (2025). https://doi.org/10.26565/2312-4334-2025-2-49
[14] M. A. Liz, T. Coelho, V. Bellotti M. I. Fernandez-Arias, P. Mallaina, and L. Obici, Neurol. Ther. **9**, 395–402 (2020). https://doi.org/10.1007/s40120-020-00217-0
[15] A. S. Wolberg, J. Thromb. Haemost. **21**, 3005-3015 (2023). https://doi.org/10.1016/j.jtha.2023.08.014
[16] T. Fournier, N. Medjoubi, and D. Porquet, Biochim. Biophys. Acta Protein Struct. Mol. Enzymol. **1482**, 157–171 (2000). https://doi.org/10.1016/S0167-4838(00)00153-9
[17] S. Yanaka, R. Yogo,and K. Kato, Biophys. Rev. **12**, 637–645 (2020). https://doi.org/10.1007/s12551-020-00698-1
[18] S. Rathmann, Z. Ahmad, S. Slikboer, H. Bilton, D. Snider, and J. Valliant, In: J. Lewis, A. Windhorst, B. Zeglis (eds) Radiopharmaceutical Chemistry. Springer, Cham. (2019). https://doi.org/10.1007/978-3-319-98947-1_18
[19] Y. Yan, H. Tao, J. He, and S-Y. Huang, Nat. Protoc. **15**, 1829–1852 (2020). https://doi.org/10.1038/s41596-020-0312-x
[20] V. Trusova, P. Kuznietsov, I. Yakymenko, and G. Gorbenko, East Eur. J. Phys. **1**, 520-524 (2026). https://doi.org/10.26565/2312-4334-2026-1-59

ВЗАЄМОДІЇ МІЖ РАДІОФАРМПРЕПАРАТАМИ ТЕХНЕЦІЮ 99m ТА БІЛКАМИ ПЛАЗМИ: ДОСЛІДЖЕННЯ МЕТОДОМ МОЛЕКУЛЯРНОГО ДОКІНГУ

Валерія Трусова[1], Пилип Кузнєцов[2], Іван Якименко[2], Галина Горбенко[1]

[1]Кафедра медичної фізики та біомедичних нанотехнологій, Харківський національний університет імені В.Н. Каразіна м. Свободи 4, Харків, 61022, Україна

[2]Кафедра фізики ядра та високих енергій імені О.І. Ахієзера, Харківський національний університет імені В.Н. Каразіна м. Свободи 4, Харків, 61022, Україна

Технецій-99m (^{99m}Tc) є найбільш розповсюдженим радіонуклідом з фізико-хімічними характеристиками, необхідними для діагностичної ядерної медицини. Радіофармпрепарати, отримані шляхом комплексоутворення між ^{99m}Tc та лігандами чи таргетними біомолекулами все ширше застосовуються для діагностичних цілей в онкології, кардіології, нефрології, неврології та інших сферах клінічної практики. Одним із чинників, що можуть впливати на клінічну ефективність сполук ^{99m}Tc, є їхні взаємодії з білками плазми крові людини. Переважна більшість досліджень такого типу взаємодій були сфокусовані на альбуміні, тоді як значно менше уваги приділялось іншим білковим компонентам плазми крові. У даній роботі метод молекулярного докінгу був застосований для оцінки можливості асоціації між серією ^{99m}Tc радіофармпрепаратів та білками плазми включаючи транстиретин, фібриноген, альфа1 кислий глікопротеїн, Fc та Fab фрагменти імуноглобуліну G. Було показано, що досліджувані сполуки технецію 99m (окрім пертехнетату) утворюють найміцніші комплекси з альфа1 кислим глікопротеїном та фібриногеном. Спорідненість TcMED, TcDTPA, TcMAG, TcECD, TcDIS та TcMEB до альфа1 кислого глікопротеїну та фібриногену виявилась вищою, ніж спорідненість цих сполук до альбуміну. Було продемонстровано, що структурні характеристики як білків плазми, так і комплексів технецію 99m визначають амінокислотний склад сайтів зв'язування. Висловлено припущення, що наявність пептидного фрагменту в структурі ^{99m}Tc сполук значно підвищує їхню спорідненість до білків плазми. Отримані результати можуть бути корисними для більш глибокого розуміння розподілу ^{99m}Tc радіофармпрепаратів в організмі.

Ключові слова: *радіофармпрепарати на основі технецію 99m, транстиретин, фібриноген, альфа1 кислий глікопротеїн, імуноглобулін G, молекулярний докінг*

East European Journal of Physics. 3. 659-664 (2026)
DOI:10.26565/2312-4334-2026-3-62 ISSN 2312-4334

QUANTITATIVE TRANSMISSION ELECTRON MICROSCOPY ANALYSIS OF AMYLOID FIBRIL MORPHOLOGY

V. Trusova[1]*, U. Malovytsia[1], O. Zhytniakivska[1], K. Chkuaseli[1], S. Bogatyrenko[2], G. Gorbenko[1]
[1]Department of Medical Physics and Biomedical Nanotechnologies, V.N. Karazin Kharkiv National University
4 Svobody Sq., Kharkiv, 61022, Ukraine
[2]Department of Materials for Reactor Building and Physical Technologies, V.N. Karazin Kharkiv National University
4 Svobody Sq., Kharkiv, 61022, Ukraine
**Corresponding Author email: valerija.trusova@karazin.ua*
Received May 5, 2026; revised July 29, 2026; accepted August 12, 2026

Amyloid fibrils are increasingly regarded as versatile protein-based nanomaterials whose functional properties depend not only on their molecular cross-β architecture but also on their supramolecular morphology. The present study was undertaken to compare the mesoscale organization of albumin, insulin, and lysozyme fibrillar assemblies using quantitative transmission electron microscopy. Representative TEM images were analyzed by a standardized image-processing workflow based on segmentation, skeletonization, orientation analysis, and connected-object morphometry. The resulting descriptors included projected fibril/aggregate area fraction, skeleton length density, apparent junction/crossover and endpoint densities, local width, object density, Feret length, aspect ratio, and orientation anisotropy. Insulin displayed the highest projected area fraction, skeleton length density, object density, endpoint density, and apparent junction/crossover density, indicating a compact and highly fragmented architecture dominated by numerous short rod-like elements. In contrast, lysozyme fibrils exhibited the greatest median Feret length and aspect ratio, consistent with a stronger contribution of longitudinal elongation and the formation of more anisometric structures. Albumin showed an intermediate morphology characterized by comparatively sparse, curvilinear fibrils and lower densities of discrete objects and endpoints. Orientation distributions were broad for all three systems, and the corresponding anisotropy indices remained low, demonstrating predominantly isotropic rather than globally aligned organization. These findings indicate that the three protein systems occupy distinct regimes of amyloid assembly, ranging from fragmentation-dominated architectures to more elongated fibrillar networks. The quantitative framework established here provides a basis for relating amyloid morphology to surface accessibility, connectivity, mechanical behavior, and the design of fibril-based hydrogels, biosensors, drug-delivery platforms, and nanocomposites.
Keywords: *Amyloid fibrils; Transmission electron microscopy; Quantitative image analysis; Fibril morphology; Supramolecular organization; Skeletonization; Orientation anisotropy; Protein nanomaterial*

Amyloid fibrils constitute a broad class of highly ordered protein assemblies characterized by a conserved cross-β structural motif [1,2]. Despite this common molecular architecture, their supramolecular morphology can vary substantially depending on protein sequence, solution conditions, aggregation pathway, fibril maturation, and sample preparation [3,4]. Accordingly, amyloid assemblies may form long isolated filaments, short rod-like fragments, laterally associated bundles, dense interconnected networks, or heterogeneous mixtures containing both fibrillar and non-fibrillar material. This mesoscale organization is functionally relevant because fibril dimensions, fragmentation, bundling, packing density, and network connectivity can influence gel formation, mechanical behavior, colloidal stability, molecular accessibility, and interactions with other biomolecular or nanoscale components [5].

Transmission electron microscopy (TEM) is among the most widely used techniques for direct visualization of amyloid fibrils because it enables assessment of their morphology at nanometer-scale resolution [6,7]. However, TEM-based assessment of amyloid morphology often remains predominantly descriptive, which limits the objectivity, reproducibility, and cross-sample comparability of structural interpretations. This limitation becomes particularly relevant when protein systems differ simultaneously in fibril abundance, contour organization, degree of overlap, and local connectivity. Quantitative image analysis is therefore essential for translating visually apparent morphological differences into reproducible and biologically interpretable structural descriptors. The need for such analysis becomes especially evident when fibrillar systems display fundamentally different modes of organization [8]. A relatively sparse population of elongated filaments cannot be compared meaningfully with a dense field of short overlapping rods using a single descriptor alone. Likewise, parameters derived from isolated fibrils may not adequately represent highly entangled or locally bundled networks. A comprehensive comparison should therefore consider several complementary features of the fibrillar architecture, including projected material coverage, fibrillar density, degree of fragmentation, apparent connectivity, directional organization, and object elongation.

In the present work, the morphology of albumin (BSAF), insulin (InsF), and lysozyme (LzF) fibrillar assemblies was examined comparatively using quantitative analysis of representative TEM images. These three systems were selected because they exhibit markedly different supramolecular organizations, ranging from relatively sparse elongated fibrils to dense populations of short fragments and extended network-like structures. The study aimed to identify and

Cite as: V. Trusova, U. Malovytsia, O. Zhytniakivska, K. Chkuaseli, S. Bogatyrenko, G. Gorbenko, East Eur. J. Phys. 3, 659 (2026), https://doi.org/10.26565/2312-4334-2026-3-62

quantify the principal morphological distinctions between the protein assemblies and to establish a coherent framework for interpreting their projected density, structural organization, connectivity, orientation, and characteristic dimensions. By integrating complementary image-derived parameters, the analysis provides a more objective description of fibril morphology than qualitative inspection alone and highlights the distinct modes of supramolecular organization adopted by the three protein systems.

METHODS

Amyloid fibrils of human insulin, chicken hen egg white lysozyme and bovine serum albumin were prepared by dissolving 10 mg of corresponding protein in 10 ml of glycine buffer, pH 2.0, followed by incubation at 60 °C for 14 days [9]. Fibril formation was confirmed by transmission electron microscopy. For sample preparation, a 10 μL aliquot of each fibril suspension was applied to a carbon-coated TEM grid and allowed to adsorb for 1 min, after which excess liquid was removed by blotting. The grids were subsequently negatively stained with 10 μL of 1.5% (w/v) phosphotungstic acid for 30 s, blotted, rinsed three times with deionized water, and air-dried. Electron micrographs were acquired using an EM-125 transmission electron microscope (Selmi, Ukraine). Representative micrographs were selected for comparative morphometric analysis in Fiji [10]. Each image was cropped to exclude scale bars, labels, montage borders, and other non-biological elements. The analyzed images had identical dimensions of 1382×876 pixels and were calibrated using a spatial resolution of 0.8 nm per pixel. Accordingly, each field represented an area of approximately 0.775 μm^2, allowing direct comparison of area-normalized descriptors among the three protein systems. Quantitative image analysis was performed using a standardized digital morphometry workflow designed to characterize the projected organization of fibrillar assemblies at the field level. The same preprocessing and segmentation procedure was applied to all images to minimize operator-dependent variability. The analyzed parameters and their description are given in Table 1.

Table 1. Quantitative descriptors used for comparative TEM morphometry

Parameter	Operational definition	Morphological significance
Projected fibril/aggregate area fraction, %	Percentage of pixels within the analyzed field assigned to fibrillar or aggregate material	Describes the proportion of the projected TEM field occupied by protein assemblies
Projected skeleton length density, μm^{-1}	Total length of the skeletonized fibrillar network normalized to the analyzed field area	Reflects the amount of projected fibrillar backbone per unit area
Apparent junction/crossover density, μm^{-2}	Number of skeleton junctions normalized to the analyzed field area	Describes the apparent connectivity or frequency of projected fibril intersections
Endpoint density, μm^{-2}	Number of skeleton endpoints normalized to the analyzed field area	Provides an indicator of fragmentation and object discontinuity
Orientation anisotropy index	Axial concentration of fibril orientations on a scale from 0 to 1	Values close to 0 indicate an isotropic or randomly oriented field, whereas values approaching 1 indicate strong preferential alignment
Orientation dispersion, °	Angular spread of the fibril-orientation distribution	Indicates a distribution of orientations
Mask-derived local width, nm	Local thickness of the segmented structure estimated from the binary mask around the skeleton centerline	Provides a comparative measure of apparent projected thickness
Connected-object density, μm^{-2}	Number of spatially separated threshold-positive objects normalized to the field area	Reflects the abundance of individually segmented structures
Feret length, nm	Maximum caliper distance across a connected segmented object	Represents the maximum projected dimension of an object and provides an approximate measure of fragment or rod length.
Aspect ratio	Ratio of the major projected object dimension to its minor dimension	Describes the fibril elongation

RESULTS AND DISCUSSION

As seen in Fig. 1, all three proteins are characterized by distinct modes of supramolecular organization despite the common cross-β character of amyloid fibrils. Specifically, BSAF formed an open population of long, curved fibrils separated by large fibril-poor regions. InsF, in turn, produced a markedly denser field dominated by numerous short rod-like elements, whereas LzF formed fewer, more extended fibrillar objects with occasional crossings and local bundling. These morphologies reflect different physical states of fibrillar matter rather than simple differences in fibril abundance. Amyloid polymorphism extends from the molecular packing of protofilaments to their mesoscale length, curvature, lateral association, and spatial organization, all of which are shaped by the balance among nucleation, elongation, fragmentation, and fibril-fibril interactions [11,12].

The conservative segmentation and skeletonization outputs are shown in Fig. 2. These images were used primarily to confirm that the quantified signal followed the visible fibrillar contours rather than broad staining gradients. The

numerical values therefore represent projected descriptors of the selected TEM fields, not bulk fibril concentration or three-dimensional network structure.

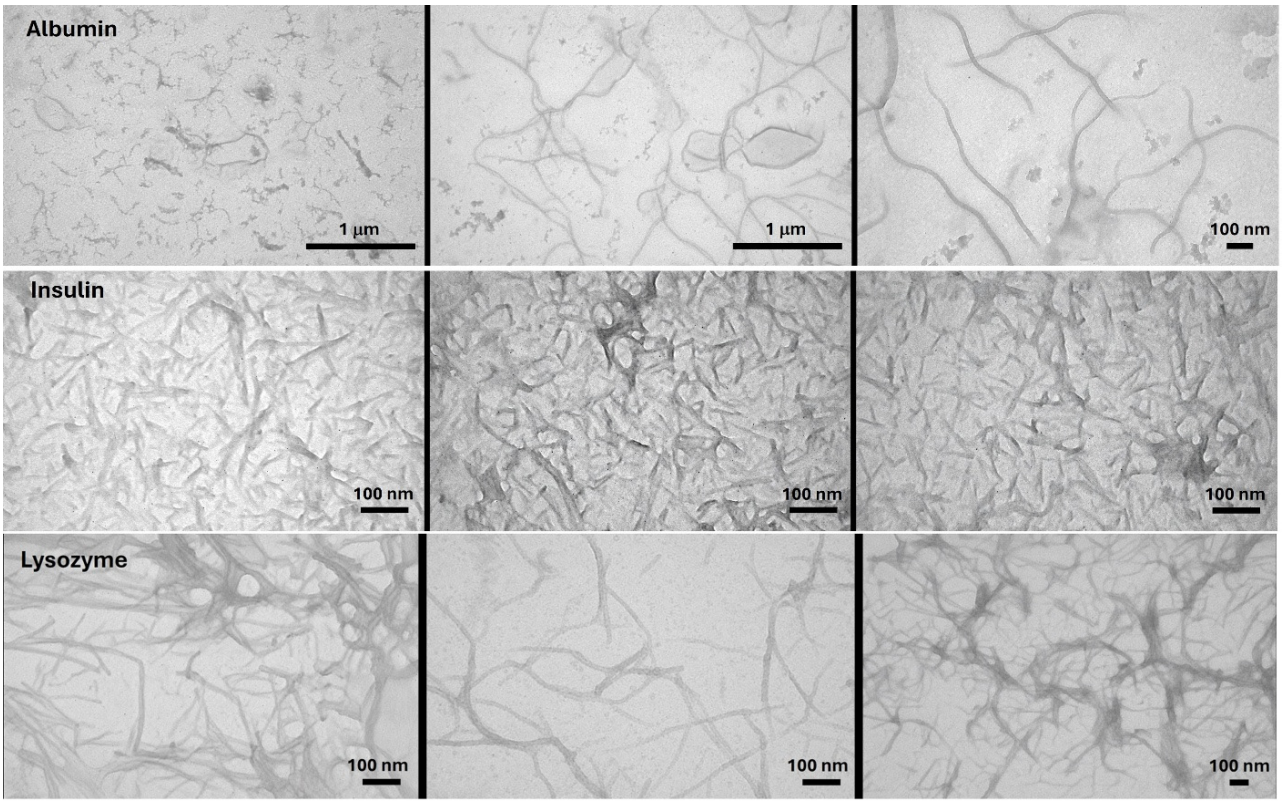

Figure 1. TEM images of albumin, insulin and lysozyme amyloid fibrils

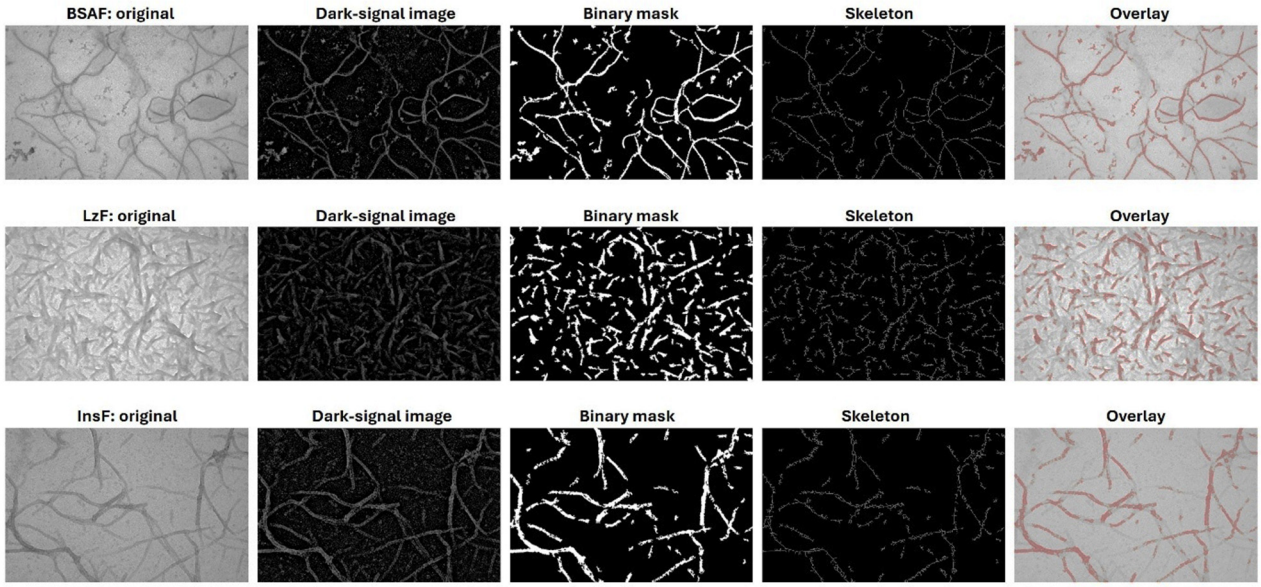

Figure 2. Quality-control representation of the image-analysis workflow. Original TEM images, extracted fibril-associated signal, binary masks, skeletons, and overlays are shown for each protein. The analysis retained the principal fibrillar structures while limiting inclusion of the heterogeneous TEM background

The quantitative parameters derived from image analysis are summarized in Table 2. Evaluation of these parameters revealed that InsF represents the most crowded and fragmentation-rich system. It showed the highest projected area fraction (14.58%), skeleton length density (30.98 μm^{-1}), connected-object density (232.32 μm^{-2}), endpoint density (2358.01 μm^{-2}), and apparent junction/crossover density (1600.40 μm^{-2}). Relatively high values of these quantities indicate that the dense insulin network is generated predominantly by a large number of short fibrillar units rather than by a few massive aggregates.

From mechanical perspective, the observed pattern of InsF is compatible with an assembly regime in which longitudinal growth is counterbalanced by breakage, repeated nucleation, or limited fibril maturation. Though TEM cannot distinguish among these pathways, it clearly demonstrates, however, a high-end-density population. Such a state can be biologically relevant because fibril ends and newly generated surfaces influence seeding, monomer recruitment, membrane contact, and cellular handling. Shortening of amyloid fibrils has been associated with enhanced particle number and altered cytotoxicity in other systems [13], although toxicity cannot be inferred from morphology alone.

Table 2. Quantitative morphometric parameters of amyloid fibrils obtained from TEM images

Metric	BSAF	InsF	LzF
Projected fibril/aggregate area fraction, %	10.41	14.58	9.85
Skeleton length density, μm^{-1}	21.09	30.98	19.34
Apparent junction/crossover density, μm^{-2}	929.27	1600.40	984.76
Endpoint density, μm^{-2}	1201.59	2358.01	1259.67
Connected-object density, μm^{-2}	101.96	232.32	80.02
Orientation anisotropy index	0.0027	0.0653	0.0634
Mean mask-derived local width, nm	5.77	5.06	5.77
Mean Feret length, nm	43.54	44.32	48.84
Mean aspect ratio	2.36	2.66	3.15

The same architecture may also be advantageous in engineered amyloid materials. A large number of short fibrillar objects provide abundant accessible surface and terminal sites for molecular adsorption or functionalization. Conversely, the limited contour length of individual rods may reduce their capacity to bridge large distances unless the particle concentration is sufficiently high to produce frequent contacts. The elevated junction density observed for InsF suggests that this requirement is met within the deposited layer, making the system potentially suitable for dense composite phases or highly populated interfacial coatings rather than sparse load-bearing networks.

In turn, LzF displayed the opposite tendency. Its projected coverage and object density were lower, yet the median Feret length (48.84 nm) and aspect ratio (3.15) were the highest among the three proteins under study. This combination indicates an elongation-dominated organization in which fewer fibrils extend over larger distances. Lysozyme is known to form extended amyloid fibrils under acidic conditions and to propagate through seeded growth, while protofibril association may also contribute to fibril development [14]. In physical terms, increased aspect ratio improves the ability of a fibril to connect spatially separated regions and lowers the concentration required for entanglement or network spanning. Accordingly, the lysozyme morphology is more compatible with reinforcement, bridging, and scaffold formation than the highly fragmented insulin architecture, although direct rheological or mechanical measurements would be required to test this prediction.

Fig. 3 illustrates the orientation plots which describe how frequently fibrillar segments are aligned at each angle within the image plane. A narrow histogram with a pronounced peak would indicate that a large fraction of fibrils shares a common preferred direction, whereas a broad or nearly uniform distribution reflects a predominantly isotropic arrangement with no dominant macroscopic alignment. The anisotropy index provides a complementary scalar measure of the same behavior: values approaching 0 correspond to random orientation, while values approaching 1 indicate strong directional ordering. As seen from this figure, all proteins exhibited broad orientation distributions. Furthermore, BSAF showed anisotropy index close to zero, whereas insulin and lysozyme displayed only slightly higher values, both below 0.07. These results indicate that none of the fibrillar populations formed a globally aligned architecture within the analyzed fields. Instead, the fibrils were distributed over many directions, consistent with isotropic deposition and local network formation. Although individual fibrils or bundles may exhibit locally coherent orientation, such local alignment does not translate into long-range orientational order at the scale of the full TEM field. In the present context, it should be noted that macroscopic alignment of amyloid fibrils emerges only when orientational interactions between elongated objects are sufficiently strong, typically at high effective concentration and aspect ratio or under external fields, flow, confinement, or surface-mediated ordering. In the absence of these conditions, fibrils may remain globally isotropic even when individual filaments are rigid and highly elongated. The broad histograms observed here, therefore suggest that the dominant differences among the three systems arise primarily from fibril abundance, fragmentation, elongation, and connectivity rather than from nematic-like ordering. This orientational isotropy also has functional implications. Accordingly, isotropic fibrillar networks are expected to exhibit more direction-independent mechanical and transport properties, whereas highly aligned assemblies may display anisotropic stiffness, diffusion, and molecular accessibility. Thus, the weak global orientation observed in all three samples indicates that their projected architectures are unlikely to impose a strong directional bias on interactions with solvent, biomolecules, or nanoscale cargo. Nevertheless, the distinct differences in fibril density and network connectivity among the samples may still lead to substantial variation in gelation behavior, surface accessibility, and mechanical reinforcement.

CONCLUSIONS

In summary, quantitative analysis of electron microscopy images demonstrated that albumin, insulin, and lysozyme fibrils adopt distinct modes of supramolecular organization despite sharing a common amyloid-like structural framework.

The main findings are as follows: i) insulin exhibited the highest projected area fraction, skeleton length density, object density, endpoint density, and apparent junction/crossover density, indicating a compact and highly fragmented architecture dominated by numerous short rod-like elements; ii) lysozyme showed the highest median Feret length and aspect ratio, consistent with the formation of more elongated fibrillar objects and a stronger contribution of longitudinal growth; iii) albumin displayed an intermediate morphology characterized by relatively sparse, curvilinear fibrils and lower densities of discrete objects and endpoints; and iv) all three systems were globally weakly oriented, as reflected by broad angular distributions and low anisotropy indices, indicating predominantly isotropic rather than nematically ordered assemblies. From the perspective of amyloid physics, these results suggest that insulin occupies a fragmentation-dominated regime with a high density of fibril ends and potential interaction sites, whereas lysozyme is characterized by more extended anisometric objects that may favor the formation of continuous fibrillar pathways. Albumin represents an intermediate organizational state between these two regimes. Such differences are expected to influence surface accessibility, intermolecular association, network connectivity, diffusion within fibrillar matrices, and the mechanical behavior of amyloid-based materials. The combined use of projected area fraction, skeleton length density, endpoint density, apparent connectivity, local width, Feret length, aspect ratio, and orientation analysis provides a coherent framework for comparative fibril morphometry. These descriptors may support the rational selection of protein fibrils for hydrogels, biosensing, biomolecular immobilization, drug delivery, and nanocomposite development.

Acknowledgements

This work was supported by the Ministry of Education and Science of Ukraine (the project "Design of novel biocompatible nanocomposites and improvement of ultrasound-based diagnostic methods for medical applications" No. 0126U001036).

ORCID

Valeriya Trusova, https://orcid.org/0000-0002-7087-071X; **Uliana Malovytsia,** https://orcid.org/0000-0002-7677-0779
Olga Zhytniakivska, https://orcid.org/0000-0002-2068-5823; **Sergiy Bogatyrenko,** https://orcid.org/0000-0002-6044-6886;
Galyna Gorbenko, https://orcid.org/0000-0002-0954-5053

REFERENCES

[1] A. Taylor, and S. Radford, Curr. Opin. Struct. Biol. **98**, 103245 (2026). https://doi.org/10.1016/j.sbi.2026.103245
[2] A. Buell, Chem. Sci. **13**, 10177 (2022). https://doi.org/10.1039/d1sc06782f
[3] D. Li, and C. Liu, Structure **31**, 1335-1347 (2023). https://doi.org/10.1016/j.str.2023.08.006
[4] R. van der Kant, N. Louros, J. Schymkowitz, and F. Rousseau, Structure **30**, 1178 (2022). https://doi.org/10.1016/j.str.2022.05.002
[5] S. Basha, D. Mukunda, A. Pai, and K. Mahato, Int. J. Biol. Macromol. **311**, 143725 (2025). https://doi.org/10.1016/j.ijbiomac.2025.143725
[6] S. Gras, L. Waddington, and K. Goldie, Methods Mol. Biol. **752**, 197 (2011). https://doi.org/10.1007/978-1-60327-223-0_13
[7] R. Polon, C. Heard, O. Gonzales-Viera, M. Macías-Rioseco, A. Mete, K. Watson, L. Woods, and A. Armién, J. Vet. Diagn. Invest. **37**, 429-438 (2025). https://doi.org/10.1177/10406387251321415
[8] Y. Baek, and M. Lee, Biochem. Soc. Trans. **52**, 1631 (2024). https://doi.org/10.1042/BST20230854
[9] L. Morozova-Roche, J. Zurdo, A. Spencer, W. Noppe, V. Receveur, D. Archer, M. Joniau, and C. Dobson, J. Struct. Biol. **130**, 339 (2000). https://doi.org/10.1006/jsbi.2000.4264
[10] J. Schindelin, I. Arganda-Carreras, E. Frise, V. Kaynig, M. Longair, T. Pietzsch, S. Preibisch, *et al*, Nat. Methods, **9**, 676 (2012). https://doi.org/10.1038/nmeth.2019
[11] J. Adamcik, and R. Mezzenga, Angew. Chem. Int. Ed. Engl. **57**, 8370 (2018). https://doi.org/10.1002/anie.201713416
[12] T. Knowles, and R. Mezzenga, Adv. Mater. **28**, 6546 (2016). https://doi.org/10.1002/adma.201505961
[13] W. Xue, and S. Radford, Biophys. J. **105**, 2811 (2013). https://doi.org/10.1016/j.bpj.2013.10.034
[14] S. Hill, J. Robinson, G. Matthews, and M. Muschol, Biophys. J. **96**, 3781 (2009). https://doi.org/10.1016/j.bpj.2009.01.044

КІЛЬКІСНИЙ АНАЛІЗ МОРФОЛОГІЇ АМІЛОЇДНИХ ФІБРИЛ МЕТОДОМ ТРАНСМІСІЙНОЇ ЕЛЕКТРОННОЇ МІКРОСКОПІЇ

Валерія Трусова[1], Уляна Маловиця[1], Ольга Житняківська[1], Катерина Чкуаселі[1], Сергій Богатиренко[2], Галина Горбенко[1]

[1]Кафедра медичної фізики та біомедичних нанотехнологій, Харківський національний університет імені В.Н. Каразіна, м. Свободи 4, Харків, 61022, Україна

[2]Кафедра матеріалів реакторобудування та фізичних технологій, Харківський національний університет імені В.Н. Каразіна, м. Свободи 4, Харків, 61022, Україна

Амілоїдні фібрили дедалі частіше розглядають як універсальні білкові наноматеріали, функціональні властивості яких визначаються не лише молекулярною крос-β-архітектурою, а й особливостями їхньої надмолекулярної морфології. Метою цієї роботи було порівняння мезомасштабної організації фібрилярних агрегатів альбуміну, інсуліну та лізоциму із застосуванням кількісної трансмісійної електронної мікроскопії (ТЕМ). Репрезентативні ТЕМ-зображення було проаналізовано за допомогою стандартизованого алгоритму цифрової обробки, що включав сегментацію, скелетизацію, аналіз орієнтації та морфометрію зв'язних компонентів. Визначено проєкційну частку площі, зайняту фібрилами й агрегатами, щільність довжини скелетизованих структур, уявну щільність вузлів/перетинів і кінцевих точок, локальну ширину, щільність об'єктів, довжину Фере, співвідношення сторін та анізотропію орієнтації. Для інсуліну було встановлено найвищі значення проєкційної частки площі, щільності довжини скелетизованих структур, щільності об'єктів, кінцевих точок і уявних вузлів/перетинів, що свідчить про формування компактної, високофрагментованої архітектури з переважанням

численних коротких паличкоподібних елементів. Натомість, фібрили лізоциму характеризувалися найбільшими медіанними значеннями довжини Фере та співвідношення сторін, що узгоджується з більш вираженим поздовжнім ростом і формуванням анізометричних структур. Для альбуміну було виявлено проміжний тип морфології, який характеризується порівняно розрідженими криволінійними фібрилами та нижчою щільністю дискретних об'єктів і кінцевих точок. Для всіх трьох систем спостерігалися широкі розподіли орієнтацій і низькі індекси анізотропії, що вказує на переважно ізотропну, а не глобально впорядковану організацію. Отримані результати свідчать, що досліджені білкові системи реалізують різні режими амілоїдної самоорганізації, від архітектур із домінуванням фрагментації до більш протяжних фібрилярних мереж. Запропонований кількісний підхід створює основу для встановлення взаємозв'язку між морфологією амілоїдів, доступністю поверхні, зв'язністю, механічними властивостями та проєктуванням фібрилярних гідрогелів, біосенсорів, систем доставки лікарських засобів і нанокомпозитів.

Ключові слова: *амілоїдні фібрили; трансмісійна електронна мікроскопія; кількісний аналіз зображень; морфологія фібрил; надмолекулярна організація; скелетизація; анізотропія орієнтації; білкові наноматеріали*

EAST EUROPEAN JOURNAL OF PHYSICS. 3. 665-680 (2026)
DOI: 10.26565/2312-4334-2026-3-63 ISSN 2312-4334

DFT INSIGHTS INTO STRUCTURAL, OPTOELECTRONIC AND THERMODYNAMIC CHARACTERISTICS OF CHALCOPYRITE $AgAl(S_{1-x}Se_x)_2$

Nabil Beloufa[1,2], Mohammed Ouled Ali[2,3], Hamza Rekab-Djabri[2,4], D. Belfennache[5], R. Yekhlef[5], Hamad M. Adress Hasan[6], Hanan F. Emrayed[6], Haneebal Saeid Khatab[7], Ghada M. Salem[8]

[1]*Hydrometeorological Institute for Training and Research IHFR, IbnouRochd.Bp 7019, Oran Algeria*
[2]*Laboratory of Micro and Nanophysics (LaMiN), National Polytechnic School Oran, ENPO-MA, BP 1523, El M'Naouer, 31000, Oran, Algeria*
[3]*Faculty of Matter Sciences, Mathematics and Computer Sciences, University of Ahmed Draia, Adrar, Algeria*
[4]*Faculty of Nature and Life Sciences and Earth Sciences, AkliMohand-Oulhadj University, 10000, Bouira, Algeria*
[5]*Research Center in Industrial Technologies CRTI, P.O. Box 64, Cheraga, 16014 Algiers, Algeria*
[6]*Chemistry Department, Faculty of Science, Omar Al-Mukhtar University, Libya*
[7]*Chemistry Department, Faculty of Education, Al-Marj, University of Benghazi, Libya*
[8]*Libyan Authority for Scientific Research, Tripoli, Libya*
**Correspondence Author e-mail: belfennachedjamel@gmail.com*
Received June 19, 2026; revised August 8, 2026; accepted August 12, 2026

In this study, we have investigated the structural, optoelectronic, and thermodynamic properties of the quaternary compound $AgAl(S_xSe_{1-x})_2$. This research employed the FP-LAPW method implemented in the Wien2k program and integrated into the density functional theory (DFT) framework. The generalized gradient approximation (WC-GGA) is used to handle the exchange and correlation potential. We have studied the impact of composition on the formation strength, apparent elastic modulus, and volume of the crystal lattice. According to the data collected, no deviation is noted in the compressibility modulus compared to the LCD law, nor in the lattice constant compared to Vegard's law. The approach of Zunger and his collaborators was used to determine the microscopic source of spatial curvature. Compared to previous theoretical research, the band gap values derived from band structure calculations based on the modified Becke-Johnson (mBJ) potential approximation show notable improvements and align much better with experimental results for ternary compounds. The optical properties indicate that the static dielectric constant $\varepsilon_1(0)$ increases with an increase in concentration x, while the optical gap energy decreases simultaneously; meanwhile, the dielectric function exhibits significant anisotropy in the zz direction. The study of the effects of thermal energy on certain macroscopic characteristics was carried out using Debye's quasi-harmonic model. Nevertheless, the alloys examined showed stability at intermediate temperatures ranging from 0 to 800 K.
Keywords: *$AgAl(S_xSe_{1-x})_2$; FP-LAPW; WC-GGA; mBJ; Vegard law; Debye's quasi-harmonic*

1. INTRODUCTION

Ternary semiconductor materials, valued for their distinct structures and physical properties, are attracting increased interest within the scientific research community because of their well-localized band gap, which makes them suitable for a variety of electronic applications [1-3]. These crystalline compounds belonging to the ternary systems I-III–VI_2 and I–IV–VI_2 are particularly significant [4,5]. Under standard thermodynamic conditions, these materials have a crystal structure similar to that of chalcopyrite. [6]. The initial study of chalcopyrite compounds was conducted because of their low conductivity [7]. They offer a multitude of applications [8], including in photovoltaic detectors, optical modulators, optical filters [9], and light-emitting diodes (LEDs) [10]. In addition, these materials can be deliberately doped with various impurities, including magnetic elements, which promotes the emergence of new categories of materials such as dispersed magnetic semiconductors (DMS) [11]. These doped chalcopyrite compounds have considerable potential for emerging technologies in the fields of spintronics [12], optoelectronic devices [13], and advanced photovoltaic systems [14].

Among the advantages of chalcopyrite semiconductors are that they are manufactured in thin layers, either p-type or n-type [15], enabling low-cost production of a variety of homo junction and hetero junction components [16]. They are direct-band gap semiconductors, a factor that minimizes the diffusion length of minority charge carriers [17]. and have a band gap energy within the optimal range for converting solar energy into electrical energy at the Earth's surface (AM1.5) [18].

The first researchers to use density functional theory (DFT) to determine the electronic structures and optical characteristics of a variety of Cu-III-VI_2 chalcopyrite ternary materials were Jaffe and Zunger [19]. Several studies [20-23] have been conducted on the electronic and electro-optical characteristics of $AgAlX_2$ (X = S, Se, Te) at atmospheric

Cite as: N. Beloufa, M.O. Ali, H. Rekab-Djabri, D. Belfennache, R. Yekhlef, H.M.A. Hasan, H.F. Emrayed, H.S. Khatab, G.M. Salem, East Eur. J. Phys. 3, 665 (2026), https://doi.org/10.26565/2312-4334-2026-3-63

pressure, which crystallize according to the tetragonal structure of space group $I\bar{4}2d$ and exhibit a direct band gap. In-depth study of these chalcopyrite semiconductors under high pressure has generated considerable scientific interest due to their phase change behavior and unique electronic characteristics. The ternary chalcopyrites $AgAlS_2$ and $AgAlSe_2$ Crystallize in a tetragonal structure of space group I-42d (No. 122), which is typical of chalcopyrite-type semiconductors. The lattice parameters reported for $AgAlS_2$ are a = 5.48 Å and c = 10.93 Å, while those for $AgAlSe_2$ are slightly larger due to the substitution of sulfur by selenium, with a = 5.71 Å and c = 11.37 Å [24, 25]. These materials have a derived structure of the sphalerite type, in which Ag^+ and Al^{3+}cations occupy distinct tetrahedral sites [19]. At 300°C and a pressure of 25 kbar (≈2.5 GPa), the $AgAlS_2$ chalcopyrite phase transitions to a high-pressure phase known as $AgAlS_2$–II, with trigonal P3ml symmetry and crystal parameters a = 3.50 Å, c = 6.84 Å, and Z = 1 [26]. In their very first research, Honeyman and Wilkinson [27] utilized iodine vapor transport to expand single crystals of $CuGaS_2$, $CuAlTe_2$, $AgGaS_2$, $AgAlS_2$, and $AgAlSe_2$ in order to measure the band gap and refractive index of the systems. Previous research has mainly focused on the use of $AgInS_2$ for photo catalysis and luminescence emission in silver-based I-III-VI_2 compounds [28]. Previous experiments carried out with similar compounds such as $AgAlSe_2$ and $AgAlS_2$ have shown that chalcopyrite materials are capable of structural phase transitions [29]. Among the chalcopyrite materials studied in this work are the compounds $AgAl(S_xSe_{1-x})_2$ with x=0, 0.25, 0.5, and 1, which belong to the I-III-VI_2 groups.

The band gap is a critical parameter for electronic performance [30]. This is because an increase in sulfur content (x) causes the gap to widen, typically from around 1.9 eV for $AgAlSe_2$ to nearly 2.6 eV for $AgAlS_2$ [26]. In addition, these materials have good chemical stability and favorable electronic transport properties, making it possible to integrate them into thin-film solar cells or infrared sensors [31]. The partial substitution of Se by S also makes it possible to optimize the position of the Fermi level and adapt the density of electronic states around the gap, thereby influencing the mobility of charge carriers [32].From a thermodynamic perspective, studies on similar materials such as $AgGaS_2$ show anisotropic behavior in terms of thermal expansion and thermal conductivity; for example, $AgGaS_2$ exhibits negative thermal expansion along the c-axis, with expansion coefficients varying depending on the crystallographic axes [33].Furthermore, investigations using modeling of vibrational and thermodynamic phenomena (via the quasi-harmonic approximation) reveal that thermal conductivity can be reduced under external pressure, while quantities such as Helmholtz free energy, entropy, and heat capacity (Cv) change significantly with temperature and pressure in $AgGaS_2$ systems [34].

The theoretical principles of the calculation are presented in Based on this principle, $AgAl(S_{1-x}Se_x)_2$ quaternary alloys can be studied in detail and comprehensively in order to optimize their properties according to chemical composition. It is important to note that this system has not yet been studied. This research aims to analyze the structural, electronic, optical, thermal, and thermodynamic properties of $AgAl(S_{1-x}Se_x)_2$ quaternary alloys. The first part also addresses the concept of the FP-LAPW method and the fundamentals of density functional theory (DFT). The second part presents the results obtained, their analysis, a discussion, and a comparison with various theoretical and experimental studies found in academic publications. Finally, the main conclusions are summarized in an overall summary.

2.COMPUTATIONAL DETAILS

We perform our calculations using the linearized augmented plane wave method and the local orbital technique (FP-LAPW+lo) [35]. This process provides a self-consistent solution to the Kohn-Sham equations, falling within the framework of density functional theory (DFT) [36, 37]. These techniques are applied in the WIEN2k code [38-40]. The generalized gradient approximation (GGA) function of Wu and Cohen (WC) [41] was used to treat the exchange and correlation potential. This method is also used to determine structural characteristics, with the aim of broadening and contrasting the various results obtained [42]. It should be noted that the GGA method tends to overestimate the lattice parameter while underestimating the band gap energies. The recent design of the Tran-Blaha technique based on the modified Becke-Johnson potential (TB-mBJ) parameterized by Koller et al. [43] represents an optimal and useful approach for determining the electronic characteristics of materials. The unit cell is divided into two zones: the first comprises non-overlapping spheres centered on each atom with a radius of Rmt, while the second represents the interstitial zone.

The wave functions, electron densities, and potentials are formulated as the product of spherical harmonics multiplied by radial functions around the atomic sites, i.e., in muffin-tin spheres with a cutoff radius L_{max} = 10. They are also represented by Fourier series in the interstitial zone with a cutoff radius $R_{mt}\times K_{max}$ = 6 (where RMT denotes the smallest radius of the MT sphere and K_{max} represents the amplitude of the largest wave vector used to expand the eigen functions of the plane wave). The separation between the core and valence electronic states is determined by an energy cutoff set at -6 Ry. In addition, we chose to set the Fourier expansion parameter G_{max}, which corresponds to the maximum reciprocal vector of the lattice responsible for accurately describing the charge density, to a value of 14. The iteration process is repeated until the total energy reaches stability at 10^{-5} Ry. The standard Monkhorst and Pack (MP) special point approach [44] was analyzed to obtain accurate Brillouin zone (BZ) integrations. For each group of 16 atoms, the k-mesh for the zinc-blende phase consisted of 7×7×4 K special points (12 K special points located in the irreducible corner of the Brillouin zone). To ensure correct convergence of the results, the choice was made on the k-meshes and basis sets.

3.RESULTS AND DISCUSSIONS

3.1. Structural properties

The structural stability of the quaternary alloy $AgAl(S_{1-x}Se_x)_2$ was investigated by optimizing the equilibrium lattice parameters (*a* and *c*) and the bulk modulus (*B*) for Se concentrations ranging from $x = 0$ to 1. A periodically repeated 16-atom ordered supercell was employed, where one, two, and three sulfur atoms were replaced by selenium for $x = 0.25$, 0.50, and 0.75, respectively (Fig. 1). This approach, widely used in first-principles studies of semiconductor alloys, efficiently captures the main effects of S/Se substitution on the structural, electronic, optical, and thermodynamic properties. Although real alloys exhibit substitutional disorder, the present calculations represent ordered configurations and should therefore be regarded as describing the general compositional trends. More advanced approaches, such as Special Quasirandom Structures (SQS) or the Coherent Potential Approximation (CPA), could provide a more realistic description of chemical disorder and are left for future work.

The equilibrium structure of each composition was determined by total-energy minimization through optimization of the internal parameter (*u*) and the *c/a* ratio. Here, u is the anion internal displacement parameter, which describes the deviation of the anion from its ideal tetrahedral position in the chalcopyrite structure and characterizes the distortion of the cation–anion tetrahedra. Since u directly affects the bond lengths and electronic structure, its optimization is essential for obtaining reliable structural and electronic properties.

For the parent compounds $AgAlS_2$ and $AgAlSe_2$, the optimized value of *u* was found to be in good agreement with the available experimental data and was therefore adopted in the subsequent calculations.

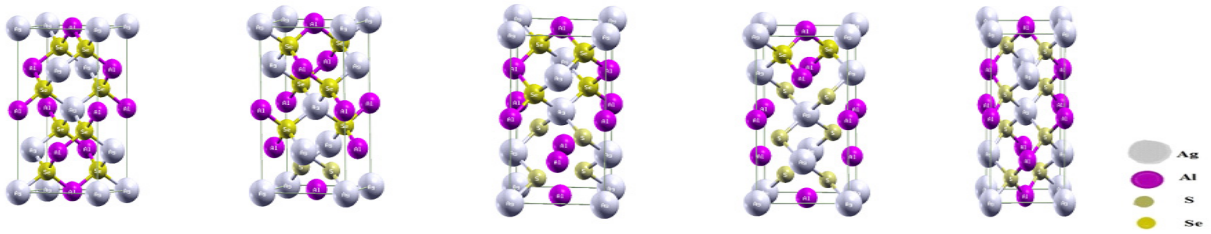

Figure 1. Cell structure of the five alloys $AgAl(S_{1-x}Se_x)_2$

The optimized structural parameters are summarized in Table 1. No theoretical or experimental data for the $AgAl(S_{1-x}Se_x)_2$ quaternary alloys are currently available in the literature, making the present results a valuable reference for future investigations. For the compounds $AgAlS_2$ and $AgAlSe_2$, the calculated lattice constants (a and c) and the corresponding c/a ratios are in excellent agreement with the available experimental data, with deviations of only 0.17% and 1.02% for $AgAlS_2$, and 1.56% and 0.50% (or 1.80% and 0.56%, depending on the experimental reference) for $AgAlSe_2$. These small discrepancies confirm the high accuracy of the present computational approach and validate the reliability of the predicted structural properties.

Table 1. The equilibrium constants, calculated as a, c, and the compressibility modulus B for $AgAl(S_{1-x}Se_x)_2$, are compared with existing experimental and theoretical data.

Compounds	Methods	*a*(Å)	*c*(Å)	*u*	*B*(GPa)	E_{tot}(eV)
$AgAlS_2$	Present work	5.60	10.49	0.29	79.22	-50857.60
	Experiment	5.72 [a] 5.69 [b] 5.13 [e]	10.13 [a] 10.26 [b] 10.30 [e]	0.29 [a] 0.30 [b] 0.30 [e]	78, 70 [c]	
	Other work	5.48 [f]	10.90 [f]	0.256 [f]	-	-
$AgAlS_{0.25}Se_{0.75}$	Present work	5.65	10.72	0.29	73.69	-58980.91
	Experiment	-	-	-	-	-
	Other work	-	-	-	-	-
$AgAlS_{0.5}Se_{0.5}$	Present work	5.83	10.45	0.29	70.59	-67104.03
	Experiment	-	-	-	-	-
	Other work	-	-	-	-	-
$AgAlS_{0.75}Se_{0.25}$	Present work	5.81	10.96	0.29	67.46	-67104.03
	Experiment	-	-	-	-	-
	Other work	-	-	-	-	-
$AgAlSe_2$	Present work	5.89	11.07	0.28	64.45	-83350.31
	Experiment	5.95 [a] 5.95 [b] 5.96 [d]	10.75 [a] 10.75 [b] 10.75 [d]	0.27 [a] 0.27 [b]	78, 70 [c]	
	Other work	5.78 [f]	11.52 [f]	0.263 [f]	-	-

Ref: [a][24], [b][45], [c][46], [d][29], [e][47], [f][28].

Figure 2 presents the variation of the crystal volume as a function of the Se concentration x for the quaternary alloy $AgAl(S_{1-x}Se_x)_2$. For comparison, the volume predicted by Vegard's law [48] is also included in figure. It can be

seen that the crystal volume deviates positively or negatively from linearity. For an $AgAl(S_{1-x}Se_x)_2$ alloy compound, the volume of the crystal lattice is formulated as follows:

$$V_{ABC_{1-x}D_x} = x.V_{ABC} + (1-x)\cdot V_{ABD}. \quad (1)$$

Where V_{ABC} and V_{ABD} denote the equilibrium crystal volumes of the ternary compounds ABC and ABD, respectively. For the $AgAl(S_{1-x}Se_x)_2$ alloys, the fitted bowing parameter is found to be only 0.01 (a.u.)^3, indicating a negligible deviation from the linear behavior predicted Vegard's law. We observe that the alloys analyzed comply with Vegard's law. This phenomenon can be explained by the slight modification of the lattice parameters of the parent ternary compounds constituting the alloy.

In the same figure the variation in compressibility coefficient in relation to concentration for $AgAl(S_{1-x}Se_x)_2$ systems. A comparison is made between the graphs obtained and those derived from the linear concentration dependence (LCD) law. A small divergence is noted in the change in the compressibility modulus in relation to concentration compared to the LCD, with a curvature index of 5.72 GPa. This small difference is mainly attributed to the slight disparity between the compressibility modulus values of the ternary compounds. It is observed that the compressibility modulus decreases as the atomic number of the substitution chalcogenide increases.

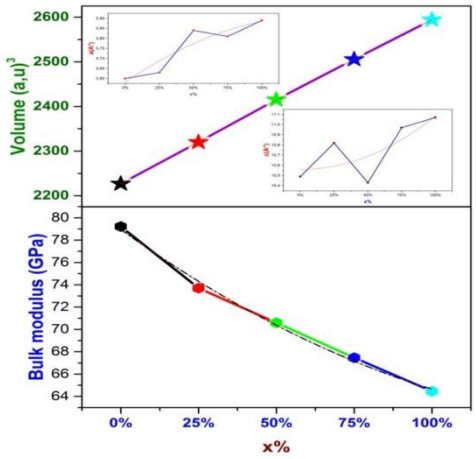

Figure 2. Variation in volume and compressibility modulus in relation to concentration, and comparison with Vegard's law for ideal ternary compounds. $AgAlS_2$ and $AgAlSe_2$

3.2. Electronic properties

The band gap is often considered a crucial criterion in the selection of a semiconductor element for optoelectronic applications, given its direct link to the wavelength at which the device operates. In this context, the dependence of the fundamental band gap on the alloy composition is of paramount importance. Thus, the electronic characteristics of $AgAl(S_{1-x}Se_x)_2$ quaternary alloys are examined, taking into account the lattice parameters that have been previously optimized.

The band structure was established along the high symmetry directions in the Brillouin zone. To refine the accuracy of the band gap values, in addition to the WC-GGA approximation, the mBJ approximation was also used. This method is known to provide band gap values that rival those measured experimentally. For the alloys analyzed, the valence band peak and the conduction band trough are located at the Γ point (see Figure 3). allows them to be classified as direct bandgap semiconductors. Table 2 presents the results for these alloys at concentrations of x = 0, 0.25, 0.50, 0.75, and 1. It also includes experimental and theoretical data for ternary compounds.

Table 2. The calculated band gaps of $AgAl(S_{1-x}Se_x)_2$

Compounds	Present work		Experimental	Other work
	WC-GGA	mBJ		
$AgAlS_2$	1.787	3.202	3.13[a], 3.186[b]	1.87[c], 2.69[c], 1.98[d]
$AgAlSe_{0.75}S_{0.25}$	1.616	2.935	-	-
$AgAlSe_{0.50}S_{0.50}$	1.424	2.766	-	-
$AgAlSe_{0.25}S_{0.75}$	1.214	2.589	-	-
$AgAlSe_2$	1.038	2.412	2.55[a]	0.98[c] 1.8[c], 1.59[e]

Ref: [a][49], [b][50], [c][51], [d][45] , [e][46]

This study only compares its results with existing experimental and theoretical data for ternary alloys, due to the lack of experimental information for the quaternary system. It should be noted that the band gap energy values determined using the WC-GGA method are lower than the expected experimental results. It is well known that DFT is a ground state-based technique and is not capable of reproducing excited states. However, the use of the mBJ approximation prevents us from accurately determining the band gap value. Figure 4 illustrates how the band gap of $AgAl(S_{1-x}Se_x)_2$ quaternary alloys varies as a function of concentration x.

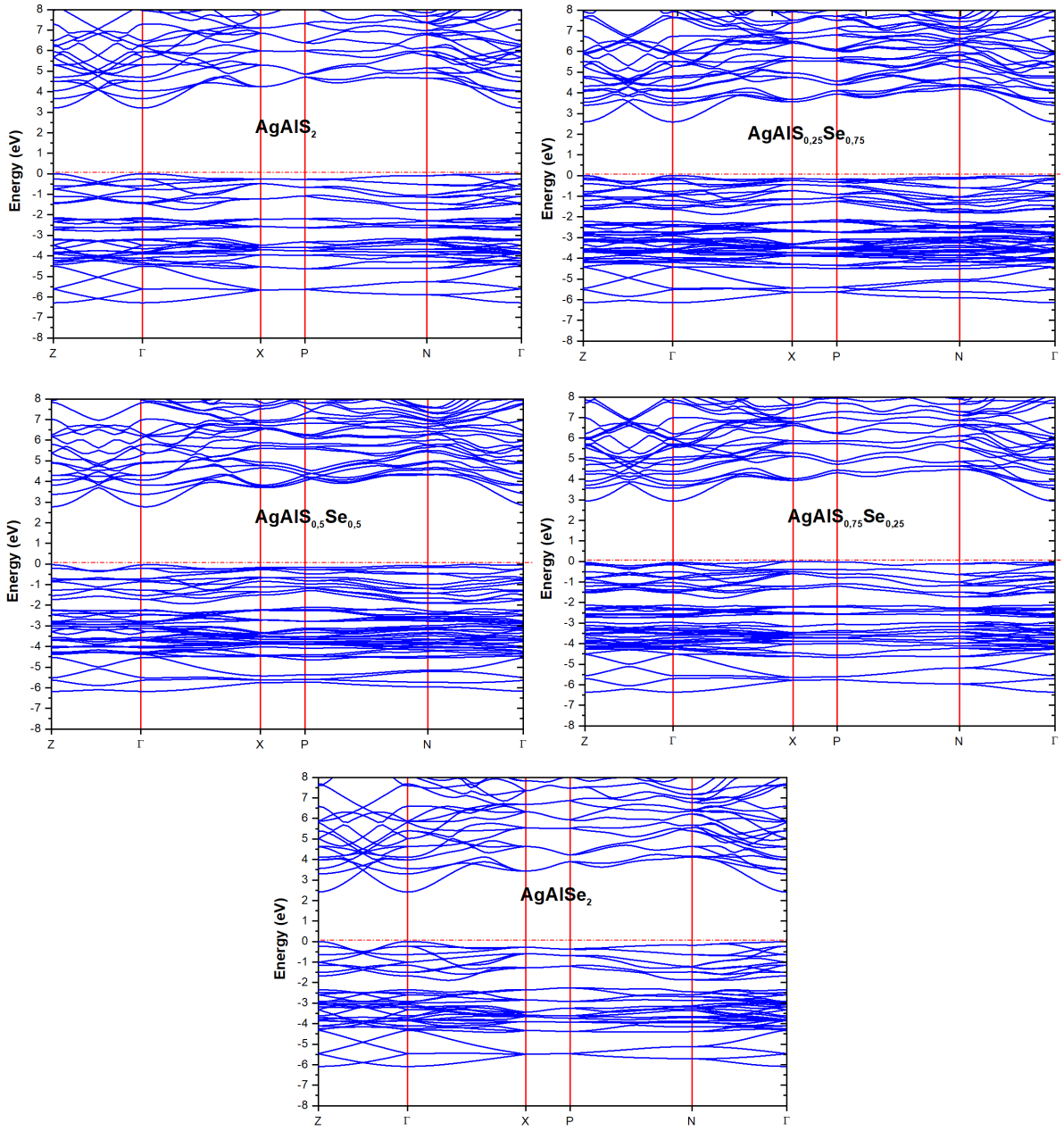

Figure 3. Band Structure of $AgAl(S_xSe_{1-x})_2$ alloys

The mBJ results indicate that the band gap energy decreases as a function of Se concentration, following a nonlinear trend. The curves represent a quadratic fit. It has been proven that the curvature parameter is mainly attributed to the difference between the lattice parameters and the ionic elements of the original ternary compounds [52, 53]. For a better understanding and explanation of the physical origins of the curvature parameter, the method developed by Bernard and Zunger [54] was adopted. This approach comprises three distinct elements that form the disorder parameter b: volume deformation (b_{VD}), charge transfer (b_{CE}), and structural relaxation (b_{SR}).

The calculations were restricted to a concentration of x = 0.5 due to the weak dependence of the curvature parameter on chemical composition. The first task is to determine the influence of volume deformation (V_D) on the disorder parameter. The comparative response of the band structures of the ternary compounds ABC and ABD to hydrostatic pressure is illustrated by their corresponding b_{VD} contribution. In this context, this response stems from the

adjustment of their specific structural configurations relative to those of the alloy V = V (x) (Vegard's law). The second contribution concerns charge transfer (CE), where the contribution b_{CE} summarizes the impact of charge transfer attributed to the behavior of atomic bonds on the value of the structural parameter a.The final step involves evaluating the variation caused by structural relaxation (S_R), from the unrelaxed alloy to the relaxed alloy by b_{SR}. Consequently, the total disorder parameter is obtained by combining these three elements.

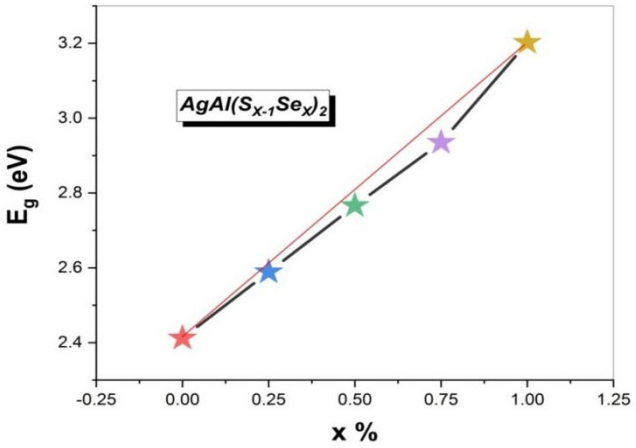

Figure 4. Variation of gap energy with concentration and comparison with Vegard's law

3.3. Optical properties

The complex dielectric function entirely determines the optical properties of materials, which are theoutcome of their interactions with electromagnetic waves and given by the following formula [55]

$$\varepsilon(\omega) = \varepsilon_1(\omega) + i\varepsilon_2(\omega). \tag{2}$$

Where $\varepsilon_1(\omega)$ and $\varepsilon_2(\omega)$ by using the Kramers–Kronig denote the real and imaginary parts of the dielectric function, respectively [55,56]

$$\varepsilon_1(\omega) = 1 + \frac{2}{\pi} P \int_0^{\infty} \frac{\omega' \varepsilon_2(\omega')}{\omega'^2 - \omega^2} d\omega'. \tag{3}$$

The following relations were used to calculate other optical quantities from $\varepsilon_1(\omega)$ and $\varepsilon_2(\omega)$, including the absorption coefficient $\alpha(\omega)$, the optical conductivity $\sigma(\omega)$, the refractive index $n(\omega)$, the extinction coefficient $K(\omega)$, the reflection coefficient R (ω), and the absorption coefficient $\alpha(\omega)$ were calculated from $\varepsilon_1(\omega)$ and $\varepsilon_2(\omega)$ and are given by the following relations [57]:

$$n(\omega) = \frac{1}{\sqrt{2}}[(\varepsilon_1{}^2(\omega) + \varepsilon_2{}^2(\omega))^{\frac{1}{2}} + \varepsilon_1(\omega)]^{1/2}, \tag{4}$$

$$K(\omega) = \frac{1}{\sqrt{2}}[(\varepsilon_1{}^2(\omega) + \varepsilon_2{}^2(\omega))^{\frac{1}{2}} - \varepsilon_1(\omega)]^{1/2}, \tag{5}$$

$$\text{Re}\,\sigma(\omega) = \frac{\omega}{4\pi}\text{Im}\,\varepsilon(\omega), \tag{6}$$

$$\alpha(\omega)\frac{4\pi}{\lambda}\text{k}(\omega), \tag{7}$$

$$\text{R}(\omega) = \frac{(\text{n}-1)^2+\text{K}^2}{(\text{n}+1)^2+\text{K}^2}. \tag{8}$$

The physical properties of $AgAl(S_{1-x}Se_x)_2$ alloys with a tetragonal crystal structure and space group D_{2d}^{12}-$I\bar{4}2d$ require two shaded tensor components in the subfigures $\varepsilon^{xx}(\omega)$ and $\varepsilon^{zz}(\omega)$ to perform the calculations [57].

Figures 5.a and 5.b illustrate the evolution of real and imaginary parts of the dielectric function as a function of photon energy in both crystal directions for each alloy. The static dielectric constant $\varepsilon_1(0)$ increases, independently of the alloy composition, in the order of magnitude between 4.31 and 4.85 for $\varepsilon_{xx}(0)$ and between 4.46 and 5.01 for $\varepsilon_{zz}(0)$ (see Table 3). Consequently, the anisotropy of $AgAlSe_2$is the most significant.

The $\varepsilon_1(0)$ component is different from the other constituent $\varepsilon_{1xx}(0)$ for the same compound, which indicates that the optical anisotropy in the zz direction is the most significant. The zero crossing of $\varepsilon_1(\omega)$= 0 corresponds to the maximum of the imaginary part $\varepsilon_2(\omega)$. This is to be expected, since when dispersion is minimal, the absorption is maximal.

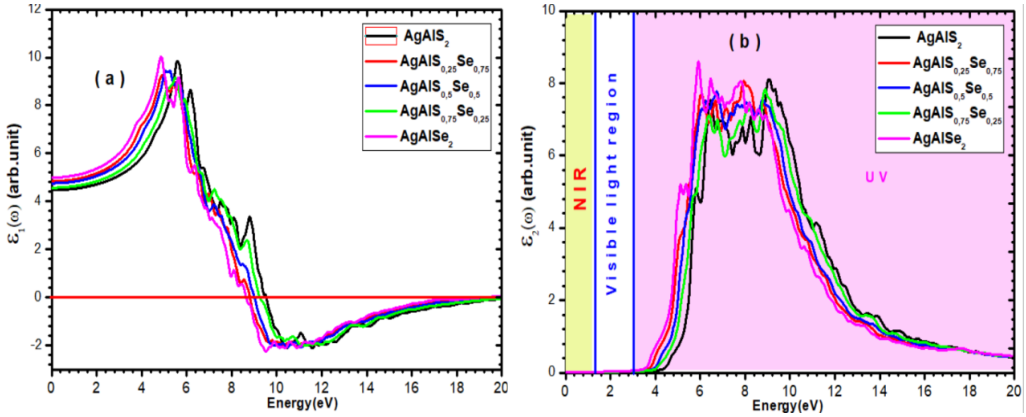

Figure 5. Real part(a) and imaginary part (b) of the dielectric function for $AgAl(S_xSe_{1-x})_2$ alloys

Table 3. Dielectric constant and refractive index (n) for $AgAl(S_{1-x}Se_x)_2$

	$\varepsilon_1^{//}(0)$	$\varepsilon_1^{\perp}(0)$	ε_{moy}	$n_1^{//}(0)$	$n_1^{\perp}(0)$	Δn
$AgAlS_2$	4.31	4.46	4.385	2.11	2.07	0.04
$AgAlSe_{0.75}S_{0.25}$	4.57	4.49	4.53	2.12	2.13	0.01
$AgAlSe_{0.50}S_{0.50}$	4.77	4.51	4.64	2.12	2.17	0.05
$AgAlSe_{0.25}S_{0.75}$	4.72	4.83	4.775	2.17	2.20	0.03
$AgAlSe_2$	4.85	5.02	4.935	2.19	2.23	0.06

Table 3 presents the static dielectric constants $\varepsilon_1(0)$, the average dielectric constant ε_{moy}, the static refractive indices n(0), and the birefringence Δn of $AgAl(S_{1-x}Se_x)_2$ alloys. The obtained results reveal a systematic evolution of the optical response with increasing Se concentration, reflecting the modification of the electronic polarization induced by the substitution of S with Se.

The static dielectric constant exhibits a gradual increase with increasing Se content in both crystallographic directions. Specifically, $\varepsilon_1//(0)$ increases from 4.31 for $AgAlS_2$ to 4.85 for $AgAlSe_2$, while $\varepsilon_1\perp(0)$ increases from 4.46 to 5.02. Consequently, the average dielectric constant rises continuously from 4.385 to 4.935, corresponding to an enhancement of approximately 12.5%. This behavior is mainly attributed to the higher electronic polarizability of Se atoms compared with S atoms, as well as to the progressive reduction of the electronic band gap. According to the Penn model, the static dielectric constant is inversely proportional to the square of the band gap; therefore, the decrease in E_g naturally leads to stronger dielectric screening and higher dielectric constants.

The static dielectric constant was estimated using the Penn model, which relates the dielectric response to the band gap and the plasma frequency [58]:

$$\varepsilon(0) = 1 + \left(\frac{\hbar\omega_p}{E_g}\right)^2. \quad (9)$$

Where $\hbar$ is the reduced Planck constant, E_g is the fundamental band gap, and ω_p is the plasma frequency, which characterizes the collective oscillation of the valence electrons in the material. The values of $\varepsilon_1(0)$ and $\varepsilon_{1zz}(0)$ are listed in Table 3.

Figure 6.a illustrates the absorption $\alpha(\omega)$ of $AgAl(S_{1-x}Se_x)_2$alloys. It is clear that the spectra of $AgAlSe_2$ have the highest intensity and the shortest width at half height $\Delta\omega$. The optical conductivity curves show the same results (Fig. 6.b), with the conductivity threshold beings lightly lower than the band gap value. These results can be explained by the fact that optical conductivity is due to inter band transitions on the one hand and intra band transitions on the other.

The variation of the refractive index $n(\omega)$ is illustrated in Figure 6c. It can be seen a variation of $n(\omega)$ between the three compounds follows the same trend as the spectrum of $\varepsilon_1(\omega)$. This is evident from the static refractive index n(0) values of 2.05, 2.12, and 2.23 for $AgAl(S_{1-x}Se_x)_2$, respectively. This value is located in the static limit and follows the relationship:

$$n(\omega) = \sqrt{\varepsilon(0)}. \quad (10)$$

The reflectivity spectra (Fig. 6.e) demonstrate a low reflected intensity in the strong absorption interval, and its decrease coincides with the minimum of the real part $\varepsilon_1(\omega)$. The spectra of the energy-loss function, shown in Figure 6.f, reflect the energy-loss of fast electrons as they pass through the material and the plasma resonance frequency ω_p [59] is also observed in the reflectivity spectrum.

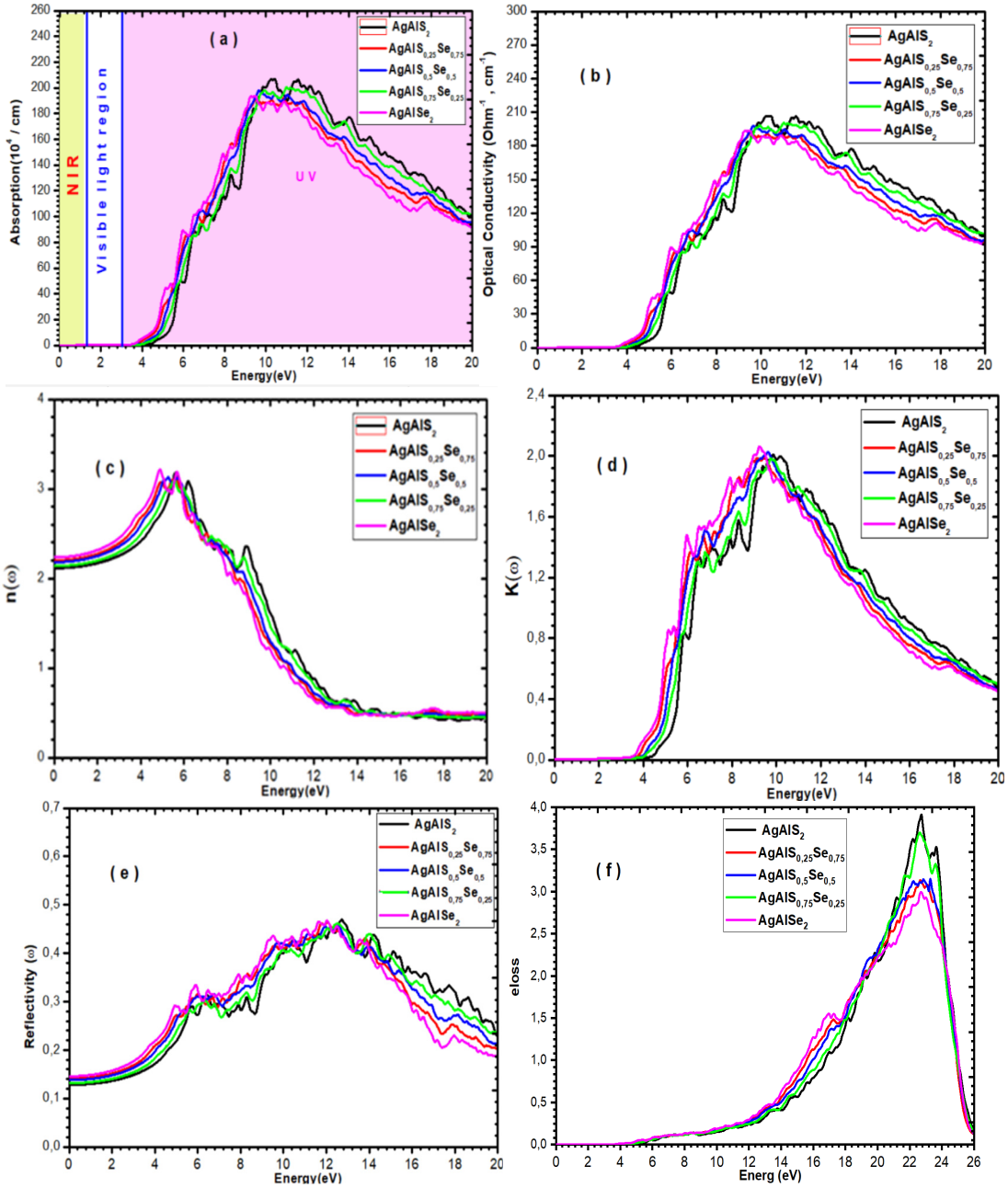

Figure 6. Calculated optical properties of $AgAl(S_xSe_{1-x})_2$ alloys:
(a) absorption coefficient (α), (b) optical conductivity (σ), (c) refractive index (n), (d) extinction coefficient (k), (e) reflectivity (R), and (f) energy-loss function (L), as functions of photon energy.

3.4. Thermodynamic properties

The thermodynamic properties of $AgAl(S_{1-x}Se_x)_2$ alloys were studied using the Debye quasi-harmonic model (QHDM) based on the FP-LAPW method. While density functional theory (DFT) provides an accurate description of the ground-state properties at 0 K, the quasi-harmonic Debye approximations can be used to extend these calculations at finite temperatures and pressures by incorporating the vibrational contribution to the free energy.

The properties at specific temperatures and pressures are obtained from the Gibbs energy of non-equilibrium systems as follows: [60]

$$G(V, P, T) = E(V) + PV + A_{vib}(V, T). \tag{11}$$

Where E(V) is the total energy, P is the external pressure, V is the crystal volume, and A_{vib} is the Helmholtz vibrational free energy calculated using the Debye approximation.

For each temperature and pressure, the equilibrium volume was obtained by minimizing the Gibbs free energy according to the condition: [61]

$$\left(\frac{\partial G}{\partial V}\right)_{P,T} = 0. \tag{12}$$

The variation in crystal volume as a function of temperature at different pressures for quaternary $AgAl(S_{1-x}Se_x)_2$ alloys is illustrated in Figure 7. It is clear that as the temperature increases, the volume also increases, but the rate of this increase is moderate as the pressure increases. However, for a given temperature, the volume decreases as the pressure increases. Furthermore, it is noted that the volume is almost constant in the temperature range 0-800 K with a setting in the range 0-20 GPa. The expansion of volume V ($bohr^3$) is almost negligible above this temperature.

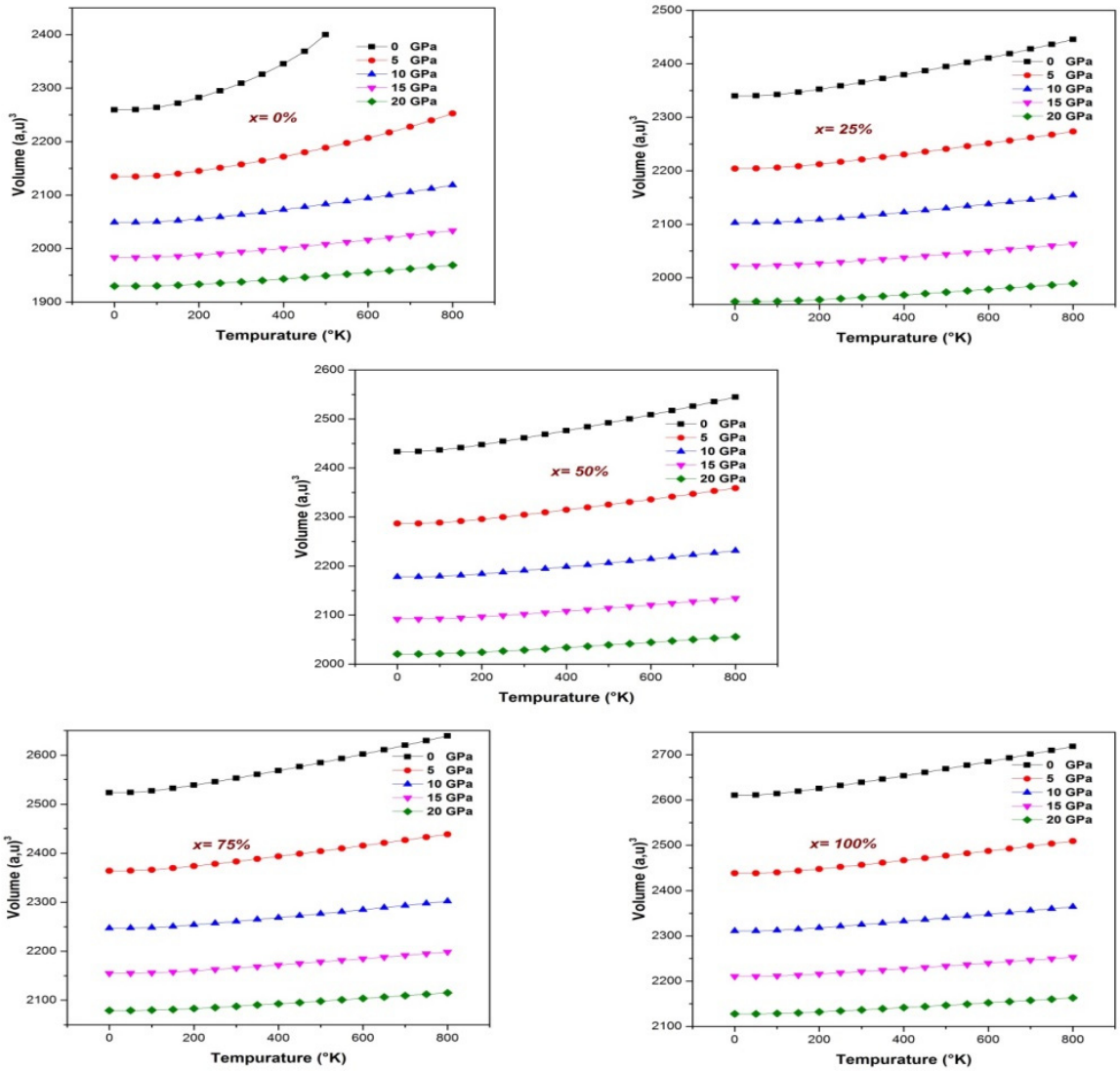

Figure 7. Volume as a function of temperature at various pressures

The same trend can be observed in the evolution of the compressibility modulus B of $AgAl(S_{1-x}Se_x)_2$alloys as a function of temperature and pressure variations; see Figure 8. It can be seen that at a given temperature, the compressibility modulus increases with pressure, but it decreases at a given pressure. However, the rate of increase in the compressibility modulus as a function of temperature is greater at low pressure, because at these pressures, the compressibility modulus is higher.

The Debye temperature θ_D is a crucial fundamental parameter in solids that is connected to physical characteristics, including specifiche at and melting temperature [62]:

$$\theta_D = \frac{\hbar}{k_B}\left(\frac{6\pi^2 n}{V}\right)^{1/3} f(\sigma)\sqrt{\frac{B_S}{M}}. \tag{13}$$

Where n is the number of atoms per formula unit, V is the molecular volume, B_S is the adiabatic bulk modulus, M is the molecular mass per formula unit, f(σ) is a function of Poisson's ratio σ, $\hbar$ is the reduced Planck constant, and k_B is the Boltzmann constant.

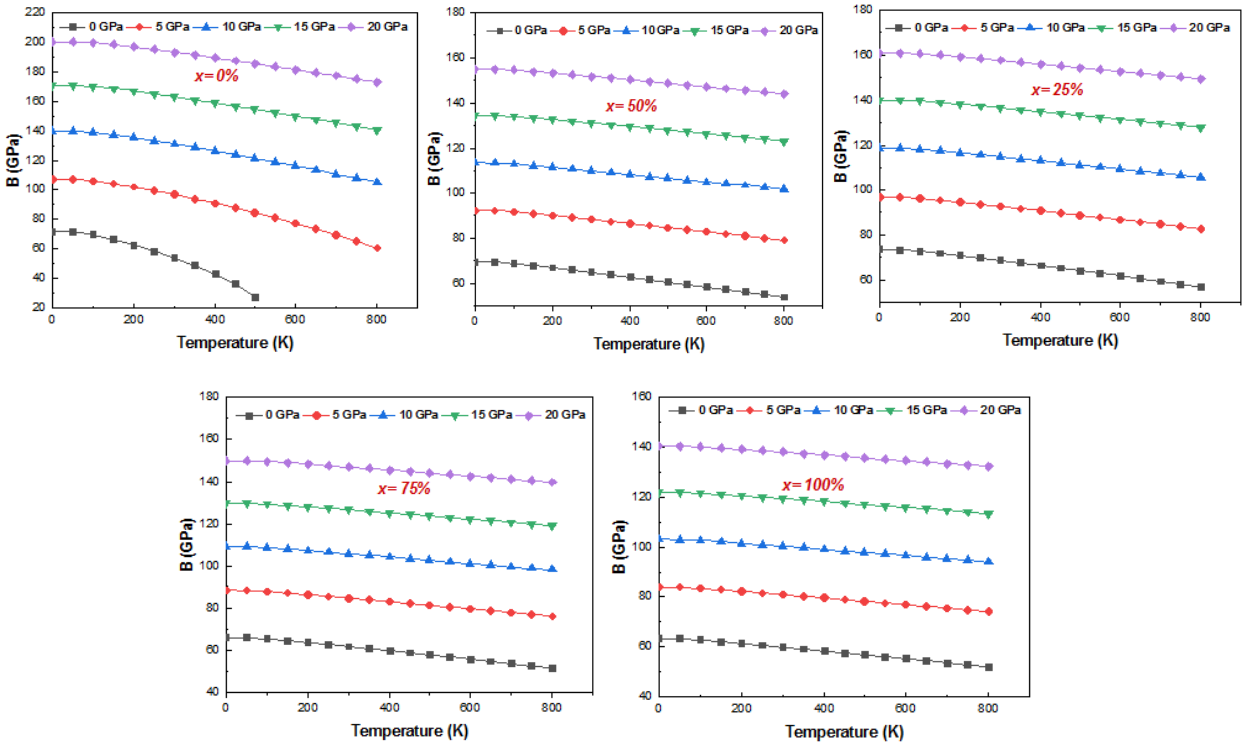

Figure 8. Bulk modulus as a function of temperature at various pressures.

B_S is the static adiabatic bulk modulus determined by the relation [63] and M is the molecular mass per unit cell:

$$B_S \cong B(V) = V\frac{d^2E(V)}{dV^2} \tag{14}$$

and $f(\sigma)$ is a function of the Poisson ratio σ expressed as [64]:

$$|f(\sigma)|^3 = 3\left[2\left(\frac{2}{3}\frac{1+\sigma}{1-2\sigma}\right) + \left(\frac{1}{3}\frac{1+\sigma}{1-\sigma}\right)\right]^{-1} \tag{15}$$

where σ is taken as 0.25 [65].

In the present work, a constant Poisson's ratio (σ = 0.25) was adopted for all alloy compositions within the quasi-harmonic Debye model. This approximation is commonly used in first-principles thermodynamic studies when the complete set of elastic constants is unavailable and provides a reasonable description of the average elastic behavior of semiconductor alloys. Although the Debye temperature depends on Poisson's ratio, moderate variations in σ have only a minor influence on the calculated thermodynamic properties compared with the effects of the equilibrium volume and bulk modulus [66]. Therefore, the use of a constant value of σ = 0.25 is expected to preserve the overall compositional trends and the main conclusions of this work.

The variation of the Debye temperature θ_D as a function of temperature at different pressures for the materials studied is illustrated in Figure 9. When the pressure is constant, the Debye temperature decreases almost linearly with increasing temperature, and at a given temperature, the Debye temperature increases with the applied pressure. This behavior has been observed in the evolution of the compressibility modulus when temperature and pressure vary. This is explained by the fact that a hard material has a high Debye temperature. Research on the heat capacity of crystals is well known in the field of condensed matter physics [67].

The heat capacity of a substance provides important information about its vibrational characteristics and is required in many applications. Figure 10 graphically illustrates how the heat capacityat constant volume C_V varies with temperature at different pressures for the $AgAl(S_{1-x}Se_x)_2$ alloys studied. Following the example of the Debye temperature parameter, there are two steps observed:

At high temperatures, the value of C_V tends towards the limit of Dulong-Petit, which all solids exhibit when heated at high temperatures. From Fig. 10, when the temperature increases, the value of C_V increases drastically at low temperatures, then the increase becomes slow at high temperatures until reaching the limit of Dulong-Petit as expected by theory. The C_V values obtainedat T = 300 K and P = 0 GPa are 371.56, 369.39, 373.72, 376.91, and 379.07 J/mol.K for $AgAlS_2$, $AgAlS_{0.25}Se_{0.75}$, $AgAlS_{0.5}Se_{0.5}$, $AgAlS_{0.75}Se_{0.25}$, and $AgAlSe_2$, respectively.

For the variation of the heat capacity at constant pressure C_p as a function of temperature at different pressures for the $AgAl(S_{1-x}Se_x)_2$systems, as shown in Fig. 11, it can be seen that at low temperature, C_p behaves similarly to C_V, i.e.,

an evolution in T^3. But at high temperatures, C_p behaves differently than C_V; rather than trending toward a constant value, it keeps rising. At 300K and atzero pressure, the obtained values for C_p are 427.63, 466.32, 489.81, 513.58, and 532.54 J/mol.K for $AgAlS_2$, $AgAlS_{0.25}Se_{0.75}$, $AgAlS_{0.5}Se_{0.5}$, $AgAlS_{0.75}Se_{0.25}$, and $AgAlSe_2$, respectively. It is noted that pressure does not have a significant effect on heat capacity. Where the heat capacity C_v and the Grüneisen parameter γ are calculated with the following relations [60]:

$$C_V = 3nk_B\left[4D\left(\frac{\theta_D}{T}\right) - \frac{3\theta_D/T}{e^{\theta_D/T}-1}\right], \tag{16}$$

$$\gamma = \frac{-dln\theta_D(V)}{dlnV}. \tag{17}$$

In the above expressions, D(x) denotes the Debye function, defined as:

$$D(x) = \frac{3}{x^3}\int_0^x \frac{t^3}{e^t-1}\,dt, \tag{18}$$

where $= \frac{\theta_D}{T}$, θ_D is the Debye temperature, and T is the absolute temperature. The Debye function accounts for the contribution of lattice vibrations to the thermodynamic properties within the quasi-harmonic Debye approximation.

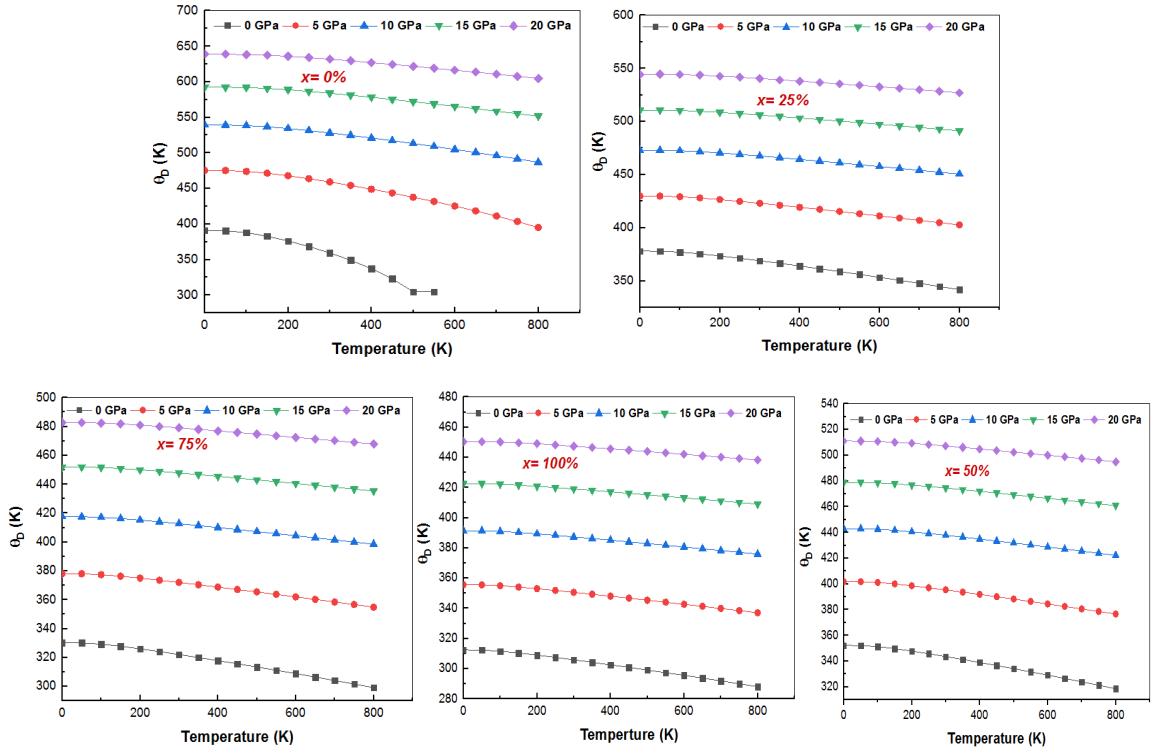

Figure 9. Debye temperature as a function of temperature at various pressures

The thermal expansion coefficient α indicates the dependence of volume on temperature at constant pressure:

$$\alpha = \frac{\gamma C_V}{B_T V}. \tag{19}$$

The variation of the thermal expansion coefficient, α as a function of temperature at different pressures for the investigated $AgAl(S_{1-x}Se_x)_2$ alloys is represented in Fig. 12. It is noted that, at a given pressure, the coefficient of thermal expansion α increases sharply for low temperatures (up to 800 K) irrespective of the alloy composition. When the temperature is greater than 800 K, the coefficient of thermal expansion α exhibits an approximately linear dependence trend and the increase rate becomes moderate, indicating that the temperature dependence of α is negligible for high temperatures. At high temperature and pressure, the coefficient of thermal expansion tends to converge towards a constant value.

The entropy S describes the distribution of matter and energy. Entropy is a metric used to quantify the disorder of a system. It has the following relation [19, 67]:

$$S = nk_B\left[4D\left(\frac{\theta_D}{T}\right) - 3ln\left(1-e^{-\theta_D/T}\right)\right]. \tag{20}$$

The variation of the entropy S with respect to temperature and pressure is presented in Fig. 13. The entropy increases sharply with increasing temperature but decreases with increasing pressure. The calculated values of entropy at T = 800 K and P = 0 GPa are 813.80, 869.26, 897.84, 923.88, and 936.89 J/mol.K for $AgAlS_2$, $AgAlS_{0.25}Se_{0.75}$, $AgAlS_{0.5}Se_{0.5}$, $AgAlS_{0.75}Se_{0.25}$, and $AgAlSe_2$, respectively.

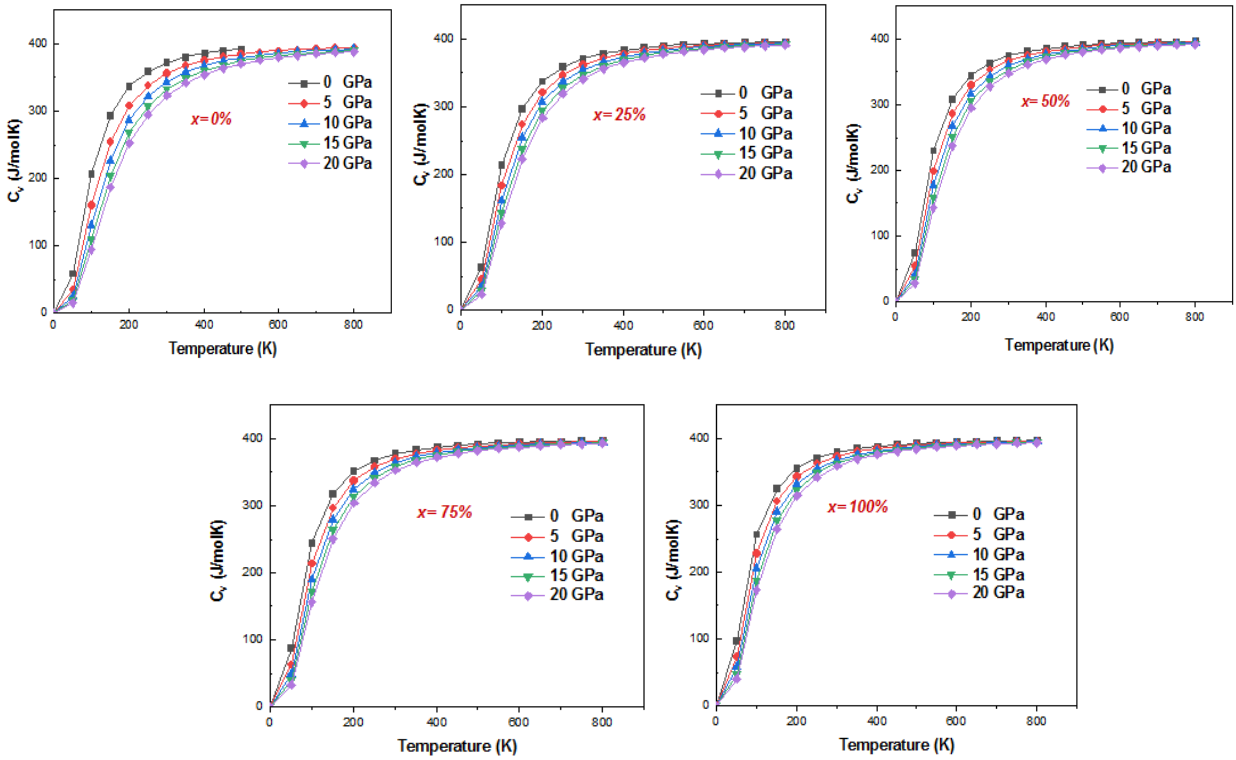

Figure 10. Heat capacity C_V as a function of temperature at various pressures

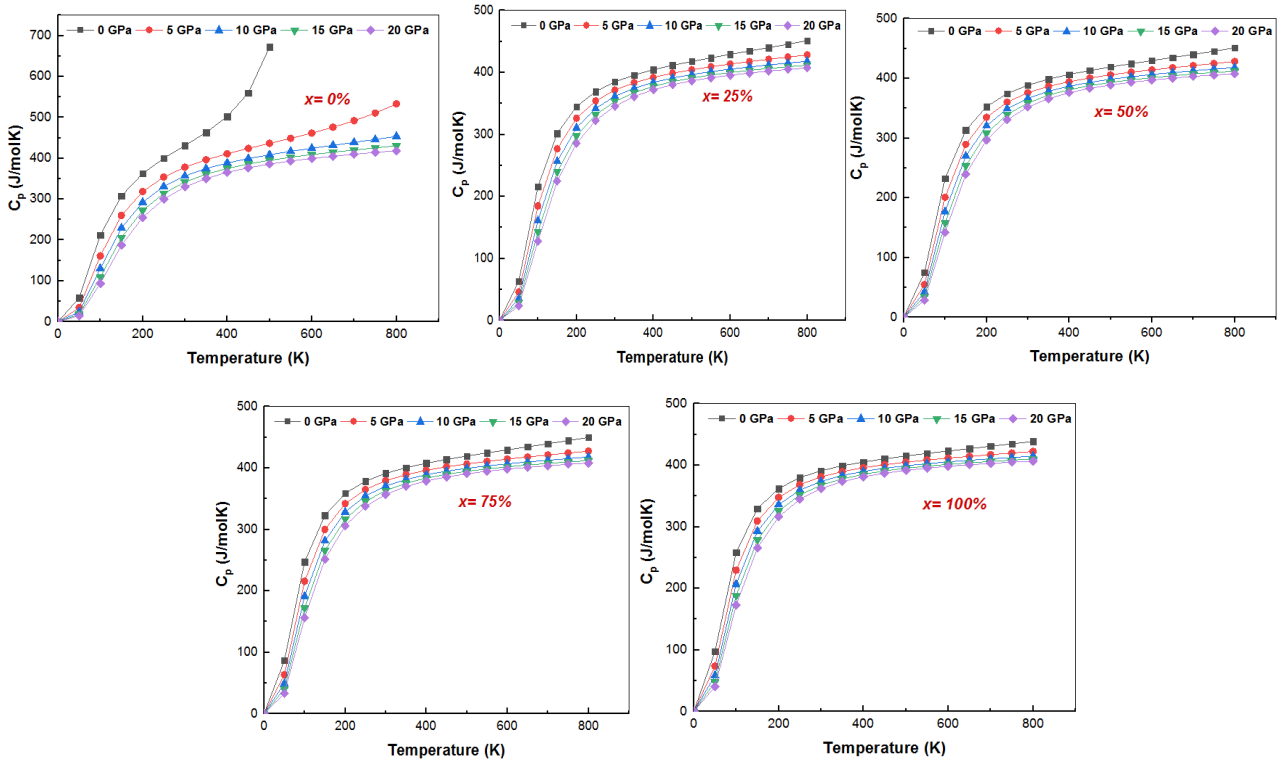

Figure 11. Heat capacity C_P as a function of temperature at various pressures.

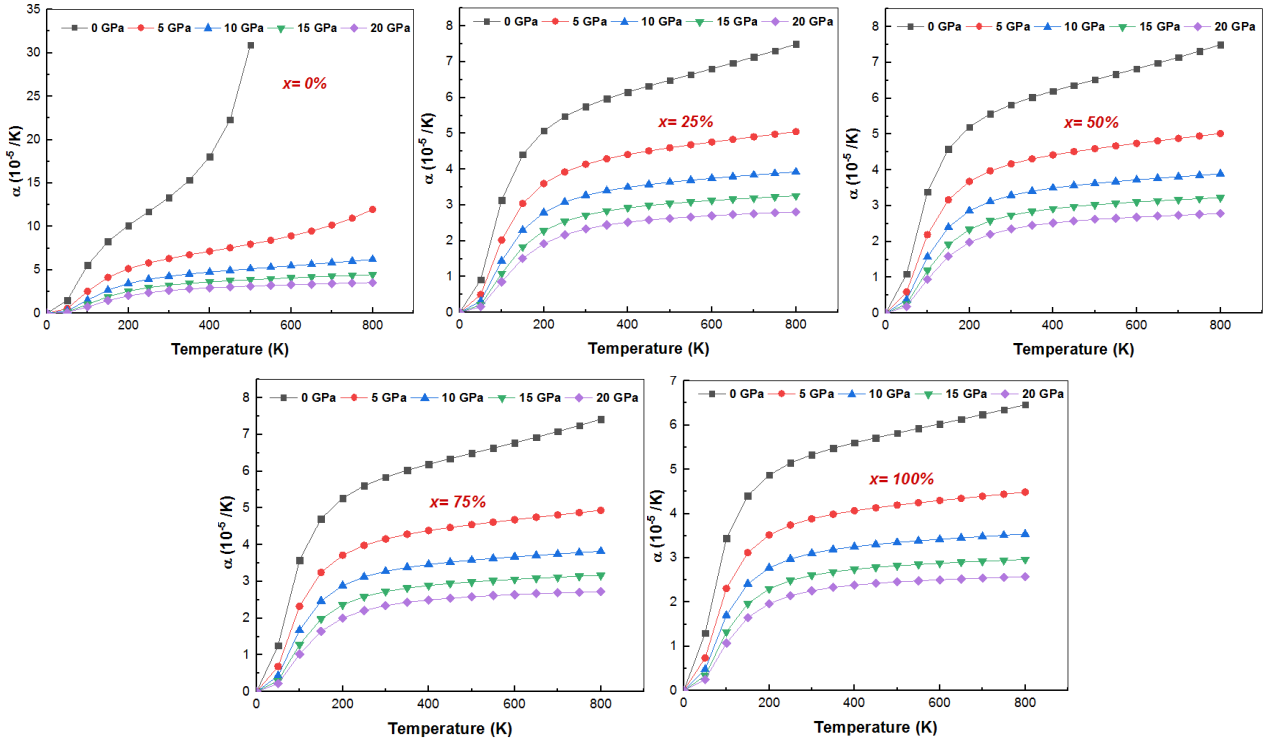

Figure 12. Thermal expansion coefficient as a function of temperature at various pressures

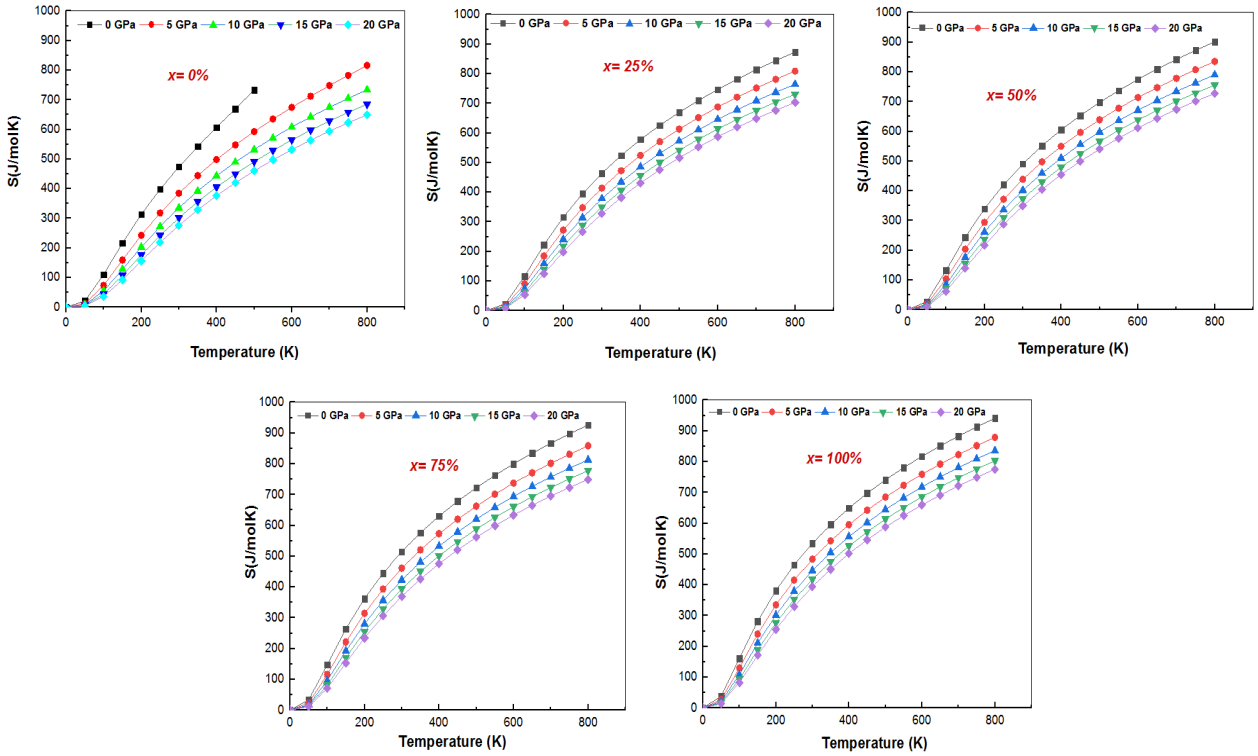

Figure 13. Entropy S as a function of temperature at various pressures

4. CONCLUSIONS

In conclusion, the structural, electronic, optical, and thermodynamic properties of $AgAl(S_{1-x}Se_x)_2$ quaternary alloys were systematically investigated using the all-electron FP-LAPW method within the framework of density functional theory. The calculated structural parameters are in good agreement with available theoretical and experimental data, confirming the reliability of the computational approach. The lattice parameters exhibit a nearly linear dependence on Se concentration, in accordance with Vegard's law, whereas the bulk modulus shows a noticeable deviation from linear

concentration dependence. Electronic structure calculations based on the modified Becke–Johnson (mBJ) potential reveal that both the parent compounds and the quaternary alloys are direct-band-gap semiconductors with the valence-band maximum and conduction-band minimum located at the Γ point. The nonlinear evolution of the band gap with composition is well described by the Zunger bowing model.

The Optical calculations demonstrate strong ultraviolet absorption and pronounced optical anisotropy, while the thermodynamic properties exhibit a significant dependence on temperature and pressure, indicating good thermal stability under varying operating conditions. Although the alloy compositions were modeled using ordered supercells, which do not explicitly account for configurational disorder, this approach successfully captures the essential composition-dependent trends. Overall, the present findings provide a comprehensive theoretical understanding of $AgAl(S_{1-x}Se_x)_2$ alloys and demonstrate their strong potential for ultraviolet optoelectronic applications, while offering a reliable foundation for future experimental studies and advanced device design.

ORCID

Nabil Beloufa, https://orcid.org/0009-0007-5099-5180;
Mohammed Ouled Ali, https://orcid.org/0009-0006-3516-6328;
Hamza Rekab-Djabri, https://orcid.org/0000-0002-2458-1335;
Djamel Eddine Belfennache, https://orcid.org/0000-0002-4908-6058;
Radhia Yekhlef, https://orcid.org/0000-0003-0646-6453;
Hamad M Adress Hasan, https://orcid.org/0000-0002-6739-8311;
Hanan F. Emrayed, https://orcid.org/0009-0008-6812-4268;
Ghada M Salem, https://orcid.org/0000-0002-1830-7049

REFERENCES

[1] F. Saker, L. Remache, D. Belfennache, K.R. Chebouki, and R. Yekhlef, Chalcogenide Lett. **22(2)**, 151 (2025). https://doi.org/10.15251/CL.2025.222.151
[2] R. Ouldamer, D. Madi, and D. Belfennache, in: *Advanced Computational Techniques for Renewable Energy Systems. IC-AIRES 2022. Lecture Notes in Networks and Systems*, vol. 591, edited by M. Hatti, (Springer, Cham. 2023). pp. 700-705, https://doi.org/10.1007/978-3-031-21216-1_71
[3] S. Mahdid, D. Belfennache, D. Madi, M. Samah, R. Yekhlef, and Y. Benkrima, J. Ovonic. Res. **19(5)**, 535-545 (2023). https://doi.org/10.15251/JOR.2023.195.535
[4] Y. Bellal, A. Bouhank, D. Belfennache, R. Yekhlef, East Eur. J. Phys. (1), 170 (2025). https://doi.org/10.26565/2312-4334-2025-1-16
[5] K. Bouferrache, M.A. Ghebouli, B. Ghebouli, M. Fatmi, S. Alomairy, T.M. Althagafi, N. Bioud, *et al*., Eur. Phys. J. Appl. Phys. **100**, 29 (2025). https://doi.org/10.1051/epjap/2025027
[6] A. Djemli, M. Reffas, K. Bouferrache, F. Benlakhdar, R. Yekhlef, D. Belfennache, and S.I. Ahmed, *et al*., Phys. Solid State, **67**(5), 356 (2025). https://doi.org/10.1134/S1063783425600499
[7] R.P. Brian, T. Kiyosawa, and K. Masumoto, Prog. Cryst. Growth Charact. **1**, 331 (1979). https://doi.org/10.1016/0146-3535(79)90002-9
[8] S. Prasad, and B.D. Pandey, Miner. Eng. **11**, 763 (1998). https://doi.org/10.1016/S0892-6875(98)00061-2
[9] H. Horinaka, S. Mononobe, and N. Yamamoto, Jpn. J. Appl. Phys. **32**, 109 (1993). https://doi.org/10.7567/JJAPS.32S3.109
[10] J. L. Shay, L. M. Schiavone, E. Buehler, and J. H. Wernick, J. Appl. Phys. **43,** 2805 (1972). https://doi.org/10.1063/1.1661599
[11] N. Uchitomi, and H. Kizaki, J. Magn. Magn. Mater. **597**, 172019 (2024) https://doi.org/10.1016/j.jmmm.2024.172019
[12] L.I. Koroleva, D.M. Zashchirinskii, T.M. Khapaeva, S.F. Marenkin, I.V. Fedorchenko, R. Szymczak, B. Krzumanska, *et al*., Phys. Solid State **51**, 303 (2009). https://doi.org/10.1134/S1063783409020164
[13] D. Belfennache, N. Brihi, and D. Madi, Proceeding of the IEEE xplore, 8th (ICMIC) (2016), pp. 497–502 (2017). https://doi.org/10.1109/ICMIC.2016.7804164
[14] K. Madoui, A Ghechi, S. Madoui, R. Yekhlef, D. Belfennache, S. Zaiou, and M.A. Ali, East Eur. J. Phys. (3), 390 (2024). https://doi.org/10.26565/2312-4334-2024-3-48
[15] O. Madkhali, Phys. Scr. **99**, 022004 (2024). https://doi.org/10.1088/1402-4896/ad1e44
[16] J. Low, J. Yu, M. Jaroniec, S. Wageh, A. Ahmed, A. Ghamdi, Adv. Mater. **29**, 1601694 (2017). https://doi.org/10.1002/adma.201601694
[17] J.Y. Tsao, S. Chowdhury, M.A. Hollis, D. Jena, N.M. Johnson, K.A. Jones, R.J. Kaplar, *et al*., Adv. Electron. Mater. **4**, 1600501 (2017). https://doi.org/10.1002/aelm.201600501.
[18] J.F. Randall, and J. Jacot, Renew. Energy, **28**, 1851 (2003). https://doi.org/10.1016/S0960-1481(03)00068-5
[19] J. E. Jaffe, and A. Zunger, Phys. Rev. B, **28**, 5822 (1983). https://doi.org/10.1103/PhysRevB.28.5822
[20] M.Ya. Rudysh, P.A. Shchepanskyi, G.L. Myronchuk, M. Piasecki, and O.S. Martyniuk, Physica B, **654**, 414731 (2023). https://doi.org/10.1016/j.physb.2023.414731
[21] S. Ullah, H.U. Din, G. Murtaza, T. Ouahrani, R. Khenata, and S.B. Omran, J. Alloys Compd. **617**, 575 (2014). https://doi.org/10.1016/j.jallcom.2014.08.058
[22] S. Kang, J. Wang, L. Yang, and S. W. Fan, Phys. Scr. **99**, 035923 (2024). https://doi.org/10.1088/1402-4896/ad23ac
[23] S. Mishra, and B. Ganguli, Solid State Commun. **151**, 523 (2011). https://doi.org/10.1016/j.ssc.2011.01.024
[24] H. Hahn, G. Frank, W. Klingler, A.D. Meyer, and G. Störger, Z. Anorg. Allg. Chem. **271**, 153 (1953). https://doi.org/10.1002/zaac.19532710307

[25] M. Yuan, D.B. Mitzi, O. Gunawan, A.J. Kellock, S.J. Chey, and V.R. Deline, Thin Solid Films, **519**, 852 (2010). https://doi.org/10.1016/j.tsf.2010.08.135
[26] M.Y. Rudysh, A.O. Fedorchuk, M.G. Brik, J. Grechenkov, D. Bocharov, S. Piskunov, A.I. Popov, and M. Piasecki, Materials, **16**, 7017 (2023). https://doi.org/10.3390/ma16217017
[27] W.N. Honeyman, and K.H. Wilkinson, J. Phys. D: Appl. Phys. **4**, 1182 (1971). https://doi.org/10.1088/0022-3727/4/8/319
[28] G.M.D. Nguimdo, E. Igumbor, S. Zambou, and D.P. Joubert, Comput. Condens. Matter. **21**, e00391 (2019). https://doi.org/10.1016/j.cocom.2019.e00391
[29] G.M.D. Nguimdo, and D.P. Joubert, Eur. Phys. J. B **88**, 113 (2015). https://doi.org/10.1140/epjb/e2015-50478-x
[30] P. Cheng, and Y. Yang, Acc. Chem. Res. **53**, 1218 (2020). https://doi.org/10.1021/acs.accounts.0c00157
[31] S. Agarwal, K. Weideman, D. Rokke, K.C. Vincent, D. Zemlyanov, and R. Agrawal, J. Mater. Chem. C, **12**, 325 (2024). https://doi.org/10.1039/D3TC03540A
[32] R.W. Robinson, Y. Han, H. Zhang, T. Ablekim, I. Khan, K.A. Persson, and A. Zakutayev, Chem. Rev. **120**, 4007 (2020). https://doi.org/10.1021/acs.chemrev.9b00600
[33] J. Wu, W. Huang, H. Liu, Z. He, B. Chen, S. Zhu, B. Zhao, Y. Lei, and X. Zhou, Cryst. Growth Des. **20**, 3140 (2020). https://doi.org/10.1021/acs.cgd.0c00018
[34] J. Yang, Q. Fan, Y. Yu, and W. Zhang, Materials **11**, 2370 (2018). https://doi.org/10.3390/ma11122370
[35] P. Blaha, K. Schwarz, G.K.H. Madsen, D. Kvasnicka, and J. Luitz, WIEN2k, An Augmented Plane Wave Plus Local Orbitals Program for Calculating Crystal Properties (Vienna, 2008).
[36] Y. Benkrima, D. Belfennache, R. Yekhlef, and A.M. Ghaleb, Chalcogenide Lett. **20**, 609-618 (2023). https://doi.org/10.15251/CL.2023.208.609
[37] K. Schwarz, P. Blaha, Comput. Mater. Sci. 28, 259 (2003). https://doi.org/10.1016/S0927-0256(03)00112-5
[38] Y. Achour, Y. Benkrima, I.Lefkaier, and D. Belfennache, J. Nano- Electron. Phys. **15**(1), 01018(5pp) (2023). https://doi.org/10.21272/jnep.15(1).01018
[39] Y. Benkrima, D. Belfennache, R. Yekhlef, M.E. Soudani, A. Souiga, and Y. Achour, East Eur. J. Phys. (2), 150 (2023). https://doi.org/10.26565/2312-4334-2023-2-14
[40] Y. Benkrima, S. Benhamida, and D. Belfennache, Dig. J. Nanomater. Bios. **18**(1), 11 (2023). https://doi.org/10.15251/DJNB.2023.181.11
[41] Y. Benkrima, M.E. Soudani, D. Belfennache, H. Bouguettaia, and A. Souigat, J. Ovonic. Res. **18(6),** 797 (2022). https://doi.org/10.15251/JOR.2022.186.797
[42] H. Rekab-Djabri, S. Zaiou, A. Azzouz-Rached, A. Benamrani, S. Daoud, D. Belfennache, R. Yekhlef, and N. Beloufa, East Eur. J. Phys. **3**, 298 (2025), https://doi.org/10.26565/2312-4334-2025-3-27
[43] D. Koller, F. Tran, and P. Blaha, Phys. Rev. B, **85**, 155109 (2012). https://doi.org/10.1103/PhysRevB.85.155109
[44] K. Choudhary, and F. Tavazza, Comput. Mater. Sci. **161**, 300 (2019). https://doi.org/10.1016/j.commatsci.2019.02.006
[45] A.H. Reshak, Physica B: Condens. Matter **369**, 243 (2005). https://doi.org/10.1016/j.physb.2005.08.038
[46] S.P. Bremner, M.Y. Levy, and C.B. Honsberg, Prog. Photovolt: Res. Appl. **16**, 225 (2008). https://doi.org/10.1002/pip.799
[47] W.N. Honeyman, and K.H. Wilkinson, J. Phys. D: Appl. Phys. **4**, 1182 (1971). https://doi.org/10.1088/0022-3727/4/8/319
[48] L. Vegard, Z. Phys. **5**, 17 (1921). https://doi.org/10.1007/BF01349680
[49] H. Harry, F. Günter, K. Wilhelm, and G.M. Anne, Z. Anorg. Allg. Chem. **271**, 153 (1953). https://doi.org/10.1002/zaac.19532710307
[50] C.H. Ho and C.C. Pan, AIP Adv. **2**, 022123 (2012). https://doi.org/10.1063/1.4718342
[51] M. Faizan, S. Li, Z. Liu, Z. Li, J. Xie, K. Zhou, Y. Fu, and L. Zhang, J. Mater. Chem. C **13**, 2853 (2025). https://doi.org/10.1039/D4TC04075A
[52] F.E.H. Hassan, H. Akbarzadeh, and M. Zoaeter, J. Phys.: Condens. Matter. **16**, 293 (2004). https://doi.org/10.1088/0953-8984/16/3/009
[53] J. Phillips, Rev. Mod. Phys. **42**, 317 (1970). https://doi.org/10.1103/RevModPhys.42.317
[54] J.E. Bernard, and A. Zunger, Phys. Rev. B, **34**, 5992(R) (1986). https://doi.org/10.1103/PhysRevB.34.5992
[55] M. Fox, Optical Properties of Solids, 2nd ed., Oxford University Press, Oxford, (2010).
[56] P.Y. Yu, and M. Cardona, Fundamentals of Semiconductors: Physics and Materials Properties, 4th ed., Springer, (2010). https://doi.org/10.1007/978-3-642-00710-1
[57] F. Wooten, *Optical Properties of Solids*, (Academic, 2016).
[58] D.R. Penn, Phys. Rev. **128**, 2093 (1962). https://doi.org/10.1103/PhysRev.128.2093
[59] G. Dresselhaus, A.F. Kip, and C. Kittel, Phys. Rev. **100**, 618 (1955). https://doi.org/10.1103/PhysRev.100.618
[60] L. Cavaleri, M. Papia, G. Macaluso, *et al*., Mater. Struct. **47**, 239 (2014). https://doi.org/10.1617/s11527-013-0058-9
[61] Ç. Yamçıçıer, S. Al, and C. Kürkçü, Physica B: Condens. Matter: 716, 417713 (2025). https://doi.org/10.1016/j.physb.2025.417713
[62] K. Randall, and A. Burnham, Propellants Explos. Pyrotech. **30**, 344 (2005). https://doi.org/10.1002/prep.200500024
[63] M. Blanco, A.M. Pendás, E. Francisco, J. Recio, and R. Franco, J. Mol. Struct.: THEOCHEM, **368**, 245 (1996). https://doi.org/10.1016/S0166-1280(96)90571-0
[64] M. Flórez, J. Recio, E. Francisco, M. Blanco, and A.M. Pendás, Phys. Rev. B, **66**, 144112 (2002). https://doi.org/10.1103/PhysRevB.66.144112
[65] E. Francisco, M. Blanco, and G. Sanjurjo, Phys. Rev. B, **63**, 094107 (2001). https://doi.org/10.1103/PhysRevB.63.094107
[66] H. Xiao, K.J. Tahir, and W.A. Goddard, J. Phys. Chem. Lett. **2**, 212 (2011). https://doi.org/10.1021/jz101565j
[67] A. Verma, and S. Bhardwaj, Phys. Scr. **79**, 015302 (2008). https://doi.org/10.1088/0031-8949/79/01/015302

DFT АНАЛІЗ СТРУКТУРНИХ, ОПТОЕЛЕКТРОННИХ ТА ТЕРМОДИНАМІЧНИХ ХАРАКТЕРИСТИК ХАЛЬКОПІРИТУ $AgAl(S_{1-x}Se_x)_2$

Набіль Белуфа[1,2], Мохаммед Улед Алі[2,3], Хамза Рекаб-Джабрі[2,4], Д. Белфеннаше[5], Р. Єхлеф[5], Хамад М. Адресс Хасан[6], Ханан Ф. Емрайєд[6], Ханібал Саїд Хатаб[7], Гада М. Салем[8]

[1]Гідрометеорологічний інститут навчання та досліджень IHFR, ІбнуРошд.Вр 7019, Оран, Алжир
[2]Лабораторія мікро- та нанофізики (LaMiN), Національна політехнічна школа Оран, ENPO-MA, BP 1523, Ель-М'Науер, 31000, Оран, Алжир
[3]Факультет наук про речовину, математики та комп'ютерних наук, Університет Ахмеда Драї, Адрар, Алжир
[4]Факультет наук про природу та життя та наук про Землю, Університет АкліМоханда-Ульхаджа, 10000, Буїра, Алжир
[5]Дослідницький центр промислових технологій CRTI, P.O. A/c 64, Черага, 16014 Алжир, Алжир
[6]Кафедра хімії, факультет природничих наук, Університет Омара аль-Мухтара, Лівія
[7]Факультет освіти, Аль-Мардж, Університет Бенгазі, Лівія
[8]Лівійське управління наукових досліджень, Триполі, Лівія

У цій роботі ми досліджували структурні, оптоелектронні та термодинамічні властивості четвертинної сполуки $AgAl(S_xSe_{1-x})_2$. У цьому дослідженні використовувався метод FP-LAPW, реалізований у програмі Wien2k та інтегрований у структуру теорії функціоналу густини (DFT). Для обробки обмінного та кореляційного потенціалу використовується узагальнене градієнтне наближення (WC-GGA). Ми вивчали вплив складу на міцність утворення, видимий модуль пружності та об'єм кристалічної решітки. Згідно із зібраними даними, не спостерігається жодних відхилень у модулі стисливості порівняно із законом LCD, а також у постійній решітки порівняно із законом Вегарда. Підхід Цунгера та його колег було використано для визначення мікроскопічного джерела просторової кривизни. Порівняно з попередніми теоретичними дослідженнями, значення ширини забороненої зони, отримані з розрахунків зонної структури на основі модифікованого наближення потенціалу Бекке-Джонсона (mBJ), показують помітні покращення та набагато краще узгоджуються з експериментальними результатами для потрійних сполук. Оптичні властивості вказують на те, що статична діелектрична проникність $\varepsilon_1(0)$ зростає зі збільшенням концентрації x, тоді як енергія оптичної щілини одночасно зменшується; водночас діелектрична функція демонструє значну анізотропію в напрямку zz. Дослідження впливу теплової енергії на певні макроскопічні характеристики було проведено з використанням квазігармонічної моделі Дебая. Тим не менш, досліджені сплави показали стабільність при проміжних температурах від 0 до 800 K.

Ключові слова: *$AgAl(S_xSe_{1-x})_2$; FP-LAPW; WC-GGA; mBJ; закон Вегарда; квазігармоніка Дебая*

East European Journal of Physics. 3. 681-688 (2026)
DOI:10.26565/2312-4334-2026-3-64 ISSN 2312-4334

STOICHIOMETRIC EVOLUTION OF MULTI-PHASE TUNGSTEN NITRIDES UNDER VARIABLE GAS FLOW AND AUXILIARY PLASMA ASSISTANCE DURING MAGNETRON SPUTTERING[G]

O.V. Maksakova*, V.M. Beresnev, I.M. Sereda, Ya.O. Hrechko, A.O. Skrypnyk, S.I. Bogatyrenko, S.V. Lytovchenko, B.O. Mazilin
V.N. Karazin Kharkiv National University, 4, Svoboby Sq., 61000 Kharkiv, Ukraine
**Corresponding author email: o.maksakova@karazin.ua*
Received _June 31, 2026; revised August 5, accepted August 15, 2026

In this work, the influence of Ar/N_2 gas mixture composition and auxiliary plasma-assisted activation on the structural-phase evolution of tungsten nitride (WN) coatings deposited via planar magnetron sputtering was systematically investigated. The coatings were synthesized using a 100-mm diameter tungsten target under varying reactive gas regimes (from 50% to 10% N_2) and two electrical configurations: an additional biased anode (+200 V) and a standard grounded anode setup. X-ray diffraction coupled with qualitative and quantitative optimization proved that the coatings possess a complex heterophase structure composed of hexagonal hcp-WN and cubic fcc-W_2N phases. It has been established that the persistent dominance of the hcp-WN phase with a highly stable (111) texture acts as a rigid energetically favored framework across all gas flow ratios. Decreasing the nitrogen content primarily affects the secondary, more compliant cubic phase component. At a critical nitrogen deficiency of 10%, the growth of the preferred (200) cubic planes becomes heavily suppressed, forcing the matrix towards grain refinement (nanocrystallization) and stimulating the structural integration of mixed-phase (220)fcc + (102)hcp configuration. Furthermore, shifting to the grounded anode configuration collapses the auxiliary glow discharge zone, dropping the near-substrate plasma density from 7.5×10^{10} cm^{-3} to 4×10^{10} cm^{-3}. The resulting reduction in adatom surface diffusion length causes rapid thermal quenching, leading to complete texture randomization, a sharp fourfold increase in the isotropic (111)fcc + (100)hcp reflection, and the accumulation of structurally imperfect phase boundaries. The application of an auxiliary biased anode serves as an effective tool to decouple the destructive effects of high-energy ion bombardment from the beneficial structural ordering induced by high-flux, low-energy plasma activation.
Keywords: *Magnetron Sputtering; Nitrides; Tungsten; XRD; Phase; Structure; Gas flow*

INTRODUCTION

Transition-metal nitrides, particularly tungsten nitrides, have garnered significant academic and industrial interest owing to their exceptional mechanical hardness, high thermal stability, remarkable wear resistance, and reliable chemical inertness [1-5]. These properties make them highly attractive for a wide range of cutting-edge applications, including diffusion barriers in microelectronics, protective coatings for high-temperature machining tools, and active components in catalytic energy conversion systems [6-10]. In the field of surface engineering, magnetron sputtering stands out as the premier deposition technique for synthesizing such thin films due to its excellent scalability, high reproducibility, and capability to deposit dense, adherent coatings at relatively low substrate temperatures [11-13].

However, the deterministic synthesis of multi-phase tungsten nitride coatings remains a complex materials science challenge. Unlike other transition metal nitrides, the W-N system exhibits a rich and complex phase diagram comprising several distinct structural configurations, primarily the hexagonal hcp-WN and cubic fcc-W_2N phases [14-15]. The competitive nucleation and spatial orientation of these phases are heavily dictated by the thermodynamic driving forces of chemical reactions at the substrate and the kinetic energy transfer to the growing film interface. Consequently, precise control over the structural-phase evolution and texturing is essential, as the final performance of the coating is inherently linked to its precise phase boundary configuration and grain orientation.

To systematically optimize the performance of the WN coatings, two critical deposition parameters can be comprehensively evaluated. The first one is a reactive gas mixture composition (i.e. Ar/N_2 flow ratio). This parameter directly regulates the chemical stoichiometry and nitrogen saturation degree of the tungsten lattice [16-17]. A precise balance of the reactive gas is critical to avoid either a total collapse of the stoichiometric crystalline phase or severe target poisoning during the sputtering process. The second one is a low-energy ion bombardment kinetics. Controlling the plasma parameters at the growth front is paramount for modulating film density, grain size, and texture crystallization [16-17]. Traditional methods often rely on high negative substrate bias voltages to accelerate ions; however, this approach frequently induces high intrinsic macrostrains, atomic displacement, and destructive lattice defects.

To overcome these structural limitations, auxiliary plasma assistance via an additional biased anode emerges as a crucial engineering tool for magnetron sputtering. This configuration enables an effective decoupling of the destructive high-energy ion impacts from the highly beneficial structural ordering driven by a high-flux, low-energy plasma activation. By effectively doubling the local plasma density without altering the safe ion impact energy threshold, the

Cite as: O.V. Maksakova, V.M. Beresnev, I.M. Sereda, Ya.O. Hrechko, A.O. Skrypnyk, S.I. Bogatyrenko, S.V. Lytovchenko, B.O. Mazilin, East Eur. J. Phys. 3, 681 (2026), https://doi.org/10.26565/2312-4334-2026-3-64

auxiliary anode dramatically accelerates the lateral surface diffusion of arriving adatoms, allowing the system to easily overcome local potential barriers and crystallize into thermodynamically preferred textures.

While separate studies have addressed either gas flow dynamics or plasma assistance [18-19], a systematic understanding of their synergistic influence on the phase transition kinetics of heterophase WN/W_2N nanocomposite systems remains insufficient.

The aim of this work is to systematically investigate the combined effects of the Ar/N_2 gas flow ratio and auxiliary biased anode configuration on the stoichiometric evolution, and phase boundary perfection of multi-phase tungsten nitride coatings deposited via reactive magnetron sputtering.

EXPERIMENTAL DETAILS

Deposition

A planar magnetron sputtering system equipped with a 100-mm diameter tungsten target and an additional anode was employed for the deposition of WN and WC coatings (see Figure 1). Prior to deposition, the vacuum chamber was evacuated using a turbomolecular pump to a base pressure of approximately 5×10^{-5} Torr. For the WN deposition, high-purity argon and nitrogen were introduced into the chamber at different Ar/N_2 flow-rate ratios. The total working pressure was maintained at approximately 9×10^{-4} Torr.

The magnetron was operated with a 100 Hz sinusoidal voltage waveform, with a peak cathode voltage of approximately 450 V and a peak discharge current of approximately 1.5 A. An additional anode was biased at approximately +200 V to generate an additional glow-discharge plasma in the region between the magnetron and the substrate. The substrate was positioned at a distance of 140 mm from the target and was electrically insulated during deposition. Under the deposition conditions, the ion energy incident on the substrate, measured using a retarding-field analyzer (RFA), was approximately (10 ÷ 12) eV with respect to substrate floating potential. Plasma density measured with Langmuir probe near the substrate was approximately 7.5×10^{10} cm^{-3} with electron temperature of about 2 eV.

The deposition time was fixed at 30 min for all experiments. The coating thickness was monitored using a quartz crystal microbalance and was approximately 500 nm for the WN coatings.

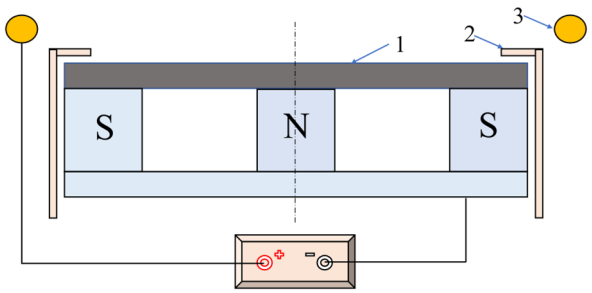

Figure 1. The scheme of experimental device: 1 – tungsten target; 2 – insulated cylinder; 3 – anode

For the deposition of WN coatings at different gas regimes, a precise gas mixing procedure based on partial pressure management was implemented. The total working pressure within the vacuum chamber was strictly maintained at a constant value of approximately 9×10^{-4} Torr, which was defined as 100% of the total gas volume. Prior to the introduction of the reactive gas, high-purity argon (Ar) was admitted into the chamber via a dedicated piezoceramic leak valve until its partial pressure reached the specific required percentage of the total working pressure (i.e., 50%, 70%, 80%, or 90%, respectively). Subsequently, high-purity nitrogen (N_2) was introduced through a separate independent leak valve to act as the reactive gas, adjusting the total pressure upward until the final working threshold of 9×10^{-4} Torr was precisely achieved. This sequential gas-feeding method ensured highly reproducible Ar/N_2 flow-rate ratios, corresponding to discrete concentrations of 50%, 30%, 20%, and 10% of N_2 in the plasma volume.

For the comparative study, a series of WN coatings was also deposited under the conventional magnetron sputtering configuration, where the additional anode was kept at the ground potential (referred to as the “grounded anode” mode). This setup represents the standard operating regime of the magnetron system without the generation of an auxiliary plasma enhancement zone. Under these conditions, the plasma density measured with the Langmuir probe in the vicinity of the substrate dropped by approximately a factor of two, yielding a value of 4×10^{10} cm^{-3}. Despite the significant decrease in plasma density, the average energy of the ions incident on the substrate surface remained practically unaltered at approximately 12 eV. All other deposition variables, including the target-to-substrate distance, working gas pressure (80 Ar / 20 N_2), and total deposition time, were maintained identical to those utilized in the biased anode experiments to ensure a direct comparison of the structural-phase evolution.

The crystal structure, phase composition, and substructural characteristics of the WN coatings were evaluated by X-ray diffraction (XRD). The XRD measurements were performed on a diffractometer utilizing a Cu-Kα radiation source (λ = 1.540600 Å) operating at an accelerating voltage of 30.0 kV and a tube current of 30.0 mA. The optical configuration of the goniometer included a 1.0° divergence slit, a 1.0° scatter slit, and a 0.15 mm receiving slit. The diffraction patterns were recorded in the theta–2theta coupled scanning mode over a 2theta angular range of 10.0°–100.0° with a step size (sampling pitch) of 0.02° and a continuous scanning speed of 2.000°/min.

Phase identification and qualitative/quantitative analysis were carried out using the Match! phase analysis software package (Crystal Impact, Bonn, Germany), coupled with the PDF-2 (Release 2004) reference database. Quantitative phase evaluation was performed via the Reference Intensity Ratio (RIR) method based on integrated profile areas. The experimental diffraction data was smoothed prior to analysis without subtracting the background or the α2 radiation component.

According to the quantitative search-match optimization, the matrix consists of a complex multi-phase nitride system dominated by two major tungsten nitride phases: a hexagonal hcp-WN phase (space group P6̄m2, lattice parameters a = 2.89 Å and c = 2.83 Å, entry No. 03-065-9410) and a cubic fcc-WN phase (space group Fm3̄m, lattice parameter a = 4.126 Å, entry No. 00-025-1257).

EXPERIMENTAL RESULTS

Structural-phase analysis at standard configuration

Figure 2 illustrates the X-ray diffraction patterns of the WN coatings deposited via magnetron sputtering under various working gas flow ratios (Ar/N_2). The corresponding substructural and phase parameters calculated from the diffraction peak profiles are summarized in Table 1.

A detailed analysis of the phase composition of individual samples revealed the important trends.

For the WN (50 Ar / 50 N_2) coating, at the maximum concentration of the reactive gas (nitrogen) in the deposition chamber, a heterophase structure is formed, consisting of a dominant hexagonal phase hcp-WN and a cubic phase fcc-W_2N. The XRD pattern exhibits a low-intensity, broadened peak at 2theta = 35.98°, corresponding to the superposition of the (111)fcc + (100)hcp planes. The main contribution to the diffraction pattern comes from the peaks at 2theta = 42.95° the (200)fcc-W_2N plane, relative intensity I/I_0 = 562.88 a.u. and 2theta = 73.36° (111)hcp-WN. The latter exhibits the maximum intensity 1000.00 a.u., indicating the formation of a pronounced axial growth texture of the hexagonal phase. A (400)fcc-W_2N peak is also detected at higher angles 2theta = 88.90°.

For the WN (70 Ar / 30 N_2) coating, the reducing the nitrogen content to 30% does not lead to a qualitative rearrangement of the crystal lattice; however, it activates structural ordering processes. The combined peak around 2theta = 35.38° becomes more pronounced I/I_0 = 63.59 a.u., (FWHM = 1.2800). A moderate increase in intensity for the (200)fcc-W_2N plane to I/I_0 = 644.97 a.u. is observed, while the full width at half maximum (FWHM) broadens slightly to 0.4000, which may indicate the generation of local microstrains due to changes in the stoichiometric coefficient. The texture of (111)hcp-WN at 2theta = 73.24° retains its dominant position.

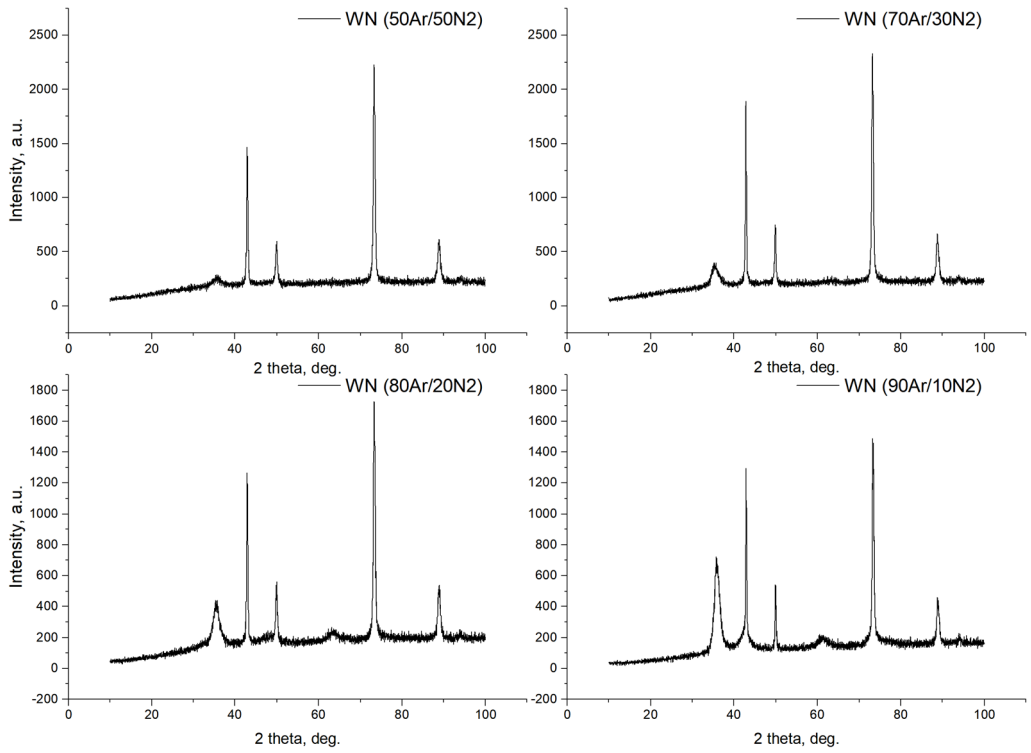

Figure 2. XRD patterns of the WN coatings deposited at different gas regimes

For the WN (80 Ar / 20 N_2) coating, at a nitrogen partial pressure of 20%, the cubic component begins to crystallize more clearly. The intensity of the (111)fcc + (100)hcp reflex doubles compared to the previous regime, reaching the intensity of I/I_0 = 135.23 a.u. Notably, in the mid-angle region of 2theta = 62.54°, the appearance of a combined (220)fcc + (102)hcp phase formation is recorded. This indicates the initiation of structural modification and the rearrangement of

the spatial orientation spectrum of the crystallites under conditions of progressive nitrogen deficiency. This indicates an expansion of the spatial orientation spectrum of the cubic crystallites under conditions of moderate nitrogen deficiency. The texture peak of the hexagonal phase at 2theta = 73.37° remains stable.

For the WN (90 Ar / 10 N_2) coating, under extreme nitrogen deficiency (10%), the phase-structural state of the system undergoes drastic changes. A sharp drop in the intensity of the (200)fcc-W_2N peak to a minimum value of I/I_0 = 49.09 a.u. is recorded, accompanied by a significant increase in its full width at half maximum to FWHM = 1.2000. In parallel, a sharp spike in the intensity of the first peak at 2theta = 35.88° up to I/I_0 = 415.78 a.u. occurs. In the mid-angle region of 2theta = 62.40°, the doublet of the (220)fcc + (102)hcp planes becomes still integrated into the structural matrix. The development of the (101)hcp-WN reflex at 2theta = 49.98° reaches its maximum I/I_0 = 611.13 a.u..

Summarizing the obtained data allows establishing a fundamental relationship between the partial pressure of the reactive gas N_2 and the phase formation kinetics in the W-N system during magnetron sputtering.

Throughout the investigated range of nitrogen concentrations (10% ÷ 50%), the framework of the coatings remains the highly textured hexagonal hcp-WN phase with a preferred orientation of the (111) crystallographic planes. The constancy of the full width at half maximum of this peak FWHM = 0.4800 and the stability of the interplanar spacing d = (1.289 ÷ 1.291) Å indicate that the average size of the coherent scattering domains (grain size) of the hexagonal matrix and its macrostrain level remain invariant to the gas mixture composition in this specific system configuration. However, the dynamics of the accompanying peaks indicate a distinct competition between the growth planes of the cubic fcc-W_2N phase. At high nitrogen flows (30% ÷ 50%), the growth of cubic grains along the (200) axis is energetically more favorable. When the N_2 concentration drops critically to 10%, growth along the (200) direction is heavily suppressed (intensity drops from 622.90 to 49.09 a.u.), with a simultaneous step-like increase in the intensity of the (111)fcc / (100)hcp planes.

The observed substructural effects are explained by changes in the nitrogen saturation degree of the tungsten lattice. In the range of N_2 = (20% ÷ 50%), the high density of the reactive gas ensures an efficient chemical reaction on the substrate, stabilizing the higher nitride phase WN and the ordered semi-nitride phase W_2N with larger, more ordered crystallites (as indicated by the narrow line of the (200)fcc peak with FWHM = (0.3600 ÷ 0.4000). Transitioning to the 20% and 10% N_2 regimes, the chemical reactivity of nitrogen becomes insufficient to complete the phase formation of stoichiometric W_2N along the stable axes. This results in grain refinement (nanocrystallization) of the cubic phase, an increase in lattice microstrains (growth of FWHM to 1.2000 for the (200) plane), and a forced restructuring of the matrix, which manifests as the emergence and integration of the mixed (220)fcc + (102)hcp phase structures.

Thus, varying the composition of the Ar/N_2 gas mixture serves as a precise tool for controlling the ratio between the cubic and hexagonal phases, and allows radically shifting the preferred orientation of the crystallites without degrading the dominant axial (111)hcp-WN texture.

Table 1. Structural-phase data of the WN coatings deposited at different gas regimes (based on XRD patterns presented in Figure 2)

No.	2 theta, deg.	d-spacing, Å	Intensity I/I_0, a.u.	FWHM	Phase	(*hkl*)
WN (50 Ar / 50 N_2)						
1	35.98	-	-	-	fcc-W_2N + hcp-WN	(111) + (100)
2	42.95	2.1040	562.88	0.3600	fcc-W_2N	(200)
3	49.97	1.8236	173.65	0.4800	hcp-WN	(101)
4	73.36	1.2896	1000.00	0.4800	hcp-WN	(111)
5	88.90	1.0999	172.22	0.6800	fcc-W_2N	(400)
WN (70 Ar / 30 N_2)						
1	35.38	2.5349	63.59	1.2800	fcc-W_2N + hcp-WN	(111) + (100)
2	42.86	2.1083	644.97	0.4000	fcc-W_2N	(200)
3	49.90	1.8260	218.83	0.4400	hcp-WN	(101)
4	73.24	1.2913	1000.00	0.4800	hcp-WN	(111)
5	88.83	1.1007	181.84	0.6400	fcc-W_2N	(400)
WN (80 Ar / 20 N_2)						
1	35.42	2.5349	135.23	1.2800	fcc-W_2N + hcp-WN	(111) + (100)
2	42.94	2.1083	622.90	0.4000	fcc-W_2N	(200)
3	49.96	1.8260	202.65	0.4800	hcp-WN	(101)
4	62.54	1.4638	-	-	fcc-W_2N + hcp-WN	(220) + (102)
5	73.37	1.2893	1000.00	0.4800	hcp-WN	(111)
6	88.93	1.0997	199.40	0.6800	fcc-W_2N	(400)
No.	2 theta, deg.	d-spacing, Å	Intensity I/I_0, a.u.	FWHM	Phase	(*hkl*)

No.	2 theta, deg.	d-spacing, Å	Intensity I/I_0, a.u.	FWHM	Phase	(*hkl*)
WN (90 Ar / 10 N_2)						
1	35.88	2.5011	415.78	1.1200	fcc-W_2N + hcp-WN	(111) + (100)
2	42.93	2.1342	49.09	1.2000	fcc-W_2N	(200)
3	49.98	1.8234	611.13	0.4000	hcp-WN	(101)
4	62.40	-	-	-	fcc-W_2N + hcp-WN	(220) + (102)
5	73.37	1.2894	1000.00	0.4800	hcp-WN	(111)
6	88.92	1.0998	201.03	0.6000	fcc-W_2N	(400)

Influence of anode configuration on the structural-phase state

To understand the role of plasma density and ion bombardment kinetics during the deposition process, a comparative analysis was performed on the WN coatings deposited at a fixed gas regime of 80 Ar / 20 N2 under two distinct electrical configurations: an additional biased anode (+200 V) and a grounded anode setup. The respective XRD patterns are shown in Figure 3, and the extracted substructural parameters are listed in Table 2.

A detailed phase and structural evaluation of the individual configurations revealed the following features.

For the WN (80 Ar / 20 N_2) coating with an additional biased anode (+200 V), under the assistance of an additional biased anode, which generates an enhanced glow-discharge plasma zone (plasma density ≈ $7.5 \cdot 10^{10}$ cm^{-3}), the coating stabilizes into a distinct heterophase structure composed of hcp-WN and fcc-W_2N phases. The diffraction profile is dominated by a highly intense and sharp peak at 2theta = 73.37°, corresponding to the (111)hcp-WN plane (I/I_0 = 1000.00 a.u.), FWHM = 0.4800). The cubic phase exhibits a strong preferred growth along the (200)fcc-W_2N plane at 2theta = 42.94° with a high relative intensity of I/I_0 = 622.90 a.u. and a narrow full width at half maximum FWHM = 0.4000. The low-angle combined reflex (111)fcc + (100)hcp at 2theta = 35.42° remains suppressed with intensity of I/I_0 = 135.23 a.u., while a weak, broad features of the mixed (220)fcc + (102)hcp phase assembly is barely traceable in the mid-angle range.

For the WN (80 Ar / 20 N_2) coating with a grounded anode, shifting to the grounded anode configuration, which represents the standard magnetron operation mode without additional plasma enhancement (plasma density ≈ $4 \cdot 10^{10}$ cm^{-3}), induces a profound redistribution of the diffraction intensities. While the dominant texture peak of the hexagonal matrix at 2theta = 73.36° (111)hcp-WN retains its absolute intensity of I/I_0 = 1000.00 a.u, its shape remains unchanged (FWHM = 0.4400). However, a drastic structural rearrangement occurs at lower angles: the combined (111)fcc + (100)hcp peak at 2theta = 36.02° experiences a fourfold intensity spike, rising to I/I_0 = 544.00 a.u. Concurrently, the (200)fcc-W_2N peak at 2theta = 42.95° drops to I/I_0 = 449.85 a.u., and its width broadens slightly to FWHM = 0.4400. Furthermore, a poorly resolved, highly diffused mixed-phase doublet of (220)fcc + (102)hcp becomes clearly visible at 2theta = 62.66°.

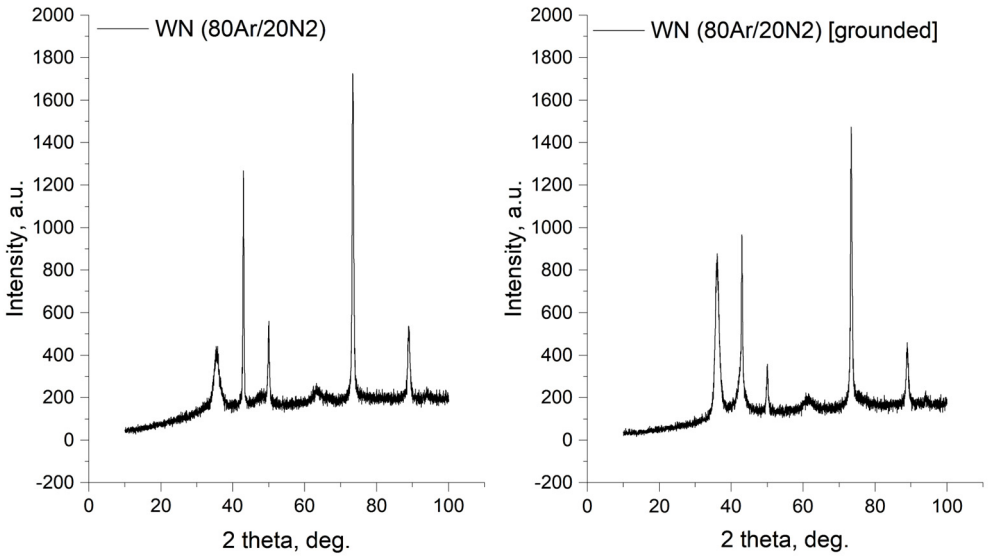

Figure 3. XRD patterns of the WN coatings deposited at 80 Ar and 20 N_2 gas regime and at non- and grounded anodes

The comparative analysis reveals the fundamental physical role of the additional biased anode in governing the phase configuration, texture development, and crystallinity of W-N systems.

1. Ion current density and surface adatom mobility. The primary mechanism driving the structural divergence between the two modes is the alteration of the plasma density near the growth front. When the additional anode is biased at +200 V, it roughly doubles the plasma density of $7.5 \cdot 10^{10}$ cm^{-3} vs. $4 \cdot 10^{10}$ cm^{-3} while maintaining a nearly constant

low ion impact energy of approximately 12 eV. This significant increase in ion flux delivers a continuous supply of low-energy momentum to the surface, effectively accelerating the lateral diffusion of arriving tungsten and nitrogen adatoms without generating structural lattice defects or severe resputtering.

This enhanced adatom mobility provides the system with the activation energy required to overcome local potential barriers, enabling the cubic W_2N phase to crystallize into its thermodynamically preferential orientation along the (200) plane. This is directly manifested in the narrow profile (FWHM = 0.4000) and high intensity of the (200)fcc peak, signaling the formation of larger, highly ordered crystalline domains.

2. Texture randomization and phase degradation via anode grounding. Upon grounding the additional anode, the auxiliary glow discharge is deactivated, causing the local ion current density to drop. Lacking sufficient plasma-assisted energy activation, the surface diffusion length of the adatoms shrinks dramatically. The arriving species are rapidly quenched at or near their landing sites, obstructing the orderly, long-range growth of the cubic lattice along preferred axes.

As a result, the texturing of the cubic component is randomized, leading to the observed deterioration of the (200)fcc growth direction and a dramatic, competitive enhancement of the isotropic (111)fcc + (100)hcp orientation at 2theta = 36.02°. The limitation in diffusion energy also hinders complete chemical phase separation, which promotes the growth of disordered, poorly crystalline interstitial networks. This directly accounts for the broadening of the existing peaks (FWHM) increases from 0.4000 to 0.4400 and the clear emergence of the highly distorted, mixed (220)fcc + (102)hcp phase doublet at 2theta = 62.66°.

In summary, the implementation of an additional biased anode acts as a crucial energetic modifier. It enables precise control over the texture and phase perfection of WN/W_2N nanocomposite coatings by substituting high-energy destructive ion bombardment with high-flux, low-energy plasma activation.

Table 2. Structural-phase data of the WN coatings deposited at different gas regimes (based on XRD patterns presented in Figure 3)

No.	2 theta, deg.	d-spacing, Å	Intensity I/I_0, a.u.	FWHM	Phase	(*hkl*)
WN (80 Ar / 20 N_2)						
1	35.42	2.5349	135.23	1.2800	fcc-W_2N + hcp-WN	(111) + (100)
2	42.94	2.1083	622.90	0.4000	fcc-W_2N	(200)
3	49.96	1.8260	202.65	0.4800	hcp-WN	(101)
4	62.54	1.4638	-	-	fcc-W_2N + hcp-WN	(220) + (102)
5	73.37	1.2893	1000.00	0.4800	hcp-WN	(111)
6	88.93	1.0997	199.40	0.6800	fcc-W_2N	(400)
WN (80 Ar / 20 N_2) [grounded anode]						
1	36.02	2.4914	544.00	1.1200	fcc-W_2N + hcp-WN	(111) + (100)
2	42.95	2.1042	449.85	0.4400	fcc-W_2N	(200)
3	50.00	1.8228	147.08	0.5200	hcp-WN	(101)
4	62.66	-	-	-	fcc-W_2N + hcp-WN	(220) + (102)
5	73.36	1.2896	1000.00	0.4400	hcp-WN	(111)
6	88.91	1.0998	192.82	0.6400	fcc-W_2N	(400)

4. DISCUSSIONS

The structural-phase evolution of the magnetron-sputtered WN coatings is governed by a complex interplay between the thermodynamic driving forces of chemical synthesis (controlled by nitrogen partial pressure) and the kinetic energy delivered to the growing film surface via ion bombardment (governed by the auxiliary anode configuration).

The persistent dominance of the hexagonal hcp-WN phase with a highly stable (111) texture across all gas flow ratios indicates that this structural matrix acts as a rigid energetically favored framework under the given non-equilibrium deposition conditions. The structural invariance of the hcp phase suggests that excess or deficiency of nitrogen primarily affects the secondary, more compliant cubic phase component.

During standard configuration experiments with high nitrogen concentrations (30%–50% of N_2), the high chemical activity of nitrogen facilitates the formation of stoichiometric cubic W_2N phase domains alongside hcp-WN. The preferential growth of these cubic crystallites along the (200) crystallographic orientation represents the minimizing of surface and strain energy under steady-state adatom diffusion. However, as the system transitions into progressive nitrogen deficiency (10% of N_2), the severe restriction of reactive species disrupts the standard nucleation pathways. The growth of the (200) cubic planes becomes heavily suppressed due to the inability to maintain proper stoichiometry along this direction. This induces a state of forced recrystallization and lattice distortion, pushing the cubic matrix towards grain refinement (nanocrystallization) and stimulating the structural integration of mixed-phase structures like the (220)fcc + (102)hcp configurations as a mechanism to accommodate high localized microstrains.

When analyzing the influence of the electrical configuration at a fixed gas regime (80 Ar / 20 N_2), the drastic restructuring observed upon applying the +200 V bias to the additional anode highlights the role of energy transfer at the

film-substrate interface. The biased anode effectively doubles the plasma density (and thus the ion current density) while maintaining a low, non-destructive ion energy profile (~12 eV). From a physical standpoint, this configuration acts as a targeted external energy deliverer that drastically enhances the lateral adatom mobility (surface diffusion length) of arriving W and N species without introducing lattice defects via atomic displacement or resputtering. The accelerated diffusion allows atoms to easily overcome local potential barriers, promoting long-range crystalline ordering and maximizing the crystallization of the thermodynamically stable cubic (200) orientation.

Conversely, when the additional anode is grounded, the auxiliary glow discharge zone collapses, causing a sharp drop in local ion flux. Under these low-flux conditions, arriving adatoms suffer from rapid thermal quenching at or near their immediate landing sites. The restricted surface diffusion prevents the system from undergoing orderly phase separation and structural relaxation. Consequently, the texturing of the cubic component undergoes complete randomization, manifesting as a competitive surge of the isotropic (111)fcc + (100)hcp reflection at 2theta = 36.02°. The lack of plasma-assisted kinetic energy halts the complete chemical synthesis, leading to the accumulation of highly distorted interstitial network boundaries and the emergence of diffused, structurally imperfect mixed-phase configurations. Thus, the auxiliary biased anode serves as an effective tool to decouple the destructive effects of high-energy ion bombardment from the beneficial structural ordering induced by high-flux, low-energy plasma activation.

CONCLUSIONS

In this study, multi-phase tungsten nitride coatings were successfully synthesized under purposefully varied deposition configurations, encompassing a wide range of reactive gas mixture ratios and distinct auxiliary anode connections, specifically tailored to systematically evaluate the competing roles of chemical stoichiometry and low-energy plasma kinetics. Based on the comprehensive structural, phase, and substructural investigation, the following conclusions can be drawn:

1. Magnetron-sputtered tungsten nitride coatings form a complex nanocomposite heterophase structure consisting of a dominant hexagonal hcp-WN phase and a secondary cubic fcc-W_2N phase. The hcp-WN matrix exhibits a rigid, invariant axial growth texture along the (111) crystallographic orientation across the entire investigated range of nitrogen concentrations (10% – 50%).
2. The partial pressure of the reactive gas selectively governs the nucleation kinetics of the compliant cubic phase. High nitrogen contents (30% – 50%) promote orderly growth along the thermodynamically favorable (200)fcc direction. Progressive nitrogen deficiency down to 10% heavily suppresses the (200) growth due to stoichiometry loss, triggering localized microstrains, nanocrystallization, and a forced restructuring into mixed (220)fcc + (102)hcp phase assemblies.
3. The implementation of an auxiliary biased anode (+200 V) doubles the local plasma density to $7.5 \cdot 10^{10}$ cm^{-3} while preserving a non-destructive ion impact energy of approximately 12 eV. This high-flux, low-energy configuration acts as a targeted external energy deliverer that drastically enhances the lateral surface diffusion of arriving W and N adatoms, allowing them to easily overcome potential barriers and form large, highly ordered crystalline domains along the preferred (200) orientation.
4. Operating the system in the standard grounded anode mode (without auxiliary plasma) causes a sharp drop in ion current density. The restricted diffusion energy forces arriving adatoms to undergo rapid thermal quenching at their immediate landing sites, obstructing orderly phase separation. This leads to total texture randomization, a massive fourfold enhancement of the isotropic (111)fcc + (100)hcp peak reflection at 2theta = 36.02°, and the emergence of highly distorted interstitial network boundaries.

Acknowledgments

V.M. Beresnev, I.M. Sereda, Ya.O. Hrechko, A.O. Skrypnyk, S.V. Lytovchenko and B.O.Mazilin were supported by the National Research Foundation of Ukraine in the framework of the project 2025.07/0146.

ORCID

Olga Maksakova, https://orcid.org/0000-0002-0646-6704; **Vyacheslav Beresnev**, https://orcid.org/0000-0002-4623-3243;
Ihor Sereda, https://orcid.org/0000-0002-9111-9853; **Yaroslav Hrechko**, https://orcid.org/0000-0001-9198-3660;
Anatoliy Skrypnyk, https://orcid.org/0009-0004-6863-6563; **Sergiy Bogatyrenko**, https://orcid.org/0000-0002-6044-6886;
Serhiy Lytovchenko, https://orcid.org/0000-0002-3292-5468; **Bohdan Mazilin,** https://orcid.org/0000-0003-1576-0590

REFERENCES

[1] O. Wenzel, V. Rein, M. Hugenschmidt, F. Schilling, C. Feldmann, and D. Gerthsen, RSC Adv. **11**, 28198-28210 (2021). https://doi.org/10.1039/D1RA04448F
[2] H. Liu, Z.-S. Wu, L. Huang, B.-W. Zhang, L.-C. Yin, C.-Y. Xu, and L. Zhen, J. Mater. Chem. A, **9**, 11323-11330 (2021). https://doi.org/10.1039/D1TA01560E
[3] X. Wu, Y. Jiang, T. Wu, B. Zuo, S. Bian, K. Lu, *et al.*, Nanomaterials, **13**, 2205 (2023). https://doi.org/10.3390/nano13152205
[4] Liang, I. Osmond, G. Krach, L.-T. Shi, L. Brüning, U. Ranieri *et al.*, Adv. Funct. Mater. 2313819 (2024). https://doi.org/10.1002/adfm.202313819
[5] S. Anwar, S. Anwar, and B. Priyadarshini, J. Mater. Res. (2024). https://doi.org/10.1557/S43578-024-01353-1
[6] H. Wang, J. Li, K. Li, Y. Lin, J. Chen, L. Gao *et al.*, Chem. Soc. Rev. **50**, 1354-1390 (2021). https://doi.org/10.1039/D0CS00415D

[7] Z. Meng, S. Zheng, R. Luo, H. Tang, R. Wang, R. Zhang, *et al.*, Nanomaterials, **12**, 2660 (2022). https://doi.org/10.3390/nano12152660
[8] Z.-G. Yang, H.-M. Xu, T.-Y. Shuai, Q.-N. Zhan, Z.-J. Zhang, K. Huang, *et al.*, Nanoscale, **15**, 11777-11800 (2023). https://doi.org/10.1039/D3NR01607B
[9] S.K. Mohanty, K.P.K. Reddy, C.-H. Wu, P.-T. Lee, K.-M. Chang, P. Busa, *et al.*, Electronics, **11**, 3432 (2022). https://doi.org/10.3390/electronics11213432
[10] S. Han, S. Yang, X. Zeng, Y. Wu, T. Liu, H. Wang, and S. Ding, Crystals, **14**, 951 (2024). https://doi.org/10.3390/cryst14110951
[11] J. Li, G.-K. Ren, J. Chen, X. Chen, W. Wu, Y. Liu, X. Chen, *et al*., JOM, **74**, 2717-2738 (2022). https://doi.org/10.1007/s11837-022-05294-0
[12] M. Sasani Ghamsari, Metals, **13**, 963 (2023). https://doi.org/10.3390/met13050963
[13] S. Sério, Coatings, **14**, 1041 (2024). https://doi.org/10.3390/coatings14081041
[14] Liang, I. Osmond, G. Krach, L.-T. Shi, L. Brüning, U. Ranieri, *et al*., Adv. Funct. Mater. **34**, 2313819 (2024). https://doi.org/10.1002/adfm.202313819
[15] S. Anwar, S. Anwar, and B. Priyadarshini, J. Mater. Res. (2024). https://doi.org/10.1557/S43578-024-01353-1
[16] L.-C. Chang, M.-C. Sung, L.-H. Chu, and Y.-I. Chen, Coatings, **10**, 1252 (2020). https://doi.org/10.3390/coatings10121252
[17] L. Bana, D. Vavassori, G. Marra, D. Dellasega, and M. Passoni**,** Surf. Coat. Technol. **514**, 132544 (2025). https://doi.org/10.1016/j.surfcoat.2025.132544
[18] Z. Wang, Y. Li, T. Hu, X. Tian, C. Gong, and H. Zhang**,** China Surf. Eng. **38**, 99-106 (2025). https://doi.org/10.11933/j.issn.1007-9289.20240109001
[19] Kosari Mehr, A. Kosari Mehr, Appl. Phys. A, **129**, 693 (2023). https://doi.org/10.1007/s00339-023-06945-y

СТЕХІОМЕТРИЧНА ЕВОЛЮЦІЯ БАГАТОФАЗНИХ НІТРИДІВ ВОЛЬФРАМУ ЗА ЗМІННОГО ПОТОКУ ГАЗУ ТА ВПЛИВУ ДОДАТКОВОЇ ПЛАЗМИ ПІД ЧАС МАГНЕТРОННОГО РОЗПИЛЕННЯ

О.В. Максакова, В.М. Береснєв, І.М. Середа, Я.О. Гречко, А.О. Скрипник, С.І. Богатиренко, С.В. Литовченко, Б.О. Мазілін
Харківський національний університет імені В.Н. Каразіна, майд. Свободи, 4, 61000 Харків, Україна

У роботі систематично досліджено вплив складу газової суміші Ar/N_2 та допоміжної плазмової активації на структурно-фазову еволюцію покриттів нітриду вольфраму (WN), осаджених методом планарного магнетронного розпилення. Покриття синтезували з використанням вольфрамової мішені діаметром 100 мм за різних режимів подачі реактивного газу (від 50 % до 10 % N_2) та за двох електричних конфігурацій: з додатковим зміщеним анодом (+200 В) і зі стандартним заземленим анодом. Результати рентгеноструктурного аналізу в поєднанні з якісною та кількісною оптимізацією показали, що покриття мають складну гетерофазну структуру, утворену гексагональною фазою hcp-WN та кубічною фазою fcc-W_2N. Встановлено, що стійке домінування фази hcp-WN з високо стабільною текстурою (111) відіграє роль жорсткого енергетично вигідного каркаса в усьому діапазоні співвідношень газових потоків. Зменшення вмісту азоту насамперед впливає на вторинний, більш структурно податливий компонент кубічної фази. За критичного дефіциту азоту (10 %) зростання пріоритетно орієнтованих кубічних площин (200) істотно пригнічується, що призводить до подрібнення зерен матриці (нанокристалізації) та стимулює структурну інтеграцію змішаної фазової конфігурації (220)fcc + (102)hcp. Крім того, застосування конфігурації з заземленим анодом призводить до зникнення зони допоміжного тліючого розряду та зниження густини плазми поблизу підкладки з $7{,}5\times10^{10}$ $см^{-3}$ до 4×10^{10} $см^{-3}$. Внаслідок цього скорочується довжина поверхневої дифузії адатомів, що спричиняє швидке термічне загартування структури, повну втрату текстурованості, різке чотириразове зростання інтенсивності ізотропного рефлексу (111)fcc + (100)hcp та накопичення структурно недосконалих міжфазних границь. Застосування допоміжного зміщеного анода є ефективним інструментом для розділення руйнівного впливу високоенергетичного іонного бомбардування та позитивного ефекту структурного впорядкування, індукованого високоінтенсивною низькоенергетичною плазмовою активацією.

Ключові слова: *магнетронне розпилення; нітриди; вольфрам; рентгенівська дифракція; фаза; структура; потік газу*

EAST EUROPEAN JOURNAL OF PHYSICS. 3. 689-702 (2026)
DOI:10.26565/2312-4334-2026-3-65 ISSN 2312-4334

NONDESTRUCTIVE ULTRASONIC EVALUATION OF TEMPERATURE-DEPENDENT MECHANICAL AND ELASTIC PROPERTIES OF PbX (X = S, Se) COMPOUNDS

Sudhanshu Tripathi[1], Praveen Singh[2], Anurag Singh[2,3], Devraj Singh[2], R. Khenata[4,5*], M. Boudjelal[4], H. Meradji[6], Ajit Kumar Maddheshiya[7], Shanay Rab[8], M. Faizan[9], S. Bin-Omran[10]**

[1]Amity Institute of Information Technology, Amity University, Sector-125, Noida – 201313, U.P., India
[2]Department of Physics, Prof. Rajendra Singh (Rajju Bhaiya) Institute of Physical Sciences for Study and Research, Veer Bahadur Singh Purvanchal University, Jaunpur-222003, U.P., India
[3]Department of Physics, Government Degree College, Babhani, Sonbhadra-231208, U.P., India
[4]Laboratoire de Physique Quantique de la matière et de Modelisation Mathematique (LPQ3M), Universite de Mascara, Mascara, 29000, Algeria
[5]Algerian Academy of Sciences & Technologies, 04- Path of Peace, Hydra- Algiers16000, Algeria
[6]Laboratoire LPR, Département de Physique, Faculté des Sciences, Université Badji Mokhtar, Annaba, Algeria
[7]Department of Physics, University of Allahabad, Prayagraj-211002, India
[8]School of Architecture, Technology and Engineering, University of Brighton, BN24AT, UK
[9]School of Materials Science and Engineering, Jilin University, Changchun, 130012, China
[10]Department of Physics and Astronomy, College of Science, King Saud University, P.O. Box 2455, Riyadh, 11451, Saudi Arabia
**Corresponding Author email: khenata_rabah@yahoo.fr; rabah_khenata@univ-mascara.dz; **Email: somran@ksu.edu.sa*
Received April 16, 2026; revised July 29, 2026; accepted August 2, 2026

A comprehensive investigation of the elastic, mechanical, and thermo-acoustic properties of lead monochalcogenides PbX (X = S, Se) has been carried out along the principal crystallographic directions ⟨100⟩, ⟨110⟩ and ⟨111⟩ within the temperature range of 0-300 K using the ultrasonic non-destructive evaluation method. The second- and third-order elastic constants (SOECs and TOECs) were computed using the Coulomb and Born–Mayer potential frameworks, confirming the elastic stability of the materials under study. Derived mechanical parameters and ultrasonic velocities were obtained from SOECs, indicating brittle mechanical behavior based on Pugh's ratio. At 300 K, the Debye temperature, Debye velocity, lattice thermal conductivity, acoustic nonlinearity parameter, and ultrasonic attenuation coefficient were evaluated along the studied orientations. Among all the directions, the ⟨111⟩ orientation exhibited the highest Debye temperature and Debye velocity. The dominant mechanism of ultrasonic attenuation was identified as Akhiezer-type, emphasizing its relevance in thermal dissipation and acoustic damping. The findings suggest that PbSe possesses superior elastic stiffness, whereas PbS exhibits enhanced thermal conductivity and stronger phonon interactions. These characteristics underscore the potential of PbS and PbSe for applications in thermoelectric and ultrasonic sensing technologies.
Keywords: *Lead monochalcogenides; Elastic properties; Mechanical constants; Thermal conductivity; Ultrasonic attenuation*

1. INTRODUCTION

To meet the growing global demand for energy, researchers are increasingly focusing on renewable energy sources, including solar energy, biofuels, wind energy, thermoelectric power, and fuel cells. Among the materials explored for these applications, lead-based chalcogenides, especially lead sulfide (PbS) and lead selenide (PbSe), have gained significant recognition in both fundamental research and practical applications due to their distinctive properties [1]. In terms of theoretical and experimental studies, the work of Zhang et al. [2] has provided important insights into the anharmonic properties of lead chalcogenides. Using density functional theory (DFT) and first-principles calculations, their research elucidates the complex interplay between phonon interactions and thermal transport properties in these materials. This foundational work underscores the importance of a detailed understanding of both the electronic and photonic contributions to the overall performance of thermoelectric materials. These materials are important in a variety of high-technology applications, including thermoelectric devices, infrared detectors, and photovoltaic cells [3]. The unique properties of PbX (X: S,Se), such as their narrow bandgap, high carrier mobility, and low thermal conductivity, make them ideal candidates for these applications [4]. Kang and Wise [5] also studied the optical properties and electronic structure of lead sulfide and lead selenide quantum dots. The elastic properties of PbX materials are crucial for understanding their mechanical stability and potential for device integration. Tripathi et al. [6] have investigated the non-linear elastic and acoustic properties of PbTe and found that the ultrasonic attenuation is lowest at 100K which is a highly stable condition. Thermophysical properties, including thermal expansion and thermal conductivity, are equally important for applications where thermal management is crucial. PbS and PbSe exhibit interesting thermal behavior, which is essential for optimizing their performance in thermoelectric applications [7]. Studies have shown that ultrasonic attenuation in chalcogenide materials varies with temperature and frequency, providing the potential for their use in temperature-sensitive

Cite as: S. Tripathi, P. Singh, A. Singh, D. Singh, R. Khenata, M. Boudjelal, H. Meradji, A.K. Maddheshiya, S. Rab, M. Faizan, S. Bin-Omran, East Eur. J. Phys. 3, 689 (2026), https://doi.org/10.26565/2312-4334-2026-3-65

applications [8]. Recent advances in the study of lead chalcogenides have provided even greater insight into their thermal, mechanical, and electronic properties. Skelton et al. [9] carried out first-principles investigations into the thermophysical properties of PbX, focusing on their lattice dynamics and temperature-dependent behaviour. Their study provided important insights into phonon softening, a phenomenon crucial for understanding the temperature dependence of thermal conductivity, which has a major impact on the thermoelectric performance of these materials. By modeling phonon-phonon interactions, the research highlights the ability of PbSe and PbTe to maintain high thermoelectric performance at high temperatures. Anwar et al. [10] explored the influence of synthesis conditions, particularly the bath temperature, on the structural and thermoelectric properties of PbSe thin films. The study found that higher temperatures during chemical bath deposition improved the crystallinity and particle size of the PbSe films, leading to better thermoelectric performance. This finding underscores the importance of controlled synthesis processes in optimizing the functional properties of PbSe for practical applications in energy conversion technologies. Chen et al. [11] demonstrated that the synthesis medium directly affects the size and morphology of PbSe nanostructures, with nanorods exhibiting superior electrochemical properties compared to other morphologies. The study also highlights the importance of structural stability in nanostructures for energy storage and conversion applications, demonstrating that smaller nanostructures exhibit better electrochemical performance, thereby further strengthening the role of PbSe in next-generation energy technologies. Jahromi and Moaddeli [12] used density functional theory to study the band structure of PbS, revealing its potential for ultraviolet photoconductive devices. The study highlights the wide applicability of PbS, which has traditionally been used in infrared technologies but is now being considered for ultraviolet applications as well, highlighting its versatility. Abe [13] observed phase transformations between PbS and PbSe during thin-film deposition, revealing significant changes in the crystalline structure that affect the material's optical properties. This transformation from PbS to PbSe during film deposition suggests new possibilities for tuning the material's properties through controlled synthesis. As studied by Bandoh et al. [14], annealing of PbSe films improved both optical and structural properties, increasing crystallite size and reducing lattice defects. This improvement in material quality translates into enhanced performance in optoelectronic devices, where crystal structure and purity are crucial to the device's efficiency. Nanocrystalline PbS thin films, as investigated by Bayisa et al. [15], were also shown to exhibit excellent optical and structural properties, with the size of the crystallites increasing as the film thickness was varied. These findings suggest that controlling the film thickness during deposition can improve the material properties, thereby enhancing the performance of PbS-based devices. Recent research has also focused on developing PbSe-based multifunctional devices. Khusayfan et al. [16] successfully produced PbSe thin films for use in photovoltaic devices, microwave resonators, and X-ray sensors. Their work highlighted the adaptability of PbSe for various high-tech applications, especially wireless communication technologies such as 5G. The structural and optical properties of PbSe thin films make them ideal for use in next-generation devices, demonstrating the material's versatility. Yang et al. [17] developed a novel electrochemical synthesis method to fabricate hierarchically porous PbSe films, which showed excellent infrared photodetection properties. These porous structures provide a large surface area, thereby improving the material's photoconductive sensitivity and making it highly effective for infrared detection at room temperature. This advancement opens new doors for the use of PbSe in low-cost, high-performance photodetectors.

The limited exploration of ultrasonic attenuation in PbX compounds motivated a detailed investigation employing ultrasonic non-destructive evaluation techniques. This study presents a systematic analysis of the anisotropic and temperature-dependent elastic, mechanical, thermal, and acoustic properties of PbX (X = S, Se) across principal crystallographic directions and within the temperature range of 0–300 K. The results provide critical insights into the behavior of these materials under varying thermal and structural conditions, emphasizing their potential relevance in industrial and functional applications. The calculated parameters are benchmarked against established data to validate the reliability of the theoretical framework, which is grounded in the Born–Mayer interaction potential model.

2. COMPUTATIONAL APPROACH

2.1 Nonlinear Elastic Behavior: SOECs and TOECs

SOEC and TOEC serve as important links between mechanical properties and dynamic behavior in crystalline materials. We have estimated the temperature-dependent SOECs and TOECs using the methodology proposed by Brugger [18]. The potential used to evaluate these elastic constants is obtained by combining the electrostatic and repulsive potentials.

$$F\ (\mathrm{r}) = F^{C}(\mathrm{r}) + F^{B}(\mathrm{r}). \tag{1}$$

The Born Mayer / repulsive potential, $F^{C}(\mathrm{r})$ and $F^{B}(r)$ are prearranged as

$$F^{C}(r) = \pm\left(\frac{e^{2}}{r}\right) \text{ and } F^{B}(r) = Aexp\left(\frac{-r}{b}\right). \tag{2}$$

Here, b characterizes the stiffness parameter, r denotes the distance between nearest-neighbour atoms, e refers to the electronic charge, and A corresponds to the interaction strength factor [18].

The lattice dynamics framework has been proposed by Leibfried and Ludwig [19], Ghate [20], Mori and Hiki [21] and the lattice energy is found to vary with temperature. Combining the static and vibrational part SOECs and TOECs ($C_{ij}$and C_{ijk}) can be defined as

$$C_{ij} = C_{ij}^{0} + C_{ij}^{vib} \quad \text{and} \quad C_{ijk} = C_{ijk}^{0} + C_{ijk}^{vib} \tag{3}$$

Here, the superscript '*vib*' indicates the vibrational component of SOECs and TOECs at elevated temperature and '*0*' depicts the static component at 0K. The formulae for computing the C_{ij} and C_{ijk} are given in literature [22].

2.2 Mechanical Parameters

The SOECs were used to estimate the mechanical parameters [23] like bulk modulus (B), shear modulus (G), Young's modulus (E), Tetragonal modulus (Cs), shear modulus (G), Cauchy pressure (C_P), Zener anisotropic factor (Z_A), Pugh's indicator (B/G) and Poisson's ratio (ν) [23] and their values are placed in Table 1.

Table 1. The formulae for the mechanical parameters of PbX

$B = \frac{(C_{11}+C_{12})}{3}$	$G = \frac{(C_{11}-C_{12}+3C_{44})}{10} + \frac{2.5(C_{11}-C_{12})C_{44}}{4[C_{44}+3(C_{11}-C_{12})]}$
$E = \frac{9GB}{G+3B}$	$Cs = \frac{C_{11}-C_{12}}{2}$; $C_p = C_{12} - C_{44}$
$Z_A = \frac{2C_{44}}{C_{11}-C_{12}}$	$\nu = \frac{3B-2G}{6B+2G}$

2.3 The Nonlinearity Parameter

The transmission of ultrasonic waves through a solid medium leads to waveform distortion, primarily influenced by the material's microstructural features. The acoustic nonlinearity parameter quantifies this effect and is defined as the negative ratio of the nonlinear to the linear terms in the finite-amplitude longitudinal wave equation, evaluated along various crystallographic directions. Breazeale's nonlinearity constant, which captures this behavior, is expressed as a linear combination SOECs and TOECs, and is given by:

$$\beta = -(3K_2 + K_3)/K_2$$

where K_2 and K_3 depends on SOECs and TOECs. The detailed expression of K_2 and K_3 are described in literature [6].

2.4 Direction-Dependent Ultrasonic Velocities

The three modes of ultrasonic wave velocities described due to ultrasonic wave propagation are namely one longitudinal (V_L), and two transverse modes namely quasi-shear (V_{S2}) and shear (V_{S1}) velocities respectively, propagating along different crystallographic orientations [24]. Due to crystal symmetry, the two shear modes degenerate along $\langle 100 \rangle$ and $\langle 111 \rangle$ directions, polarised along $\langle 100 \rangle, \langle 001 \rangle, \langle 1\bar{1}0 \rangle$ and $\langle \bar{1}10 \rangle$ planes. The formulae for these velocities are described in literature [24]. The average of these velocities defined at Debye average velocity (V_D) given as

$$V_D = \left[\frac{1}{3}\left\{\frac{1}{{V_L}^3} + \frac{1}{{V_{S1}}^3} + \frac{1}{{V_{S2}}^3}\right\}\right]^{-\frac{1}{3}} \tag{4}$$

2.5 Thermoacoustic Properties

Another important parameter that describes the material thermophysical characteristics is Debye temperature (θ_D) which depends on material parameters and Debye velocity [25] given as

$$\theta_D = \frac{h}{k_B}\left(\frac{3nN\rho}{4\pi M}\right)^{\frac{1}{3}} V_D \tag{5}$$

Where h, k_B, n, N, ρ, M and V_D are Planck constant, Boltzmann constant, number of atoms per unit cell, Avogadro number, density of substance, molecular weight of substance and Debye average velocity, respectively.

The thermal conductivity κ is directly influenced by Debye temperature θ_D [26] given as

$$\kappa = \frac{AM\delta T_D^3 n^{1/3}}{\gamma^2 T} \tag{6}$$

Where A = 3.04×10^{-8}; M is defined as average atomic mass in amu; δ (in Å) is the cube root of volume per atom; γ is the Grüneisen parameter calculated in different directions of ultrasonic wave propagation within the temperature regime 0-300K.

Thermal relaxation time τ_{th} [27] determined as the time taken by phonon particles to regain thermal equilibrium given as

$$\tau_{th} = \frac{1}{2}\tau_L = \tau_S = \frac{3\kappa}{C_V V_D^2} \tag{7}$$

Where C_V represents the specific heat at constant volume, calculated with the help of the AIP Handbook [28]. The transformation of thermal to acoustic energy defined as the acoustic coupling constant [29] is given as

$$D = 9\langle (\gamma_i^j)^2 \rangle - \frac{3\langle \gamma_i^j \rangle^2 \rho c_V T}{E_0} \tag{8}$$

The propagation of ultrasonic waves through matter can be used to provide details about it. The details provided by the wave are related to amplitude and phase, yet they can be interpreted to reveal many features within matter. When

ultrasonic waves are generated and propagate within a material, energy is lost due to scattering, absorption, and the difference in acoustic impedance of two different materials at their interface [30].

The factors affecting the ultrasonic attenuation coefficient in an ideal crystal are thermoelastic relaxation mechanism (TRM), phonon-phonon interaction (PPI), and electron-phonon interaction (EPI). The thermal attenuation caused during the maintenance of the equilibrium process for the transfer of energy between compressed and rarefied region when the ultrasonic wave passes through the crystal [31,32], defined as

$$\left(\frac{\alpha}{\nu^2}\right)_{\text{th}} = \frac{4\pi^2 < \gamma_i^j >^2 kT}{2\rho V_L^5}. \tag{9}$$

The ultrasonic attenuation resulting from p-p interactions, applicable to both longitudinal and shear waves under defined conditions, is given as follows: $\omega\tau \ll 1$ (where τ denotes the thermal relaxation time and ω represents the angular frequency) is [33].

$$\left(\frac{\alpha}{\nu^2}\right)_l = \frac{4\pi^2 \tau_{th} E_0 \, (D_L/3)}{2\rho V_L^3}. \tag{10}$$

$$\left(\frac{\alpha}{\nu^2}\right)_s = \frac{4\pi^2 \tau_{th} E_0 \, (D_S/3)}{2\rho V_S^3}. \tag{11}$$

Here E_0 represents the thermal energy density obtained from the AIP handbook, while V_L and V_S represent the velocities for the longitudinal and shear modes of propagation, respectively.

3. RESULTS AND DISCUSSION

The SOECs and TOECs for PbS and PbSe in the temperature range of 0 to 300 K are evaluated using the lattice parameter obtained from literature [2,34] and hardness parameters (b = 0.303Å) for PbS and PbSe [35]. The SOECs and TOECs are affected by both the anharmonic lattice vibrations and thermal expansion coefficient [36]. The obtained values of SOECs and TOECs for PbX are listed in Table 2.

Table 2. SOECs and TOECs of PbX [in (GPa)]

Temp. (K)	Material	C_{11}	C_{12}	C_{44}	C_{111}	C_{112}	C_{123}	C_{144}	C_{166}	C_{456}
0		93.92	11.28	11.28	-1198.5	-39.05	16.84	16.84	-39.05	16.84
50		97.66	10.80	10.90	-2022.3	-37.18	14.31	16.88	-39.16	16.84
100		98.56	10.33	10.86	-2021.5	-35.59	11.77	16.85	-38.98	16.84
150		99.93	9.83	10.82	-2026.2	-33.81	9.20	16.83	-38.82	16.84
200	PbS	101.39	9.32	10.76	-2032.1	-31.96	6.61	16.78	-38.86	16.84
300		104.43	8.30	10.64	-2045.7	-28.22	1.42	16.68	-38.20	16.84
0		100.86	13.08	13.08	-2089.8	-45.53	19.29	19.29	-45.53	19.29
50		103.89	12.61	12.64	-2116.4	-43.85	16.82	19.34	-45.63	19.29
100	PbSe	105.19	12.10	12.60	-2119.7	-42.11	14.28	19.32	-45.46	19.29
150		106.71	11.57	12.54	-2125.8	-40.24	11.71	19.28	-45.25	19.29
200		108.29	11.03	12.48	-2132.7	-38.33	9.13	19.22	-45.01	19.29
300		111.34	9.92	12.30	-2145.1	-34.36	3.89	19.05	-44.37	19.29

As shown in Table 2, the longitudinal elastic constant C_{11} increases with temperature, while the compression coefficient C_{12} and elastic constant C_{44} decrease with increasing temperature. The elastic constant C_{44}, which is responsible for the shear modulus perpendicular to the applied stress, is slightly decreasing with temperature. From the increasing C_{11} and decreasing C_{12}, C_{44}, it can be inferred that the selected PbX becomes stiffer and softer at higher temperatures. Cauchy's criterion for isotropic cubic crystals is derived from the assumption that the internal forces of the material are perfectly central and the material is stress free. The Cauchy criteria $C_{12}^0 = C_{14}^0$, $C_{112}^0 = C_{166}^0$, $C_{123}^0 = C_{144}^0 = C_{456}^0$. [37] proposed by Cousin [38] are valid at absolute 0K, for PbS and PbSe but fail at higher temperatures, which implies that at 0K the interaction forces are central but have increasing ionic character as the temperature increases. The TOECs estimated using the theory proposed by Brugger [18] and are utilized to analyze the acoustical and thermal phonon interactions and other anharmonic properties of the material under examination. It is obvious from Table 2 that the magnitude of C_{111} is decreasing with increasing temperature, while the magnitude of C_{112}, C_{123} and C_{166} are increasing with temperature. The elastic constant C_{144} is nearly constant due to the small effect of the vibrational part, while C_{456} is constant at every temperature due to the absence of vibrational energy. The TOECs pattern of PbX (X: S,Se) are similar to that of lead telluride [6] and tin monochalcogenides [38].

Figure 1 depicts the deviation plot for SOECs of the present work with previously reported values by experimental and theoretical methods [2, 39, 40]. The variation of SOECs obtained in the present work relative to previously reported values in the literature is ≈ ±10%, due to differences in the computational approach. The observed variations in elastic constants as depicted in Fig. 1, with previously reported values are due to their dependency on temperature-dependent lattice parameters, anharmonic phonon contribution and thermal expansion effect which is linked through the Grüneisen

parameters which connect the mechanical (elastic) and thermal properties of a crystalline solid. The elastic constants at elevated temperatures can be attributed to the increased contribution of vibrational energy. This implies that, with rising temperature, atomic interactions and the corresponding interaction potentials within the crystal lattice are modified due to the influence of non-central forces. Consequently, a comprehensive understanding of the temperature dependence of elastic constants is essential for accurately predicting the effects of thermal conditions on a material's mechanical strength, stiffness, and the interatomic force dynamics across adjacent crystallographic planes. The Born stability criterion,$\{[(C_{11}+2C_{12})/3]>0;\ C_{44}>0;\ [(C_{11}-C_{12})/3]>0\}$is satisfactorily fulfilled by the obtained values of elastic constants.

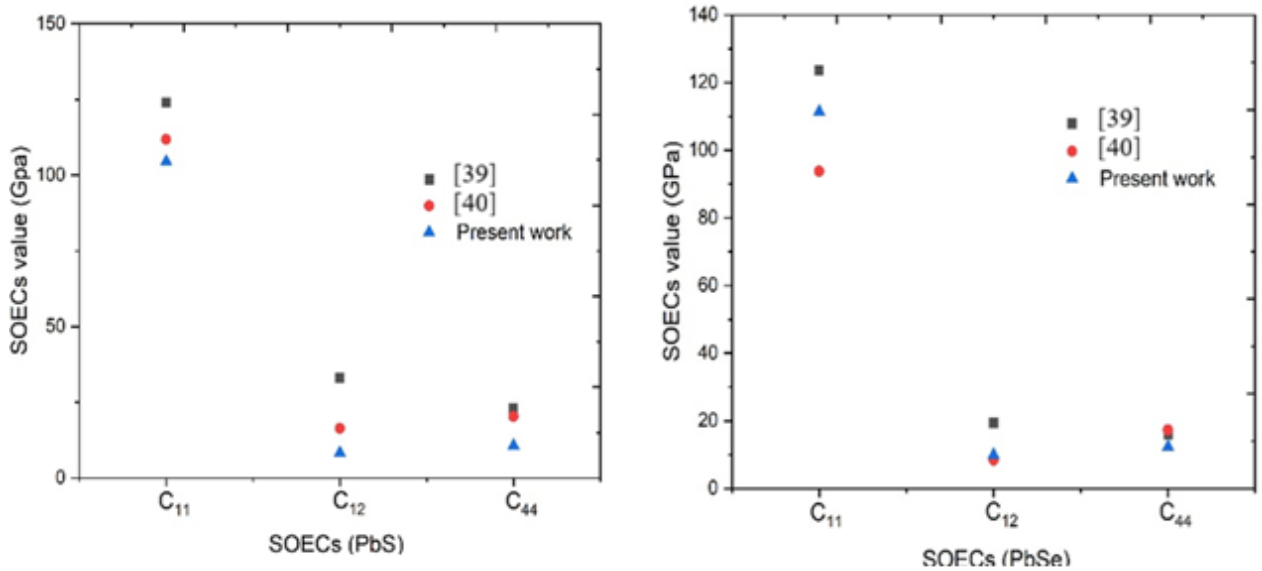

Figure 1. Deviation plot for SOECs of PbS and PbSe

Therefore, while PbX (X: S,Se) is confirmed to be mechanically stable under the Born criterion, it remains imperative to analyze the evolution of its mechanical parameters with temperature to assess its suitability for high-temperature applications. To analyze the mechanical properties of PbX (X: S, Se), various mechanical parameters are calculated for PbS and PbSe using the expressions defined in Table 1, within the temperature regime 0–300K and are depicted in Table 3.

Table 3. The mechanical parameters of PbX (X; S,Se)

Material	Temp. (K)	*E* (GPa)	*B* (GPa)	*B** (GPa)	*G* (GPa)	*B/G*	Z_A	*ν*	*Hv*	C_P (GPa)	C_S (GPa)
PbS	0	50.34	38.83	54.6	19.60	1.66	0.27	0.28	3.27	0	41.32
	50	50.82	39.75	53.6	19.74	1.66	0.26	0.28	3.31	-0.10	43.43
	100	51.06	39.74	51.6	19.85	1.64	0.25	0.28	3.41	-0.53	44.16
	150	51.46	39.86	49.5	20.02	1.62	0.24	0.28	3.53	-0.98	45.04
	200	51.86	40.04	47.2	20.19	1.60	0.23	0.28	3.65	-1.43	46.03
	300	52.67	40.34	42.3	20.53	1.57	0.22	0.28	3.88	-2.34	48.06
PbSe	0	55.81	42.34	48.4	21.79	1.66	0.29	0.28	3.67	0	43.88
	50	55.99	43.04	47.6	21.82	1.66	0.28	0.28	3.68	-0.03	45.64
	100	56.38	43.13	46.2	21.98	1.64	0.27	0.28	3.79	-0.49	46.53
	150	56.81	43.28	44.7	22.16	1.63	0.26	0.28	3.91	-0.96	47.56
	200	57.23	43.45	43.1	22.34	1.61	0.25	0.28	4.03	-1.44	48.62
	300	57.96	43.73	39.9	22.65	1.58	0.24	0.27	4.26	-2.37	50.71

*Ref [2]

As depicted in Table 3, Young's modulus, responsible for the stiffness of the material, is increasing with an increase in temperature for PbX (X: S, Se), and the value of for PbSe is higher than PbS. Thus, PbSe is stiffer than PbS, which is highest at 300 K. The obtained values of *E* for PbX (X: S, Se) are nearly similar to those reported by Seetawan et al. [41] at 300 K using the molecular dynamics method. The bulk modulus indicates a material's resistance to changes in volume. PbS is more compressible than PbSe, which is highest at 300 K for PbX. The reported values of *B* for PbS are 62.8 GPa by experimental method [39] and equal 55.7 GPa and 65.6 GPa, calculated by GGA and LDA methods [2], respectively. As depicted in Table 3, the estimated value of *B* in the present work at 300 K is 40.34 GPa, indicating deviations of 5.4% to 19% due to differences in the approach used.

Modulus of rigidity (*G*) represents the behaviour of the material to resist change in size and shape. In the present study, *G* values increase with increasing temperature for selected PbX (X: S, Se). As the reported values of *Cs* and

Shear modulus for PbSe are higher than those of PbS at 300K, as depicted in Table 3, it indicates that PbSe is stiffer and harder than PbS, as it resists deformation more under both shear and elastic distortions. A similar result has been reported by Seetawan et al. [41] at elevated temperatures, which justifies our approach.

Pugh's index (B/G) compares fracture to toughness which measures the ductility and brittleness of materials. If the Pugh index is more than 1.75, then the selected compound is ductile; otherwise, it is brittle. It is evident from Table 3 that Pugh's ratio for both PbS and PbSe is less than 1.75, indicating that both materials are brittle at all temperatures examined in the present work. Poisson's ratio is an important variable for defining the behavior of intermolecular forces. The relation $0.5>\nu>0.2$ is valid for non-central forces and ionic values are around 0.25. In the present case as Table 3 shows, values are approximately 0.28 which satisfy the relation of non-central. Thus, the ν values predict that the inter-atomic forces are non-central and ionic in nature. For brittle materials, the Cauchy pressure is $Cp=(C_{12}-C_{44})$ <0 and the Poisson ratio is $\nu < 0.3$. Table 3 shows that Cp <0 and ν <0.3, which predicts that PbS and PbSe are brittle in nature, which validates our previous prediction (on the basis of Pugh's index) of the brittle nature of both materials in the present investigation. The Zener anisotropy index (Z_A) is a dimensionless quantity that measures the isotropy of a cubic crystal. For isotropic materials Z_A value is equal to 1. Table 3 shows that the Zener index is different from 1, which indicates that the selected PbX are anisotropic in the temperature range 0-300 K. Figure 2 presents the combined plot of the Cauchy pressure Cp/Y versus the G/B ratio for PbX (X: S, Se) over the temperature range of 0–300 K. The observed downward trend toward the lower right corner of the plot is attributed to the directional nature of bonding in the material, which promotes brittle behaviour, revealing the anticipated mechanical response based on theoretical predictions.

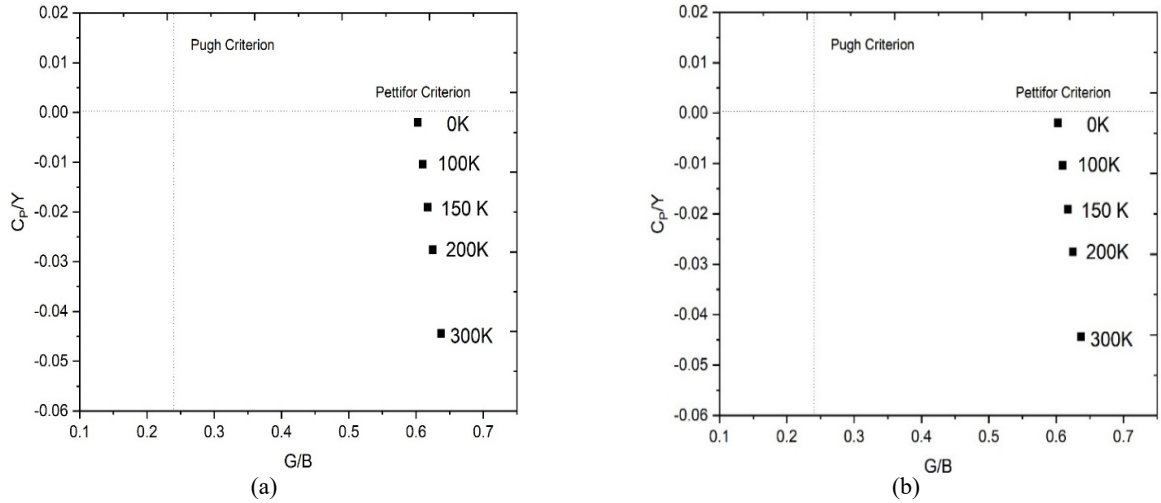

Figure 2. Renormalized Pugh and Pettifor criteria for (a) PbS, (b) PbSe within the temperature range 0-300K

The estimated SOECs and TOECs were utilized to compute the nonlinearity parameters $K2$ and $K3$ [6], which are subsequently used to evaluate the temperature-dependent Breazeale's nonlinearity parameter β across the temperature range of 0–300 K. The variation of β along different principal directions of wave propagation is illustrated in Fig. 3, highlighting the anisotropic nonlinear elastic behavior of PbX (X:S,Se) with respect to temperature.

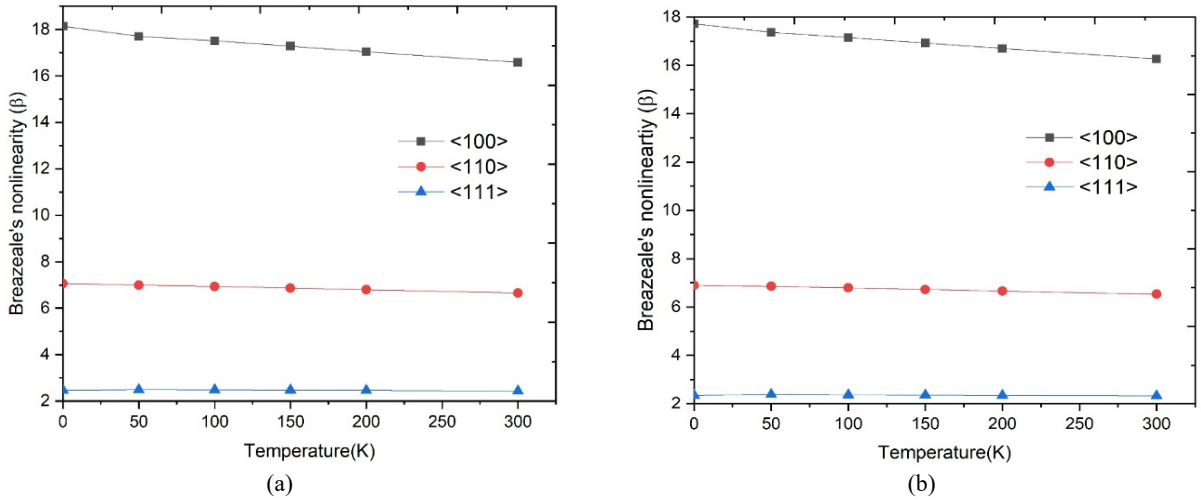

Figure 3. Orientation-dependent Breazeale's nonlinearity constant with temperature (a) PbS (b) (PbSe)

Figure 3 reveals that the maximum value of the nonlinearity parameter β is observed along the ⟨100⟩ crystallographic direction, while the minimum value is recorded along the ⟨111⟩ direction. Furthermore, it is evident that the nonlinear parameter β for PbX (X= S, Se) does not exhibit a consistent trend with increasing temperature, indicating a complex dependence on thermal effects. The nonlinearity parameter β does not remain uniform across different crystallographic orientations; however, a general linear decreasing trend in its value is observed as the temperature increases. Ultrasonic velocity measurements are employed to gain insights into the microstructural characteristics of the material.

To validate and extend our calculations, 3D visualizations showing the directional dependence of Young's modulus (E), bulk modulus (B), and shear modulus (G) are presented in Figs. 4,5, and 6 respectively. These visualizations also include their 2D projections on the (100), (010) and (001) planes. The calculations for B and G are based on established relations given in the literature [42], while the values of G are further elaborated using references from the literature [43].

$$\frac{1}{B} = (S_{11} + 2S_{12})(l_1^2 + l_2^2 + l_3^2) \tag{12}$$

$$\frac{1}{E} = S_{11} - 2\left(S_{11} - S_{12} - \frac{1}{2}S_{44}\right)(l_1^2 l_2^2 + l_2^2 l_3^2 + l_3^2 l_1^2) \tag{13}$$

$$\frac{1}{G} = S_{44} - 4\left(S_{11} - S_{12} - \frac{1}{2}S_{44}\right)(\sin^2\theta\cos^2\theta + 0.125\sin^4\theta)(1 - \cos 4\varphi) \tag{14}$$

Here, $S_{ij} = C_{ij}^{-1}$ denotes the elastic compliance matrix, which is obtained as the inverse of the elastic constant matrix. The terms l_1, l_2, and l3 denote the 3D directional cosines corresponding to the x-, y-, and z-axes, respectively.

A material is classified as isotropic if its 3D and 2D plots exhibit spherical and circular symmetries, respectively; deviation from these symmetries indicates anisotropy. As shown in Figs. 4, 5, and 6, the bulk modulus exhibits isotropic behavior, maintaining consistent spherical symmetry in its 3D representation. In contrast, both Young's modulus (E) and shear modulus (G) deviate significantly from spherical symmetry in their 3D diagrams and from circular symmetry in their 2D projections, highlighting their inherent anisotropic properties.

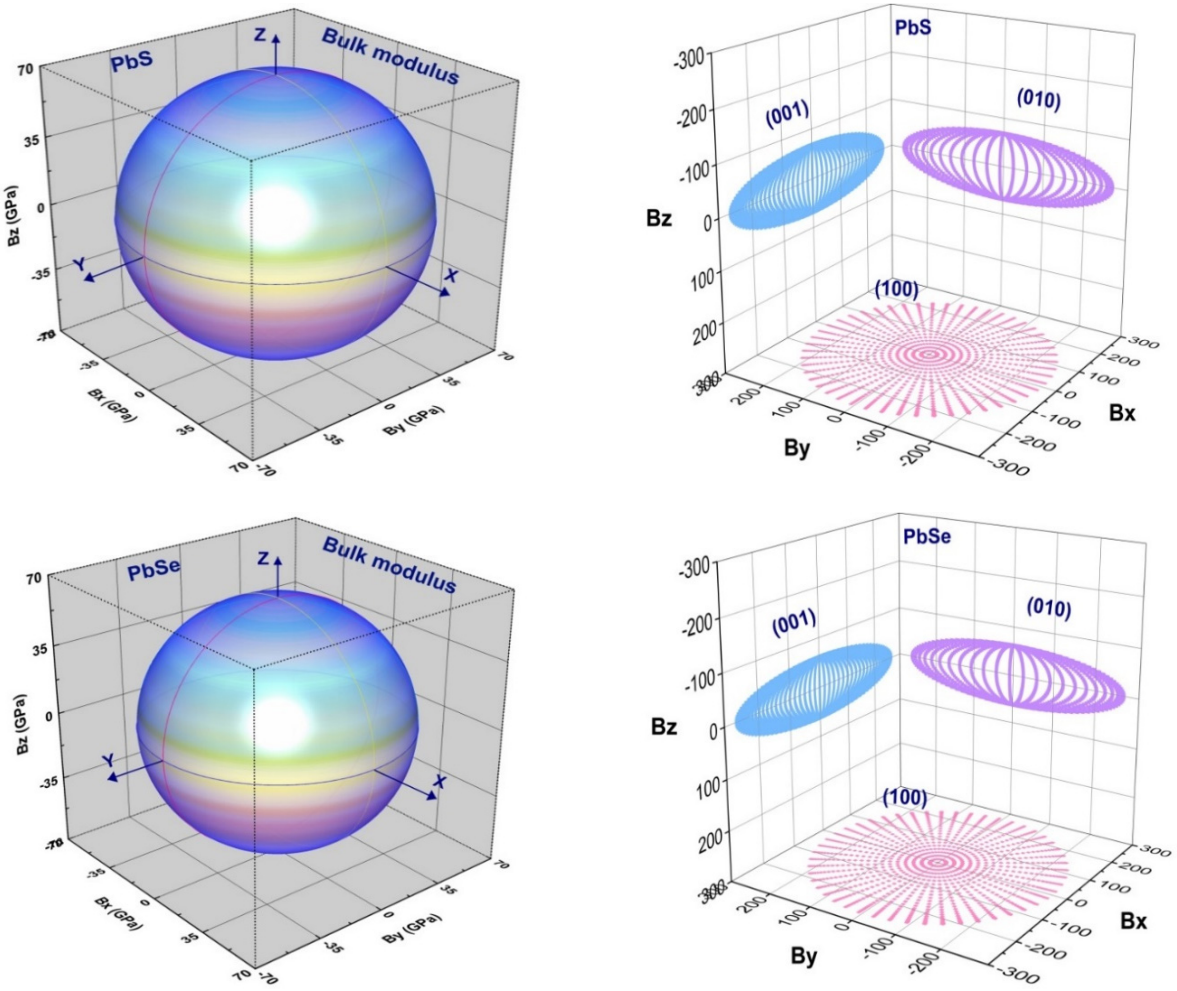

Figure 4. 3D-directional dependence of the bulk modulus (B, in GPa) for PbX and its projection in dissimilar planes

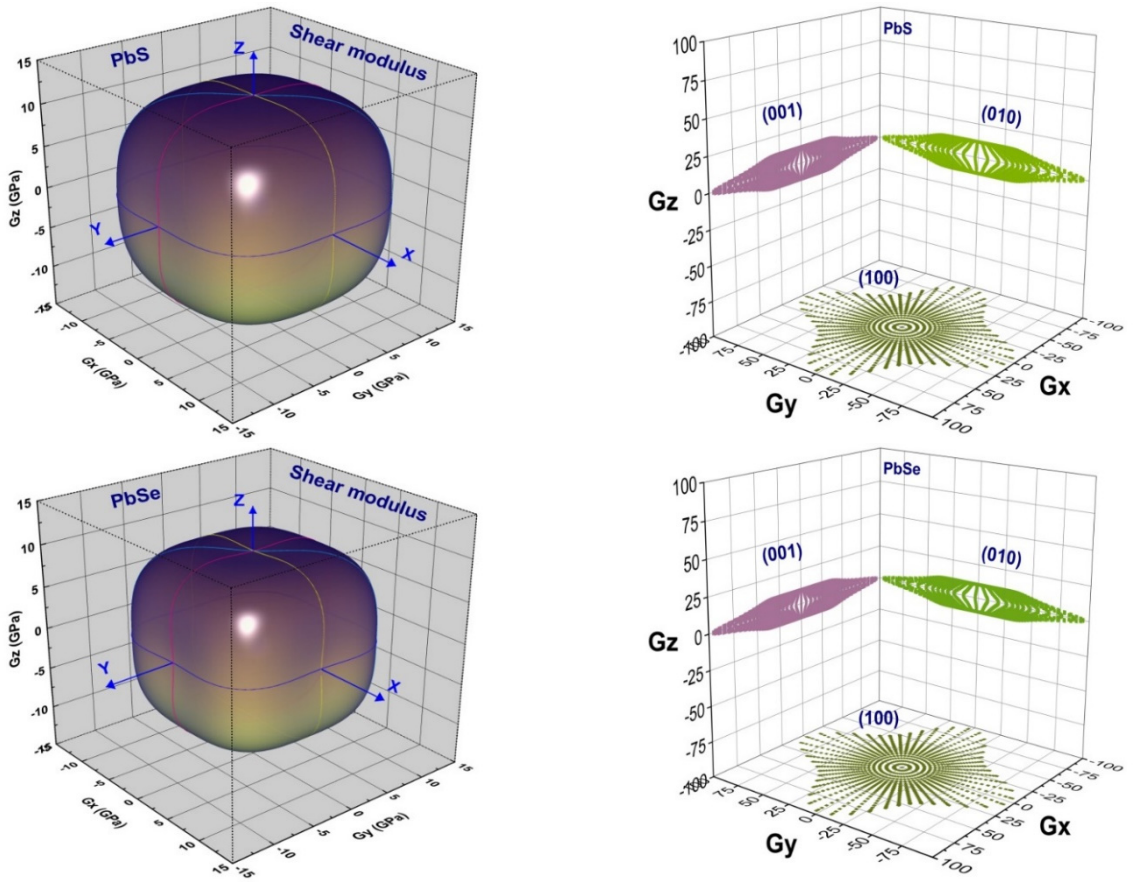

Figure 5. 3D-directional dependence of the shear modulus (*G*, in GPa) and its projections in dissimilar planes for PbX

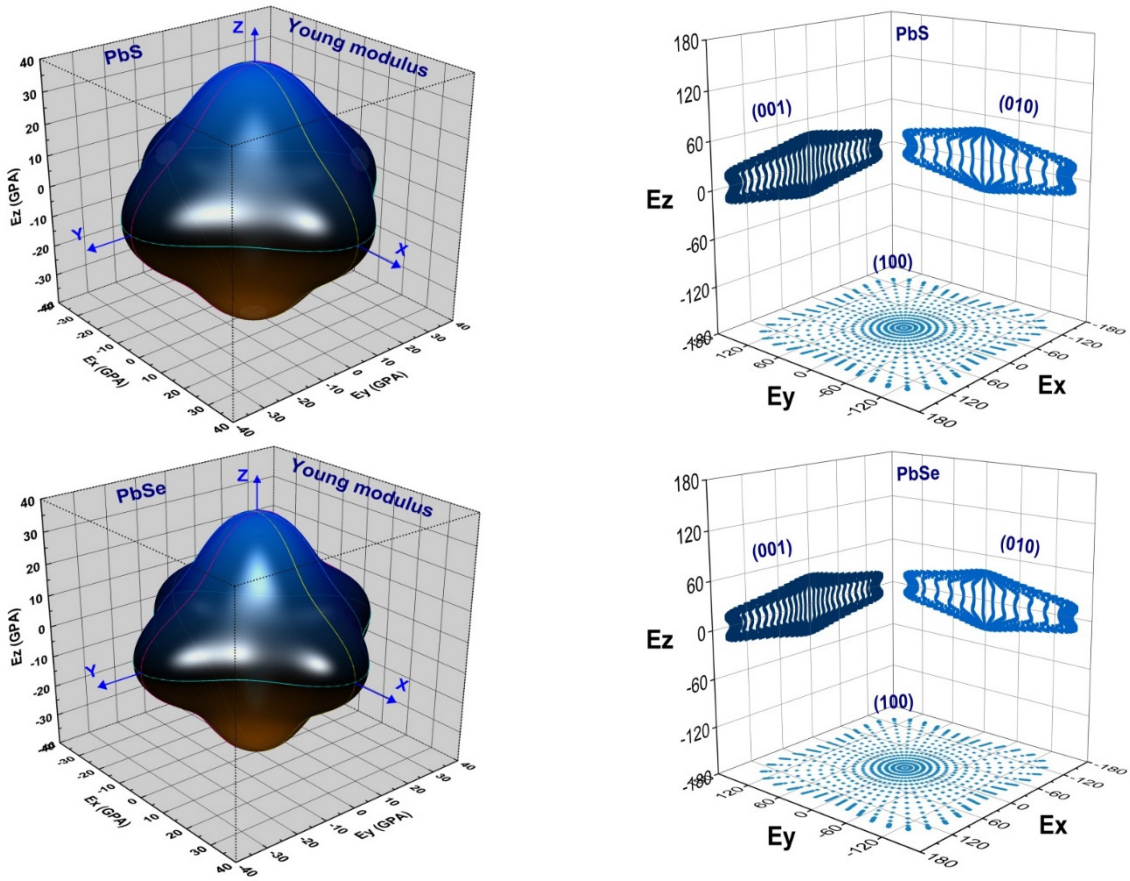

Figure 6. 3D-directional dependence of the Young's modulus (*E*, in GPa) and its projections in dissimilar planes for PbX

Ultrasonic velocity provides information about the microstructure, texture, and damage in materials [44]. The temperature-dependent ultrasonic velocities e.g., longitudinal ultrasonic velocity, shear ultrasonic velocity and quasi-shear ultrasonic velocity along the $\langle 100\rangle, \langle 110\rangle$and $\langle 111\rangle$ direction, with the direction of polarization along $\langle 100\rangle, \langle 001\rangle, \langle 1\bar{1}0\rangle$ and $\langle \bar{1}10\rangle$ are evaluated using SOECs and densities of PbX in the temperature range 0 - 300K are depicted in Table 4.

Table 4. Ultrasonic velocities (in 10^3m/s) of PbS and PbSe

Orientation	Temp.	PbS				PbSe			
	(K)	V_L	V_{S1}	V_{S2}	V_D	V_L	V_{S1}	V_{S2}	V_D
$\langle 100\rangle$	0	3.5107	1.2169	1.2169	1.3840	3.5255	1.2698	1.2698	1.4429
	50	3.5789	1.1964	1.1964	1.3616	3.5782	1.2485	1.2485	1.4197
	100	3.5963	1.1939	1.1939	1.3589	3.6003	1.2464	1.2464	1.4175
	150	3.6212	1.1916	1.1916	1.3565	3.6264	1.2435	1.2435	1.4104
	200	3.6475	1.1885	1.1885	1.3532	3.6531	1.2401	1.2401	1.4109
	300	3.7018	1.1820	1.1820	1.3462	3.7043	1.2313	1.2313	1.4015
$\langle 110\rangle$	0	2.8955	1.2169	3.2930	1.6883	2.9382	1.2698	3.2889	1.7546
	50	2.9237	1.1964	3.3760	1.6656	2.9560	1.2485	3.3539	1.7309
	100	2.9274	1.1939	3.4026	1.6631	2.9632	1.2464	3.3868	1.7293
	150	2.9362	1.1916	3.4384	1.6611	2.9724	1.2435	3.4240	1.7269
	200	2.9465	1.1885	3.4757	1.6582	2.9817	1.2401	3.4619	1.7239
	300	2.9653	1.1820	3.5516	1.6519	2.9981	1.2313	3.5353	1.7150
$\langle 111\rangle$	0	2.6590	2.0269	2.0269	2.1712	2.7144	2.0354	2.0354	2.1868
	50	2.6694	2.0679	2.0679	2.2086	2.7171	2.0662	2.0662	2.2143
	100	2.6674	2.0819	2.0819	2.2204	2.7179	2.0836	2.0836	2.2297
	150	2.6692	2.1010	2.1010	2.2370	2.7196	2.1032	2.1032	2.2470
	200	2.6709	2.1208	2.1208	2.2542	2.7214	2.1231	2.1231	2.2645
	300	2.6752	2.1611	2.1611	2.2890	2.7223	2.1614	2.1614	2.2974

Table 4 predicts that the longitudinal ultrasonic velocities for PbX dominate the shear velocities, suggesting that the compressional mode plays a key role in ultrasonic wave propagation. The longitudinal velocity for PbS is highest at 300 K and occurs along the along $\langle 100\rangle$ direction and remains almost constant along the $\langle 111\rangle$ direction in the 0-300 K temperature regime due to the dependence of velocity on the second order elastic constants. The shear velocity V_{S2} due to transverse propagation is highest for PbS with $\langle 110\rangle$ at 300 K. The Debye velocity is increasing with temperature, when the wave is propagating in $\langle 111\rangle$ direction and decreasing with temperature for other two directions of propagation for both PbS and PbSe. Pei and Liu [45] reported the longitudinal, transverse and average velocity for PbS 4.08×10^3 ms^{-1}, 1.84×10^3 ms^{-1}, 2.04×10^3 ms^{-1} respectively at 300K and for PbSe 3.82×10^3 ms^{-1}, 1.72×10^3 ms^{-1}, 1.91×10^3 ms^{-1} respectively at 300K. The obtained longitudinal, shear and Debye average velocities for PbS for ultrasonic wave propagating in $\langle 100\rangle$ direction is 3.70×10^3 ms^{-1}, 1.18×10^3 ms^{-1}, 1.34×10^3 ms^{-1} respectively and for PbSe is 3.70×10^3 ms^{-1}, 1.23×10^3 ms^{-1}, 1.40×10^3 ms^{-1} respectively at 300K. Hence the present investigated values of the wave velocities are comparable with the previous findings reported experimentally [45]. The slight variations in the wave velocities of present investigations observed may be due to the consideration of wave propagation in all three directions along the $\langle 100\rangle, \langle 110\rangle$and $\langle 111\rangle$ direction, with the direction of polarization along $\langle 100\rangle, \langle 001\rangle, \langle 1\bar{1}0\rangle$ and $\langle \bar{1}10\rangle$, however experimentally reported data have not considered the same and may also involve experimental errors during the measurement process.

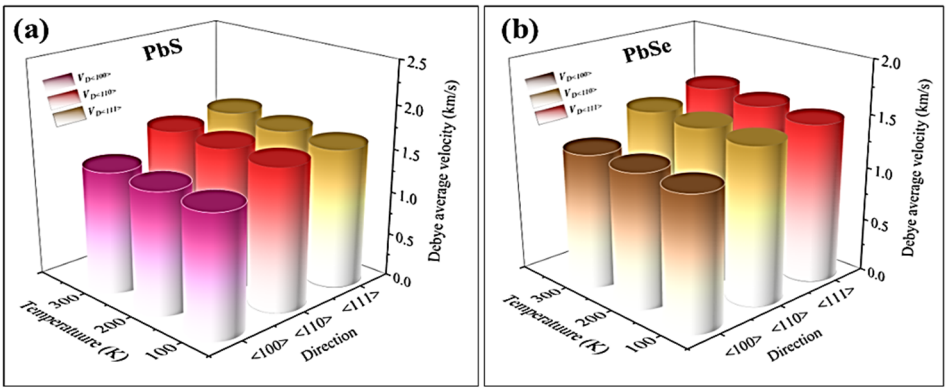

Figure 7. Debye average velocity in 100-300K temperature range along $\langle 100\rangle, \langle 110\rangle$ and $\langle 111\rangle$ for (a) PbS (b) PbSe

Table 4 and Fig.7 show that the Debye mean velocities are highest in the $\langle 111\rangle$ and lowest in the $\langle 100\rangle$ direction respectively. The Debye characteristic temperature of a solid material provides details about the vibration spectrum, elastic properties and thermodynamic properties of the material. It is the highest normal mode of oscillation of a

crystalline material and combines elastic properties such as thermal expansion, phonon dispersion, specific heat, thermal conductivity and lattice enthalpy [42]. The Debye temperature, as a bridge between elastic and thermal properties, is calculated by Eq. (5). The Debye temperature for PbS and PbSe is shown in Figures 8,9.

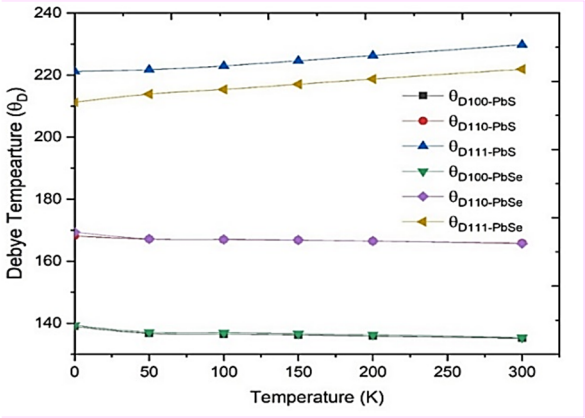

Figure 8. Debye temperature along ⟨100⟩, ⟨110⟩ and ⟨111⟩ for (a) PbS (b) PbSe

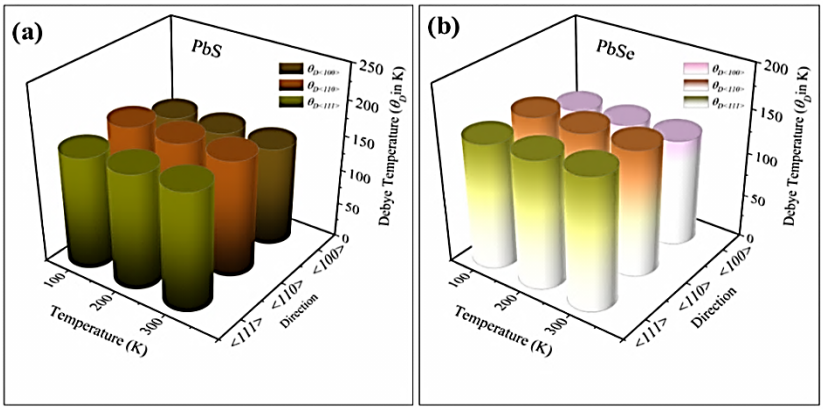

Figure 9. Debye average temperature in 100-300K temperature range along ⟨100⟩, ⟨110⟩ and ⟨111⟩ for (a) PbS (b) PbSe

Figure 9 shows that the Debye characteristic temperature for PbSe is lower than that for PbS because θ_D is inversely proportional to the cube of the molecular weight. The decreasing value of the Debye temperature as temperature increases is due to its dependence on the Debye velocity, which is a function of the second-order elastic constant. The Debye characteristic temperature is highest in the ⟨111⟩ direction, while it is lowest in the ⟨100⟩ direction for PbX. The Debye mean velocity is used to calculate the Debye characteristic temperature, which is used to estimate the thermal conductivity. The thermal conductivity is then used to calculate the thermal relaxation time, which is further used to calculate the nonlinearity parameter (acoustic coupling constant) and acoustic attenuation. The calculated values of thermal conductivity, nonlinearity parameter, and attenuation for PbS and PbSe are given in Tables 5 and 6, respectively. The thermal relaxation time along three crystallographic directions ⟨100⟩, ⟨110⟩ and ⟨111⟩ at 300K for PbS and PbSe is shown in Fig. 10.

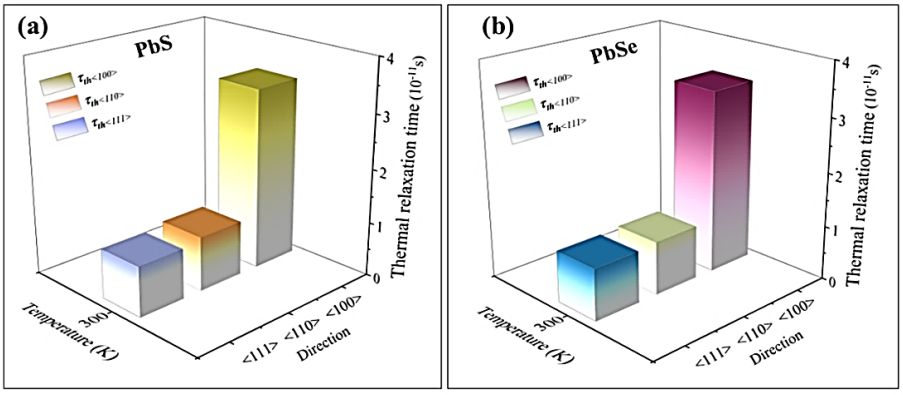

Figure 10. Thermal relaxation time at 300K along ⟨100⟩, ⟨110⟩ and ⟨111⟩ for (a) PbS (b) PbSe

Thermal conductivity is an indicator of thermal performance that is highest for PbS along the ⟨110⟩ direction at 300K. Thus, PbS along ⟨110⟩ has better thermal behavior than PbSe. Ultrasonic wave propagation through the material causes distortion in the phonon distribution. Wei et. al [46] reported the lattice thermal conductivity for PbS as 2.19 W/mK, while experimentally reported values are 2.52 W/mK, 2.38 W/mK, and 2.56 W/mK, respectively [45,47,48]. As depicted in Table 5, the thermal conductivity for PbS at 300 K under the present investigation is 3.84, 4.87, and 4.43 along the ⟨100⟩, ⟨110⟩ and ⟨111⟩ direction of wave propagation, respectively.

Table 5. κ(w/mK), D_L, D_{S1}, D_{S2}, $(\frac{\alpha}{\nu^2})_{th}$, $(\frac{\alpha}{\nu^2})_l$, $(\frac{\alpha}{\nu^2})_{S1}$, $(\frac{\alpha}{\nu^2})_{S2}$, $(\frac{\alpha}{\nu^2})_{total}$ ($\times 10^{-17}$ Nps^{2}m^{-1}) for PbS

Direction	Temp.	κ	D_L	D_{S1}	D_{S2}	$(\frac{\alpha}{\nu^2})_{th}$	$(\frac{\alpha}{\nu^2})_l$	$(\frac{\alpha}{\nu^2})_{S1}$	$(\frac{\alpha}{\nu^2})_{S2}$	$(\frac{\alpha}{\nu^2})_{total}$
⟨100⟩	50	3.78	32.12	1.023	1.023	0.01	16.79	7.166	7.166	31.141
	100	3.79	31.95	1.023	1.023	0.03	46.66	20.41	20.41	87.515
	150	3.80	31.39	1.022	1.022	0.04	77.38	35.36	35.36	148.14
	200	3.81	30.82	1.022	1.022	0.05	108.36	51.93	51.93	212.27
	300	3.84	29.74	1.021	1.021	0.07	163.64	86.38	86.38	336.47
⟨110⟩	50	4.74	39.85	0.622	62.77	0.16	28.57	3.257	14.61	46.593
	100	4.74	40.58	0.621	62.05	0.32	84.82	9.571	41.29	136.00
	150	4.79	40.32	0.619	61.28	0.45	147.05	16.90	69.59	233.99
	200	4.81	39.92	0.618	60.63	0.56	211.71	24.95	97.86	335.08
	300	4.87	39.07	0.615	59.62	0.73	342.60	42.58	152.16	538.07
⟨111⟩	50	4.30	28.19	40.23	40.23	0.33	11.67	17.91	17.91	47.823
	100	4.32	29.49	39.77	39.77	0.64	35.86	50.86	50.86	138.22
	150	4.35	29.18	39.26	39.26	0.92	63.28	87.29	87.29	238.78
	200	4.37	28.50	38.83	38.83	1.18	90.57	123.25	123.25	338.25
	300	4.43	26.91	38.13	38.13	1.64	141.83	190.62	190.62	524.71

Table 6. κ(w/mK), D_L, D_{S1}, D_{S2}, $(\frac{\alpha}{\nu^2})_{th}$, $(\frac{\alpha}{\nu^2})_l$, $(\frac{\alpha}{\nu^2})_{S1}$, $(\frac{\alpha}{\nu^2})_{S2}$, $(\frac{\alpha}{\nu^2})_{total}$ ($\times 10^{-17}$ Nps^{2}m^{-1}) for PbSe

Direction	Temp.	κ	D_L	D_{S1}	D_{S2}	$(\frac{\alpha}{\nu^2})_{th}$	$(\frac{\alpha}{\nu^2})_l$	$(\frac{\alpha}{\nu^2})_{S1}$	$(\frac{\alpha}{\nu^2})_{S2}$	$(\frac{\alpha}{\nu^2})_{total}$
⟨100⟩	50	3.56	30.84	1.003	1.003	0.016	20.36	7.801	7.801	35.978
	100	3.57	30.68	1.003	1.003	0.031	34.88	15.05	15.05	65.013
	150	3.58	29.53	1.002	1.002	0.043	59.00	24.83	24.83	108.71
	200	3.59	28.97	1.002	1.002	0.052	82.20	36.34	36.34	154.93
	300	3.61	27.92	1.001	1.001	0.067	125.16	61.12	61.12	247.46
⟨110⟩	50	4.43	36.88	0.619	58.61	0.1441	20.767	2.315	11.29	34.522
	100	4.45	39.54	0.618	57.74	0.2731	35.051	19.76	92.03	147.12
	150	4.47	37.37	0.616	56.92	0.3837	106.68	12.01	53.15	172.22
	200	4.50	36.96	0.614	56.20	0.4784	153.49	17.71	74.54	246.23
	300	4.55	36.15	0.610	55.11	0.6267	248.25	30.25	115.3	394.51
⟨111⟩	50	4.01	27.02	37.73	37.73	0.2582	9.3199	14.79	14.79	39.170
	100	4.03	31.40	37.17	37.17	0.4989	19.763	153.0	153.0	90.869
	150	4.05	27.99	36.65	36.65	0.7197	51.832	73.36	73.36	199.27
	200	4.08	27.34	36.18	36.18	0.9219	74.480	103.7	103.7	282.96
	300	4.12	25.75	35.45	35.45	1.283	112.46	154.7	154.7	423.14

The thermal relaxation time, τ_{th} for PbS and PbSe is of the order of 10^{-11} second, which confirms the semiconducting nature of the chosen materials [49]. τ_{th} is shortest along ⟨110⟩ and the highest along ⟨111⟩ as shown in Fig. 10, from which it can be inferred that the change in thermal energy to recover the phonon shape is faster along the ⟨110⟩ direction. The non-linearity parameter i.e. acoustic coupling constant is the parameter that quantifies the conversion of acoustic energy into thermal energy via the phonon interaction mechanism. The longitudinal coupling constant is higher in the ⟨110⟩ direction at 100K while the shear coupling constant is higher in the ⟨111⟩direction at 50K. The total coupling constant sum of longitudinal and shear coupling constants, is highest in the ⟨110⟩ direction, from which it can be inferred that the conversion of thermal to acoustic energy is highest in the ⟨110⟩ direction. The higher value of the coupling constant of PbS compared to PbSe shows that the conversion rate from thermal to acoustic energy is higher for PbS than for PbSe. It is clear from Table 5 that the loss due to the phonon-phonon (p-p) viscous process (Akheizer loss) dominates the thermal loss. The Ultrasonic attenuation due to the thermoelastic relaxation process is inversely proportional to the acoustic velocity [50].

Tables 5 and 6 clearly shows that ultrasonic attenuation caused by the thermoelastic relaxation mechanism is minimal compared to that from p-p interaction. This indicates that most of the ultrasonic energy loss happens as the system reaches equilibrium among different phonon branches and wave propagation directions. The similar values for ultrasonic attenuation among different directions of wave propagation reported previously [51] validate our findings and the approach we performed. The acoustic attenuation due to the thermoelastic relaxation process is largest in the ⟨111⟩ direction and smallest in the ⟨100⟩ direction for PbS and PbSe. The Akheizer damping at 300K is larger in the ⟨111⟩

direction and smaller in the ⟨100⟩ direction. Ultrasonic attenuation refers to the loss of energy in ultrasonic waves as they propagate through a material. It provides information on the microstructure, particle size, porosity, stress state and heterogeneity of the material. The total ultrasonic attenuation of PbS and PbSe is shown in Fig. 11 in the ⟨100⟩, ⟨110⟩ and ⟨111⟩ directions.

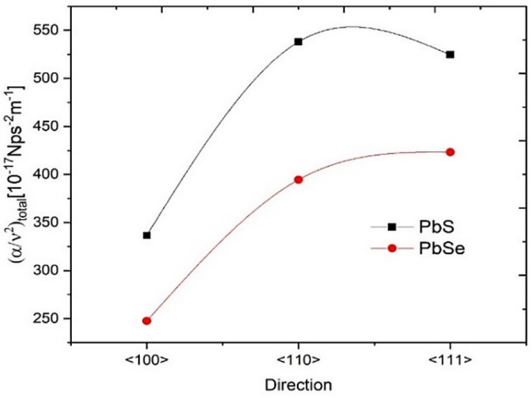

Figure 11. Total attenuation of PbS and PbSe along <100>, <110>, <111> direction

Figure 11 shows that PbS has higher attenuation values than PbSe, which imposes limitations on the applications of PbS. The ultrasonic attenuation coefficient shows that PbS is more suitable for applications that require minimal signal loss, such as in ultrasonic transducers and sensors. PbSe with large attenuation is used for applications where controlled energy dissipation is beneficial.

4. CONCLUSIONS

The Born potential model has been successfully applied to calculate the second- and third-order elastic constants and compared with existing results to validate the theory. The elastic constants are highest for PbSe indicating that PbSe is highly elastically stable. Pugh index, Cauchy pressure and Poisson ratio confirm that PbS and PbSe are brittle in nature in the temperature range 0-300 K. Zener anisotropy index indicates that PbS and PbSe are anisotropic. The thermal performance of PbS is better due to higher values of thermal conductivity and Debye temperature. The relaxation time is of the order of 10^{-11} second which validates the semiconducting nature of PbS and PbSe in the temperature range 0- 300K and in ⟨100⟩, ⟨110⟩ and ⟨111⟩ direction. The thermal energy to acoustic energy conversion is highest in the ⟨111⟩ direction for PbX. The attenuation coefficient of PbS is lower than that of PbSe. The total attenuation for both PbS and PbSe is the lowest in the⟨100⟩ direction, indicating that the ⟨100⟩ direction is the most suitable direction for wave propagation. These results offer a baseline for designing and improving PbX-based thermoelectric materials, sensors, and non-destructive ultrasonic evaluation systems.

Acknowledgements

The authors (PS, AS, DS) thank the Department of Science and Technology, New Delhi for providing support under DST-PURSE scheme (SR/PURSE/2024/230) to V.B.S. Purvanchal University, Jaunpur, Uttar Pradesh. Author Bin-Omran acknowledges the ongoing research funding program (ORF-2026-82), King Saud University, Riyadh, Saudi Arabia. For the purpose of open access, the author(s) have applied a Creative Commons Attribution (CC-BY) license to any Author Accepted Manuscript version arising from this submission.

ORCID

Sudhanshu Tripathi, https://orcid.org/0000-0001-8865-7987; **Praveen Singh,** https://orcid.org/0009-0006-7119-9119;
Anurag Singh, https://orcid.org/0009-0001-3877-9510; **Devraj Singh,** https://orcid.org/0000-0002-3011-2375;
R. Khenata, https://orcid.org/0000-0002-5573-1711; **M. Boudjelal,** https://orcid.org/0000-0001-6844-3789;
H. Meradji, https://orcid.org/0000-0002-3359-3725; **Ajit Kumar Maddheshiya,** https://orcid.org/0009-0005-0225-9387;
Shanay Rab, https://orcid.org/0000-0003-1203-6492; **M. Faizan,** https://orcid.org/0000-0003-1600-5095;
S. Bin-Omran, https://orcid.org/0000-0001-6097-2344

REFERENCES

[1] N. M. Ravindra, and V.K. Srivastava, "Properties of PbS, PbSe, and PbTe," Physica Status Solidi (a), **58**(1), 311(1980). https://doi.org/10.1002/pssa.2210580139

[2] Y. Zhang, X. Ke, C. Chen, J. Yang, and P.R.C. Kent, "Thermodynamic properties of PbTe, PbSe, and PbS: First-principles study," Physical Review B, **80**(2), 024304 (12 pp.) (2009). https://doi.org/10.1103/PhysRevB.80.024304

[3] L.D. Zhao, S.H. Lo, J. He, H. Li, K. Biswas, J. Androulakis, C.I. Wu, T.P. Hogan, D.Y. Chung, V.P. Dravid, and M.G. Kanatzidis, "High performance thermoelectrics from earth-abundant materials: Enhanced figure of merit in PbS by second phase nanostructures," Journal of the American Chemical Society, **133**(50), 20476–20487 (2011). https://doi.org/10.1021/ja208658w

[4] K. Biswas, J. He, I.D. Blum, C. I Wu, T.P.Hogan, D.N.Seidman, V.P. Dravid, and M.G. Kanatzidis, "High-performance bulk thermoelectrics with all-scale hierarchical architectures," Nature, **489**(9), 414-418 (2012). https://doi.org/10.1038/nature11439

[5] Kang, and F.W. Wise, "Electronic structure and optical properties of PbS and PbSe quantum dots," Journal of the Optical Society of America B, **14**(7), 1632-1646 (1997). https://doi.org/10.1364/JOSAB.14.001632
[6] S. Tripathi, R. Agarwal, and D. Singh, "Nonlinear elastic, ultrasonic and thermophysical properties of lead telluride," International Journal of Thermophysics, **40**(8), 78 (2019). https://doi.org/10.1007/s10765-019-2539-8
[7] Zair, B. E. Nabil Brahmi, and S. Bekhechi, "Structural, electronic and thermoelectric properties of PbS, PbSe and their ternary alloy $PbSe_{1-x}S_x$," International Journal of Modern Physics C, **34**(10), 2350130 (2023). https://doi.org/10.1142/S0129183123501309
[8] P. Priyadarshini, D. Sahoo, and R. Naik, "A review on the optical properties of some germanium-based chalcogenide thin films and their applications," Optical and Quantum Electronics, **54**(3), 166191 (2022). https://doi.org/10.1007/s11082-022-03564-4
[9] J. M. Skelton, S. C. Parker, A. Togo, I. Tanaka, and A. Walsh, "Thermal physics of the lead chalcogenides PbS, PbSe, and PbTe from first principles," Physical Review B, **89**(20), 205203 (2014). https://doi.org/10.1103/PhysRevB.89.205203
[10] S. Anwar, S. Anwar, and B. K. Mishra, "Effect of bath temperature on PbSe thin films prepared by chemical synthesis," Materials Science in Semiconductor Processing, **40**(Dec. 2015), 910-916 (2015). https://doi.org/10.1016/j.mssp.2015.07.077
[11] X. Chen, Y. B. Zhu, Z. Xing, G. Tang, and H. Fan, "Synthesis of PbSe nanostructures with different size and morphology and their electrochemical properties," Journal of Materials Science: Materials in Electronics, **27**(10), 1151–1157 (2016). https://doi.org/10.1007/s10854-015-3864-8
[12] H.D. Jahromi, and M. Moaddeli, "Lead sulfide: a new candidate for optoelectronics applications in the ultraviolet spectral range," Materials Research Express, **6**(11), 116220 (2019). https://doi.org/10.1088/2053-1591/ab513d
[13] S. Abe, "Phase transformation from PbS to PbSe: S in hot-wall deposition of nanocomposite thin film with evaporation sources of PbS and ZnSe," Discover Applied Sciences, **3**(1), 212 220 (2021). https://doi.org/10.1007/s42452-021-04236-w
[14] C.K. Bandoh, I. Nkrumah, F.K. Ampong, R.K. Nkrumah, and F. Boakye, "Effect of annealing on the structure and optical properties of lead selenide and cadmium selenide thin film prepared by chemical bath deposition," Chalcogenide Letters, **18**(2), 81-89 (2021). https://doi.org/10.15251/CL.2021.182.81
[15] B. Batu and T. Tamasgen, "Effects of thickness on optical and structural properties of lead sulfide (PbS) thin film prepared by chemical bath deposition," Journal of Natural Sciences Research, **13**(9), 1-6 (2022). https://doi.org/10.7176/JNSR/13-9-01
[16] N. Khusayfan, H. Khanfar, and R.N. Alharbi, Fabrication and characterization of lead selenide thin film as X-ray sensors, photovoltaic devices and microwave resonators," Applied Physics A, **129**(9), 639 (8 pp.) (2023). https://doi.org/10.1007/s00339-023-06909-2
[17] C. Yang, X. Zhang X, P. Li, S. Chen, and S. Feng, "Electrochemical synthesis of hierarchical porous PbSe film and its infrared photodetection properties," Applied Surface Science, **663**, 160145 (2024). https://doi.org/10.1016/j.apsusc.2024.160145
[18] K. Brugger, "Thermodynamic definition of higher order elastic coefficients," Physical Review, **133,** A1611-A1612 (1964). https://doi.org/10.1103/PhysRev.133.A1611
[19] G. Leibfried, and W. Ludwig, "Theory of anharmonic effects in crystals," in: *Solid State Physics*, vol. 12, edited by F. Seitz, and D. Turnbull (Academic Press, New York, 1961), pp. 275-444. https://doi.org/10.1016/S0081-1947(08)60656-6
[20] P.B. Ghate, "Third order elastic constants of alkali halide crystals," Physical Review, **139**(5A)**,** A1666-A1674 (1965). https://doi.org/10.1103/PhysRev.139.A1666
[21] S. Mori, and Y. Hiki, "Calculation of the third- and fourth-order elastic constants of alkali halide crystals," Journal of the Physical Society of Japan, **45**(5), 1449-1456 (1978). https://doi.org/10.1143/JPSJ.45.1449
[22] J. Bala, S.P. Singh, A.K. Verma, D.K. Singh, and D. Singh, "Elastic, mechanical and ultrasonic studies of boron monopnictides in two different structural phases," Indian Journal of Physics, **96**(11), 3191-3200 (2022). https://doi.org/10.1007/s12648-021-02278-9
[23] S. Tripathi, R. Agarwal, and D. Singh, "Elastic, mechanical and ultrasonic properties of nanostructured IIIrd group phosphides," MAPAN – Journal of Metrology Society of India, **36**(1), 97–107 (2021). https://doi.org/10.1007/s12647-020-00412-2
[24] Singh, and D. Singh, "Investigation of alkali halide crystals AX (A = Li, Na, K; X = F, Cl, Br) by elastic, mechanical and ultrasonic analysis," Zeitschrift für Naturforschung A, **78**(10), 947-958 (2023). https://doi.org/10.1515/zna-2023-0138
[25] Cz. Jasiukiewicz, and V. Karpus, "Debye temperature of cubic crystals," Solid State Communications, **128**(5), 167-169 (2003), https://doi.org/10.1016/j.ssc.2003.08.008
[26] C. Tripathy, D. Singh, and R. Paikaray, "Behaviour of elastic and ultrasonic properties of curium monopnictides," Canadian Journal of Physics, **96**(5), 513-518 (2018). https://doi.org/10.1139/cjp-2017-0491
[27] J. Bala, and D. Singh, Elastic and ultrasonic properties of fermium monopnictides," Engineering and Applied Science Research, **47**(2), 182-189 (2020). https://ph01.tci-thaijo.org/index.php/easr/article/view/216247
[28] D.E. Gray, *American Institute of Physics Handbook*, 3rd ed. (McGraw-Hill, New York, 1972).
[29] D. Singh, "Behaviour of acoustic attenuation in rare-earth chalcogenides," Materials Chemistry and Physics, **115**(1), 65-68 (2009). https://doi.org/10.1016/j.matchemphys.2008.11.025
[30] Y. I. Hwang, D. Sung, H.J. Kim, S. J. Song, K. B. Kim, and S. S. Kang, "Propagation and attenuation characteristics of an ultrasonic beam in dissimilar metal welds," Sensors, **20**(21), 6259-6276 (18 pp.) (2020). https://doi.org/10.3390/s20216259
[31] W. P. Mason, Effect of impurities phonons processes on the ultrasonic attenuation of germanium crystal, quartz and silicon, In: *Physical Acoustics. vol III B*, edited by W. P. Mason (Academic Press, New York, 1965), pp 237-286. https://doi.org/10.1016/B978-0-12-395669-9.50013-8
[32] D. Singh, A. Kumar, V. Bhalla, and R. K. Thakur, "Mechanical and thermophysical properties of actinide monocarbides," Modern Physics Letters B, **32**(21), 1850248 (2018). https://doi.org/10.1142/S0217984918502482
[33] D. Singh, D.K. Pandey, D. K. Singh, and R.R. Yadav, "Propagation of ultrasonic waves in neptunium monochalcogenides," Applied Acoustics, 72(10), 737-741 (2011). https://doi.org/10.1016/j.apacoust.2011.04.002
[34] E.M. El-Menyawy, G.M. Mahmoud, R.S. Ibrahim, F.S. Terra, H. El-Zahed, and I.K. El Zawawi, "Structural, optical and electrical properties of PbS and PbSe quantum dot thin films," Journal of Materials Science: Materials in Electronics, **27**(10), 10070-10077 (2016). https://doi.org/10.1007/s10854-016-5080-6
[35] M.P. Tosi, Cohesion of ionic solids in the Born model, In: *Solid State Physics, vol 16*, edited by F. Seitz, and D. Turnbull (Academic Press, New York, 1961), pp. 1–120. https://doi.org/10.1016/S0081-1947(08)60515-9
[36] J.F. Nye, *Physical Properties of Crystals: Their Representation by Tensors and Matrices*. (Oxford University Press, New York 1985).

[37] C.S.G. Cousins, "New relations between elastic constants of different orders under central force interactions," Journal of Physics C: Solid State Physics, **4**(10), 1117-1123 (1971). https://doi.org/ 10.1088/0022-3719/4/10/020
[38] A. Singh, S. Tripathi, and D. Singh, "Elastic, thermophysical and ultrasonic investigation of tin monochalcogenides," Modern Physics Letters B, **38**(32), 2450280 (2024). https://doi.org/10.1142/S0217984924502804
[39] O. Madelung, M. Schulz, and H. Weiss, editors, *Numerical Data and Functional Relationships in Science and Technology Landolt-Bornstei, New Series,* vol. 17, (Springer, Berlin, 1983).
[40] H. Takia, M.A. Rahman, R. Moshiur, M.M. Rahaman, and K. Hossen, "The substantive characteristics of layered PbX (X= S, Se, and Te) compounds: An ab-inito investigations," International Journal of Physics, **10**(2), 102-110 (2022). https://doi.org/10.12691/ijp-10-2-3
[41] T. Seetawan, and H. Wattanasarn, "First principle simulation mechanical properties of PbS, PbSe, CdTe and PbTe by molecular dynamics," Procedia Engineering, **32**, 609-613 (2012). https://doi.org/10.1016/j.proeng.2012.01.1316
[42] P. Ravindran, L. Fast, P. Korzhavyi, B. Johansson, J. Wills and O. Eriksson, "Density functional theory for calculation of elastic properties of orthorhombic crystals: Application to $TiSi_2$," Journal of Applied Physics, **84**(9), 4891(1998). https://doi.org/10.1063/1.368733
[43] H. Ozisik, E. Deligoz, G. Surucu, and H.B. Ozisik, Anisotropic elastic and vibrational properties of Ru_2B_3 and Os_2B_3: a first-principles investigation," Materials Research Express, **3**(7), 076501 (2016). https://doi.org/10.1088/2053-1591/3/7/076501
[44] Kumar, "Ultrasonic velocity ratio: An effective tool for in-situ materials characterization," Acta Acustica united with Acustica, **104**(2), 251-258 (2018). https://doi.org/10.3813/AAA.919167
[45] Y. L. Pei, and Y. Liu, "Electrical and thermal transport properties of Pb-based chalcogenides: PbTe, PbSe, and PbS," Journal of Alloys and Compounds, **514**(2), 40-44(2012). https://doi.org/10.1016/j.jallcom.2011.10.036
[46] L. Wei, J. F. Chen, Q. Y. He, and W. Teng, "Study of lattice thermal conductivity of PbS," Journal of Alloys and Compounds, **584**(1), 381-384 (2014). https://doi.org/10.1016/j.jallcom.2013.09.081
[47] S. Johnsen, J. Q. He, J. Androulakis, V. P. Dravid, I. Todorov, D. Y. Chung, and M. G. Kanatzidis, "Nanostructures boost the thermoelectric performance of PbS," Journal of the American Chemical Society, **133**(10), 3460–3470 (2011). https://doi.org/10.1021/ja109138p
[48] L.D. Zhao, S.H. Lo, J.Q. He, H. Li, K. Biswas, J. Androulakis, C. Wu, *et al*., "High performance thermoelectrics from earth-abundant materials: Enhanced figure of merit in PbS by second phase nanostructures," Journal of the American Chemical Society, **133**(50), 20476–20487 (2011). https://doi.org/10.1021/ja208658w
[49] D. Singh, R.R. Yadav, and A.K. Tiwari, Ultrasonic attenuation in semiconductors," Indian Journal of Pure and Applied Physics, **40**(12), 845-849 (2002). https://nopr.niscpr.res.in/handle/123456789/26219
[50] K. Ono, "A comprehensive report on ultrasonic attenuation of engineering materials, including metals, ceramics, polymers, fiber-reinforced composites, wood, and rocks," Applied Sciences, **10**(7), 2239 (52 pp.) (2020). https://doi.org/10.3390/app10072230
[51] K.M. Raju, R.K. Srivastava, A. Kumar, and S. Devi, "Acoustical investigation of lead chalcogenides," Physica B: Condensed Matter, **405**(23), 4855-4857 (2010). https://doi.org/10.1016/j.physb.2010.09.018

НЕРУЙНУЮЧА УЛЬТРАЗВУКОВА ОЦІНКА ТЕМПЕРАТУРО-ЗАЛЕЖНИХ МЕХАНІЧНИХ І ПРУЖНИХ ВЛАСТИВОСТЕЙ СПОЛУК PbX (X = S, Se)

Судханшу Тріпаті[1], Правін Сінгх[2], Анураг Сінгх[2,3], Деврадж Сінгх[2], Р. Кхената[4,5], М. Буджелал[4], Х. Мераджи[6], Аджит Кумар Маддхешія[7], Шанай Раб[8], М. Файзан[9], С. Бін-Омран[10]

[1]Інститут інформаційних технологій Аміті, Університет Аміті, Сектор-125, Нойда – 201313, Уттар-Прадеш, Індія
[2]Кафедра фізики, Інститут фізичних наук ім. професора Раджендри Сінгха (Раджу Бхайя), Університет Вір Бахадур Сінгх Пурванчал, Джаунпур-222003, UP, Індія
[3]Факультет фізики, Державний коледж, Бабхані, Сонбхадра-231208, UP, Індія
[4]Лабораторія фізики квантової механіки та математичного моделювання (LPQ3M), Університет Маскара, Маскара, 29000, Алжир
[5]Алжирська академія наук і технологій, 04- Шлях світу, Гідра-Алжир16000, Алжир
[6]Лабораторія LPR, Департамент фізики, Факультет природничих наук, Університет Баджі Мохтар, Аннаба, Алжир
[7]Кафедра фізики Аллахабадського університету, Праяградж-211002, Індія
[8]Школа архітектури, технологій та інженерії, Брайтонський університет, BN24AT, Великобританія
[9]Школа матеріалознавства та інженерії Цзилінського університету, Чанчунь, 130012, Китай
[10]Кафедра фізики та астрономії, коледж науки, Університет короля Сауда, а/с 2455, Ер-Ріяд, 11451, Саудівська Аравія

Проведено всебічне дослідження пружних, механічних та термоакустичних властивостей монохалькогенідів свинцю PbX (X = S, Se) вздовж основних кристалографічних напрямків ⟨100⟩, ⟨110⟩ та ⟨111⟩ у діапазоні температур 0–300 K з використанням ультразвукового неруйнівного методу оцінки. Пружні постійні другого та третього порядку (SOEC та TOEC) були розраховані з використанням кулонівської та борнівсько-майєрівської потенційних моделей, що підтверджують пружну стабільність досліджуваних матеріалів. Похідні механічні параметри та швидкості ультразвуку були отримані з SOEC, що вказує на тендітну механічну поведінку, засновану на коефіцієнті Кнута. При температурі 300 K були визначені температура Дебая, швидкість Дебая, теплопровідність грат, параметр акустичної нелінійності та коефіцієнт ультразвукового згасання вздовж досліджуваних напрямків. Серед усіх напрямків орієнтація ⟨111⟩ показала найвищу температуру Дебая та швидкість Дебая. Домінуючим механізмом ультразвукового згасання було ідентифіковано механізм типу Ахіезера, що підкреслює його роль у тепловіддачі та акустичному демпфуванні. Результати показують, що PbSe має чудову пружну жорсткість, тоді як PbS демонструє підвищену теплопровідність і сильніші фононні взаємодії. Ці характеристики підкреслюють потенціал PbS та PbSe для застосування в термоелектричних і ультразвукових сенсорних технологіях.

Ключові слова: *монохалькогеніди свинцю; пружні властивості; механічні константи; теплопровідність; ультразвукове згасання*